AUREA IÑURRITEGUI MARROQUIN | Crowned spherical gear couplings working at high misalignment applications: Geometry generation, loaded tooth contact analysis and experimental validation

Mondragon Unibertsitatea

DOCTORAL THESIS

CROWNED SPHERICAL GEAR COUPLINGS WORKING AT HIGH MISALIGNMENT APPLICATIONS: GEOMETRY GENERATION, LOADED TOOTH CONTACT ANALYSIS AND EXPERIMENTAL VALIDATION

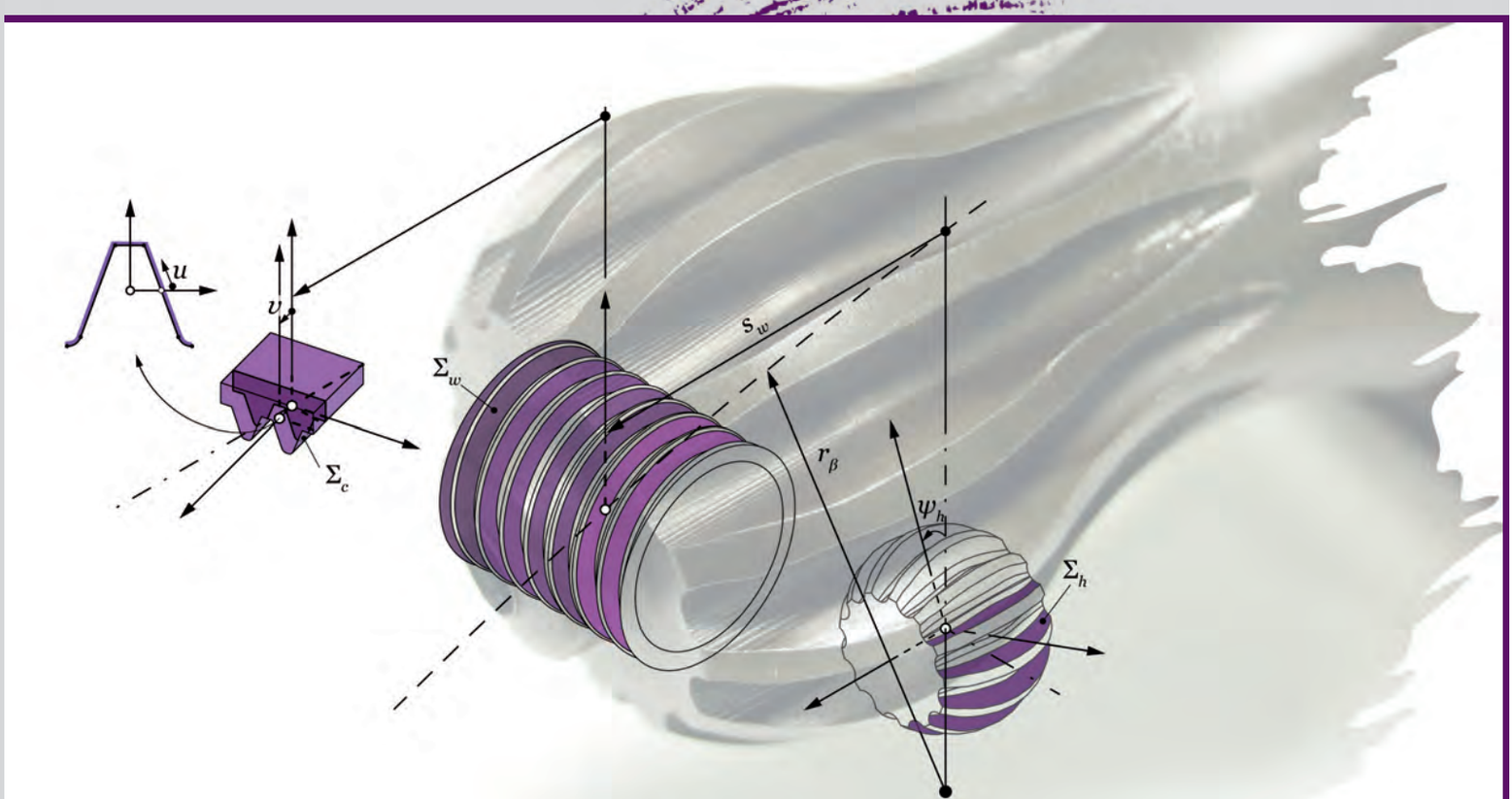

AUREA IÑURRITEGUI MARROQUIN | Arrasate-Mondragón, 2023

Mondragon Unibertsitatea

Faculty of Engineering

Mechanical and Industrial Production Department

Division of Mechanical Design

Ph.D. Dissertation

Crowned spherical gear couplings working at high misalignment applications

Geometry generation, loaded tooth contact analysis, and experimental validation

---

by:

Aurea Iñurritegui Marroquin

Supervised by:

Dr. Jon Larrañaga Amilibia

Dr. Aitor Arana Ostolaza

A Thesis submitted in partial fulfillment of the requirements for the degree of

Doctor of Philosophy in Applied Engineering

4th January 2023

Gracias a vosotros,

Con todo mi cariño para mami y papi...

Abstract

Spherical gear couplings are commonly used mechanical components to transmit power between highly misaligned rotating shafts. Their main geometry characteristic is the appearance of undercut sections on the hub when machining a high amount of longitudinal crowning. This possibility is even more significant when gear couplings with a low number of teeth are manufactured directly on the shaft. Current geometry generation models in the literature avoid the generation of undercut sections. Furthermore, it is a matter of disagreement among the existing models, since the generated tooth surfaces of the hub vary depending on the analytical model employed. In fact, these variations influence the contact characteristics and the load distribution of the gear coupling.

Moreover, gear couplings working at high misalignment angles cause a drastic decrease in the number of teeth in contact. In consequence, higher tooth-root stresses in those in contact are suffered and result in the failure of the component by tooth root breakage. However, the scientific literature has focused on gear couplings working in applications where the misalignment angles are below 1°, thus mainly centered on failures other than bending fatigue, such as fretting or surface wear. Thus, there is a lack of sizing methods oriented to higher misalignment angles, therefore current components working at these conditions may be oversized, or which is even more critical, sometimes undersized.

This thesis covers the existing gap in the generation of the crowned hub tooth surface geometry, with the development of a novel mathematical model which assesses the complete thread surface of the cutting tool and considers its cutting tool path. Moreover, this model can accurately generate undercut profiles that may appear on the hub.

Furthermore, the achievable misalignment angle of this type of gear coupling is discussed, assessing the influence of the geometry and manufacturing variables on this value. It gives an overview of the preliminary design phase and helps the designer to find out the most suitable design parameters to avoid as much as possible further geometrical issues, without compromising the achievable maximum misalignment angle.

Finally, a loaded tooth contact analysis is carried out with a finite element model to understand the load distribution among the teeth and the bending tooth root stress in terms of the applied torque and the working misalignment angle. Moreover, the results are experimentally correlated with a real gear coupling which works in such high misalignment applications.

The results from the geometry generation model reveal that deviations between the generated crowned tooth surfaces with models existing in the literature are significant and modify the undercut cross sections beginning or even the contact conditions. At the same time, it is proved that the generated geometry is in good agreement with experimental data and highlights that the existing models in the literature to determine the maximum misalignment angle are not applicable for highly crowned gear couplings. Moreover, from the loaded tooth contact analysis, it is observed that different mechanical behaviors arise at low or high misalignment angles since teeth in the pivoting position lose contact. This results in a tooth root stress history change from a sinusoidal cycle to a pulsating cycle, which may affect the fatigue life of the gear coupling.

In conclusion, this research analyzes in depth the geometry and mechanical behavior of gear couplings working in applications at high misalignment angles ($\gamma \geq 3°$) with the developed analytical and numerical models. Also, demonstrates that the attained results differ from those obtained when applying current generating and rating standards.

Keywords:

spherical gear coupling, high misalignment, geometry generation, undercutting, load distribution, tooth root bending stress, finite element analysis.

Resumen

Los acoplamientos dentados abombados son componentes mecánicos frecuentemente utilizados para la transmisión de potencia entre ejes giratorios desalineados. La característica geométrica más relevante es la aparición de secciones con interferencia de tallado al mecanizar la gran cantidad de abombamiento longitudinal. La posibilidad aumenta cuando acoplamientos con un reducido número de dientes se mecanizan directamente sobre el eje del acoplamiento. Sin embargo, la mayoría de modelos analíticos evitan generar secciones con interferencia de tallado. Además, existe desacuerdo entre los modelos existentes más desarrollados puesto que la geometría de la superficie del diente generada varía en función del modelo analítico empleado. Asimismo, estas diferencias conllevan un efecto en las condiciones de contacto y la distribución de carga.

Por otro lado, los acoplamientos que trabajan a elevados ángulos de desalineación presentan una drástica disminución del número de dientes en contacto durante su funcionamiento, lo que implica tensiones del pie mas altas en aquellos dientes en contacto y origina el fallo por fatiga del pie. Sin embargo, la bibliografía se centra en acoplamientos que trabajan en ángulos de desalineación inferiores a 1°, por lo que está enfocada a otros tipos de fallos, e.g., al fallo por desgaste o fretting. Es por ello que existe una carencia de métodos de dimensionamiento para acoplamientos que trabajan en desalineaciones altas, y los componentes que operan en estas condiciones pueden estar sobredimensionados, o a veces subdimensionados.

Esta tesis recoge un modelo analítico para la generación de la geometría de las superficies dentadas abombadas, considerando la superficie helicoidal completa de la fresa madre y la trayectoria de la herramienta de tallado. Asimismo, el modelo genera con precisión las secciones con interferencia de tallado que puedan aparecer en el eje del acoplamiento.

Se discute el ángulo de desalineación alcanzable, mostrando la influencia de los parámetros geométricos y del proceso de fabricación en este valor. Esto ofrece una visión general de la fase de diseño preliminar, y permite a los diseñadores escoger los parámetros de diseño con los que evitar en la medida de lo posible problemas geométricos (apuntamiento o interferencia de tallado), sin comprometer el ángulo de desalineación máximo alcanzable.

Por último, se realiza un análisis de contacto bajo carga mediante el desarrollo de un modelo de elementos finitos para comprender la distribución de carga y las tensiones en el pie del diente en función del par aplicado y el ángulo de desalineación. Además, los resultados se contrastan experimentalmente con un acoplamiento dentado abombado que trabaja a grandes ángulos de desalineación.

Los resultados de los modelos de generación de la geometría demuestran que las desviaciones entre las superficies dentadas generadas con los modelos existentes en la literatura son notables, y modifican el inicio de la interferencia de tallado o incluso las condiciones de contacto. Asimismo, se ha comprobado que la geometría generada está en buen acuerdo con la geometría medida y se evidencia que los modelos de la bibliografía para determinar el ángulo de desalineación máxima no son aplicables para acoplamientos dentados abombados. Por otra parte, a partir del análisis de contacto bajo carga se observan diferentes comportamientos mecánicos a bajos o altos ángulos de desalineación, ya que los dientes en la posición de pivotamiento pierden el contacto a medida que el ángulo de desalineación aumenta. La consecuencia es un cambio en el ciclo de las tensiones en el pie del diente, que pasa de tener un ciclo sinusoidal a un ciclo pulsante, el cual puede afectar en la vida a fatiga del componente.

En conclusión, esta tesis analiza en profundidad la geometría y el comportamiento mecánico de acoplamientos dentados que trabajan en desalineaciones angulares altas ($\gamma \geq 3°$) mediante los modelos analíticos y numéricos desarrollados. Además, demuestra que los resultados alcanzados aplicando las normativas vigentes difieren en gran medida de los obtenidos con los modelos planteados.

Palabras clave:

acoplamiento dentado abombado, desalineación elevada, generación de la geometría del diente, interferencia de tallado, distribución de carga, tensión del pie, análisis por elementos finitos

Laburpena

Abonbamendu handiko horzdun akoplamenduak desalineazio angeluar handiko ardatz birakorren artean potentzia transmititzeko erabiltzen diren elementu mekanikoak dira. Beraien ezaugarri geometriko nagusia abonbamendua mekanizatzerakoan hortzen oinean agertzen den interferentzia da. Hau gertatzeko aukera handitu egiten da hortz kopuru txikiko akoplamenduak zuzenean ardatzean mekanizatzen direnean. Bibliografian dauden modelo gehienak oineko interferentziak sortzea saihesten dute. Gainera, modelo aurreratuenen artean desadostasunak daude, sortutako hortzaren geometria desberdina baita erabilitako eredu analitikoaren arabera. Izan ere, desberdintasun horiek eragina dute hortzen arteko karga banaketan edota kontaktu baldintzetan.

Bestalde, desalineazio angeluar handietan lan egiten duten akoplamenduetan kontaktuan dauden hortz kopurua nabarmen murrizten da, kontaktuan geratzen diren hortzen oineko tentsioak handituz eta ondorioz hortz oinaren haustura eraginez. Literatura 1° azpiko desalineazio angeluarretan zentratzen da gehienbat, ondorioz, beste mota bateko akatsak ikertzen ditu, hala nola, higadura edo gainazal nekea. Alabaina, ez dago desalineazio angelu handiagoetara dimentsionatzeko metodorik. Beraz, baldintza horietan lan egiten duten egungo elementuak gaindimentsionatuta egon daitezke, edo are kritikoagoa dena, noizbehinka azpidimentsionatuta.

Tesi honetan, aurrez aipatutako baldintzetan lan egiteko behar diren hortzen geometria generatzeko modelo analitiko bat garatu da. Eredu honek, fresa amaren gainazal helikoidal osoa eta beronen ibilbidea hartzen ditu kontuan. Horrez gain, modeloa gai da akoplamenduan ager daitezkeen hortzen oineko interferentziak zehaztasunez sortzeko.

Horrez gain, abonbamendu handiko horzdun akoplamenduek era egokian lan egin dezaten gehieneko desalineazio angeluar onargarria eztabaidatzen da, parametro geometrikoek eta fabrikazio prozesuak duten eragina aztertuz. Honek aurretiko diseinu fasearen ikuspegi orokorra eskaintzen du. Bide batez, diseinatzailearentzat erreminta baliagarria da akoplamenduarentzat parametro egokiak hautatzen laguntzen diolako arazo geometrikoak saihesteko.

Azkenik, kargapeko kontaktuaren analisia egin da elementu finituen modelo bat garatuz. Honek, aplikatutako momentuaren eta desalineazio angeluarraren arabera karga banaketa eta hortzaren oineko tentsioak nola aldatzen diren ezagutzea ahalbidetzen du. Gainera, emaitzak esperimentalki egiaztatu dira desalineazio angeluar handietan lan egiten duen abonbamendu handiko horzdun akoplamendu batekin.

Geometria sortzeko modeloaren emaitzek, literaturako ereduekin sortutako hortzen gainazal abonbatuen arteko desbiderapenak esanguratsuak direla erakusten dute. Gainera, desbiderapen hauek oineko interferentziaren hasieran eta kontaktu baldintzetan eragina dutela frogatu da. Era berean, generatutako geometria neurtutakoarekin bat datorrela egiaztatu da eta agerian geratzen da bibliografian dauden desalineazio angeluar maximoa kalkulatzeko modeloak ez direla aplikagarriak abonbamendu handiko akoplamenduentzat. Bestalde, kargapeko kontaktuaren analisitik abiatuta, desalineazio angelu baxuetan eta altuetan portaera mekaniko desberdinak ikusi dira; izan ere, pibotatze-posizioan dauden hortzek kontaktua galtzen dute desalineazio angelua handitzean. Honek hortzaren oineko tentsioen ziklo mota aldatzea dakar, ziklo sinusoidal batetik ziklo pultsatzaile batera igaroz, eta nekearekiko portaera aldatuz.

Laburbilduz, tesi honek sakon ikertzen ditu desalineazio angeluar handietan ($\gamma > 3^\circ$) lan egiten duten abonbamendu handiko horzdun akoplamenduen geometria eta portaera mekanikoa, horretarako garatutako modelo analitiko eta numerikoen bitartez. Horrez gain, lorturiko emaitzak gaur egun indarrean dauden araudiak aplikatuta lortzen diren emaitzekin konparatzen ditu, desberdintasun nabariak daudela ondorioztatuz.

Hitz klabeak:

abonbamendu handiko horzdun akoplamendua, desalineazio handia, hortzaren geometria generazioa, oineko interferentzia, hortzaren oineko tentsioa, elementu finituen analisia.

No one who achieves success does so without acknowledging the help of others.
—Alfred North Whitehead

Acknowledgments

There is no big science behind these lines, but they are a little proof of the support and encouragement I had along this journey. A lot of people came across during these years and I hope I have shown my gratitude personally to all of you. Now I would like to leave some of these feelings and thank you words written down so that if one day someone who didn't know me reads this document, he/she will realize all the people who in one way or another have helped me to complete this work. I really wish and trust I leave no one behind in the following paragraphs.

Gracias por todos los consejos brindados, el tiempo que aún no teniéndolo me habéis dedicado y la experiencia compartida durante estos años a mis directores de tesis (oficiales y no oficiales). Gracias a Jon, Aitor e Ibai por confiar a veces más que yo misma en lo que podía conseguir y animarme cada día a superar nuevos retos. Jon, por todo tu apoyo, tantas horas peleándonos con los ± 1 del mallado y esos cafés motivacionales cuando no pasaba por mis mejores momentos. Aitor, por la enciclopedia andante que eres, por hacer lo difícil fácil y aconsejarme en los momentos de bloqueo. Ibai, por tu disposición siempre para ir más allá, cuestionar los resultados hasta dar con la incógnita y por darte cuenta de todos esos detalles de los que la mayoría de los mortales ni se habían percatado. Gracias por estas y otras tantas y tantas...

Diseinu Mekanikako departamentuarekin batera, eskerrik asko Mondragon Unibertsitateari tesi hau betetzeko aukera emateagatik, laguntza ekonomikoarengatik, bertan eskuragarri izan ditudan software eta kalitate handiko laborategi eta ekipamendu teknologikoagatik.

I would also like to dedicate part of this section to thank Professor Ignacio González-Perez who shared all his expertise during the research stay I did at the Polytechnic University of Cartagena. I will always remember his patience, commitment, and the good advice given. Also, thank you

for being a friend and such a good hiking planner in Murcia during the hard times of the covid pandemic.

Pero todo lo anterior no hubiese sido posible sin mis papis. Quisiera agradecer de todo corazón el cariño, fuerza, amor, comprensión, paciencia, apoyo, ánimo y un largo etcétera infinitas e incondicionales que mis padres me han brindado siempre y en especial durante estos años. Esos días cuando os contaba los problemas que tenía programando en Matlab para generar la superficie de la famosa muñequilla, me mirabais con cara de asombro y admiración, y pese a no estar segura de si me habíais entendido, erais y siempre sois capaces de motivarme y animarme a intentarlo otra vez al día siguiente. Cada logro de este camino ha sido celebrado por ellos como si hubiesen estado peleándose cada día con el posicionamiento de los nodos en el mallado de elementos finitos, con las ecuaciones diferenciales o con las medidas de las galgas. No tengo espacio para escribir todos esos momentos que me han animado y ayudado a lograr alcanzar el final de este trayecto, pero solo quiero deciros: gracias, gracias y gracias. También quisiera dedicarle esta tesis a la memoria de mi abuela que falleció el día que me publicaron mi primer paper. Siempre le maravilló que estudiase tanto y me animo a seguir adelante.

Eskerrik asko ia tesi osoan zehar nirekin elkarlanean ibili den Irene Berganzo ikasleari. Pandemia garaian, simulazioak telematikoki egiten, eta ondoren entsegu esperimentalekin asko lagundu didazula badakizu. Plazer bat izan da zurekin lan egitea. Honekin batera eskerrik asko ere, Julen Maskarianori entseguetan eskainitako laguntzagatik. Eskerrik beroenak liburutegiko langileei aurkitu didazuen liburu, artikulu eta tesiengatik, hizkuntza guztietan eta batzuk hain zaharrak digitalizatuta ere ez zeudela.

Thank you to all my colleagues and friends from the university and outside of it that always supported me. Thank you to Ainara, Andrea, David, and Laura for those daily coffee or lunch breaks to unburden oneself or talk about refurbishing an apartment, wedding planning, Crossfit, or weekend plans. Also, thanks David for all the tips on the figures post-processing with Illustrator and your 3D vision. You know that when I started the thesis, I thought this software was useless... To those friends who from the distance have always encouraged me to follow my dreams and always believed in me. Thank you, Lucy & Rosemary, Kholoud & Arnaud, Anne, Maria & Joost and a long etc.

El éxito es tan solo la punta del iceberg de multitud de dudas, problemas a resolver, mucho esfuerzo y constancia, de determinación... ¡Y por eso os quiero dar las gracias a todos vosotros por impulsarme en el camino a la cima!

Declaration of Authorship

I hereby declare that this dissertation and the work described in it are the product of my own work and that, to the best of my knowledge, it contains no previously published material except where the necessary acknowledgments have been made by means of citations. This Ph.D. thesis has not been submitted for any other degree or diploma of Mondragon Unibertsitatea or other institutes of higher education. The copyright of this document including data, figures, tables, and text rests with the author, and all the assistance received in preparing it has been acknowledged. Researchers are free to copy, distribute or transmit the thesis on the condition that they attribute it appropriately, that they do not use it for commercial purposes, and that they do not alter, transform or build upon it.

Signed: *Aurea Iñurritegui Marroquin*

Arrasate-Mondragon, 4th January 2023

Contents

List of Figures

List of Tables

If we knew what we were doing, it would not be called research, would it?
—Albert Einstein

Nomenclature

Variables	Unit	Description
b	mm	face width of the gear coupling
b_{eff}	mm	effective face width of the gear coupling
C	-	number of teeth in contact
C_{eff}	-	number of effective teeth in contact
C_β	µm	amount of longitudinal crowning in the hub
d_p	mm	pitch diameter of the gear coupling
E_c	mm	center distance between the generating and generated surface in internal gears
F	N	applied force in the test bench
F_p	µm	pitch deviations
F_t	N	applied force in each tooth for tooth root stress calculation
F_α	µm	profile deviations
F_β	µm	lead deviations
f_a	mm/s	manufacturing axial feed
f_r	mm/s	manufacturing radial feed
f_w	rad/s	manufacturing rotational
h_{eff}	mm	effective tooth height
h_t	mm	hub tip height
j_n	rad	normal clearance
K_B	-	rim thickness factor
K_v	-	dynamic factor
k	-	clearance factor
k_a, Y_α	-	load application factor
k_F, κ, K_o	-	overload coefficient
k_{ls}, Z_δ	-	load sharing factor
k_m, K_H	-	load distribution factor
m_n	mm	normal module

P	kW	transmitted power
Q	-	manufacturing class
R	-	fatigue stress ratio
$\mathbf{r}$	mm	measured tooth profile vector
r_c	mm	crowning radius of the hub
r_p, r_g, r_h	mm	pitch radius of the gear coupling
$r_{p,w}$, r_w	mm	hob pitch radius
r_t	mm	hub tooth transverse crowning radius
r_β	mm	tool path radius
$s_{c1,2}$	mm	hub or sleeve space width
s_w	mm	hob displacement during hub generation
t_{c1}, s_l, t_{c2}	mm	hub or sleeve tooth width
u	mm	profile surface parameter
v	mm	lead surface parameter
v_c	mm/s	manufacturing cutting speed
Y, Y_s, Y_J, c_c	-	stress concentration factor
Y_β	-	helix angle influence factor
z	-	number of teeth in the gear coupling
Z_Q	-	quality factor
z_h	mm	axial position along the face width of the hub
Z_q, Y_F, α_{kk}, $\alpha_{k\phi}$, k_ϕ, K_s, c_b		form factor

α	rad	pressure angle
Γ	Nm	applied torque
$\Gamma_{\max}$	Nm	max load supported by the first teeth engaged
Γ_{avg}	Nm	average supported by each tooth of the gear coupling
γ	$^\circ$	misalignment angle
$\gamma_{\max}$	$^\circ$	maximum misalignment angle
Δ_{hw}	mm	vertical displacement of the hob during generation
δ	µm	geometry deviations of the tooth surface in the normal direction
$\delta_{\max}$	mm	max. contact point displacement from the middle section
ϵ	$^\circ$	experimental deviation for the measured max. misalignment
ε	-	crowning ratio
θ	rad	angular rotation of the node in the hub
θ_i	rad	angular position of the hub

λ_{w}	rad	hob lead angle
ξ	rad	jam angle [Guo13]
ρ	mm	hub profile radius
Σ_c		rack-cutter tooth surface
Σ_h		generated hub tooth surface
Σ_w		generating hob-thread tooth surface
σ_a	MPa	alternating stress
σ_m	MPa	mean stress
$\sigma_{\max}$	MPa	maximum tooth root stress
$\sigma_{\theta\theta}$	MPa	tooth root bending stress
ϕ_w	rad	hob rotation during hub generation
ψ_h	rad	generation parameter of the hub
ψ_w	rad	generation parameter of the hob
ω	rpm	rotational speed of the gear coupling

Coordinate systems	**Description**
$(x_f,\, y_f,\, z_f)$	cartesian fix coordinate system of the gear coupling
$(r,\, \theta,\, z_f)$	cylindrical coordinate system principal directions
$S_c,\, S_w,\, S_h,\, S_p$	auxiliary coordinate system for hub tooth surface generation

Acronym	**Description**
AGMA	American Gear Manufacturers Association
CMM	Coordinate Measuring Machine
DIN	*Deutsches Institut für Normung*
EAP	End of Active Profile
FE	Finite Element
ISO	International Organization for Standardization
LTCA	Loaded Tooth Contact Analysis
SAP	Start of Active Profile
TCA	Tooth Contact Analysis

The greatest challenge to any thinker is stating the problem in a way that will allow a solution.
—Bertrand Russell

1 | Introduction

This chapter introduces the main topics and objectives of the present Ph.D. thesis. It briefly defines the geometrical characteristics and working conditions of highly crowned gear couplings and determines the hypothesis and objectives that motivated the research. The chapter also provides background information and the motivation for the study. Highly crowned gear couplings are characterized by their longitudinal crowning to enable working in high misalignment angles and they may present undercut sections. The misalignment angle together with the undercut sections is responsible for the failure of these components by tooth root fatigue breakage. However, it is highlighted that scientific literature review has pointed toward working conditions with small misalignment angles, and little research has been done on high misalignment angles from the analytical, numerical, or experimental point of view. Finally, technical objectives are defined and the outline of this dissertation is described.

1.1 Background and framework

Current research trends in the industrial sector focus on the development of lighter, higher power density, and safer machines and components. Moreover, they must be as cheap as possible and require minimum maintenance. Addressing power transmission components in any kind of industry (transportation, energy, metallurgy, etc.), belts, gears, and couplings are the ones most commonly used and frequently their replacement is difficult and costly due to their inaccessibility (e.g., aircraft engine) [Mil17]. Among all types of couplings, this research is focused on gear couplings, which are used to transmit power between misaligned rotating shafts. They are preferred over other non-splined connections because of their high power density and capacity to accommodate axial, radial, or angular misalignments [Man86; Cor07; Hah14]. Their applications in industry are wide [Dud57b; Bro79]: wind power generation, trains, compressors, rolling mills, etc.

Involute teeth gear couplings consist of a toothed shaft (named hub in the following), meshed with an internal toothed gear (named sleeve) with the same number of teeth, equally spaced around the pitch circle and parallel to the axis of rotation. Fig. 1.1(a) shows a highly crowned spherical gear coupling, misaligned by γ angle. This is composed of a highly crowned toothed hub and a commonly straight sleeve [Ohs12; Gua19b]. They are manufactured with two main tooth profile modifications to allow working at misaligned conditions: the longitudinal crowning, which is defined by the amount of crowning (C_β) as stated in ISO 21771 [Int07] and depicted

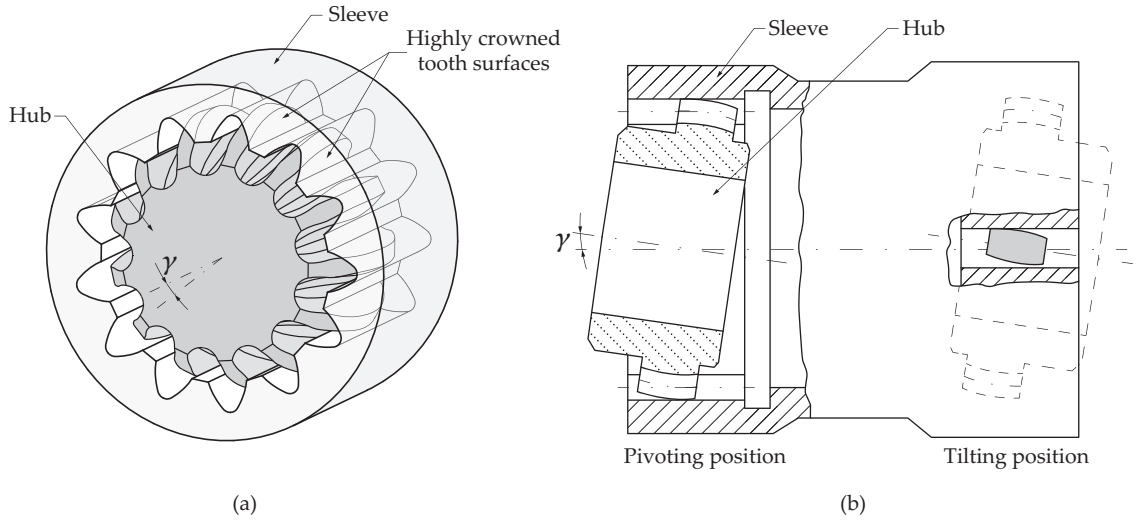

Figure 1.1: (a) a spherical gear coupling, and (b) characteristic angular positions in a misaligned gear coupling (adapted from [Glo10]).

in Fig. 1.2(c) and the tip crowning (Fig. 1.2(b)). These modifications are controlled by the manufacturing process and enable centering the contact along the face width, preventing tooth interference when pivoting around the sleeve (Fig. 1.1(b)).

The analytical generation of these types of geometries is carried out with mathematical models that are principally based on the rack-cutter edge geometry and use a one-parameter envelope model [Mit00; Kel14; Gua18]. However, they were never employed to generate highly crowned tooth surfaces, which require a small tool path radius (r_β) to produce such amount of crowning ($C_\beta \gg 100$ µm), as can be observed in Fig.1.2(b,c). Small tool path radii together with small parts where the hub teeth are manufactured directly on the shaft [Lar16; Ula18] introduce new problems to their generation including the appearance of singularities. As stated in [Lit04], the appearance of singular points on the generated surface is the warning that the surface may be undercut during the generation process. Nevertheless, earlier cited generation models avoid their generation.

Spherical gear couplings owe their name to the tip crowning of the gear blank, which gives them a spherical shape suitable to avoid interference during operation in misaligned conditions.

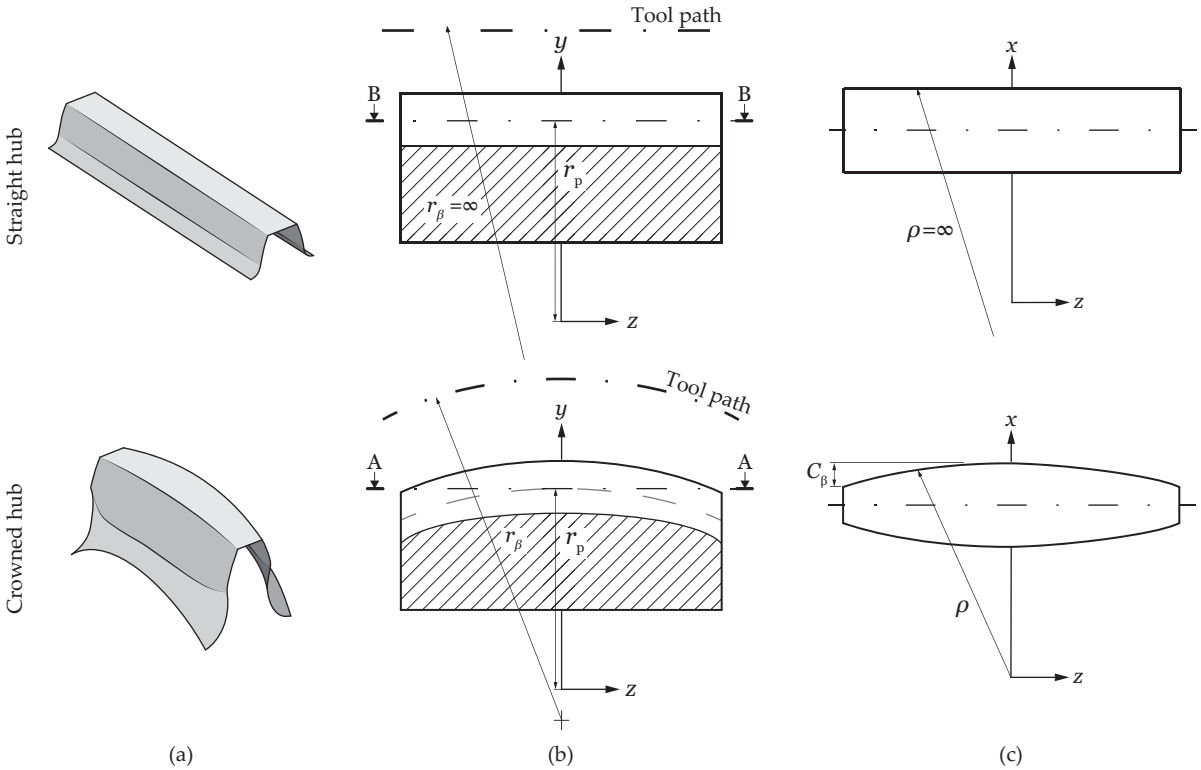

Figure 1.2: Tool path radius and generated longitudinal crowning for (a) straight and (b) circular tool paths (adapted from [Oct14]).

This can be observed in Fig. 1.1(b) where the gear coupling hub tooth surfaces require a spherical shape to enable the pivoting and avoid interference. In the same manner, the hub tooth surfaces need to be crowned for the tilting position.

In Fig. 1.2 a straight gear coupling hub tooth surface and that of a spherical crowned gear coupling can be compared. As observed, the straight tooth is characterized by an infinite transverse radius ($\rho = \infty$), manufactured by a straight tool path ($r_\beta = \infty$). This is the most frequent type of gear coupling used in industry, e.g., in wind turbines. They are straight or with a small amount of crowning, adapted to low misalignment applications below 1° (caused by operating vibrations [Guo16], manufacturing tolerances, or assembly errors [Alf06]). In consequence, the longitudinal sliding occurring between the hub and the sleeve tooth surfaces causes fretting damage [Xue19; Lee22; Gua22; Med02a; Err12; Bak05] and surface wear [Ku75; Med02b; Guo16; Xia22], which is enhanced by the improper lubrication. Indeed, this type of failure represents 75% of all gear coupling failures [Loc13; Dud57b].

It is true that high misalignment angles, above 3°, may limit power capacity, however, some machinery requires spherical gear couplings to work in those high misalignment angles; e.g., [Man86] described the use of gear spindles in heavy-duty, high torque applications for a maximum misalignment angle of 6°.

Spherical gear couplings are featured by a considerable amount of longitudinal crowning of the hub tooth surfaces, which is generated by a small finite tool path radius (r_β) of the manufacturing hob (typically circular or parabolic), as represented in Fig. 1.2(b,c). This type of spherical gear coupling fails due to the misalignment angle and represents 20% of the total failures [Gua19b]. This leads to tooth root breakage failure [Ye21], which may be significantly increased in highly crowned spherical gear couplings due to the presence of undercut sections [Ohs12; Lar16; Ula18].

1.2 Motivation

Even if scientific literature research in gear couplings working at high misalignment angles is scarce, the industry requires the use of spherical gear couplings for certain applications (e.g. metallurgical industry). Table 1.1 summarizes some of the gear couplings that can be found in the market from principal gear coupling manufacturers. These, and research focused on crowned gear couplings from scientific literature are depicted in Fig. 1.3. Here, gear couplings are

Table 1.1: Maximum and minimum working conditions of gear couplings in the industry.

Company	**Cases**	γ [°]	$\mathbf{\Gamma}$ [Nm]
Amerigear [Ame]	iv, xvi	0.75-1.5	215 - 6745·10^3
Jaure [Regb]	xii, xiii	1.0	3600 - 407·10^3
Jaure [Rega]	xi	3.0	11·10^3 - 7810·10^3
Kop-Flex [Regc]	ii, xiv	1.0	1921 - 131·10^3
Kumera [Kum]	iii, xv	1.0	2300 - 325·10^3
Lovejoy [Lov]	i	0.75 - 1.5	859 - 114·10^3
Maina [Mai11]	vii, viii	1.0 - 6.0	4320 - 489·10^3
Punk [Pun]	xi	5.0	216 - 108·10^3
Renk [Ren]	vi, x	3.0	783 - 8342·10^3
Sure-Flex [Sur]	v	0.75 - 1.5	855 - 207·10^3

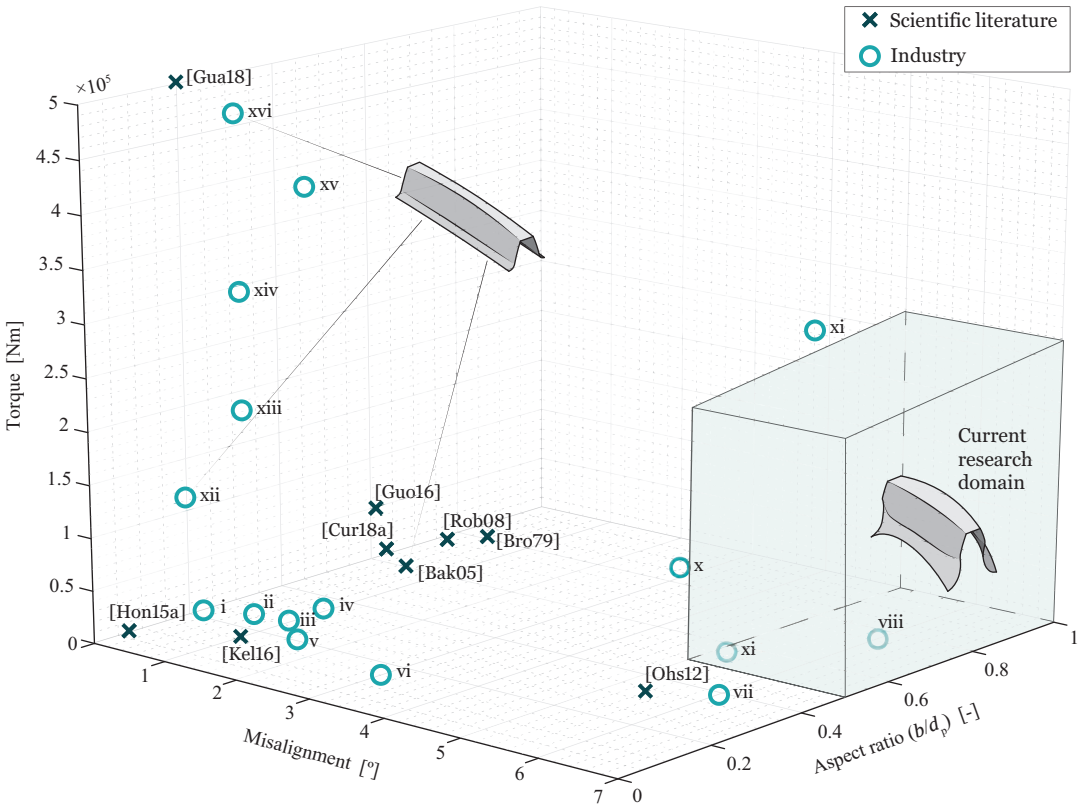

Figure 1.3: Benchmark of gear couplings in scientific literature and industry.

arranged regarding their maximum torque capacity, maximum misalignment, and size (ratio between the face width and the pitch diameter). It is herein observed, that most scientific literature is centered on low misalignment angles and low aspect ratios, thus mainly focused on wear or fretting failures.

However, there are applications where high misalignment angles are present and small gear couplings are employed [Ohs12; Lar16; Ula18], where undercut sections are likely to appear and principally fail due to tooth root breakage [Man86; Her99; Kro09].

On the one hand, the generation of undercut sections for such highly crowned gear couplings has not been addressed in the scientific literature. Moreover, no design guidelines exist for these types of gear couplings.

On the other hand, tooth root breakage failure and tooth root stresses are not investigated in scientific literature. In fact, current standards and sizing equations [Dud57b; Hen83; Man86; Ced94; Deu02; Int05; Bec05; Oct14; Ame20] are mainly derived from gear tooth root bending calculations and consider the effect of the misalignment angle with coefficients, in a similar manner in which the manufacturing quality, the type of load or the stress concentrations effect are taken into account.

However, the misalignment coefficients are proposed for low angles ($\gamma < 1.5°$) mainly related to vibrations or assembly errors of the system, and applications at high angles are referred to as special cases. As a result, the effect of high misalignment angles ($\gamma \gg 1.5°$) is not considered and to avoid early failure, no optimized designs are employed in applications that work in such conditions. Therefore no competitive designs are developed to meet current industrial challenges.

As a consequence of the previous, no experimental correlations of the mechanical behavior or the geometry of highly crowned gear coupling exist in literature.

1.3 Hypothesis and research objectives

Based on the research opportunities identified previously in the introduction and in the literature review throughout Chapter 2, the following research hypothesis is proposed:

> *To accurately predict tooth root stresses of spherical gear couplings operating at high misalignment angles, it is necessary to generate the undercut sections of the tooth surfaces and the length of the gear coupling that supports the load.*

Therefore, the main objective of the present thesis is **to improve the accuracy of the sizing methods of spherical gear couplings working at high misalignment angles by predicting and evaluating tooth root stresses**. To achieve this goal, the following four research objectives are defined:

O.1 : To analytically generate accurate spherical hub tooth surfaces by a hob thread surface and implement an algorithm for detecting singularities (i.e. undercut, pointed teeth).

O.2 : To determine the maximum misalignment angle for a given geometry and establish design guidelines to avoid singularities.

O.3 : To develop a finite element model that considers the generated spherical gear coupling geometry to analyze load distribution and tooth root stresses under different working conditions.

O.4 : To experimentally observe and verify the generated geometry and mechanical behavior of spherical gear couplings at high misalignment angles.

1.4 Dissertation outline

The dissertation is organized into 4 chapters and 4 appendices which flow in a sequential manner.

Chapter 1 introduces the context and motivation of this thesis. The characteristics of spherical gear couplings are described together with the challenges it presents. This is followed by the formulation of the research hypothesis and the technical objectives of the current research.

Chapter 2 covers the literature review, which describes in detail the topics presented in the introduction. It provides up-to-date information on the main geometry generating methods, the current sizing standards, and the numerical and experimental methods to analyze the mechanical behavior of spherical gear couplings. At the end of this chapter, a critical review of the state of the art is included.

Chapter 3 summarizes the research carried out in the thesis by means of publications. Three of these were published in international high-impact journals in the subject area, while the last one is under review. These are divided to give answers to the defined objectives in the following manner (Fig. 1.4). First, the geometry of the gear coupling is determined and the most important design parameters are calculated, such as the maximum misalignment angle. Then, this geometry is meshed and the mechanical behavior and tooth root stress are computed. Finally, the numerically obtained results are experimentally correlated.

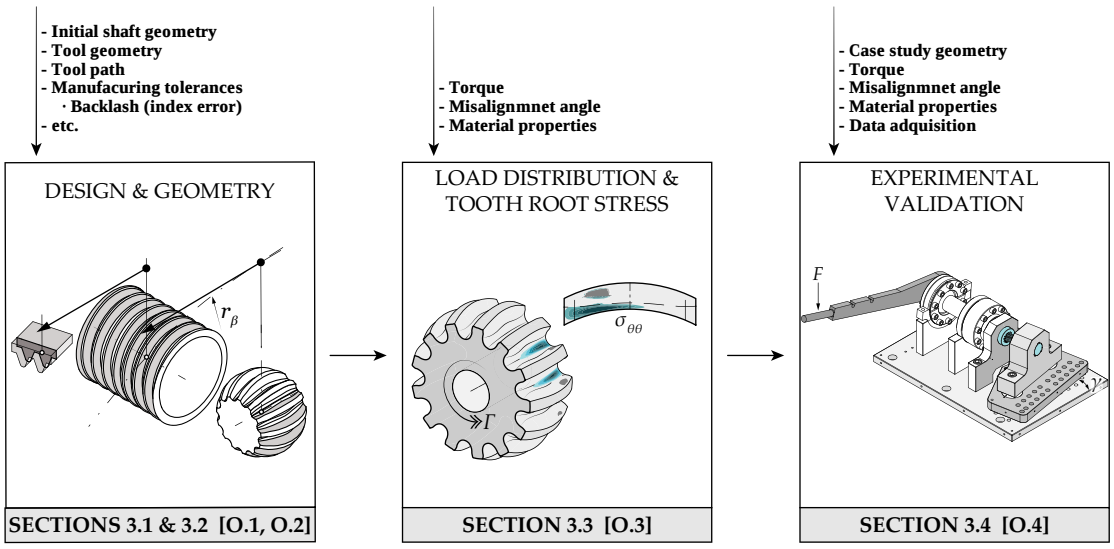

Figure 1.4: Research overview of the current thesis.

Chapter 4 summarizes the major conclusions of this thesis answering to the initial hypothesis and the research objectives established in Chapter 1. Moreover, future research areas are identified.

Appendix A includes the first publication, which accomplishes research objective [O.1]. It presents the development of a mathematical generation model for the gear coupling tooth surfaces which considers the tool path and the whole thread surface of the generating tool.

Appendix B contains the second publication, which fulfills objective [O.2]. It examines the influence of the main design parameters on the maximum achievable misalignment angle and provides design guidelines to prevent the appearance of geometrical singularities.

Appendix C shows the third publication, which addresses objective [O.3]. It analyzes numerically the load distribution and the evolution of tooth root stress in terms of the applied torque and misalignment angle.

Appendix D presents the fourth publication, which achieves objective [O.4]. This publication presents the experimental results obtained with a real highly crowned spherical gear coupling. These results support the conclusions obtained from the analytical geometry generation model (Appendix A, B) and those from the finite element model (Appendix C).

Everything is hard before it is easy.

—Goethe

2 | Literature Review

This chapter reviews the current state of knowledge on gear couplings operating in misaligned conditions. The purpose is to identify research opportunities on the aforementioned topic and to formulate the thesis hypothesis and objectives. First of all, some generalities related to the gear couplings are described, which include among others, the kinematic behavior and the common types of failures. Then, the geometry of the gear couplings is described in detail, assessing its principal tooth modifications and the existing models for the geometry generation of the tooth surfaces. Next, the load distribution of misaligned gear couplings is presented, addressing the differences in comparison with those working in aligned conditions. Special focus is paid to the tooth root stresses since this is the parameter to be observed when evaluating tooth root breakage. The principal standards for sizing are also described. Finally, conclusions are withdrawn and a critical review is developed to identify research opportunities in the field of study.

2.1 General aspects of spline couplings

2.1.1 Tooth geometry characteristics

Spherical gear couplings operate at misaligned conditions thanks to two tooth surface modifications on the hub: the longitudinal crowning (or barrelling) of the hub tooth profile (Fig. 2.1(a)) and the tip crowning of the hub blank (Fig. 2.1(b)). Moreover, these modifications also enable absorbing assembly errors or profile inaccuracies produced in the manufacturing process or in the heat treatment process.

To let the teeth pivot freely when misalignment angles are significant, as shown in Fig. 2.1(b) the gear blank of the hub requires a tip crowning (also referred to as spherical shape) to avoid interference with the sleeve. This is achieved by machining the gear blank with the spherical shape previous to the tooth hobbing.

As defined in ISO 21771 [Int07], tooth flank line crowning is the continuously increasing deviation from the mid point of the flank symmetrically along the face width of the tooth (Fig. 2.1(a)). Depending on the manufacturing method different types of profile crowning exist, e.g., generated in arc, ellipse, or hyperboloid shape. Its main objective is to prevent edge contact [Ben17; Gua19a] and to center the contact between the hub and the sleeve [Alf06; Ren68]; increasing the contact surface [Nea80; Gua19c] and reducing tooth root stresses [Ben17]. For

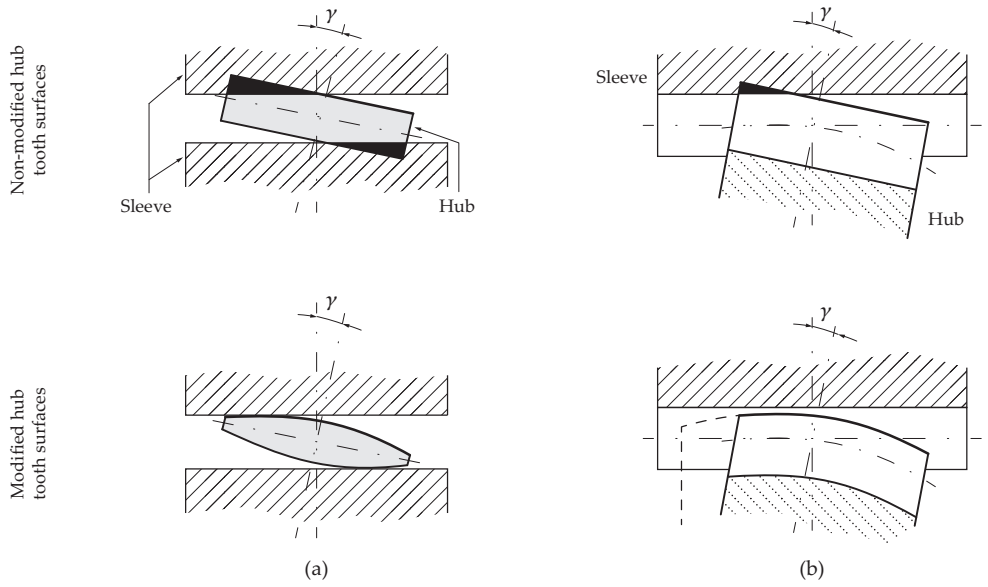

Figure 2.1: Spherical hub tooth surface modifications: (a) longitudinal crowning and (b) tip crowning (adapted from [Oct14]).

instance, the Vari-Crown ® geometry proposed by [Ren68] increases the contact area significantly by means of a variable crowning radius along the face width, where the maximum of it is located at the load angle. [Lag12] also proposed a longitudinal natural flank modification (similar to the one obtained naturally by surface wear after a number of cycles), which improved up to 30% the load carrying capacity and wear resistance of the gear coupling. More recently, [Gua19a] introduced a novel crown gear coupling, with both, the profile crowning modification along the tooth profile and the longitudinal crowning modification along the face width, which also centers the contact point and avoids the tip interference.

However, the amount of crowning must be controlled and defined by the application, since, undesired effects might be achieved; i.e., an increase of the tooth root stresses and/or the contact stresses [Pad60; Bec05; Hot08; Gua19c]. In Fig. 2.2, the effect of the misalignment angle and the amount of crowning can be qualitatively observed. Moreover, the effect of an excessive crowning for a slight misalignment requirement can be observed [Pad60]. Indeed, the contact surface decreases (from *(2,2)* to *(3,2)* in Fig. 2.2) and thus load capacity is reduced as a result of the high concentrated stresses. For that reason, the flattest curve (the smallest amount of crowning) that suits a specific angular requirement will provide the maximum load capacity per tooth [Pad60]. In this regard, [Mar19] determined the relation between the amount of longitudinal crowning, the gear coupling face width, and the misalignment angle, for designs working at low misalignment angles ($\gamma < 1°$).

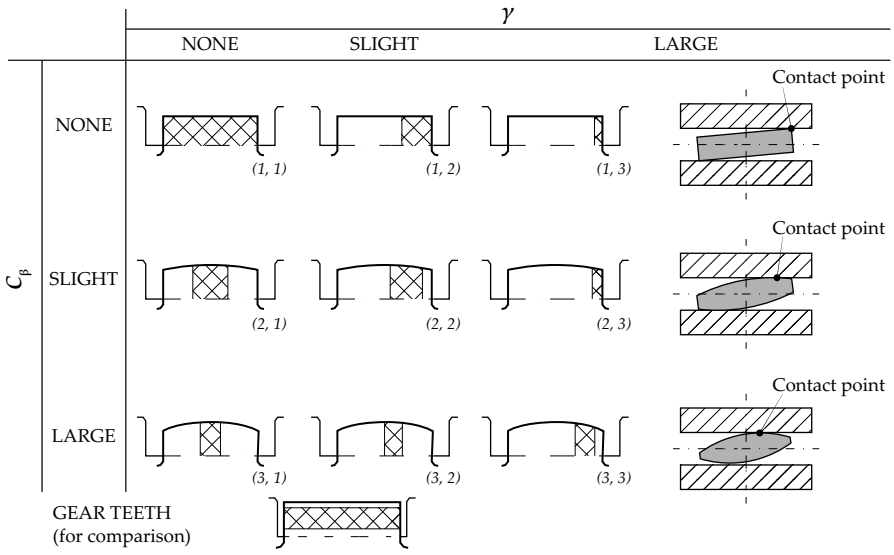

Figure 2.2: Effect of the misalignment angle and the amount of longitudinal crowning (adapted from [Nea80; Pad60]).

2.1.2 Kinematic behavior in misaligned conditions

In ideal aligned conditions, all the teeth are engaged and the contact point is centered on the face width [Hon14b]. However, even from the slightest misalignment angle, the behavior becomes complex and the relative position between the hub and the sleeve teeth differ along the meshing angular position [Oct14; Nea80; Pad60].

The relative motion between the hub and the sleeve is composed of pivoting (or swinging) and tilting movements, corresponding to the angular positions in the parallel and in the perpendicular planes to the misalignment angle as observed in Fig. 2.3(a). The contact position changes accordingly with the angular position of the tooth as can be seen in Fig. 2.3(b,c).

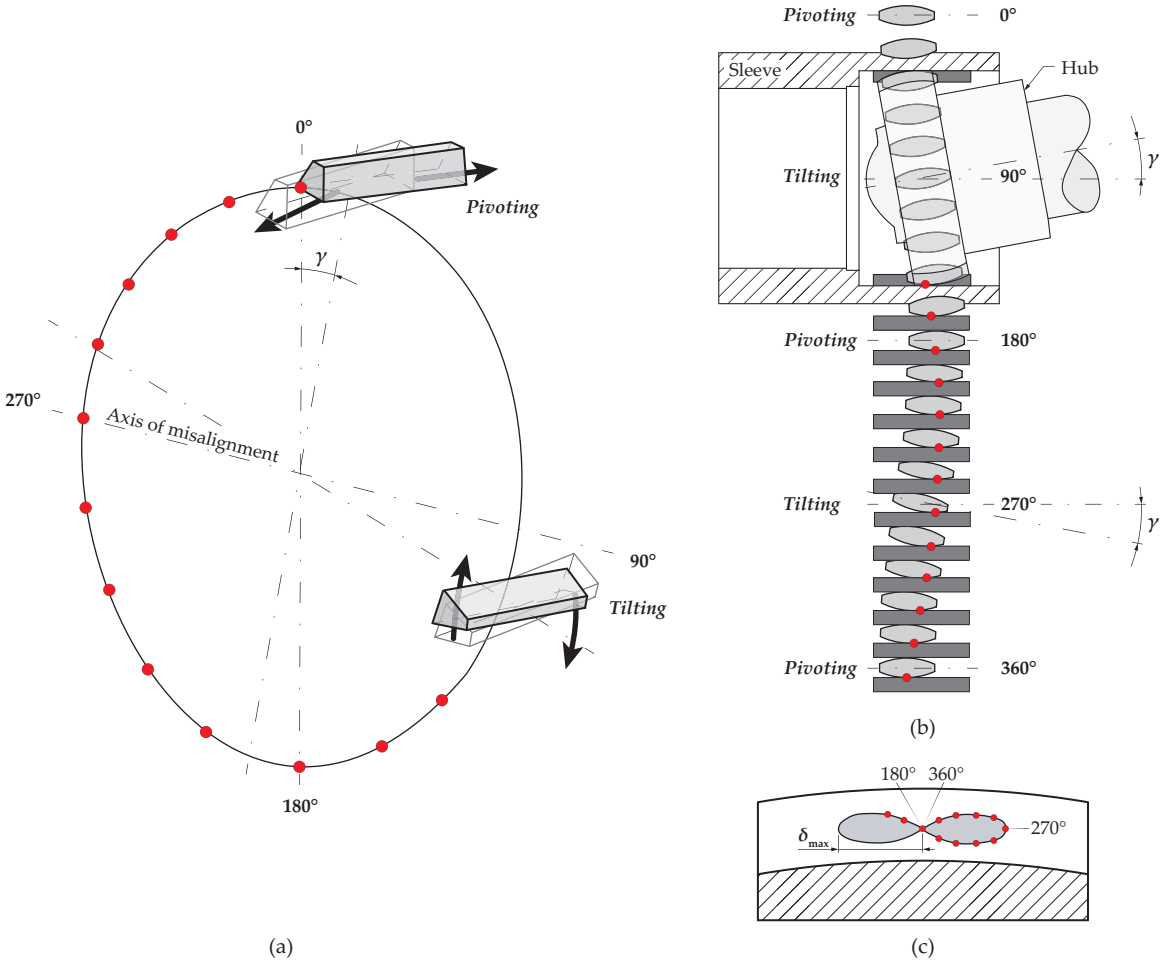

Figure 2.3: Kinematics of misaligned gear couplings: (a) tooth characteristic positions (adapted from [Nea80]), (b) tooth rollout showing tooth contact in misaligned conditions (adapted from [Pad60]), and (c) contact pattern in the tooth profile [Oct14].

The contact displaces further away from the reference section in the tilting angular position, while it rests in the central section in the pivoting one. The maximum distance that the contact point displaces ($\delta_{\max}$) along the face width is calculated by Eq. (2.1) by some authors [Guo16; Cur18a].

$$\delta_{\max} = r_c \sin(\gamma) \cos\left(2\pi \frac{z_i}{z}\right) \tag{2.1}$$

where, r_c is the crowning radius, γ the misalignment angle, z_i each of the teeth of the gear coupling, and z the total number of teeth in the gear coupling.

Moreover, each tooth passes twice by the tilting and the pivoting angular positions for each rotation. The movement along the hub active profile is depicted in Fig. 2.3(c), where a *lemniscata* shape contact pattern is represented, as observed by several authors [Alf06; Gua18; Nak88; Bün00].

The tilting angular position is the most critical one because the teeth in this position are the first to come into contact and suffer the highest stresses [Sil10]. As they have the smallest clearance value [Alf06], this angular position is the one that determines the achievable maximum misalignment by the gear coupling. Eq. (2.2) was proposed by [Guo16] and serves to define the achievable maximum misalignment angle as being smaller than the jam angle (ξ) only relating tooth geometrical parameters.

$$\xi = \min\left\{\cos^{-1}(\Gamma_0), \quad \sin^{-1}\left(\frac{b}{2r_\beta}\right), \quad \sin^{-1}\left[\frac{s_{c2} - t_{c2}}{b\sin(\alpha)}\right]\right\} \tag{2.2}$$

where, Γ_0 is the solution of geometrical parameters developed in [Guo16], b the face width, r_β the crowning radius, s_{c2} the sleeve circular space width, t_{c2} the sleeve tooth circular thickness and α the pressure angle.

Another approach to determine the maximum misalignment angle is found in Eq. (2.3) proposed by Beckmann [Bec05]. In contrast to the relations proposed by Guo et al. [Guo16], this includes the clearance value (k) between the hub and sleeve, the module (m_n) and the pressure angle (α) as variables to calculate the misalignment angle, while it does not consider the gear coupling face width (b).

$$\gamma_{\max} = \arccos\left(1 - \frac{2km_n \tan(\alpha)}{4r_c - \pi m_n tan(\alpha)}\right) \tag{2.3}$$

All in all, these equations were only used in small misalignment angles below 1.5° and no correlation for higher angles was found. Finally, other methods including mathematical simplifications related to smaller misalignment angles were disregarded, such as the one proposed by Marano et al. [Mar19].

2.1.3 Failure modes in spline couplings

Contact surface fatigue and wear

The most common use of gear couplings is in applications of low misalignment angles ($\gamma \ll 1.5°$). The excessive compressive stress at the contact surface leads to the wear of the active profile by three different phenomena: abrasive wear, worm tracking, and fretting wear. Damage occurring as a result of surface wear [Ku75; Med02b; Oct14; Guo16; Xia22] caused principally by improper lubrication represents 75% of all gear coupling failures [Loc13; Dud57b].

Abrasive wear or three-body wear is a continuous damage process, combining a complex set of phenomena (mainly influenced by sliding movement between bodies) leading to debris emission, active profile modification, and initial clearance evolution. It can cause or accelerate the development of other failure modes, such as fretting. Worm tracking is a particular damage type for gear couplings, characterized by the appearance of *tracks* in the perpendicular direction to the sliding speed [Cor07; Cal75]. These tracks correspond to a wear failure mode in which large metal particles are removed from the contacting teeth. The exact cause of this phenomenon is not yet well understood [Oct14]. [Cal75] considers that it is related to a combination of several factors: insufficient lubrication, significant misalignment, and unfavorable sliding conditions with speeds around $0.1-0.3$ m/s. Some heavy spalling might sometimes also be called worm tracking [Cor07]. Fretting wear is a special wear process, very usual in gear couplings, and occurs at the contact area between the hub and the sleeve under load and when they are subjected to small relative motions (small amplitude oscillatory motion) by vibration or some other external force [Xue19; Lee22; Gua22]. It has experimentally been demonstrated that a small misalignment angle of $\gamma = 0.05-0.17°$, increases the wear damage and that formulas in standards [Ame20; Dud57b] provide approximated stress states, leading to an overestimated fatigue life [Cur17].

These types of failures can be reduced if the friction between the active profiles is decreased, either improving the surface roughness, the lubrication or hardening the contact surfaces. As a fundamental way to prevent fretting, [Ame20] proposes making designs for no relative motion

between the contact surfaces. However, this is only possible theoretically, as the parts will never be totally aligned. Furthermore, a minimum film thickness must be ensured if low wear rates are desired. Together with this, the latest researches show the high importance of lubricant conditions in the reduction of power losses, by decreasing the friction of the components [Mur18]. Moreover, [Mil17] proposed that a flow of oil should go through the splines ideally, removing particles generated by wear and cooling the system. Also, [Cal75] showed that higher rotation speeds had a beneficial effect on the contact nature, as lubrication conditions were improved.

Even if a variety of equations can be found in scientific literature to calculate tooth contact stresses, Eq. (2.4) is the general equation proposed by [Ame20]. Then, different coefficients are employed to account for the effect of loading, type of material, etc.

$$\sigma_{\mathrm{f}} = \frac{2000\,\Gamma\,k_{\mathrm{m}}}{d_{\mathrm{p}}\,z\,b\,h_{\mathrm{eff}}} \qquad [\mathrm{MPa}] \tag{2.4}$$

Tooth root breakage

The next most common failure stems from misalignment (20%), which leads to tooth root breakage failure [Ye21]. Moreover, the latter is significantly increased in highly crowned spherical gear couplings, as undercut sections are frequent [Ula18]. Since an excessive misalignment angle leads to edge contact, a high-stress concentration occurs which entails tooth root breakage as observed in Fig. 2.4(b). Another issue of load concentrations comes from undercut sections, that is why design standards limit the tooth surface geometry up to the point where undercut sections exist [Hon14b]. Therefore, geometries with undercut singularities are generally discarded in the design phase of spherical gear couplings. Moreover, concerning high misalignment

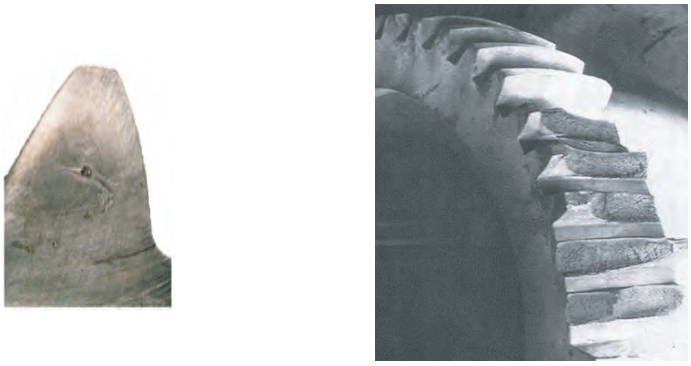

(a) (b)

Figure 2.4: (a) tooth root crack initiation [Ame20], and (b) tooth root breakage [Man86].

applications [Her99; Nak88; Kro09], such as in rolling-mills, a major displacement of the contact point during operation is predicted, which will consequently increase the entrainment velocity. Thus, lubricant will correctly flow across the tooth surfaces, reducing the risk of wear failure. Indeed, [Her99] affirmed that tooth root breakage occurred when misalignment angles of $\gamma > 3°$ were present in their fully-crowned gear couplings.

Tooth root failure is detected by the appearance of cracks in the root as shown in Fig. 2.4(a). These are caused by either fatigue cycles or by a few overload cycles. It has experimentally been observed [Lee03] that even in straight gear couplings when torque overload conditions are present, spline couplings do not fail by fretting, but by plain fatigue in the spline toot-root fillet. Thus, it is expected this failure to be of great importance in gear couplings working in high misalignment angles, as overloads can occur more easily due to the decrease on the number of teeth in contact.

Tooth root breakage may also occur due to maximum shear stress concentration on the root, as shown numerically and experimentally by [Par14].

Other types of failures

Other types of gear coupling failures [Dud57a; Cre78; Man86; Loc13; Oct14; Mil17] include sleeve bursting or shear breakage on the pitch line as can be observed in Fig.2.5.

Shear stress on the pitch-line of the the hub is not commonly calculated as the risk of tooth breakage is almost non-existent in gear couplings [Oct14]. Indeed, for pitch line shear failure all the members of the hub and the sleeve must be sheared. Nevertheless, when spacing errors increase or misalignment is too big, the number of teeth in which load is shared decreases, thus shear failures can progress gradually through the spline joint one tooth at a time [Ame20]. When calculating tooth shear stress, it is usually assumed that teeth shear off at the pitch line [Dud57b], however, due to the kinematics in misaligned conditions, it may occur away from it [Ced94].

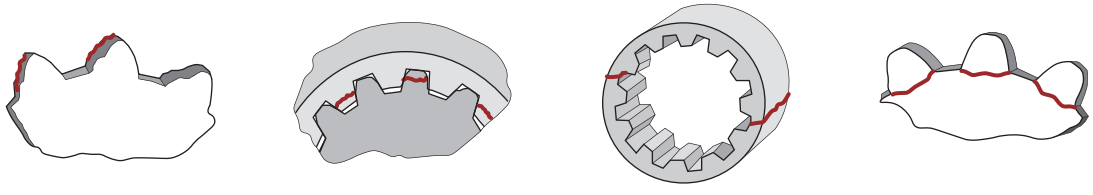

Figure 2.5: Common failures of gear couplings adapted from [Dud57b].

Sleeve bursting or hoop failure may occur by overload in a thin-walled sleeve that turns out to be the weakest part of the connection. [Ame20] states the three main forces causing this failure: the radial component force at the pitch-line, the tooth bending moment, and the centrifugal force. The sleeve wall section carries the bursting stress generated by the radial component force at the pitch-line caused by the pressure angle of the gear coupling. Moreover, the tensile stress generated in the internal tooth bending is also present. Finally, if the sleeve rotates at a high speed, the hoop stress due to the centrifugal forces becomes a significant component of the overall state stress of the tooth root from the sleeve.

2.2 Geometry of highly crowned gear couplings

2.2.1 Hub and sleeve manufacturing

To a great extent, spline manufacturing is very similar to gear manufacturing, as the involute profile is the standard tooth profile for both geometries. There is a wide range of manufacturing methods for gears, based on their applications and the required tolerances [Gup17a]. Among the advanced gear manufacturing processes, the most employed are the material-removing ones, where, machining is the preferred process. Within the machining processes, generating and profiling gear-cutting technologies exist. In a generating process, the shape of the gear tooth is the result of a composite rotation between the tool and the workpiece, e.g., gear hobbing. However, in a profiling process, the shape of the gear tooth is cut into the workpiece by the shape of the cutting tool, e.g., gear milling.

Generating gear-cutting processes are the most commonly used and produce the gear tooth profile by the rolling movement of the tool around the workpiece. In fact, it enables the generation of an involute profile by means of a tool with a straight profile. Other advantages of this process include the flexibility in the gear design as the same tool can be used to manufacture different geometries with the same module. However, the kinematic behavior and the tool design are more complex [Klo14] than the tools used in profiling gear-cutting technologies. In Fig. 2.6 various generating processes can be observed, which employing a different tool geometry and kinematics they produce the same virtual tooth profile.

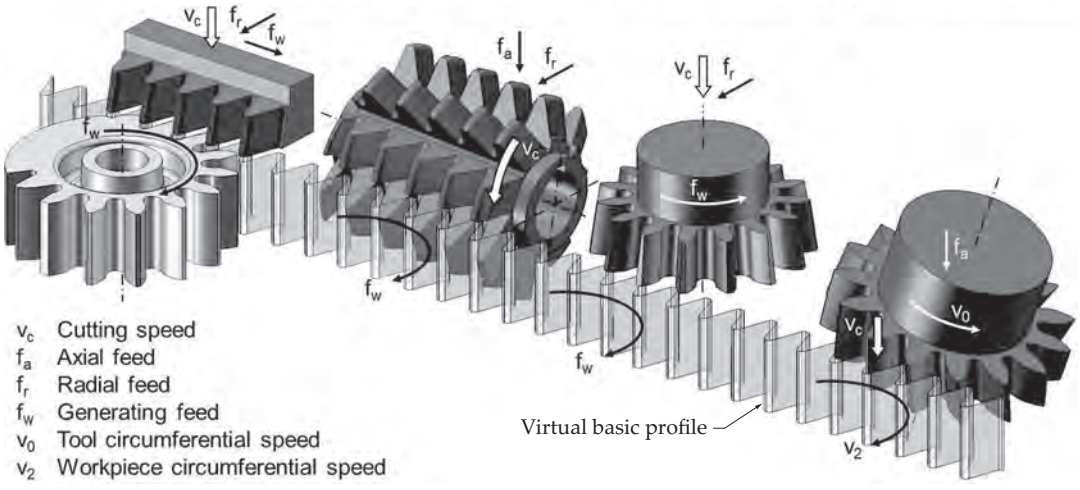

Figure 2.6: Overview of generating gear cutting processes (from left to right): generation with rack-cutter, gear hobbing, generation with pinion-cutter, and gear skiving (adapted from [Klo14]).

Gear hobbing (Fig. 2.6) is the most efficient and productive generating process for cutting high-quality external gears in industry [Gim94; Bou08; Bre15] considering the demand for continuous gear manufacturing processes, in terms of cost and productivity. In this process, the hob and the workpiece rotate with a continuous rotational relationship (f_w). This way, the workpiece advances one tooth for each revolution of the cutter (in a single start hob). In addition, while rotating, the hob is fed axially along the face width (f_a) to generate gradually the face width of the teeth, until the complete gear is generated.

Manufacturing by a pinion-cutter is a process used for internal and external gears, in which the kinematics can be described by two rolling cylindrical gears with an additional feeding movement of the tool. Thanks to the small run-out length and the possibility of using small tools it offers advantages in the production of internal gears and parts with interfering contours [Klo14].

On the other side, the shape of the tools for gear profiling processes is based on the counterpart profile of the finished gear tooth profile, thus every gear design requires its own tool. The principal technologies used in gear manufacturing are: gear single gap form milling, gear planning, gear shaping, and gear broaching.

Employed methods to manufacture the hub of the gear coupling include either the generation by a disk or by a hob. This process allows the mass production of gear couplings of various dimensions. In hobbing machines, a hob is mounted in a spindle that skews a certain angle and rotates, while the blank workpiece is mounted in another spindle. The longitudinal crowning tooth surface modification in spur gears is achieved in the finishing stage with a grinding wheel or a shaver. In fact, the amount of the modification is in the order of magnitude of a few microns.

Nevertheless, in highly crowned spherical gear couplings the amount of the longitudinal crowning can reach the order of magnitude of millimeters, and thus, this is generated directly during the manufacturing state. In this manner, the hob spindle displaces along the workpiece face width with a circular or parabolic tool path. The radius of the tool path employed is related to the amount of longitudinal crowning desired and at the same time, this is closely linked to the achievable misalignment angle. For gear coupling designs below 1.5°, Table 2.1 shows the equations currently employed by different authors in their analytical models to determine the tool path radius.

On the other hand, the manufacturing of the sleeve is less complex than that of the hub, since the teeth are normally straight [Ohs12; Gua19b]. Among the generating and profiling manufacturing procedures, gear shaping is the most widely used manufacturing process, due to

Table 2.1: Tool path radius for the longitudinal crowning definition of gear couplings.

Authors	Equation
Octrue et al. / Beckmann [Oct14; Bec05]	$r_\beta = m_n \left(\dfrac{\frac{k}{2} + \frac{\pi}{4}(1-\cos\gamma)}{1-\cos\gamma} \right) \tan\alpha + r_{\mathrm{p,w}}$
Cuffaro / Dudley [Cuf13; Dud57b]	$r_\beta = 0.9\dfrac{d_\mathrm{p}}{2}\tan\alpha + r_{\mathrm{p,w}}$

its' reliability and precision [Kel12].

2.2.2 Analytical generation of hub tooth surfaces

Although gear hobbing represents the main procedure to manufacture the hub [Gua19b; Ohs12], most of the analytical generation methods presented in scientific literature simplify the hobbing process with the cutting edge of the rack-cutter tooth surface.

One of the analytical simplifications considers just the geometry of the hob middle cross-section [Mit00; Gua19b]. Fig. 2.7(a) shows a schematic representation of the model, where each hub tooth profile section is generated in a single-enveloping process [Lit04]. In each of the sections along the face width a different profile shift coefficient is employed. Indeed, the profile shift coefficient is dependent on the distance between the current cross section and the reference section; i.e., the profile shift coefficient is null in the reference section while it decreases as the cross section is located farther away from it. The complete tooth surface is obtained as a cumulative of 2D tooth profiles, thus it is not straightforward to determine the normal vectors.

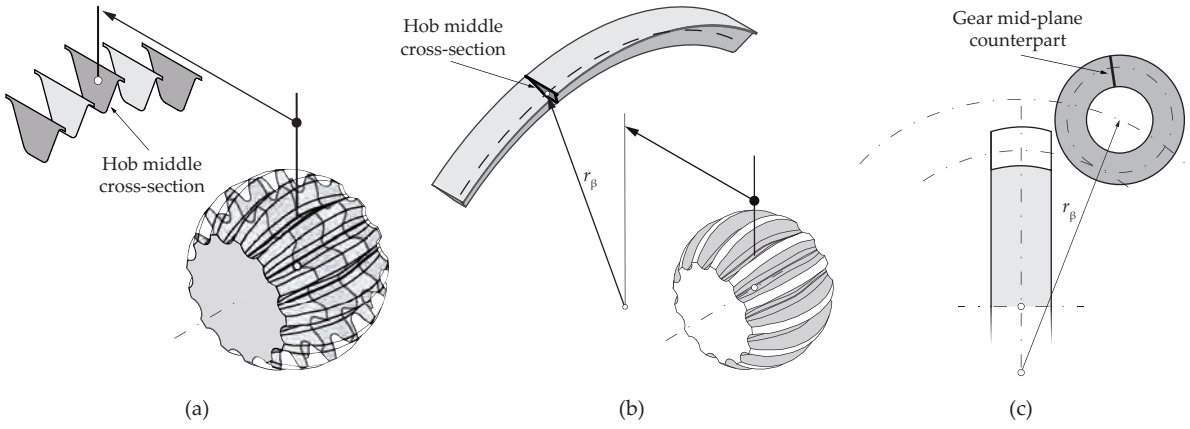

Figure 2.7: Models for the derivation of the crowned hub tooth surface: (a) [Mit00; Gua19b], (b) [Cha08; Kel14], and (c) [Zan04; Gua18].

Another simplification used by [Cha08; Kel14] consider the path of the cutting edge of the hob middle cross-section to obtain the generating tooth surface. The hub tooth surface then results from the set of independent cross sections rotated around the blank workpiece as observed in Fig. 2.7(b). This is also a single-enveloping process [Lit04] and the application of different tool paths is not straightforward. Moreover, this method does not allow the existence of undercut sections when reduced tool path radii (r_β) are used.

Other authors [Zan04; Gua18] first, create a form-cutting wheel which is used to cut the designed gear surface by pure intersection with the gear blank. The milling cutter is created from the mid-plane counterpart tooth geometry. Then, the circular tool path of the form wheel is established, as shown in Fig. 2.7(c), with the coordinate system kinematic relationships. In [Gua19b] it is observed that this model gives similar results to the method which considers that all the planes containing the center of the displacement circle are equal to the middle section (Fig. 2.7(a)), as in both cases the tooth profile of the generating tool has the same profile shift coefficient.

Even if some authors have compared different generating models [Gua19b; Kel14], they have never analyzed geometries of high longitudinal crowning. These works concluded that the tooth profiles coincided in the middle section and that deviations between the different models increased as the tooth profile section was farther away from the middle section of the hub. Anyhow, the differences were considered to be insignificant in all the studied cases. Moreover, non of them compared mathematically obtained tooth surfaces with real manufactured parts to define the most precise method.

Although the described models can be accurate for small crowning value geometries, higher amounts of crowning require the consideration of all the 3D geometry of the generating tool surface. A hob may be regarded as a set of cutting edges distributed along its thread and as a result, the thread surface of the cutting tool has to be considered to achieve an accurate generation model. Indeed, a precise tooth geometry will ensure a solid foundation for any type of future analysis, e.g., tooth contact analysis or stress analysis.

Singularities of the hub tooth surface

The appearance of singular points on the generated surface is the warning that the surface may be undercut during the generation process [Lit89].

When this happens, the gear fillet and the involute shape of the active profile are no longer

in tangency (Fig. 2.8). This leads to a weakening of the strength of the tooth, as tooth root thickness is decreased. Even if scientific literature has made a great effort to prevent undercut sections during tooth surface generation [Lit04], the existence of undercutting in spherical gear couplings is almost unavoidable, especially in small parts where the hub teeth are manufactured directly on a shaft [Ula18]. Moreover, due to the big amount of longitudinal crowning values (compared with crowned tooth modifications in gears) the small generating tool path radius favors the appearance of undercut sections.

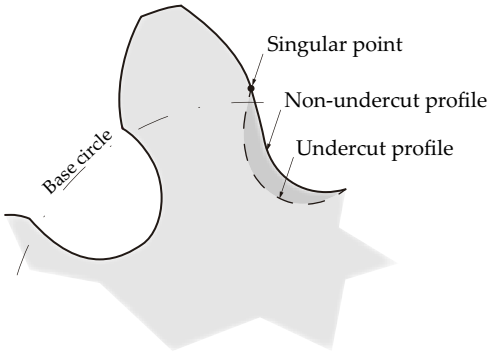

Figure 2.8: Undercut tooth profile (adapted from: tec-science web).

Surface envelope theorem

Generation of a gear tooth surface by a hob (or a worm) thread surface was introduced by Litvin et al. [Lit89; Lit04] founded on differential geometry and later used for the generation of face-gear drives [Lit02; Lit05], noncircular gears [Lit07; Lit09] or screw rotors [Wu14]. Other models, also generate all kinds of gear drives on the basis of the basic law of gearing, such as the works [Zim16; Jia19]. Furthermore, other authors [Ved10; Klo16] account for the effect in the generated gear tooth surfaces of the hob geometry variations (e.g. caused by tool wear or regrinding). In this manner, the surface topography and the surface roughness parameters can be obtained.

The theory of enveloping curves and surfaces was represented in differential geometry by [Fav57] and further developed by [Lit89; Lit04] in the theory of gearing. According to this theorem, the generating surface Σ_1 is represented in coordinate system S_1 by two independent parameters (u, θ) as follows (2.5):

$$\mathbf{r}_1(u,\theta) \in C^2, \quad \frac{\partial \mathbf{r}_1}{\partial u} \times \frac{\partial \mathbf{r}_1}{\partial \theta} \neq \mathbf{0}, \quad (u,\theta) \in E \tag{2.5}$$

The generated surface Σ_2 is produced by the thread of the hob considering a double-enveloping process. This is represented with two independent parameters (ϕ, ψ) and fulfills the necessary conditions of existence with the equations of meshing (2.6):

$$\begin{aligned} f\left(u,\theta,\phi,\psi\right) &= \mathbf{N}_2^{(1)} \cdot \frac{\partial \mathbf{r}_2}{\partial \phi} = 0 \\ f\left(u,\theta,\phi,\psi\right) &= \mathbf{N}_2^{(1)} \cdot \frac{\partial \mathbf{r}_2}{\partial \psi} = 0 \end{aligned} \tag{2.6}$$

To provide the required line contact at every instant between the generating and generated tooth surfaces, Σ_2 is determined as the envelope to the family of surface of Σ_1 generated in coordinate system S_2 as (2.7):

$$\mathbf{r}_2\left(u,\theta,\phi,\psi\right) = \mathbf{M}_{21}\left(\phi,\psi\right)\mathbf{r}_1\left(u,\theta\right) \tag{2.7}$$

The simultaneous consideration of Eqs. (2.6, 2.7) gives as a result the envelope surface Σ_2. Fig. 2.9 shows graphically the one-parameter envelope generation process of the active tooth profile. This process is more visible than the two-parameter envelope since there is only one independent variable (ϕ) and generation occurs in a 2D plane. However, during the generation of the tooth surface in the two-parameter $(\phi,\ \psi)$ envelope process previously described, the tool position $(\mathbf{r}_1)$ will also change in $z\,y$ plane simultaneously, i.e. it is a 3D generation procedure.

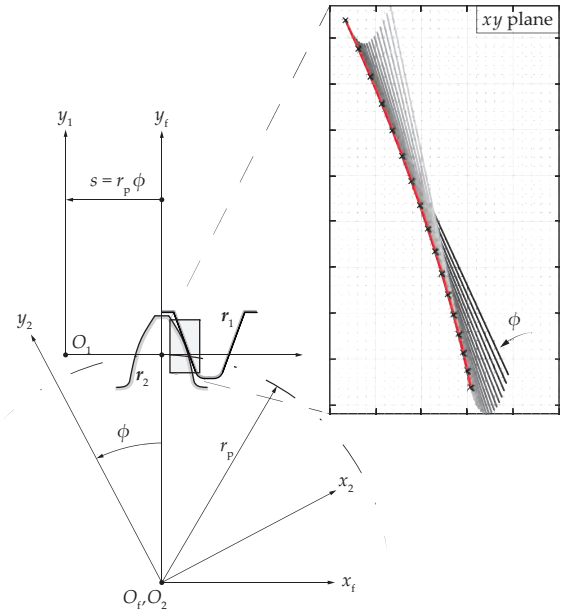

Figure 2.9: One-parameter envelope method for the tooth active profile generation (adapted from [Lit04]).

Nevertheless, it is necessary to outline that this method allows obtaining a theoretical surface Σ_2 which differs from the real one as it is shown in Fig. 2.10. This is explained by the fact that parameters ϕ (angle of rotation of the tool surface Σ_1) and ψ (feeding of this surface) are not completely independent because of the kinematic chain of the machining-tool. Indeed, the feeding parameter ψ is related to the angle of rotation ϕ and may be expressed by a function $\psi = f(\psi(\phi))$. Both, the real and the theoretical surfaces coincide in a line and the deviations define the so-called machining marks of the generated surface, which occur even when the machining is produced by an infinite number of cutting edges [Lit75; Deb11], e.g., an abrasive worn. Moreover, the feeding movement of the hob is also translated into tooth profile errors, as is shown in Fig. 2.10(b) where small waviness perpendicular to the cutting edge appears.

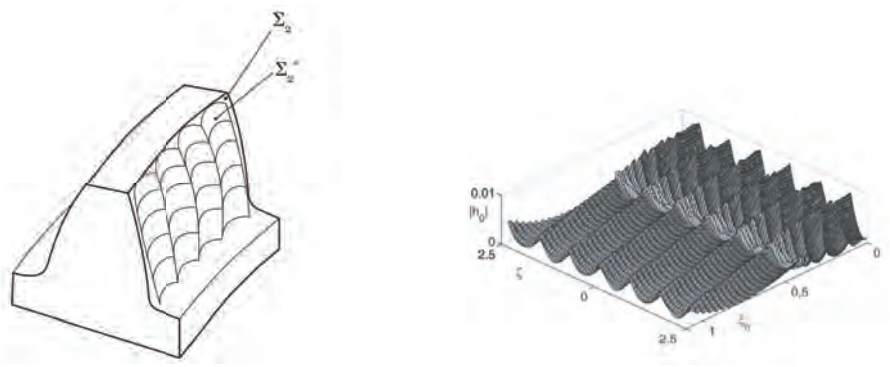

(a) (b)

Figure 2.10: (a) difference between the manufactured (Σ_2^*) and the theoretical (Σ_2) gear surfaces (adapted from [Lit96]), and (b) manufactured tooth surface topology [Ved10].

2.2.3 Analytical generation of sleeve tooth surfaces

Related to the aforementioned two-parameter envelope method, a similar concept is used for the generation of internal gears and the sleeve of gear couplings [Kel16]. This is used to generate non involute [Cha98; Li15], symmetric or non-symmetric tooth profiles [Yan07].

During the process, the center distance (E_c) between the generating and generated surfaces varies constantly (Fig. 2.11) and it is possible to relate it to the angular position of the generating surface (ϕ_2) by a linear equation (known as the pseudohypocicloid, Eq. (2.8)) as explained in [Lit04].

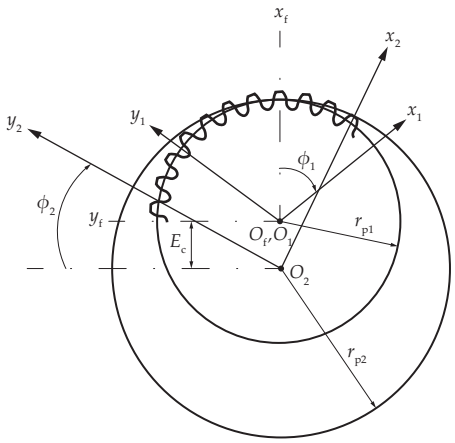

Figure 2.11: Mathematical model for generating internal gear tooth surfaces [Lit04; Yan07].

$$E_c(\phi_2) = E_c^0 + \frac{2.25 m_n}{2\pi a}\phi_2 \tag{2.8}$$

where, E_c^0 is the initial value of the center distance and parameter a the number of revolutions gear 2 will perform for the whole process of generation.

2.2.4 Clearance distribution

The clearance is the necessary gap between two teeth engaged in a mesh for smooth rotation. A zero backlash is the theoretically ideal working condition, however, in practice a minimum distance between the teeth is needed to enable the relative movement [Ced94], to accommodate tooth profile errors without jamming [Oct14], or to accommodate thermal distortions [Ara19], among others. Moreover, in misaligned conditions, clearance is also necessary to enable motion between gear coupling teeth [Hen83; Ced94; Ohs12] and has an optimal value so that efficiency and precision are not reduced or the vibration levels do not increase too much [Guo16]. Smaller clearance values may also be obtained by changing the curvature radius along the tooth and achieving an equalized tooth surface-bearing area [Hak11]. [Alf06] showed that the most influential factors in the clearance distribution (or backlash) are the misalignment angle, the tooth surface longitudinal crowning, and the tooth angular position. Also, [Ohs12] presented a new tooth profile for hubs to obtain good tooth contact and proposed a method to calculate tooth clearance based on the interpolated profile surface. These results were validated with experimental tests using a gear-marking compound.

Table 2.2 summarizes some of the equations used in scientific literature to calculate the theoretical normal clearance (j_n). Here, r_p corresponds to the pitch radius, ρ to the transverse longitudinal crowning radius, γ to the misalignment angle, θ to each tooth angular position, and α to the pressure angle.

Table 2.2: Clearance distribution definitions in the scientific literature.

Authors	Equation
Renzo et al. / Guo et al. [Ren68; Guo16]	$j_n = \frac{r_p \tan^2(\gamma) \sin^2(\theta)}{2 \tan(\alpha)}$
Marano et al. [Mar19]	$j_n = \frac{\rho \gamma^2 \sin^2(\theta)}{2}$

In aligned and ideal conditions, if no manufacturing errors are considered, clearance distribution is constant (Fig. 2.12(a)) and all the teeth engage at the same time. However, in misaligned conditions, the clearance value differs depending on the angular position due to the crowned tooth surface and the displacement of the contact point. As it is observed in Fig. 2.12(b) the clearance distribution presents a sinusoidal distribution, being minimum in the tilting angular positions (A, C) and maximum in the pivoting ones (B).

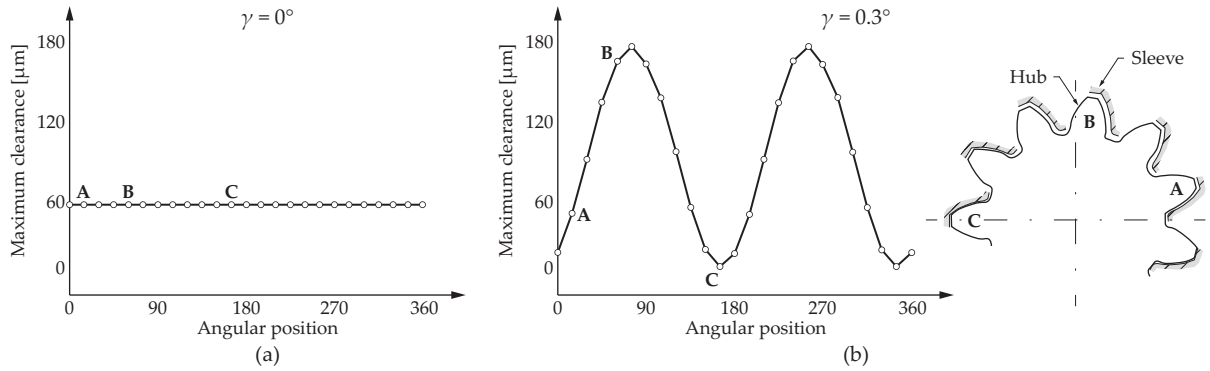

Figure 2.12: Clearance distribution in (a) aligned and (b) misaligned conditions (adapted from [Gua18; Alf06]).

2.2.5 Manufacturing errors

However, tooth errors may play an important role in clearance distribution, increasing or decreasing it. Tooth errors are mainly caused by manufacturing errors [Gup17b] (e.g., profile errors, lead errors, pitch errors, etc.) or operating conditions [Loc13] (e.g., vibrations, thermal movements, etc.). Indeed, the manufacturing quality (manufacturing tolerances) can double the

load supported by the gear coupling tooth, due to the increase of the normal force and the reduction of the number of teeth in contact [Oct14].

ISO 4156 standard [Int05] defines the allowable total manufacturing deviations, considering the module, the number of teeth, and the machining tolerances, as a function of the manufacturing quality level. [Kro11] showed the most influential of the three parameters was the module, giving evidence that with bigger pitch diameter values, the machining tolerances and the deviation allowances were higher.

The same standard [Int05] classifies the three most important manufacturing deviations as, pitch deviations (F_p), profile deviations (F_α), and lead deviations (F_β). Since not all errors will occur at their maximum amounts at the same time, individual deviations are added together statistically and 60% of the total is considered to determine the effect they have on the spline fit as determined in Eq. (2.9).

$$\lambda = 0.6\sqrt{F_p^2 + F_\alpha^2 + F_\beta^2} \tag{2.9}$$

The most influencing tooth error in gear couplings is the tooth indexing error (or pitch error) [Bün00; Ben17], which can make maximum tooth contact stresses duplicate [Hon15b]. The distance between adjacent tooth profiles is modified as shown in Fig. 2.13(a), causing an uneven clearance distribution and making the teeth come into contact earlier or later than they should. Indeed, positive indexing errors will make the clearance value decrease and thus, the teeth will come in contact earlier and carry a bigger amount of load [Hon15a; Kro13]. On the contrary, negative indexing errors increase the distance between adjacent teeth, and thus they can even lead to no contact in some teeth.

[Hon15b] analyzed the influence of randomly generated indexing errors on spline coupling manufactured inside a tolerance class (Fig. 2.13(b)). This work proposed probability distributions of the load-sharing factors for different manufacturing classes and revealed that tighter tolerance classes exhibit more favorable load-sharing characteristics, which will usually represent better

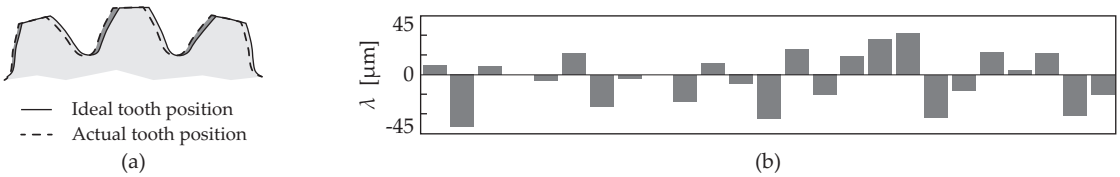

Figure 2.13: (a) indexing error effect [Hon15b], and (b) random indexing errors inside machining class 7 (ISO 4156 [Int05]).

durability. Moreover, [Glo10] added that the tooth of the hub and sleeve with opposite sign deviations should be paired to equalize their unfavorable influence on load distribution.

Three different ways were identified in scientific literature to consider the effect of indexing errors during the sizing of gear couplings: (i) the most widely employed, applies safety coefficients to decrease the number of teeth in contact as manufacturing quality decreases [Bec05; Ame20; Glo10], e.g., [Bec05] research reveals that indexing errors can imply an increase of 22% in the stress values of the gear coupling. Machining quality safety coefficients [Bec05; Glo10] are depicted in Fig. 2.14. Both works conclude that low-quality couplings have an increased influence on load distribution, while it is observed that the effect is more remarkable at lower torque values (Fig. 2.14(b)) ; (ii) measuring the real parts and introducing those modifications in the numerical [Tje01a; Hon15b] or analytical models [Cur13a] ; and (iii) statistically predicting tooth clearance values based on the manufacturing quality limits as proposed in the works [DeC06; Sil10; Hon15a]. [DeC06; Sil10] conclude that as standard deviation increases, the first tooth engaging carries an increasing fraction of the total load. Moreover, it demonstrates that depending on the torque level clearance distribution shape has a different effect on the stiffness of the gear coupling. I.e., at low torques, the uniform distribution leads to a stiffer coupling, while at higher torques the normal distribution results in a stiffer coupling.

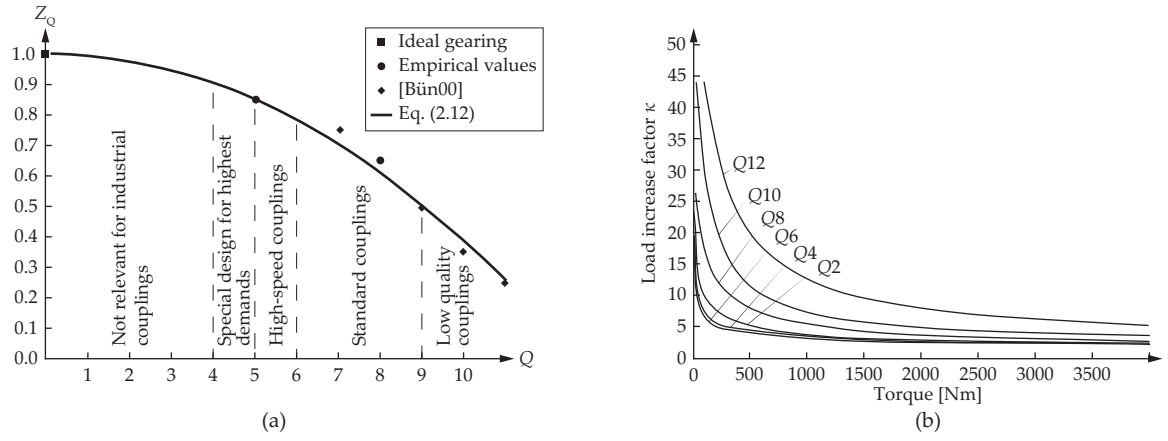

Figure 2.14: Safety coefficients to account for indexing errors: (a) Z_Q (adapted from [Bec05]), and (b) κ (adapted from [Glo10]).

2.3 Load distribution

Due to the complex kinematics of misaligned gear couplings and the effect of multiple variables, analytical models exist to analyze the influence of each of the variables individually; e.g., clearance distribution [Alf06; Nak88; Vol82] or load distribution [Guo16; Elk02], among others. However, it is known that parameters are interrelated and that they cannot be independently analyzed, especially when high misalignment angles are present. Finite element models are widely used in gear analysis lately (e.g. [Mao07; Iñu18; Gon17; Luo19; Rod21]). That is why, their use in gear couplings has also grown: from 2D models to determine the effect of pitch errors [Kro13] to 3D models to analyze the impact of the misalignment angle [Mar19; Von20; Dup20].

Stiffness

Normally the hub is the one that determines the ultimate coupling capacity [Pad60], as the sleeve has wider and stiffer teeth. In aligned working conditions, the stiffness value is constant without considering the effect of the manufacturing errors (Fig. 2.15(a)) and all the teeth make contact at the same time. Thus, the load is equally distributed among all the teeth of the coupling as shown in Fig. 2.16(a) and contact pressure distribution is equivalent for every tooth (Fig. 2.17(a)).

However, in misaligned conditions, due to the non-uniform clearance distribution and the additional tilting moments generated by the kinematics [Cur14b; Hon14a], tooth engagement sequence plays a significant role, and load is no longer uniformly distributed. As it can be seen in Fig. 2.15(b) the stiffness varies with every tooth engaged, i.e., every change of the slope means

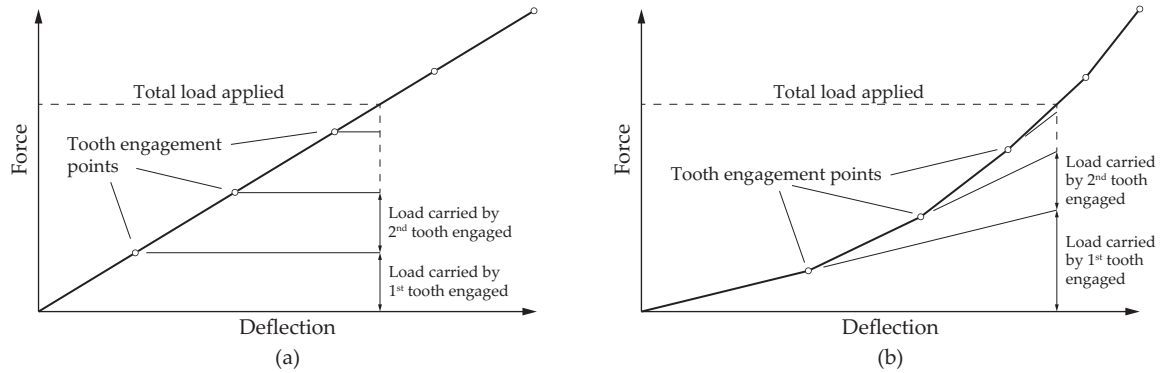

Figure 2.15: Torsional stiffness in (a) aligned and (b) misaligned conditions (adapted from [Sil10]).

other teeth coming into contact. The first engaging tooth is the one with the smallest clearance value (in the tilting position), which will deform as the charge increases until the next smallest clearance tooth pair gets into contact. The process will continue until a sufficient number of tooth pairs are in contact to support the transmitted load.

To help determine the tooth stiffness empirically, [Cur13a] designed a hexapod measuring device capable of monitoring deformations in the six degrees of freedom and reaching a misalignment $\gamma \approx 0.2°$. This research showed good agreement with theoretical and numerical models, concluding that tooth stiffness calculation considering only bending, shear, and tooth root deflection is appropriate. It also showed the non-linear effect misalignment angle has on the stiffness of the gear coupling, evidencing the lack of investigation on this topic in scientific literature.

Load sharing

The consecutive tooth engagement process causes the load supported by each tooth not to be equal [Rob08], and thus the teeth that make contact earlier support a higher percentage of the total load (Fig. 2.16(b)). In the load distribution example shown in Fig. 2.16 due to the misalignment angle, the first tooth engaging will pass from bearing the 10% of the load in aligned (a) to bearing the 18% in misaligned (b) conditions. This is translated as having approximately only half of the teeth which are in contact carrying the total load.

Common design practices would assume uniform loading on all the teeth engaged. However, this would predict a lower force on the first tooth engaged than the one it is actually carrying and would fail before the prediction.

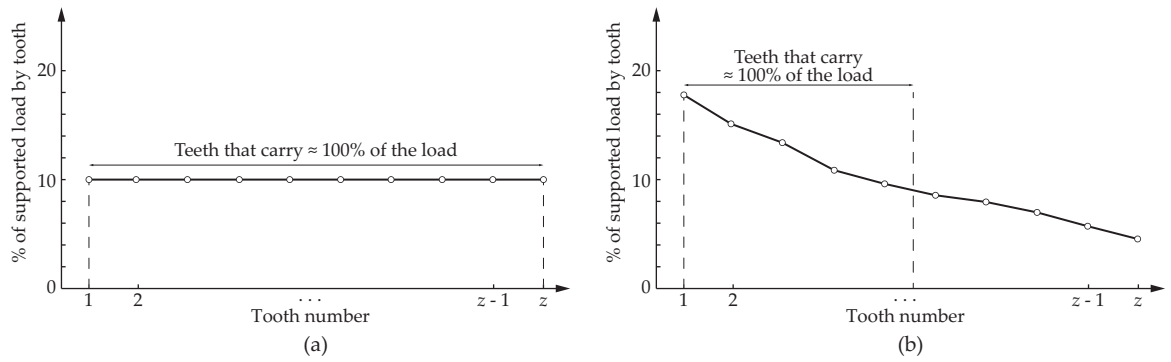

Figure 2.16: Load sharing in (a) aligned and (b) misaligned conditions (adapted from [DeC06; Rob08]).

To experimentally analyze the influence the misalignment angle has in the load distribution, test benches with special designs are required [Hak11; Bak05; Cuf14; Gua21; Guo16]. These authors created test rigs principally to analyze the influence of the misalignment angle in the wear phenomena and consequently were designed up to a maximum misalignment angle of $\gamma = 1°$. Some of them were also used to validate analytical models to predict the induced loads caused by torque, misalignment angle (up to 0.8°), and friction [Guo16].

Contact stress distribution

A higher load sharing in the first tooth engaged (those in the tilting angular position) implies higher contact stresses as observed in Fig. 2.17(b). Here, the non-uniform load distribution can be observed in a 0.2° misaligned gear coupling [Gua19a]. This non-uniformity was also numerically observed by other authors [Hon14b; Med02b], but always at low misalignment angles.

There is limited empirical data concerning crowned gear couplings, especially in misaligned conditions, which leaves most of the existing numerical and analytical with no validation. Furthermore, this issue has been remarked by several authors over the years [Cur13a; Ben17; Cur18b; Gua21].

Among the few existing numerical-experimental correlations, [Cuf12] designed a static test bench to determine the pressure distribution along the face width in aligned conditions up to $\Gamma_{max} = 26.2$ Nm. Employing pressure-sensitive films and the color intensity interpretation of the pressure variations film, they validated the FE model proposed (Fig. 2.19(b)). Sometime later, [Gua21] used the same technique to correlate the contact pattern of crowned gear couplings up to $\gamma = 0.8°$ misalignment angle (Fig. 2.19(a)). [Par14] also validated a FE model for a straight-sided spline shaft with photoelastic tests with less than a 10% error.

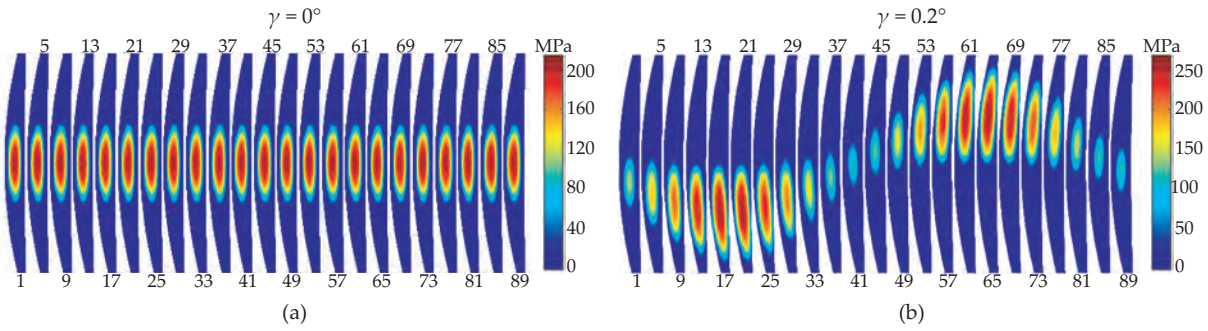

Figure 2.17: Contact stress distribution in (a) aligned and (b) misaligned conditions [Gua19a].

Even if much experimental work has not been correlated with numerical results, the finite element models have permitted analyzing the influence of design parameters. Among them, the longitudinal crowning radius is the principal characteristic of spherical gear couplings working in misaligned conditions. [Gua19c] created a FE model and developed a loaded tooth contact analysis to determine the influence of the meshing position, the torque, the misalignment angle, and the amount of longitudinal crowning. The work concluded that in misaligned conditions of 0.2° the optimal crowning radius (r_c) is the one where the contact point locates at a distance of 0.2 times the face width from the middle section ($\delta_{\max} = 0.2b$). This way Fig. 2.18(a) shows how a small enough crowning radius (r_c = 1000 mm) allows all the teeth to be in contact without the undesired edge contact observed by several authors in scientific literature [Gua18; Ben17; Hon14b; Von20; Dup20].

Similarly, [Hon14b] proved at a misalignment angle of 0.12° that a moderate amount of longitudinal crowning (C_β) can reduce load concentrations effectively while maintaining the load carrying capacity of the gear coupling, as depicted in Fig. 2.18(b). However, showed that an excessive value of longitudinal crowning increased contact stresses and reduced the load-bearing capacity of the coupling (case of $C_\beta = 60$ µm in Fig. 2.18(b)).

Ultimately, an appropriate amount of longitudinal crowning increases the contact surface between the hub and the sleeve tooth surfaces and reduces contact stresses [Pad60; Ren68; Lag12], while it also contributes to increase the number of teeth in contact.

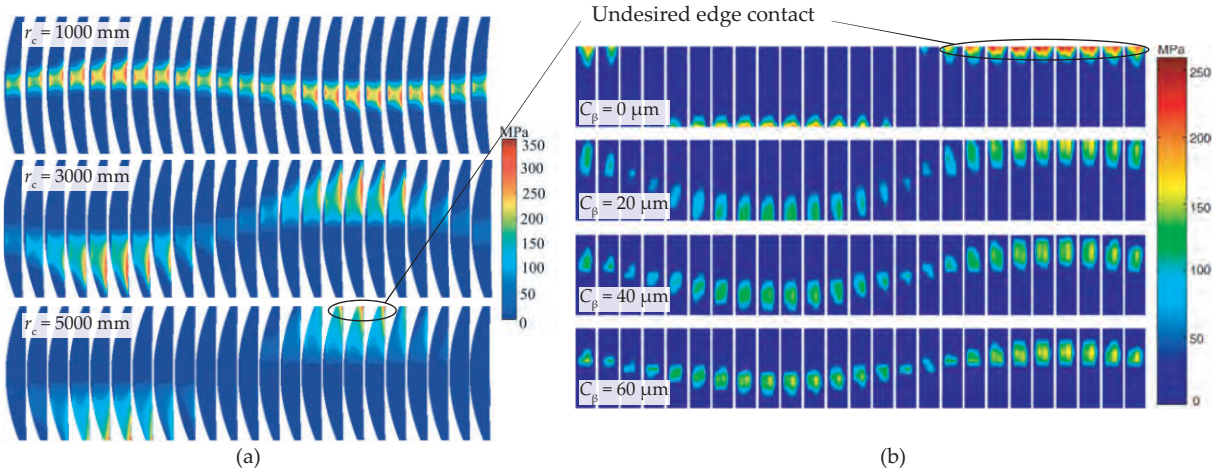

Figure 2.18: Influence in the load distribution and contact stresses of: (a) the crowning radius (r_c) at $\gamma = 0.2°$ [Gua19c], and (b) the amount of crowning (C_β) at 0.12° [Hon14b]

2.3.1 Effective face width

In scientific literature, it has been observed that contact oscillates around the middle section with a nanometers amplitude due to the relative motion that vibrations or assembly/manufacturing errors ($\gamma \ll 1°$) cause. This was fundamentally analyzed from the fretting and wear perspective of the tooth surfaces [Cal75; Lee03; Lee03; Bak05; Cor07].

However, at higher misalignment angles ($\gamma \leq 3°$) and related to the kinematics described in Section 2.1.2, authors have analytically and numerically proved that the contact point displaces along the active tooth profile and face width [Guo16; Cur18a; Gua18; Nak88]. In fact, the evolution of the contact point caused by the misalignment angle results in undesired load concentrations and a variation of the effective face width supporting the load [Nea80; Bün00]. Bünder [Bün00] also stated that a gear coupling with longitudinal crowning working in misaligned conditions would not withstand the load in the whole face width nor in its entire height. These observations have been recently validated experimentally using a gear marking compound [Gua21; Ohs12] as observed in Fig. 2.19(a). However, little information concerning the testing techniques is given. Together with that, [Elk02; Cur13a] showed that deformations increased in misaligned

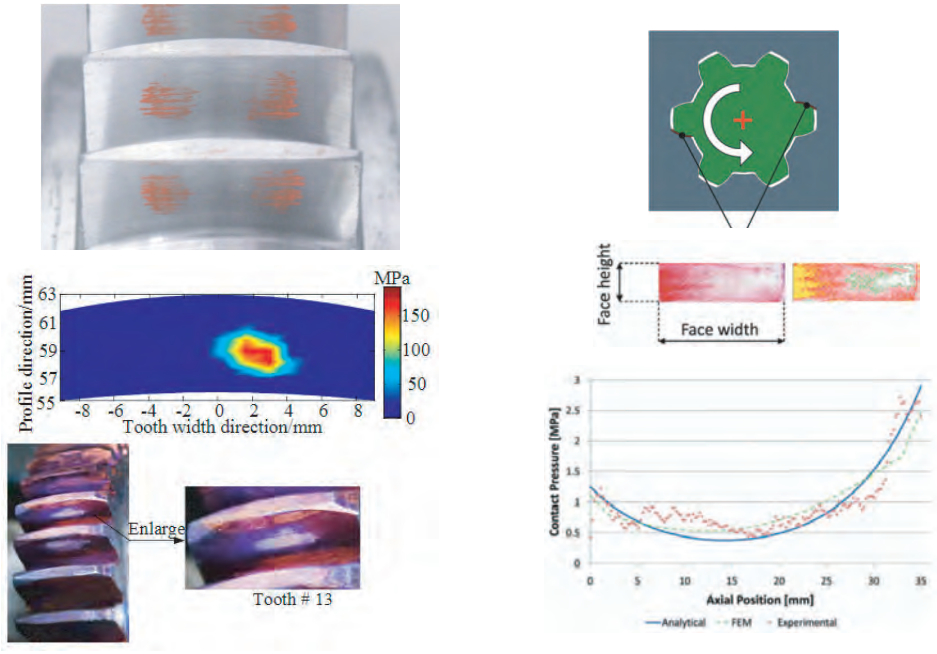

(a) (b)

Figure 2.19: (a) contact pattern in misaligned conditions with gear marking compound: top [Ohs12] ($\gamma = 4°$) and bottom [Gua21] ($\gamma = 0.8°$), and (b) load distribution along the face width with pressure sensitive films [Cuf12]

conditions in face of those suffered in aligned conditions, for the same number of teeth in contact. In Fig. 2.19(b) the contact pressure distribution along the active tooth surface of a straight gear coupling is observed detected with pressure sensitive films [Cuf12].

All this leads to the conclusion that in highly misaligned conditions only part of the face width of the tooth will support the load and that this will significantly affect the tooth stiffness.

2.3.2 Number of teeth in contact

Scientific literature has outlined that the main consequence of misaligned working conditions is the reduction of the number of teeth in contact [Cur13b; Hon14b; Guo16; Gua18] (being all the works focused on $\gamma \leq 1°$).

Fig. 2.20(a) shows some of the references used currently to determine the number of teeth in contact up to 8° misalignment. These relations are either experimental [Pad60] (non-information is found concerning the experimental setup) or analytical [Hen83; Man86; Bün00], and do not account for the influence of the applied torque or tooth stiffness. Moreover, the most conservative standards or sizing criteria [Dud57b; Ced94; Ame20] assume that half the teeth carry the load regardless of the gear coupling geometry or the working conditions.

Moreover, in most of the cases, tooth deformations are calculated considering that the resultant contact force is located in the pitch diameter [Ren68; Elk02; Bar06; Cha10; Guo16; Vau17; Dup20]. However, [Cur14a] showed that especially in misaligned conditions the resultant

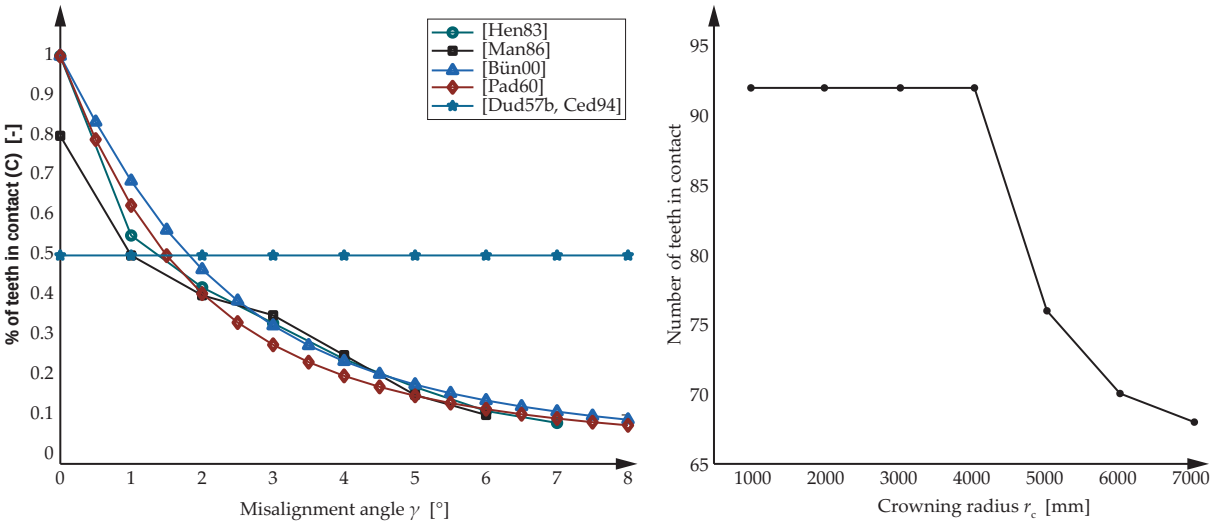

Figure 2.20: Number of teeth in contact in terms of (a) the misalignment angle [Hen83; Man86; Bün00; Pad60; Dud57b; Ced94], and (b) the crowning radius for $\gamma = 0.2°$ [Gua19c].

contact normal force varied from the pitch diameter and affected the tooth stiffness calculation. E.g., even in a small axial misalignment of 0.08 mm, where the location of the resultant contact force differs only 3% from the pitch diameter, the tooth stiffness calculation might vary up to a 15%.

Design parameters have also shown their effect on the number of teeth in contact. In fact, in Fig. 2.20(b) it is shown how a high value of the crowning radius implies a reduction of the number of teeth in contact, additionally to the edge contact shown in Fig. 2.18(a).

Previously, it has been seen that misaligned working conditions present a non-uniform clearance distribution, which leads to a sequential tooth engagement and thus, to a non-uniform load sharing, where the first teeth to engage support the highest stresses. That is why, [Cav71; DeC06] proposed estimating the effective number of teeth in contact (C_{eff}) dividing the average load supported by each tooth (Γ_{avg}) by the load carried in the first teeth engaged (Γ_{max}) as defined in Eq. (2.10).

$$C_{\text{eff}} = \frac{\Gamma_{\text{avg}}}{\Gamma_{\text{max}}} = \frac{\Gamma/z}{\Gamma_{\text{max}}} \tag{2.10}$$

2.3.3 Tooth root stress

As a rotating component, fatigue failure studies are common for straight-sided spline shafts [Yos76; Cam65] principally focusing on the torsion phenomena and the torsional shear stresses. However, it has been shown that gear couplings suffer other types of stresses, such as bending or axial stresses. For that reason, [Vol82] analyzed several load combinations to determine which of them was the most critical. The work concluded that torsion and bending must be taken into account to study the stress-strain state and that all stress components (contact, shear, and normal) need to be considered in the analysis. Indeed, three types of cracks, transverse, inclined, and longitudinal, arise; thus, each design case needs to be analyzed. Together with that, [Tje01b] affirmed that the 78% of the shear stress is caused by pure torsion and 22% by bending of the spline tooth. The work states that the bending component increased as the non-uniformity of the load distribution increased, which is the case for the gear couplings working in misaligned conditions [Guo16; Hon14b; Gua18; Cur13b] (explained in previous section).

For the empirical evaluation of tooth root stresses, the most employed technique is to place strain gages in the tooth root region [Her99; Gui05; Lig08; Hot08; San11; Mar12; Ben17; Lis17] as can be seen in Fig. 2.21.

[Gui05] validated with good accuracy numerical tooth root stress values of straight or helical gears that mesh with a face gear, but with only a few points. As shown in Fig. 2.21(a) five gages were installed along the face width and the wires coiled. Each measurement was repeated three times, but information concerning the data acquisition or the type of gages was not available. [Hot08; Hot11] instrumented a helical and hypoid gear (Fig. 2.21(b)) to analyze the influence of the longitudinal crowning at a maximum misalignment angle of $\gamma \approx 0.11°$. In this work, a multichannel strain gage conditioning unit to amplify the signal of each of the gages was used, obtaining clear and concluding results. As observed in Fig. 2.21(c), [San11] also instrumented spur-gears to determine the influence of tooth root geometry in fatigue and static conditions. Results were within a 6% error compared with a 2D boundary element model and concluded that an asymmetric tooth profile with an elliptical root shape gave the best results, increasing the mean life by more than 30 times.

Concerning gear couplings, [Her99] discussed the design optimization of mill-spindles up to $\gamma = 3°$ misalignment angle, with experimental excellent correlations in tooth root bending with a strain gage test setup. However, no information was given about the testing bench or the acquisition procedures. More recently, [Mar12] analyzed numerically and experimentally the load distribution along the length of the joint. The gages were positioned at 45° in a full-bridge

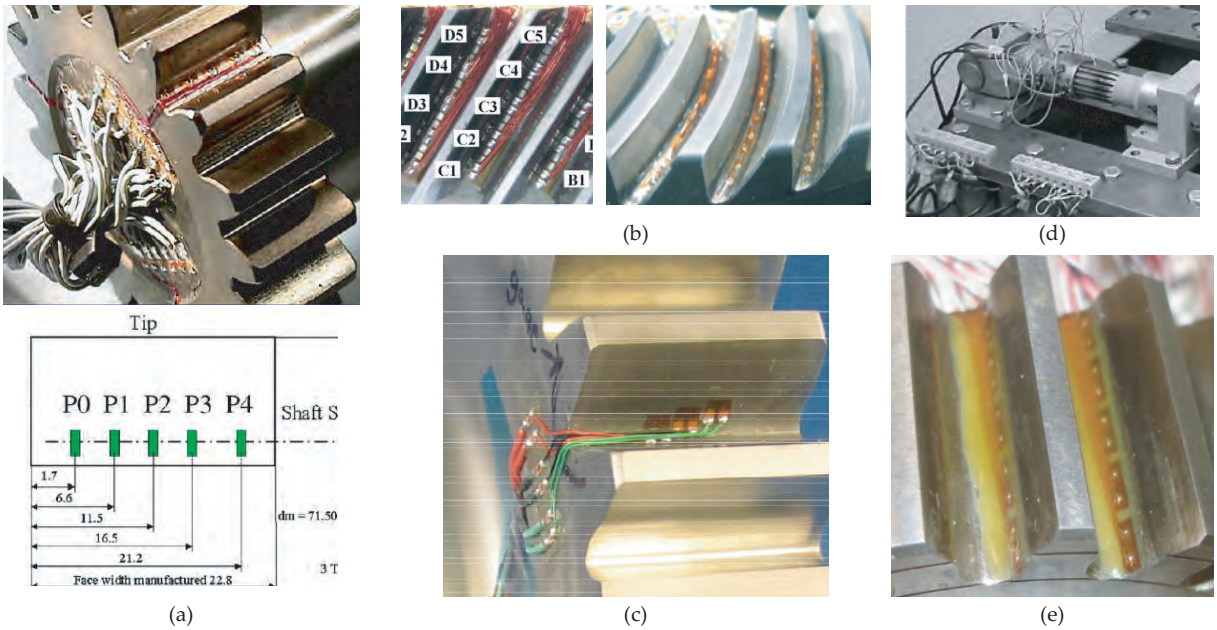

Figure 2.21: Experimental tooth root stress measurement with strain gages:
(a) $m_n = 4$ mm [Gui05], (b) gage length: 0.787 mm, $m_n = 2.04$ mm [Hot08; Hot11], (c) gage length: 0.38 mm, $m_n = 4.23$ mm [San11], (d) [Mar12], and (e) $m_n = 4$ mm [Ben17].

arrangement to measure the maximal shear stress generated by the applied torque (Fig. 2.21(d)). The work concluded that as torque increased, the influence of manufacturing errors decreased. [Ben17] instrumented with miniature strain gages a tooth along the face width (Fig. 2.21(e)), placing them below the start of the active profile (SAP), to capture the influence of the longitudinal crowning and the misalignment angle. Quarter-bridge strain gages were employed with an acquisition frequency of 100 Hz. It was concluded that the strain gage closer to the side where torque was applied suffered higher stresses and that the torque-stress relation was non-linear, resulting from the increase of the contact surface and the joint stiffness (similar observations to that in [Guo13]).

Aside from the strain gage measurement, another employed technique in scientific literature is the one based on the measurement of the deformations undergone by the tooth [Daf17]. In this work, a static test rig was designed for spur and helical gears and tangential deformations were measured with a coordinate measuring machine (CMM). This is a direct method to determine tooth root stress, however not applicable for gear couplings since they are constantly covered.

2.3.4 Gear coupling sizing standards for tooth root failure

Table 2.3 summarizes the different equations currently employed to calculate tooth root stresses. At the end of the table, those used for tooth bending stress calculation in gears (for comparison purposes) are included. In fact, all the equations have the same structure and are derived from tooth root bending calculations applied in gear standards; the force divided by the resistant cross-section of the tooth (geometry parameters), multiplied by a series of coefficients that account for different aspects which affect tooth root stresses, e.g. , stress concentrations, quality, working conditions, etc.

Existing standards (DIN 5466 [Deu02], ISO 4156 [Int05], AGMA 6123-B06 [Ame06], AGMA 945-1-B20 [Ame20]) and research works [Dud57b; Bec05; Ced94; Oct14] are mainly focused on small misalignment angles, and spherical gear couplings for high misalignment applications are referred to as special cases. All in all, coefficients to account for the effect of the misalignment angle (even if low, $\gamma < 1°$) are considered as shown in the third column of Table 2.3.

The use of security coefficients is the most widespread technique among standards, as they are conservative and relatively easy to use. Two relevant coefficients for spherical gear coupling working in misaligned conditions account for the number of teeth in contact (k_{ls} or Z_δ) and the effective face width (k_m) supporting the load.

Table 2.3: Current equations in the literature to determine tooth root bending stress in gear couplings.

Author/Standard	Equation	Coeffs. $\rightarrow f(\gamma)$
Dudley [Dud57b]	$\sigma = \frac{F_t}{b\,m_n} \cdot \left[\frac{4}{z\,Y}\right]$ (US units)	-
Cedoz et al. [Ced94]	$\sigma = \frac{F_t}{b\,m_n} \cdot \left[\frac{2}{z^2\,Y_F}\right]$ (US units)	-
DIN 5466 [Deu02]	$\sigma = \frac{Ft}{b\,h_{\text{eff}}} \cdot \left[Y_\alpha \left(\alpha_{kk} + \alpha_{k\phi}\left(1 - k_\phi^{-1}\,\frac{d_p^2+d_i^2}{d_p^2-d_i^2}\right)\right)\right]$	-
Beckmann [Bec05] / Octrue et al. [Oct14]	$\sigma = \frac{F_t}{b\,m_n} \cdot \left[\frac{2\,k_a\,Z_\delta\,Z_q}{z\,Z_Q}\right]$	Z_δ ($\leq 3°$)
Lagutin et al. [Lag12]	$\sigma = \frac{F_t}{s_l^2} \cdot [6\,c_c\,c_b]$ (US units)	-
AGMA 945-1-B20 [Ame20]	$\sigma = \frac{F_t}{b\,m_n} \cdot \left[\frac{2000\,k_m\,k_a\,k_{ls}}{z\,Y}\right]$	k_m ($\leq$ 0.458°), k_{ls}
ISO 6336-3 [Int06]	$\sigma = \frac{F_t}{b\,m_n} \cdot [Y_F Y_S Y_\beta]$	-
AGMA 2001-D04 [Ame04]	$\sigma = \frac{F_t}{b\,m_n} \cdot \left[\frac{K_o\,K_v\,K_s\,K_H\,K_B}{Y_J}\right]$	-

The load sharing factor (k_{ls})

Standards employ the load sharing factor (k_{ls} or Z_δ) to account for the number of teeth carrying the load. Some works [Dud57b; Ame20; Ced94] consider a constant value of 2.0 (half of the teeth in contact) in formulas and do not account for the evolution of this parameter based on the working conditions. Thus, it is expected that this criterion will oversize the coupling to a great extent under certain conditions. [Dud57b] also suggests that it is acceptable for gear couplings to wear to the point that all the teeth are in contact. However, it is not a safe assumption to accept that wear in all gear couplings will result in improved loading without causing other issues, e.g., increased backlash or debris.

Furthermore, several factors may be of relevance when determining the load sharing factor coefficient: the manufacturing variations effect in the clearance value, the form errors, the material of the gear coupling, the applied load and misalignment angle, etc. For instance, a coupling with a very low stiffness may have good load sharing even if manufacturing quality is very low. Meanwhile, a very stiff gear coupling will require high accuracy to achieve good load sharing [Ame20]. Considering all these facts, [Ame20] defines the load sharing factor range from 2.0 to 3.0. Similarly, [Bec05] proposes a quadratic polynomial Eq. (2.11) which range

from 1.0 to 3.1. This equation is based on the values obtained by [Pad60] for misalignment angles $0° \leq \gamma \leq 3°$, who stated that the values presented corresponded to the current knowledge from many years of operating experience with crowned gear couplings.

$$k_{ls} \leftrightarrow Z_\delta = 0.120\gamma^2 + 0.336\gamma + 1 \tag{2.11}$$

The load distribution factor (k_m)

The load distribution factor (k_m) considers the length of the face width actually carrying the load. In [Ame20] it is defined as a factor dividing the face width by the amplitude of the contact pattern on the active profile surface.

However, the recommendation provided by most authors is in terms of the axial misalignment and face width of the gear coupling. This way, for instance, [Ame20] sets a value of 1.0 for quasi-aligned ($\gamma < 0.23°$) cases, and up to 3.0 for a misalignment of $\gamma \approx 0.5°$. In addition to the misalignment angle required by the design, this coefficient is also influenced by other factors, such as the manufactured helix error, the additional axis misalignment due to the pivoting errors, vibrations, etc. Nevertheless, no research is found concerning the more accurate determination of this coefficient.

Other coefficients

Other coefficients used in gear coupling standards include: the application factor (k_a), the quality factor (Z_Q), the form factor (c_b, Y_F, Z_q), and the stress concentration factor (c_c, Y).

The application factor (k_a) accounts for the uniformity (or lack of it) of the load applied. This is classified according to the power source and the type of load. A value range from, 1.0 for uniform loads, to 2.8 for heavy shocks, is established [Dud57b; Ame20]. In any case, the most reliable data is obtained from experimental measurements, e.g., [Bec05] determines empirically a range of values from 1.25 to 2.0.

The quality factor (Z_Q) considers the influence of the manufacturing class in the contact ratio and the contact pattern. Indeed, if the manufacturing quality decreases, the tolerances increase. In consequence, bigger indexing errors lead to less number of teeth in contact, and thus, higher stresses in those with contact. [Bec05] proposes coefficient values for quality levels $1 \leq Z_Q \leq 11$ which follow Eq. (2.12), and were also depicted in Fig. 2.14.

$$Z_Q = -0.006123Q^2 + 1 \tag{2.12}$$

The form factor (c_b, Y_F, Z_q) accounts for the impact of geometric variables in tooth root stresses. To determine it, [Bec05] considers the effect of the number of teeth in the gear coupling and the addendum modification of the teeth to calculate the module-normalized tooth root thickness and the distance to the force application point. In this manner, as the number of teeth or the tooth addendum modification increases, the form factor decreases.

Finally, the stress concentration (c_c, Y) factor may be calculated from the tooth thickness, the number of teeth, the pressure angle, and the tooth root radius. The common values employed for gear couplings of $\alpha = 30°$ are 1.5 for the sleeve and 0.5 for the hub [Ame20].

2.4 Critical review of the state of the art

Literature review shows that spherical gear couplings are employed to transmit power between shafts due to their high power density compared to other non-splined connections and their capacity to accommodate axial, radial, or angular misalignment [Man86]. However, they are referred to as special cases in standards.

As far as geometry generation models for crowned gear couplings are concerned, models in scientific literature have been developed to generate geometries with large pitch diameters and crowning radius (small amount of crowning), and no experimental correlation has been conducted. Moreover, these generation models do not consider the appearance of singularities (undercut). Nevertheless, highly crowned spherical gear couplings do present them, as they are generated with a small tool path radius to achieve a large amount of crowning in the hub tooth surfaces, i.e., in the order of some millimeters. Generation models based on the two-parameter envelope consider the helicoidal threaded surface of the hob during generation and have shown their potential, versatility, and solid mathematical foundation with the generation of other types of gears, such us, hypoids, noncircular gears, or face-gear drives. For this reason, it is concluded that the generation of highly crowned tooth surfaces must be based in a two-parameter envelope methodology.

Most of the studies related to gear couplings in scientific literature were limited to working conditions with misalignment angles below 3°. In any of the cases, research has shown that load distribution is highly dependent on the tooth geometry and the working conditions. To this aim, optimal tooth geometry adapted to the misalignment angle or mechanisms to avoid high misalignment are designed. It is reported that the crowning radius has a strong influence on the contact pattern and the number of teeth in contact together with the clearance value. Nevertheless, the influence of other design parameters in the misalignment angle or in the appearance of singularities is not readily available, particularly when concerning high misalignment angles.

Regarding their mechanical behavior, literature shows evidence of the reduction of the number of teeth in contact and the displacement of the contact point from the middle section at low misalignment angles. In fact, this generates radial forces and tilting moments which do not exist in aligned conditions, causing the load to be no longer uniformly distributed. The complexity of the load distribution and all the variables involved make finite element models very suitable

tools for their analysis. In spite of it, some of these tools have principally been used in very low misalignment angles ($\gamma \ll 1°$) or do not have any experimental validation. Moreover, the simplifications in standards and the criteria employed during sizing are expected not to be adequate when applied to high misalignment applications, since non-desired under sizing of the components may occur. That is why uncertainty still exists in the mechanical performance of gear couplings working in such conditions.

Fretting fatigue and surface wear are the principal failures of gear couplings working in low misalignment angles, so not much interest is drawn to tooth root stresses in scientific literature. However, in applications where spherical gear couplings are employed ($\gamma \gg 3°$), tooth root breakage failure is the principal failure, since the number of teeth in contact is drastically reduced. Some works in the literature determine this relationship but do not account for the effect of the stiffness or the working conditions.

Tooth root stresses are analytically calculated based on gear tooth root stress ISO 6336 standard [Int06] equations and the effect of the misalignment angle is considered with some coefficients to account for the number of teeth in contact and the effective face width. Nevertheless, the effect of high misalignment angles has not been quantified in these coefficients, thus large security coefficients are used, even for relatively small misalignment angles ($\gamma \leq 3°$). Based on the existing simplified analytical models to determine the number of teeth in contact, it is expected that high misalignment angles will present a different behavior, and the impact of the tooth surface geometry or stiffness will be remarkable. That is why it is required to accurately calculate it with numerical models which have been experimentally validated. Moreover, no analytical or numerical approach was found in scientific literature to define the effective face width of the gear coupling supporting the load.

In brief, most scientific literature is focused on large crowning radius gear couplings, working in aligned conditions and subject to small misalignment angles ($\gamma < 1°$) to compensate for system vibrations or assembly errors. Large misalignment angles are avoided, and thus, for applications where high misalignment working conditions exist, no standardized design criteria are available for tooth root stress calculation.

Action is the foundational key to all success.

—Pablo Picasso

3 | Summary of the contributions

This chapter presents the summary of the contributions presented in the thesis to fulfill the research objectives presented. These summaries are intended to provide a quick overview of the research and the main results obtained. The first publication addresses objective 1 and presents an analytical model to generate the geometry of the hub and sleeve tooth surfaces and an algorithm to determine undercut sections. The second publication which answers to objective 2, presents an algorithm to calculate the maximum misalignment angle and discusses the impact of design variables in the hub geometry and in the maximum misalignment angle. The third one addresses objective 3 and describes the finite element model employed to study the mechanical behavior of gear couplings. Finally, the fourth publication answers objective 4 and presents an experimental validation of the previously developed analytical and numerical models to analyze highly crowned spherical gear couplings. The complete publications can be found in the Appendices.

3.1 Tooth geometry generation

Literature review shows different analytical models to generate straight or slightly crowned external teeth, such as the profile shift method, cutting disc method, or the one-parameter envelope method. However, when these models are applied to generate highly crowned hubs they are not capable of generating undercut sections, or these are generated in the wrong place. This occurs principally in small pitch diameters and small crowning radius geometries, especially when the teeth of the hub are directly manufactured on a shaft.

Moreover, even if some geometry comparisons have been done between existing models [Gua19b; Kel14], differences have always been considered negligible, and they have never been compared to experimental data.

Thus, with the aim of accomplishing the first objective of the thesis, this publication[1] (see Appendix A) covers the following tasks:

- Background that supports the need for a new analytical geometry generation model.
- The complete analytical generation model for the hub and sleeve tooth surfaces.
- An algorithm to detect and generate undercut sections in the hub tooth surface.
- Geometry comparisons with other existing models in literature to prove the existing differences and the need for the proposed model.
- An unloaded tooth contact analysis to demonstrate that the geometry deviations affect the contact conditions.

Motivation

The manufacturing process commonly used for gear couplings includes hobbing and form milling for the hub, and manufacturing by a pinion-cutter for the sleeve. The geometry of such tools stems from the basic rack-cutter geometry, thus, the mathematical models existing in scientific literature are in most cases based on it directly.

With the aim of understanding the analytical models existing in literature [Gua19b; Ohs12; Mit00; Kel14; Cha08] a virtual generation model was created in a CAD-CAM program adapting

[1] *[Iñu21] A. Iñurritegui et al. "Computerized generation and tooth contact analysis of spherical gear couplings for high misalignment applications". In: Mechanism and Machine Theory 164 (2021), pp. 1–22.*

the analytical approach employed [Iñu20]. The model was first validated by generating a straight gear coupling. Deviations below ± 3 µm were achieved between the analytical and CAD-CAM geometries, which were related to the numerical errors to find intersections between them.

Next, a crowned geometry was generated virtually and analytically. As shown in Fig. 3.1 it was concluded that deviations between the hobbing process (which is considered to be the real manufacturing process) were elevated when compared to other manufacturing processes derived from the analytical approaches. Plotted in a K-diagram, deviations are calculated against the one-parameter analytic model [Kel14] for the active profile geometry in plane $z = 17.5$ mm. It was expected this to be the most accurate analytical model, nevertheless, it is demonstrated that it is not the best approach and that neither of the models employed gives the same result (especially at the beginning and end of the active profile). This work permitted an understanding of the hobbing process kinematics in detail and the need to consider the whole thread surface of the machining hob was proved.

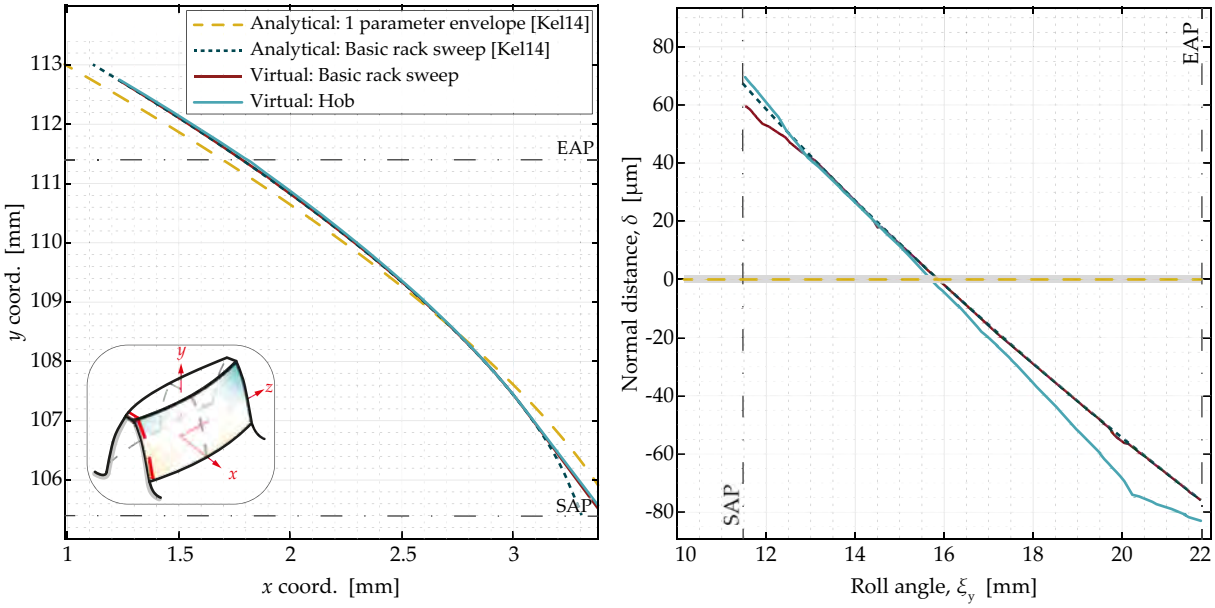

Figure 3.1: Active profile and deviations between different models.

Developed analytical model

Publication [Iñu21] presents a novel analytical model to more accurately generate spherical hubs which may contain undercut sections. The mathematical model is summarized in Fig 3.2 with the principal variables involved and described in the following lines.

The rack cutter generating tooth surface Σ_c is represented in coordinate system S_c as:

$$\mathbf{r}_{\mathrm{c}}(u,v) = \mathbf{M}_{\mathrm{cb}}(v)\,\mathbf{M}_{\mathrm{ba}}\,\mathbf{r}_{\mathrm{a}}(u) = \mathbf{M}_{\mathrm{cb}}(v)\,\mathbf{M}_{\mathrm{ba}}\,[u \quad 0 \quad 0 \quad 1]^{\mathrm{T}} \tag{3.1}$$

where $\mathbf{M}_{\mathrm{cb}}$ and $\mathbf{M}_{\mathrm{ba}}$ are coordinate transformation matrices, u is the first surface parameter in the profile direction, and v is the second surface parameter in the feed direction.

Coordinate transformation (3.2) from system S_c to system S_w and consideration of the meshing equation (3.3) allows the determination of the hob thread surface Σ_w from the rack-cutter tooth surface Σ_c:

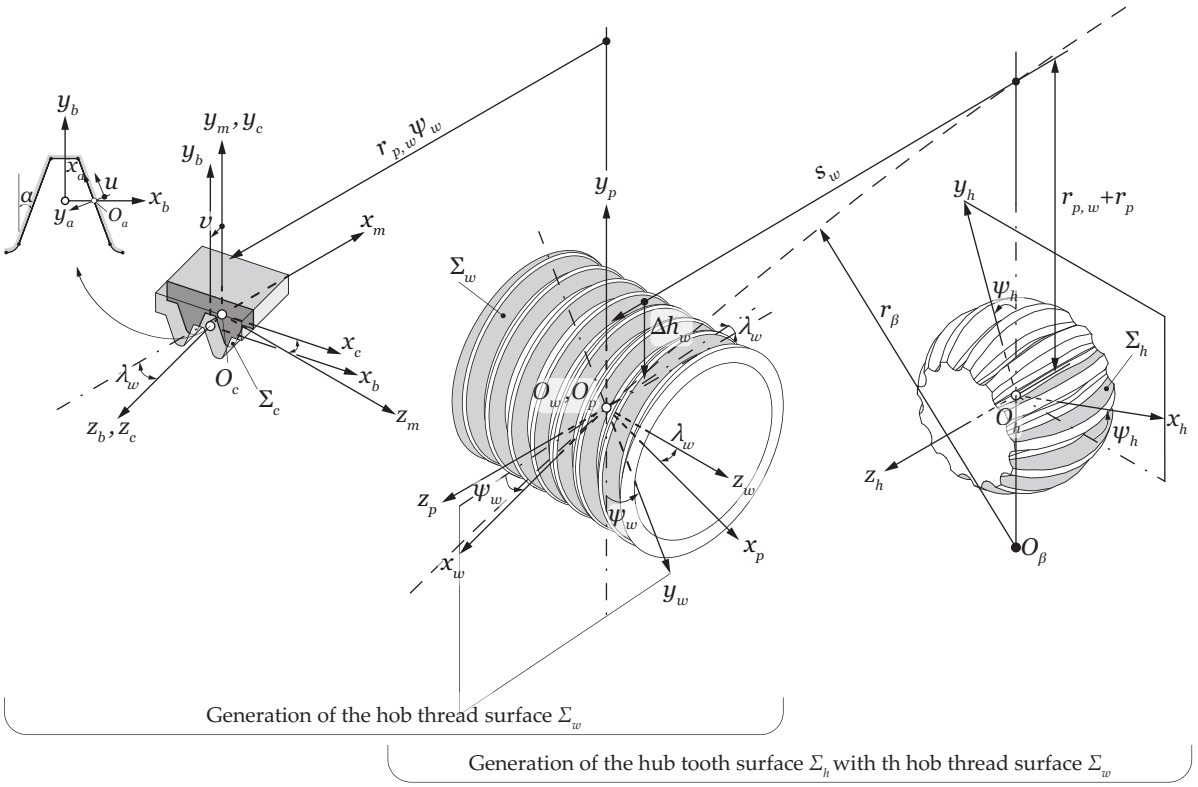

Figure 3.2: Derivation of the hub tooth surface, with the prior determination of the hob thread surface.

$$\mathbf{r}_{\mathrm{w}}(u,v,\psi_w) = \mathbf{M}_{\mathrm{wm}}(\psi_w)\,\mathbf{M}_{\mathrm{mc}}\,\mathbf{r}_{\mathrm{c}}(u,v) \tag{3.2}$$

$$f_1(u,v,\psi_w) = \left(\frac{\partial \mathbf{r}_{\mathrm{w}}}{\partial u}\times\frac{\partial \mathbf{r}_{\mathrm{w}}}{\partial v}\right)\cdot\frac{\partial \mathbf{r}_{\mathrm{w}}}{\partial \psi_w}=0 \tag{3.3}$$

Here, ψ_w is the generation parameter for the hob thread surface, and $\mathbf{M}_{\mathrm{wm}}$ and $\mathbf{M}_{\mathrm{mc}}$ are the coordinate transformation matrices.

Coordinate transformation (3.4) from system S_w to system S_h and the consideration of a double-enveloping process according to [Lit04] with two independent parameters of generation ϕ_w and s_w (3.5, 3.6) enables the determination of the hub tooth surface Σ_h by the rotation of the hob thread surface along a curved tool path:

$$\mathbf{r}_{\mathrm{h,a}}(u,v,\psi_w,s_w,\phi_w) = \mathbf{M}_{\mathrm{hp}}(s_w,\phi_w)\,\mathbf{M}_{\mathrm{pw}}\,\mathbf{r}_{\mathrm{w}}(u,v,\psi_w) \tag{3.4}$$

$$f_2(u,v,s_w,\phi_w) = \left(\frac{\partial \mathbf{r}_{\mathrm{h,a}}}{\partial u}\times\frac{\partial \mathbf{r}_{\mathrm{h,a}}}{\partial v}\right)\cdot\frac{\partial \mathbf{r}_{\mathrm{h,a}}}{\partial \phi_w}=0 \tag{3.5}$$

$$f_3(u,v,s_w,\phi_w) = \left(\frac{\partial \mathbf{r}_{\mathrm{h,a}}}{\partial u}\times\frac{\partial \mathbf{r}_{\mathrm{h,a}}}{\partial v}\right)\cdot\frac{\partial \mathbf{r}_{\mathrm{h,a}}}{\partial s_w}=0 \tag{3.6}$$

Here, $\mathbf{M}_{\mathrm{hp}}$ and $\mathbf{M}_{\mathrm{pw}}$ are the coordinate transformation matrices. $\mathbf{M}_{\mathrm{hp}}$ is the matrix that determines the plunging (Δh_w) of the hob in accordance with the tool path shape.

The simultaneous consideration of all Eqs. (3.3 - 3.6) enables the hub tooth surface to be generated from the rack cutter surface and hob tooth surface definition.

Algorithm to detect singularities

During the process, the following algorithm summarized in Fig. 3.3 was considered to make possible the detection of three different types of cross-sections and determine the interval of the values for the active and fillet profile parameters. The three types of cross-sections are represented in Fig. 3.3: (i) no-undercut region, (ii) undercut region, and (iii) only-fillet region.

The algorithm calculates the hub tip height and the tooth profile radii along the active profile. If the profile radii from tip to bottom decrease constantly, the active profile is free of singularities and the cross section is located in region (i). However, if it increases, tangency will no longer exist between the active profile and the fillet. Solving a set of seven equations and seven unknowns the radius of the intersection point (singular point) is obtained. If this point is beyond the hub tip height the cross section is located in region (iii), while if it is below, the section is located in region (ii).

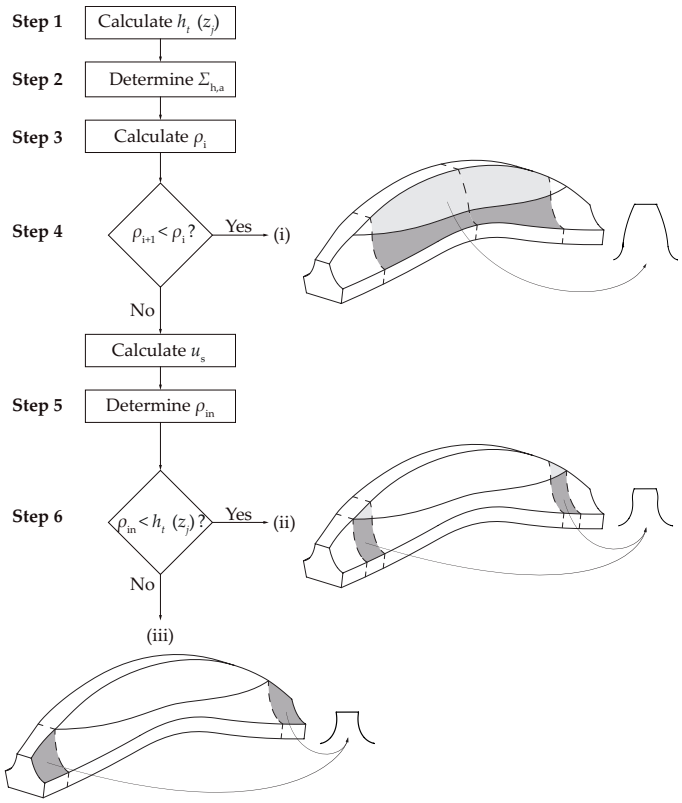

Figure 3.3: Algorithm to detect undercut and identify the region for each cross-section.

Results

The proposed hub model is compared with two existing models where a cutting edge is considered as a generating tool of the hub. Model 1 [Kel14] is a one-parameter envelope model, which considers a circular sweep of the cutting edge of the middle cross-section of the hob. Model 2 [Kel14; Gua19b] generates the tooth surfaces of the hub in a one-parameter envelope model by a set of independent cross sections with the cutting edge geometry of the hob and a variable profile shift coefficient.

The comparison shows that normal deviations are significant between the hub tooth surface generated with the different models, especially away from the reference plane (middle plane). Fig. 3.4(a) represents the 3D geometry of the proposed model and model 2, which presents the highest deviations. Moreover, the cross section at which undercut occurs in the proposed model is compared in Fig. 3.4(b) to display the differences in the geometries obtained with models 1 and 2. These exceed the maximum manufacturing deviations set by ISO 4156 standard [Int05]. Moreover, the deviations in the location where undercut sections start are relevant.

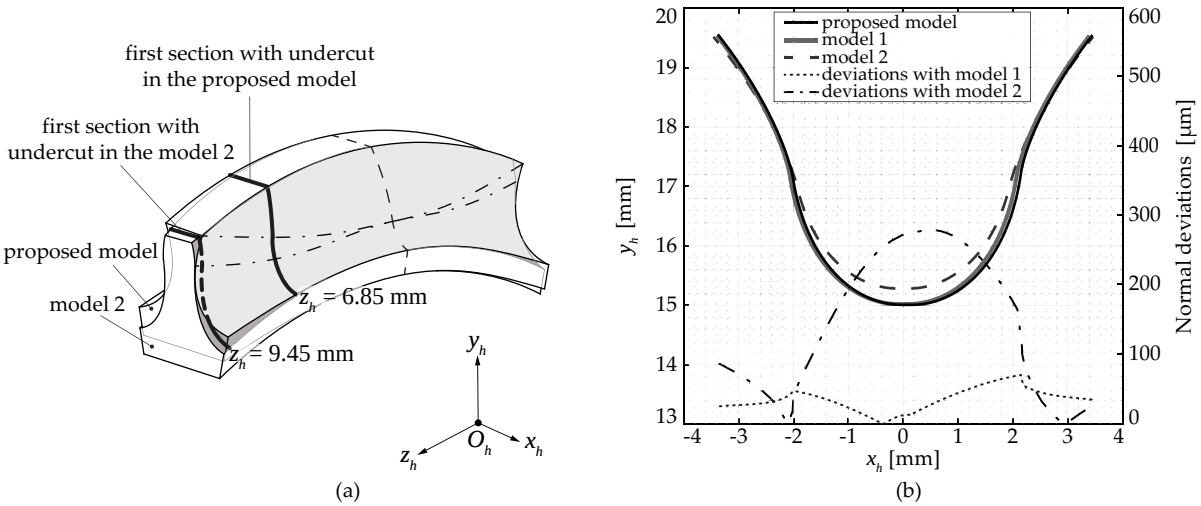

Figure 3.4: (a) comparison of the 3D geometry of the proposed model and that from scientific literature, and (b) comparison of $z_h = 6.85$ mm cross-section in every model analyzed.

Furthermore, from the application of the unloaded tooth contact analysis and clearance calculation, disparities are observed when a misalignment angle is present. The proposed model predicts slightly larger shifts of the contact point as the misalignment angle increases, which gives bigger clearance values than those predicted by models in scientific literature. For instance, at $\gamma = 6°$ differences at the location of the contact point rise up to 144 µm between the proposed model and Model 1, and clearance value deviations up to 15 µm.

Conclusions

The model presented and the comparisons with other models in the literature have permitted demonstrating that deviations with regard to the existing models in literature are significant in highly crowned spherical couplings and that they exceed the maximum values established in ISO 4156 standard [Int05]. Moreover, it enables the accurate detection of undercut sections and permits generating tooth surfaces adapted to different tool paths.

The deviations encountered in the geometry and clearance values when using different geometry generation models reveal the need for experimental validation. Furthermore, these differences may affect the working conditions (e.g., the achievable maximum misalignment angle) or the calculated bending strength of the hub. That is why analytical and numerical models that consider the accurate gear coupling geometry need to be developed.

3.2 Parametric analysis of design variables

Literature review shows very few works of spline couplings working at high misalignment angles. Anyway, it is always remarked that the misalignment angle is one of the most critical parameters for the failure to occur. However, the influence of each of the design parameters on the achievable maximum misalignment angle is not known. Moreover, the applicable maximum misalignment angle is an important parameter for designers, and its analytical determination is only employed for lower angles ($\gamma \leq 1.5°$). Thus, there is a lack of knowledge to choose the appropriate geometry parameters from the design point of view, also sustained by the lack of experimental validation of the maximum misalignment angle.

The manufacturing process is responsible for the tooth surface geometry of the hub and the sleeve, and both will be responsible for the achievable maximum misalignment angle as concluded from the first publication [Iñu21]. Moreover, it is already known that undercut is not desired in gears due to the weakening of the tooth root and that highly crowned spherical gear couplings are prone to their appearance. For all these reasons and since no design guidelines exist for high misalignment applications in current standards, the second publication[2] (see Appendix B) covers the following gaps in response to the second objective of the thesis:

- An algorithm to determine the maximum misalignment angle in view of the existing limitations in the equations found in scientific literature.
- The application of the analytical generation model to a wide range of design parameter values of the hub, and an analysis of the achievable maximum misalignment angle and geometrical properties (i.e. existence of singularities).
- The influence of the design parameters in the maximum misalignment angle and design guidelines to avoid the existence of singularities.

Maximum misalignment angle definition

As observed in Fig. 3.5 to calculate the maximum misalignment angle the sleeve is fixed and the angle at which the hub makes contact with the sleeve is sought in the tilting angular position. In the contact point, tooth surface points and normals are equal, thus a system of five

[2] *[Iñu22] A. Iñurritegui et al. "Spherical gear coupling design space analysis for high misalignment applications". In: Mechanism and Machine Theory 173 (2022), pp. 1-21.*

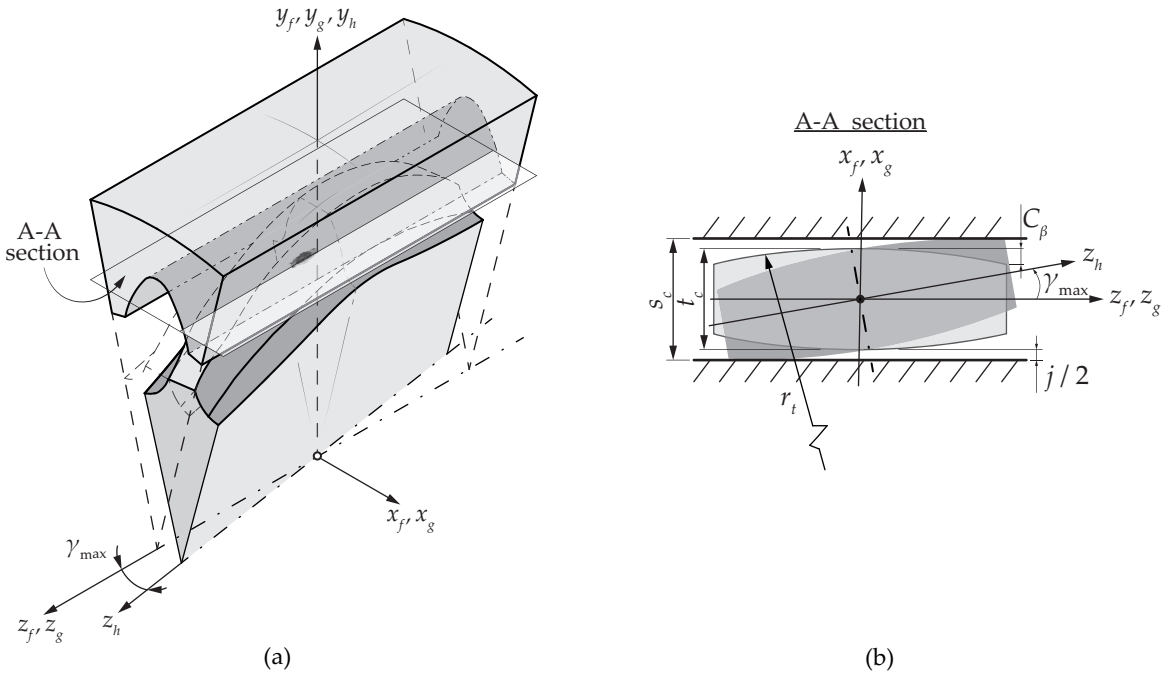

Figure 3.5: (a) maximum misalignment angle determination, and (b) pitch-plane section with relevant parameters for its definition.

independent scalar equations with five unknowns is constructed. The unknowns are the hub tooth surface parameters $\{u_\mathrm{h}, v_\mathrm{h}\}$, the sleeve tooth surface parameters $\{u_\mathrm{g}, v_\mathrm{g}\}$, and the maximum misalignment angle $\{\gamma\}$. The equations are summarized in Eqs. (3.7, 3.8) in the fix coordinate system S_f, taking into account that Eq. (3.8) represents only two independent scalar equations since $|\mathbf{n}_f^{(\mathrm{hub})}| = |\mathbf{n}_f^{(\mathrm{sleeve})}| = 1$.

$$\mathbf{r}_f^{(\mathrm{hub})}(u_\mathrm{h}, v_\mathrm{h}, \gamma) = \mathbf{r}_f^{(\mathrm{sleeve})}(u_\mathrm{g}, v_\mathrm{g}) \tag{3.7}$$

$$\mathbf{n}_f^{(\mathrm{hub})}(u_\mathrm{h}, v_\mathrm{h}, \gamma) = \mathbf{n}_f^{(\mathrm{sleeve})}(u_\mathrm{g}, v_\mathrm{g}) \tag{3.8}$$

Fig. 3.6 shows the maximum misalignment angle calculated with equations in literature and with the proposed algorithm. **L3** represents a big pitch diameter and a small crowning radius geometry where all the approaches give similar results. However, **CS1** and **CS3** are smaller pitch diameter gear couplings: **CS1** has a higher crowning ratio, and **CS3** a smaller one (i.e. big amount of longitudinal crowning). It is observed that differences between the equations from literature and the proposed algorithm increase considerably for the last two cases since the effect of the face width or the crowning radius are not considered in the equations.

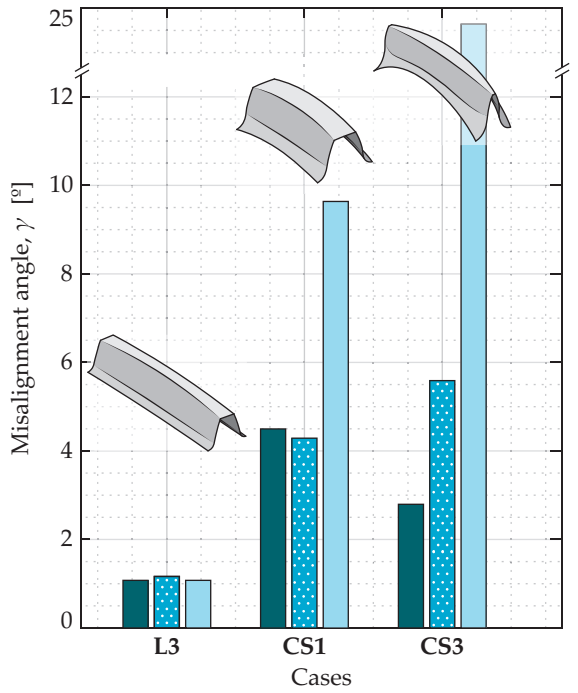

Cases		**L3**	**CS1**	**CS3**
d_p	[mm]	1016	99	99
m_n	[mm]	10.16	3	3
z	[-]	100	33	33
α	[°]	20	30	30
b/d_p	[-]	0.125	0.30	0.30
j	[mm]	0.64	0.71	0.71
ε	[-]	3.94	1.00	0.40
γ_{max}	[°]	0.80	4.50	2.94

Figure 3.6: Maximum misalignment angle according to literature and the proposed algorithm.

These results conclude that the methodology proposed can be applied to every type of geometry and that the transverse crowning radius cannot be approximated to the crowning radius by $r_t = r_c/\tan(\alpha)$ in highly crowned spherical gear couplings.

Influence of the design variables

The influence of the design variables in the maximum achievable misalignment angle is analyzed in the range of values described in Fig. 3.7. Minimum and maximum values were defined inside ISO 4156 standard limitations [Int05]. The reference value is the middle value for each of the design variables shown in the table from Fig. 3.7.

Fig. 3.7 shows a summary of the results obtained, after generating all the geometries. In this graph, each of the corners refers to the design variables analyzed (corresponding to a line of the table), while the different colors (points) refer to the minimum, the reference, and the maximum value of each variable. Geometries generated crossing these variables, are not represented herein, for ease of understanding, while the deep analysis can be consulted in the publication [Iñu22].

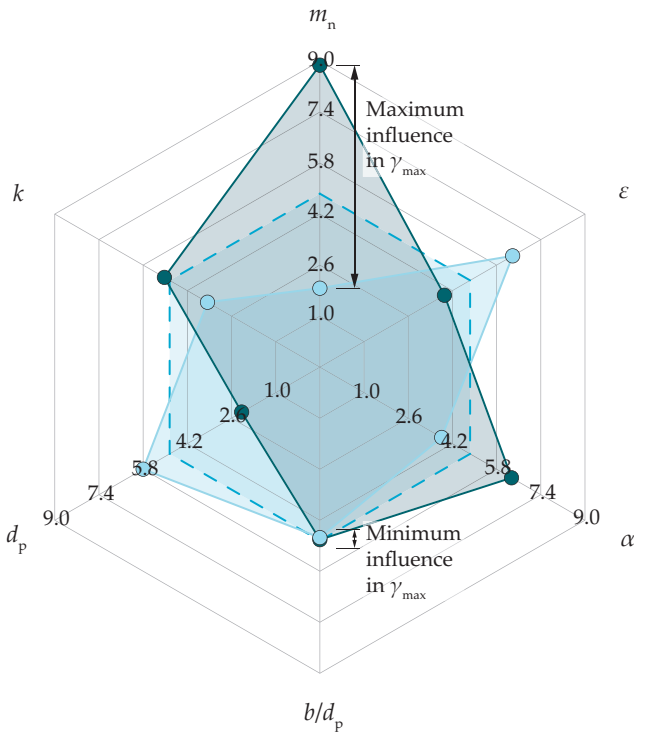

Parameter		Value range				
m_n	[mm]	0.5	⟶	3.0	⟵	8.0
ε	[-]	0.4	⟶	0.7	⟵	1.0
α	[°]	20	⟶	30	⟵	45
b/d_p	[-]	0.15	⟶	0.30	⟵	0.90
d_p	[mm]	36	⟶	50	⟵	200
k	[-]	0.04	⟶	0.07	⟵	0.08

Figure 3.7: Achievable maximum misalignment angle in terms of the design variables described.

From Fig. 3.7 it is observed that the maximum misalignment angle can be calculated for every geometry and that the variables with a greater impact in the misalignment angle are: the module, the pressure angle, and the crowning ratio. In fact, the influence of the pitch diameter is also remarkable. This is linked to the effect of the number of teeth since a variation of the pitch diameter with a constant module implies a change in the number of teeth, and therefore in the tooth profile.

Finally, design guidelines were provided with diagrams. The limiting conditions of existence (useful flank, undercut, and pointed teeth) can be seen in terms of the design variables so that geometries adapted to a certain space and an achievable maximum misalignment angle can be chosen. An example of this graph is depicted in Fig. 3.8, where the geometries in different zones of the graph are represented, in terms of the number of teeth and the crowning ratio. In colors, the range of the achievable maximum misalignment is shown and the dotted space represents the region in which no undercut sections nor pointed teeth occur. For instance, for a given maximum misalignment angle of $\gamma = 6°$, a geometry with $z = 10$ and $\epsilon = 0.95$ would be preferable in the face of a $z = 20$ and $\epsilon = 0.60$ as the second one would present undercut sections that would weaken the tooth root.

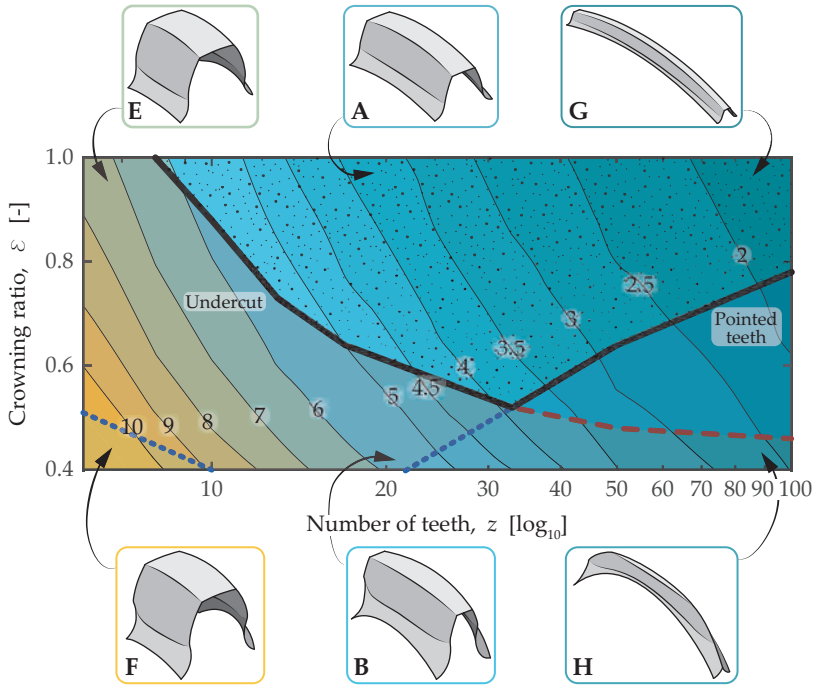

Figure 3.8: Conditions of existence in terms of the crowning ratio and number of teeth for an achievable maximum misalignment angle ($d_p = 50$ mm, $\alpha = 30°$, and $b/d_p = 0.3$).

Similar analyses were carried out in terms of the pressure angle, the aspect ratio, the pitch diameter, and the clearance factor. This research permitted concluding that the defined procedure is suitable to find out geometries without undercut sections or tip pointing to withstand a certain misalignment angle. Moreover, it is observed that high-pressure angle geometries give rise to hubs with verified geometric tooth surfaces at high misalignment angles. Nevertheless, there are still some working conditions ($\gamma > 5°$) where the existence of undercut sections is unavoidable, which in consequence will need to be accurately generated.

Even if these results are very valuable for a preliminary design phase, they require validation with a loaded tooth contact analysis, for which a numerical model is required. Indeed, in load conditions, the number of teeth in contact will vary as the misalignment angle increases, and thus, the flexibility of the gear coupling will change giving as a result a slightly larger misalignment angle.

3.3 Load distribution and tooth root stress

Scientific literature specifies that 20% of failures in gear couplings occur caused by the misalignment angle and these fail due to tooth root breakage. To this end, it is important to calculate tooth root stresses. Even if the relevant works in literature focus on low misalignment angles ($\gamma \leq 1.5°$), it is concluded that the number of teeth in contact and the contact position change considerably in terms of the misalignment angle. Thus, the load distribution changes and consequently the tooth root stresses. To calculate the latter, current standards use equations derived from the gear calculations and coefficients to consider the effect of the misalignment angle. However, these coefficients only account for the effect of low misalignment angles and are very conservative, since the behavior at high misalignment angles is uncertain.

To this aim, and answering to the third objective of the current thesis the third publication[3] (see Appendix C) covers:

- The definition of a computerized finite element model for spherical gear couplings working at high misalignment applications.
- The analysis of the influence of the misalignment angle and the applied torque on the number of teeth in contact and tooth root stresses in high misalignment angles ($\gamma \gg 1.5°$)

Developed finite element model

The finite element model generation is automatized and it is created from the generated analytical hub and sleeve geometries. Both parts are meshed based on the meshing procedure described in [Arg02], with the novelty that a finer mesh is set in the cross-sections of potential contact zones along the face width, which transitions into a coarser mesh to the edges of the component as shown in Fig. 3.9(b). This provides smaller elements in those zones with higher stress gradients without increasing the computational cost. The hub mesh and a cross-section mesh can be seen in Fig. 3.9(b).

The FE model is assembled setting the misalignment angle to the sleeve and letting free one of the degrees of freedom of the hub to apply the torque. A cylindrical coordinate system (r, θ, z_f) is defined to carry out the simulation and facilitate post-processing (Fig. 3.9(a)).

[3] *[Iñu23] A. Iñurritegui et al. "Load distribution and tooth root stress of highly crowned spherical gear couplings working at high misalignment angles". In: Mechanism and Machine Theory 179 (2023), pp. 1-21*

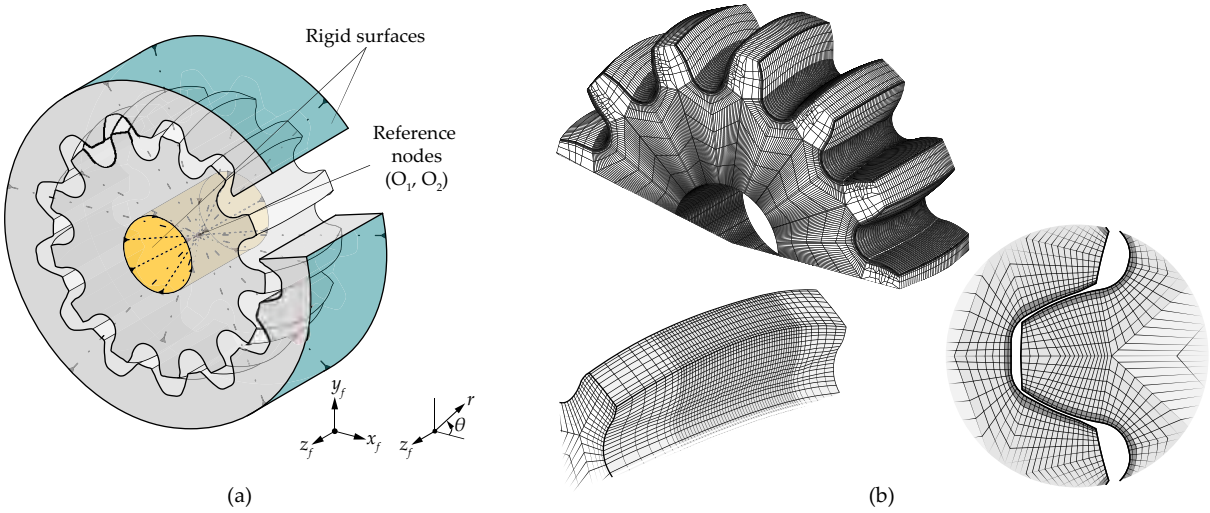

Figure 3.9: (a) FE model assembly with the definition of the rigid surfaces and the reference nodes, and (b) FE mesh in the face width and in the cross section.

From the simulation the next information was extracted: (i) the number of teeth in contact from the contact status output of the nodes, (ii) the load distribution calculated from the contact normal force of the nodes in contact, and (iii) the bending ($\sigma_{22} = \sigma_{\theta\theta}$) tooth root stress in each of the tooth root elements.

Tooth root stress cycle

Since the principal objective of this study is to deduce the tooth root stress distribution, Fig. 3.10 depicts the maximum tooth root bending stress cycle for different misalignment angles. It is observed that each tooth passes twice through each position in each revolution; maximum values in the tilting angular position and minimum values in the pivoting one.

According to this cycle, Fig. 3.10(b) and (c) represent the mean and alternating stress levels of the cycle in terms of the applied torque and misalignment angle. In these graphs, two different trends can be observed (divided with a slash and dotted line).

The first behavior is up to $\gamma \leq 1.5°$, where a sinusoidal fluctuating stress cycle is observed (positive fatigue stress ratio, $R > 0$). Here, teeth do not completely lose contact in any angular position and stress values oscillate around the stress value of the aligned case. The second behavior arises from $\gamma > 1.5°$, where teeth lose contact in the pivoting position, thus stresses descend to zero in those angular positions. This produces a repeated tensile (or pulsating tension) stress cycle ($R = 0$). This pulsating stress cycle has not been previously discussed in scientific literature related to gear coupling tooth root fatigue and hence, this work highlights that the behavior is more complex than expected and that it needs a deeper understanding.

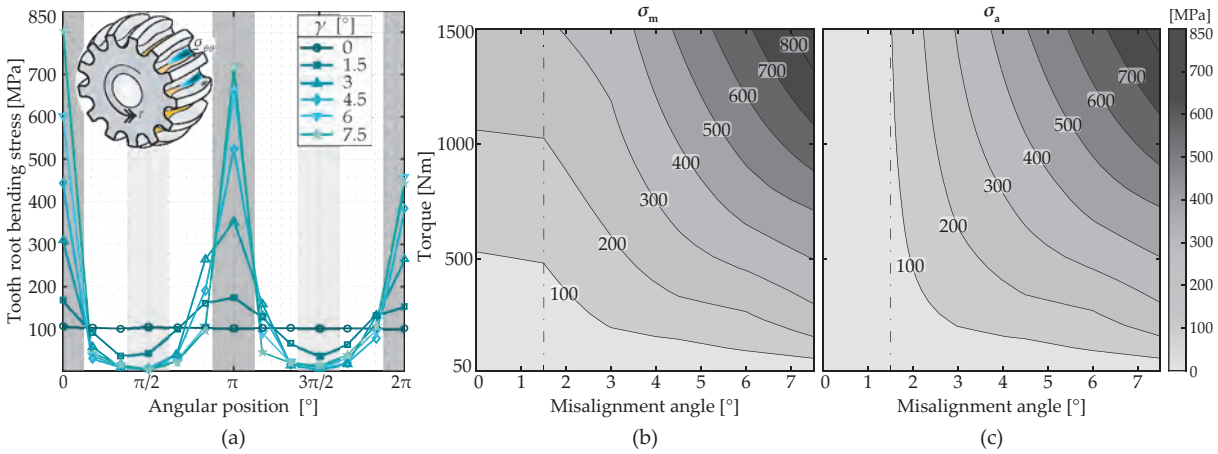

Figure 3.10: (a) maximum tooth root bending stress cycle of a gear coupling at $\Gamma = 500$ Nm in terms of the misalignment angle, (b) the mean stress level, and (c) the alternating stress level in terms of the applied torque and the misalignment angle.

Undercut influence

From the geometrical part, undercut sections have shown to be trivial for tooth generation. In Fig. 3.11 their effect on tooth root stress can also be observed. Stresses are very low and close to the values of the aligned case along the cycle except in the tilting section (contact section). This is a stress concentration section and it is especially remarkable in high misalignment angles ($\gamma > 3°$) where the contact point is located closer to the undercut section beginning (see the stress increase at 0° angular position for $\gamma = 7.5°$).

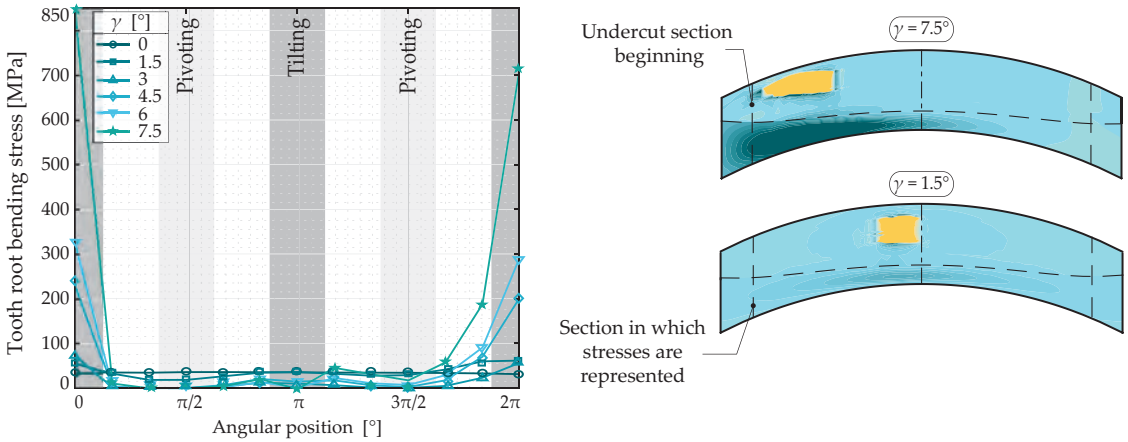

Figure 3.11: Maximum tooth root bending stress cycle at $\Gamma = 500$ Nm at the undercut beginning section.

Effective face width and number of teeth in contact definition

Although some research works state that the effective face width of the teeth decreases when misalignment occurs, AGMA 945 B20 [Ame20] determines the load distribution factor dividing the face width by the contact amplitude. However, remarkable differences exist in the maximum displacement of the contact point between the existing calculations and the results obtained from the FE model due to the effect of the misalignment angle. In addition, no other calculation model was found in literature to determine the effective face width.

Fig. 3.12 shows the new suggested method to define the effective face width supporting the load. Here, the effective face width (b_{eff}) is defined by calculating the length of the face width that is bearing stresses above the 70% of the maximum tooth root bending stress ($0.3\,\sigma_{\max}$), as shown in Fig. 3.12(a). It can be seen that this length does not significantly vary with the misalignment angle, even if the contact amplitude increases. Nevertheless, according to the method proposed in AGMA 945 B20 [Ame20] higher values would be expected in aligned conditions.

The number of teeth in contact is defined following Eq. (3.9) taking into account the effective number of teeth that carry the load. This is a more representative value than the number of teeth in contact and it is obtained by dividing the average load supported by each tooth (Γ_{avg_j}), and the load carried by the most charged one ($\Gamma_{\max_j}$). For instance, in aligned conditions $C = C_{\text{eff}}$, meaning all the teeth are equally loaded.

$$C_{\text{eff}} = \frac{\Gamma_j}{\Gamma_{\max_j}} = \frac{\Gamma/z}{\Gamma_{\max_j}} \tag{3.9}$$

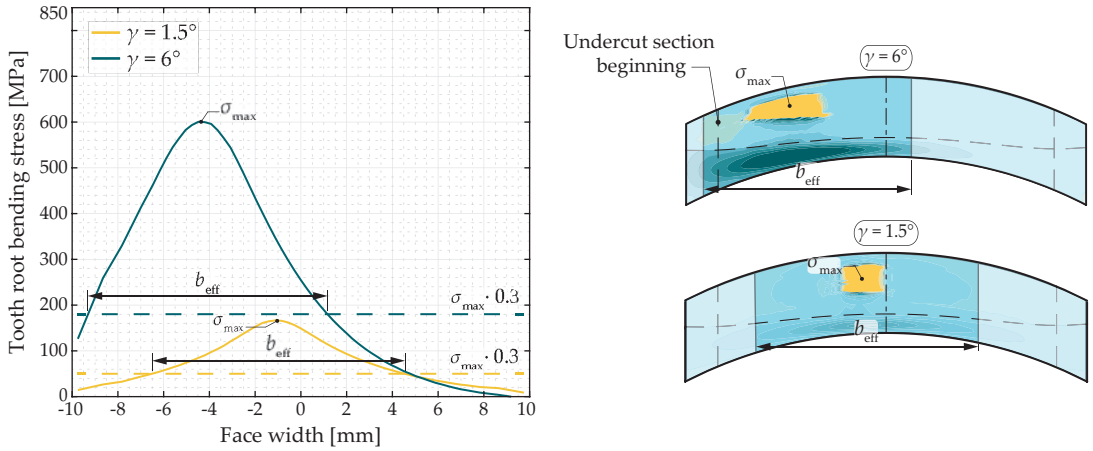

Figure 3.12: Suggested definition of the effective face width (b_{eff}) for highly crowned gear couplings.

Tooth root stress calculation semi-analytical approach

With the proposed new effective face width calculation method and the consideration of the effective number of teeth in contact, tooth root stresses are calculated as observed in Fig 3.13 and following Eq. (3.10).

$$\sigma = k_a \, k_m^* \, k_{ls}^* \, \frac{2000\,\Gamma}{d_p^2 \, b \, Y} \tag{3.10}$$

where, $k_a = 1$ is the application factor, k_m^* the load distribution coefficient, k_{ls}^* the load sharing coefficient, Γ the applied torque, d_p the pitch diameter, b the face width, and $Y = 0.5$ the stress concentration factor.

Employing the current standards (Fig 3.13(a)) even at low misalignment angles, significant differences emerge, and undersize the stresses suffered by the component. For this reason, it is concluded that sizing spherical gear couplings working in high misalignment angles can result in a premature breakage of the element, due to the undersized results obtained with the current standard.

By contrast, Fig. 3.13(b) shows the results obtained with the recalculated coefficients (k_m^* , k_{ls}^*). Predicted values are very close to those from the LTCA at low or high misalignment angles, with a maximum deviation below the 10%.

The proposed model allows for future work to focus on the influence of different design parameters (e.g. , z, α, etc.) in the tooth root stress of highly crowned spherical gear couplings.

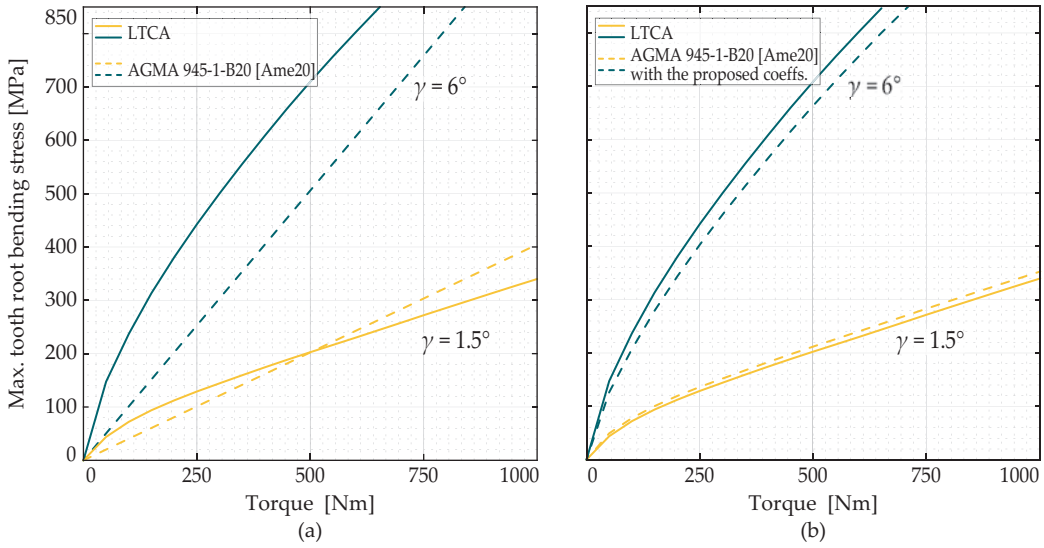

Figure 3.13: Comparison of the maximum tooth root bending stress at $\gamma = 1.5°$ and $\gamma = 6°$: (a) between LTCA and [Ame20], and (b) between LTCA and [Ame20] with the new recalculated coefficients k_m^* and k_{ls}^* deduced from LTCA results.

3.4 Experimental validation

Literature review has shown few works correlating gear coupling mechanical behavior with experimental data. Moreover, most of the existing test rigs are designed for low misalignment angles ($\gamma \ll 1°$). However, the geometry and the mechanical behavior of spherical gear couplings working in misaligned working conditions have presented deviations with respect to the current standards and state of knowledge. Analytically generated geometries were never compared to experimental measurements, and the number of teeth in contact or contact pattern was never correlated with experimental tests in high misalignment angles. That is why an experimental correlation to verify the analytical and numerical model results is required.

Therefore, the fourth publication[4] (see Appendix D) includes the following topics answering the fourth and last objective of this thesis:

- The design of a static test rig to study spherical gear couplings in high misalignment angles.
- Finding a correlation between the tooth surfaces generated with the analytical generation model and the manufactured part.
- An experimental study of the mechanical behavior of highly crowned spherical gear couplings working at high misalignment applications: the maximum misalignment angle, stiffness, number of teeth in contact, and the contact pattern.

Test rig design

For the experimental tests, a specifically developed test rig (Fig. 3.14) was designed and constructed. This test rig is inspired by similar test benches in scientific literature [Cuf12; Ben17], with the feature that it is specially intended to withstand high misalignment angles in a controlled manner. It is composed of two principal parts: the static one, where the sleeve is located and the torque is applied, and the moving part, where the hub is placed and the misalignment angle is set.

The misalignment is applied by means of the pivoting system shown in Fig. 3.14(a). Together with the holes in the moving part and the base of the test rig, a misalignment angle up to 10° can be set, with steps of 1°. The misalignment angle is applied in the clockwise direction. To fix the

[4] *Numerical-experimental analysis of highly crowned spherical gear couplings working in high misalignment applications*

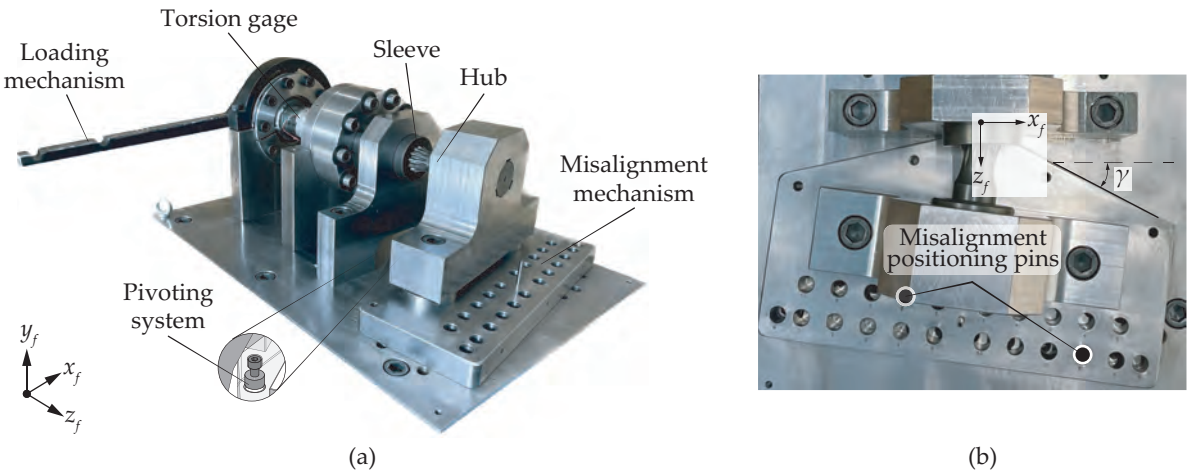

Figure 3.14: (a) the designed test rig with its important parts, and (b) the misalignment mechanism with the positioning pins at $\gamma = 7°$.

system at the desired misalignment angle, two positioning pins are aligned with the corresponding holes on the base plate on which the moving part slides (see the case of $\gamma = 7°$ in Fig. 3.14(b)).

Geometry correlation

The geometry comparison was achieved by comparing the generated geometry with the point cloud reconstructed from the measured geometry. Fig. 3.15 shows the measured hub (a) and the reconstructed hub tooth space together with the one generated (b). The deviations (δ) between both tooth profiles (generated vs. reconstructed) were calculated inside the potential contact region, i.e., $z = \pm 6$ mm. The normal distance from the generated tooth profile (normal vectors are calculated during the generation) to the reconstructed one is measured. The deviations at the edge of the analyzed region ($z = -6$ mm) are illustrated in Fig. 3.15(c), since deviations farther from the middle section will be higher.

Fig. 3.15(c) shows the variations on the whole left side tooth surface of the spherical gear coupling. Deviations are classified in accordance with the manufacturing tolerance classes defined in ISO 4156 standard [Ame20]. Deviations below the highest manufacturing class 4 ($\delta = \pm 23$ µm) are considered negligible, while the maximum tolerances are those corresponding to class 7 ($\delta = \pm 92$ µm). The indexing errors calculated correspond to the manufacturing class 6 ($\approx \pm 50$ µm), and the deviations between the reconstructed and generated tooth surfaces are below this class. Thus, it is demonstrated that the analytically generated geometry [Iñu21] has good agreement with the manufactured geometry.

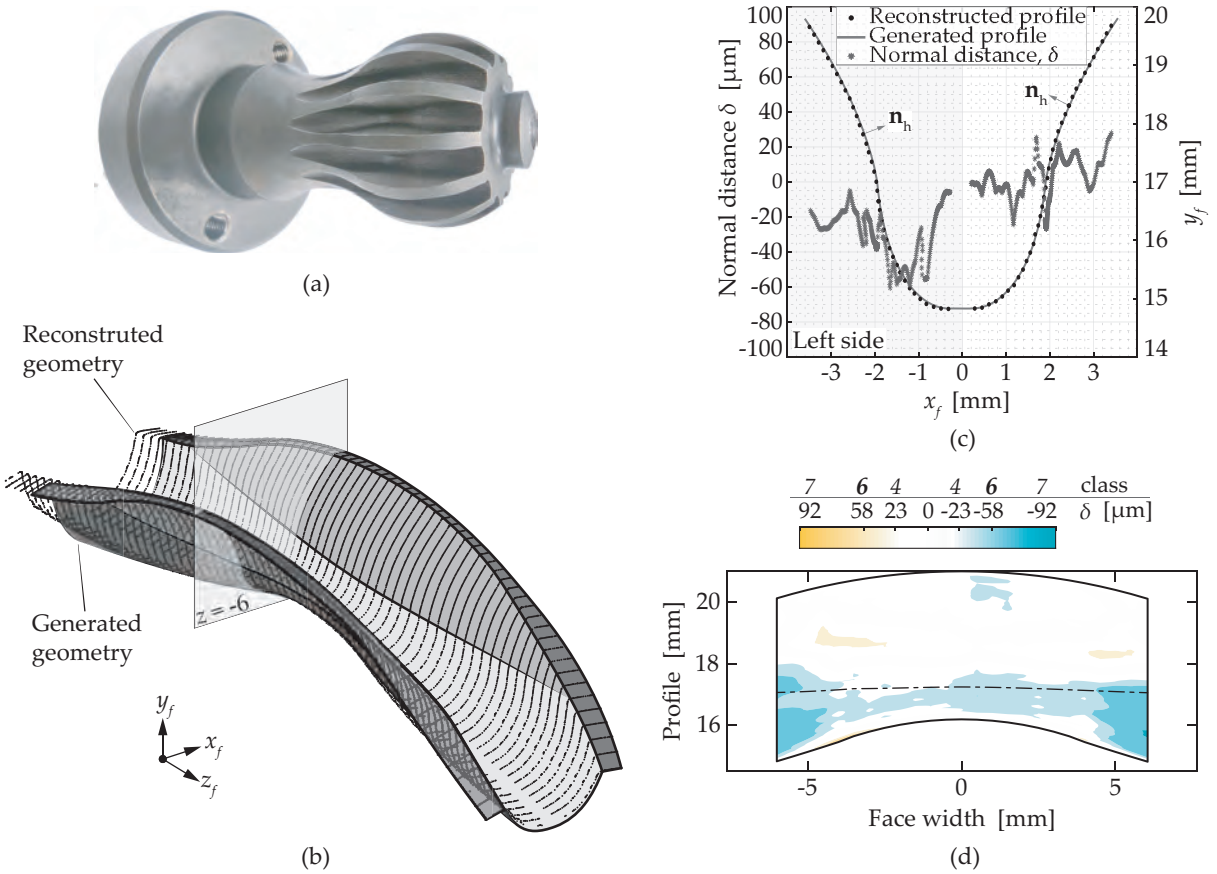

Figure 3.15: (a) measured spherical hub, (b) the reconstructed and generated hub tooth space, (c) comparison of the tooth profiles and the normal deviations δ of $z = -6$ mm cross-section, and (c) the normal deviations δ of the left side hub tooth surface.

Contact pattern correlation

With the test rig design shown in Fig. 3.14 static tests were carried out using a steel blue layout fluid and post-processing the results with a developed algorithm based on color image segmentation clustering [Jin10]. In Fig. 3.16 the location of the centroid of the contact region is compared for some working conditions; the straight line represents the loaded tooth contact analysis results, while the circles represent the experimental data.

At low torque values and as the misalignment angle increases, slight deviations are observed in the number of teeth in contact (case: $\Gamma = 100$ Nm, $\gamma = 3°$), and in the position of the tooth in contact (case: $\Gamma = 100$ Nm, $\gamma = 7°$). These differences are caused by the effect of indexing errors and variable clearance (see Figure 12(b) in Appendix D) but are almost negligible at higher torque values. The differences in the centroid position between empirical and numerical data do not exceed 15% in extreme working conditions (high misalignment angle and low torque), and

represent the behavior of highly crowned spherical gear couplings working in high misalignment applications.

Moreover, for one of the cases ($\Gamma = 500$ Nm,$\gamma = 3°$) the origin of the centroid position results can be observed in a comparison of the contact pattern post-processed from the experimental tests and that obtained from the loaded tooth contact analysis. It can be said that the contact pattern follows the same trend in both the experimental and numerical results. The ± 1 tooth difference is related to the effect of indexing errors or the possible errors in the experimental contact detection. Thus, it is asserted that the contact pattern detection technique proposed is adequate to experimentally analyze the contact path and to determine the number of teeth in contact in highly crowned spherical gear couplings.

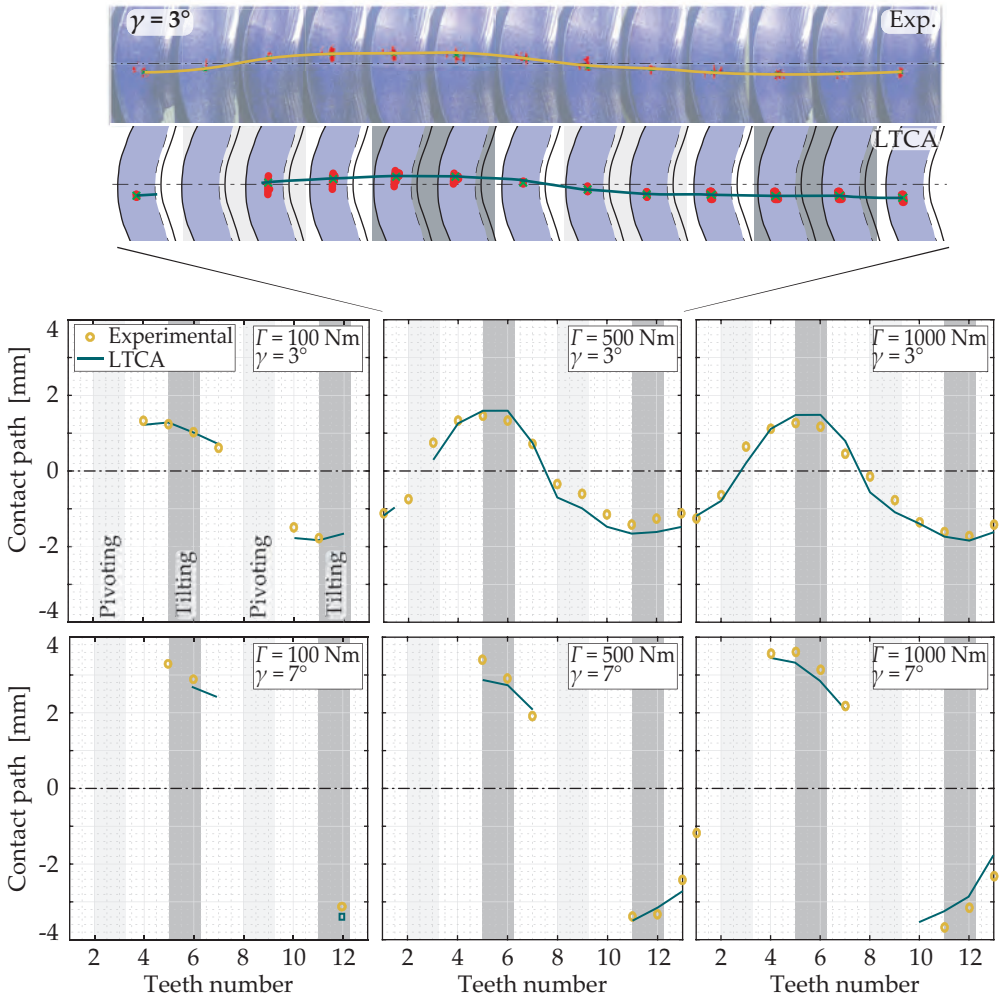

Figure 3.16: Contact pattern centroid position evolution in terms of the applied torque and misalignment angle: experimental tests vs. loaded tooth contact analysis, and the contact pattern comparison at $\Gamma = 500$ Nm and $\gamma = 3°$.

Fig. 3.17(a) shows the experimental centroid location evolution of the case study in terms of the misalignment angle for an applied constant torque value of $\Gamma = 500$ Nm. Moreover, in line with the axis in which the misalignment angle was applied, teeth in the tilting and the pivoting positions are highlighted. The contact pattern evolves from a sinusoidal contact pattern along the reference section at low misalignment angles to a larger amplitude and non-constant contact pattern as the misalignment angle increases. As the misalignment angle increases the number of teeth in contact decreases, i.e., teeth that correspond to the pivoting angular position lose contact as the misalignment angle increases (i.e., teeth in positions 2-3 and 8-9).

Fig. 3.17(b) illustrates the results obtained from the experimental tests and those from the loaded tooth contact analysis at different torque values, together with references currently employed to determine the number of teeth in contact in terms of the misalignment angle (up to $\gamma \leq 8°$) [Dud57b; Man86; Bün00; Pad60]. Both the experimental and numerical values get closer to the values from literature as torque decreases. Indeed, only the small torque values will follow the literature trend and the rest of the working conditions will be above it. This proves that the relations from literature are not applicable for high misalignment applications, since nearly in most working conditions more teeth will be in contact. Furthermore, on the other side, certain working conditions have considerably fewer teeth in contact than the widely used design criteria (50% teeth in contact). No such empirical results have previously been shown in scientific literature.

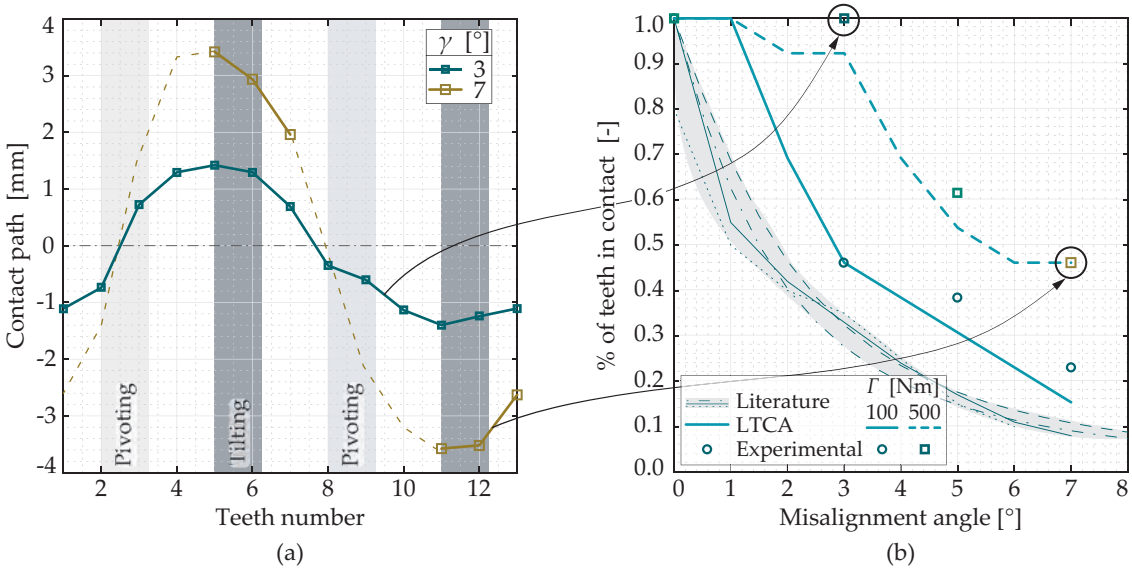

Figure 3.17: (a) Contact pattern at $\Gamma = 500$ Nm as a function of the misalignment angle, and (b) the normalized number of teeth in contact in scientific literature [Dud57b; Man86; Bün00; Pad60], experimental tests, and loaded tooth contact analysis for different torque values.

If you don't write, nothing will change.

—Unknown

4 | Conclusions and Future Work

This chapter summarizes the principal contributions of the thesis. At this point, it is fundamental to recall the main objective of this work which has been stated as: "to improve the accuracy of the sizing methods of spherical gear couplings working at high misalignment angles by predicting and evaluating tooth root stresses". To this aim, it has been necessary to accurately generate the tooth surfaces and the undercut sections of highly crowned spherical gear couplings with the development of a new analytical generation model. Then, an algorithm to determine the maximum misalignment angle was created and the influence of the design parameters on it were studied. Next, a finite element model was developed to analyze the load distribution and tooth root stresses in misaligned conditions, and finally an experimental study was conducted to validate the results obtained from the previously developed models. In the following, the main conclusions relative to each of the initial objectives are gathered, and recommendations for future work are highlighted.

4.1 Conclusions

The main conclusions derived from the research carried out on this thesis are herein summarized:

Analytical tooth surface generation

- It is demonstrated that the hob thread surface (manufacturing tool) must be considered during the generation of highly crowned spherical hubs, to accurately capture the exact geometry and the singularities (e.g., undercut sections) that arise frequently.

- Deviations in the generated tooth surface between the proposed model and the existing models in scientific literature exceed the maximum deviation established by ISO 4156 standard [Int05]. This is especially relevant in the location of the beginning of undercut sections and in cross-sections away from the middle of the hub. Moreover, it is proven that these differences affect the location of the contact point and the clearance distribution.

- It is proven that this model enables the generation of hubs with different tool paths. Furthermore, considering the tool path entry and exit during generation showed satisfactory results to generate large tooth surfaces avoiding the thinning of the teeth (tip pointing).

Design guidelines to maximize the achievable misalignment angle

- The proposed algorithm to determine the maximum misalignment angle is adapted to any gear coupling, and it is not limited to small longitudinal crowning values, as it is the case of current equations employed. Moreover, all design parameters including, the face width, module, crowning radius, pressure angle, and clearance must be considered when determining the achievable maximum misalignment angle.

- The proposed design guidelines are effective to choose a gear coupling geometry that maximizes the achievable misalignment angle without singularities (tip pointing or undercutting). Even though, it is observed that for certain conditions the presence of undercut sections is unavoidable. In this manner, high-pressure angles followed by the module are key design parameters for high misalignment applications, to achieve designs with few teeth and free of undercut sections.

Finite element model

- The proposed finite element model is capable of representing the mechanical behavior of highly crowned spherical gear couplings and allows analyzing the influence of the design variables. Moreover, the mesh and boundary conditions are automatically adapted to any type of gear couplings.

- Tooth root stresses increase considerably at high misalignment values because of the drastic decrease in the number of teeth in contact and the non-homogeneous load distribution. These phenomena are not correctly represented by current standards, and thus, over- or under-estimate tooth root stress values. In contrast, this research provides evidence that they can be accurately calculated if the load distribution and the load-sharing coefficients are correctly determined. In this manner, the effective face width and the effective number of teeth in contact need to be predicted.

- Tooth root stress cycle in the undercut section presents similar stress values to the aligned case along the cycle except for the tilting position. In fact, it is observed that this is a stress concentration location along the cycle, which will need to be considered especially when the contact point displaces due to the misalignment angle nearby the undercutting section. This effect is not currently considered in standards, nor in the numerical models, since undercut sections were not accurately generated.

- The stress state between the tilting and the pivoting angular positions changes significantly at high misalignment angles which leads to a complex tooth root fatigue life. The loss of contact of some of the teeth at high misalignment angles entails a change in the fatigue cycle, from a sinusoidal fluctuating stress cycle ($\gamma \leq 1.5°$) to a pulsating tension stress cycle ($\gamma > 1.5°$). Consequently, the fatigue life of the component might be reduced, and this is not taken into account in current standards.

Experimental geometry and mechanical behavior

- Satisfactory results were obtained with the designed static test bench for high misalignment gear couplings and the test techniques described in the current thesis. Tests can be carried out up to $\gamma = 10°$ in a repeatable and controlled manner.

- The analytical geometry generation model is in good agreement with the manufactured gear coupling. On the one hand, the undercut section beginning is predicted with less than a 3% error. On the other hand, the differences along the tooth surfaces are related to manufacturing errors and do not exceed the manufacturing class 6 defined in ISO 4156 standard [Int05].

- The analysis of the contact pattern has allowed the experimental validation of the number of teeth in contact and the contact path evolution of the numerical results in terms of the misalignment angle and the applied torque. A decrease in the applied torque does not have a significant effect on the contact path and only reduces the number of teeth in contact. However, an increase in the misalignment angle reduces the number of teeth in contact and increases the contact path amplitude. In addition, it has been shown that teeth in the tilting angular position have the biggest contact imprint and that those in the pivoting position are the first to lose contact. Moreover, it is empirically demonstrated that certain working conditions have considerably fewer teeth in contact than the conservative criterion considered in some standards and that the predictions are highly dependent on the geometry of the gear coupling and the working conditions.

4.2 Recommendations for future work

With the knowledge acquired from the thesis and the developed models, the following research lines are proposed and divided into the three main research groups studied throughout the thesis:

Design and Geometry

With the analytical geometry generation model developed, undercut sections of highly crowned spherical gear couplings are generated and the influence of the principal design variables (e.g. module, pressure angle, etc.) is studied. However, there are still some geometry parameters which can be further analyzed.

It has been noted that the tip relief or chamfer at the tip of the teeth of the gear coupling is necessary to center the contact and prevent edge contact in misaligned conditions. It is known that the implementation of the tip relief modification has an effect on the load distribution of spur gears [Ped10; Xu21]. Nevertheless, the effect of the amount of tip relief or its shape on the contact pattern, clearance distribution, and tooth root stresses of highly crowned gear couplings has not been thoroughly investigated. Further research is needed to understand the influence of these variables on the performance and durability of the system.

Another area for further analysis is the effect of the entry and exit of the tool path on the generated geometry. This can help to ensure that the generated and manufactured parts match appropriately in long face width parts where the teeth of the hub are directly machined on the shaft. Additionally, the model can be used to analyze the influence of different tool path shapes on the tooth surface geometry to reduce tooth root stresses. For example, a tool path that generates a smaller crowned tooth surface while still allowing for the desired misalignment angle and enabling a larger contact region, may decrease tooth root stresses and increase the lifespan of the component.

Load distribution and tooth root stress

With the developed finite element model tooth root stresses have been calculated and their evolution in terms of the applied torque and misalignment angle have been stated. In current standards only coefficients to account with the effect of the misalignment angle up to 3° are determined. To address this issue, a numerical method has been proposed to accurately estimate the most relevant coefficients (load sharing and load distribution factors) for calculating tooth

root stresses. Based on these results, it would be interesting to derive an analytical expression that does not rely on the computational cost of numerical analysis.

Moreover, it has been demonstrated that the stress state changes from the tilting angular position to the pivoting position. This is not considered in current standards, and it is expected to have a detrimental effect on the fatigue life of the component. That is why it requires further investigation.

Experimental validation

The test rig designed to analyze the mechanical behavior of highly crowned spherical gear couplings has demonstrated its potential in this work. Nonetheless, to fully validate the finite element model and the proposed methodology to calculate tooth root stresses, an experimental analysis is required. In addition, it is also important to test the proposed methodology to define the effective face width and the resulting load distribution under high misalignment conditions.

Moreover, additional tests with different spherical gear couplings geometries could be conducted to compare with the analytical results obtained from the achievable maximum misalignment angle.

Finally, experimental tests that examine the influence of the tooth root stress cycle variation on the fatigue life of the component could be performed.

References

[Alf06] M.A. Alfares, A.H. Falah, and A.H. Elkholy. "Clearance distribution of misaligned gear coupling teeth considering crowning and geometry variations". In: *Mechanism and Machine Theory* 41.10 (2006), pp. 1258–1272.

[Ame] Altra industrial Motion Ameridrives. *Amerigear mill spindles*.

[Ame04] American Gear Manufacturers Association. *ANSI/AGMA 2101-D04: Fundamental rating factors and calculation methods for involute spur and helical gear teeth*. 2004.

[Ame06] American Gear Manufacturers Association. *AGMA 6123-B06: Design manual for enclosed epicyclic gear drives*. 2006.

[Ame20] American Gear Manufacturers Association. *AGMA 945-1-B20: Splines – Design and Application*. Virginia: American Gear Manufacturers Association, 2020.

[Ara19] A. Arana. "Thermal Distortion Effects on Cylindrical Gear Teeth Contact". PhD thesis. Mondragon Unibertsitatea, 2019.

[Arg02] J. Argyris, A. Fuentes, and F.L. Litvin. "Computerized integrated approach for design and stress analysis of spiral bevel gears". In: *Computer Methods in Applied Mechanics and Engineering* 191.11-12 (2002), pp. 1057–1095.

[Bak05] R. Baker. "Durability of steel spline couplings". PhD thesis. University of London, 2005.

[Bar06] A. Barrot, M. Paredes, and M. Sartor. "Determining both radial pressure distribution and torsional stiffness of involute spline couplings". In: *Proceedings of the Institution*

of Mechanical Engineers, Part C: Journal of Mechanical Engineering Science 220.12 (2006), pp. 1727–1737.

[Bec05] R. Beckmann. "Beitrag zur Auslegung und Konstruktion von Balligzahn - Kupplungen". PhD thesis. Chemmitz Technology University, 2005.

[Ben17] M. Benatar, D. Talbot, and A. Kahraman. "An experimental investigation of the load distribution of spline joints under gear loading conditions". In: *Journal of Advanced Mechanical Design* 11.6 (2017), pp. 1–12.

[Bou08] K.D. Bouzakis et al. "Manufacturing of cylindrical gears by generating cutting processes: A critical synthesis of analysis methods". In: *CIRP Annals. Manufacturing Technology* 57.2 (2008), pp. 676–696.

[Bre15] C. Brecher, M. Brumm, and M. Krömer. "Design of gear hobbing processes using simulations and empirical data". In: *9th CIRP Conference on Intelligent Computation in Manufacturing Engineering* (2015), pp. 484–489.

[Bro79] H.W. Brown. "A reliable spline coupling". In: *Transactions of the ASME. Journal of Engineering for Industry* 101 (1979), pp. 421–426.

[Bün00] C. Bünder. "Analyse der Beanspruchungen der Verzahnung von Zahnkupplungen". PhD thesis. Technische Universität Dresden, 2000.

[Cal75] M. Calistrat. "What causes wear in gear-type couplings?" In: *Hydrocarbon Processing* 54.1 (1975), pp. 53–57.

[Cam65] L. Camillo and K. Rim. *On mapping functions for torsional analysis of splined shafts.* Tech. rep. State University of Iowa, 1965, pp. 1–22.

[Cav71] J. Cavaillès and F. Groix. "Etude de la répartition de la charge appliquée sur un accouplement délignable à petites dents fonctionnant en position délignée". In: *Bulletin de l'Association Technique Maritime et Aéronautique* (1971).

[Ced94] R.W. Cedoz and M.R. Chaplin. *Design guide for involute splines.* Society of Automotive Engineers, 1994.

[Cha08] L.C. Chao and C.B. Tsay. "Contact characteristics of spherical gears". In: *Mechanism and Machine Theory* 43.10 (2008), pp. 1317–1331.

[Cha10] K.W. Chase, C.D. Sorensen, and B.J. DeCaires. “Variation analysis of tooth engagement and loads in involute splines”. In: *IEEE Transactions on Automation Science and Engineering* 7.4 (2010), pp. 746–754.

[Cha98] S.L. Chang and C.B. Tsay. “Computerized tooth profile generation and undercut analysis of gears manufactured shaper cutters”. In: *Transactions of the ASME. Journal of Mechanical Design* 120.1 (1998), pp. 92–99.

[Cor07] J. Corcoran et al. “Advances in gas turbine couplings”. In: *36th Turbomachinery symposium* (2007), pp. 157–172.

[Cre78] A.B. Crease. “Gear couplings for high powers and speeds”. In: *Tribology International* 11.1 (1978), pp. 49–57.

[Cuf12] V. Cuffaro, F. Curà, and A. Mura. “Analysis of the pressure distribution in spline couplings”. In: *Proceedings of the Institution of Mechanical Engineers, Part C: Journal of Mechanical Engineering Science* 226.12 (2012), pp. 2852–2859.

[Cuf13] V. Cuffaro. “Prediction Method for the Surface Damage in Splined Couplings”. PhD thesis. Politecnico di Torino, 2013.

[Cuf14] V. Cuffaro, F. Curà, and A. Mura. “Test rig for spline couplings working in misaligned conditions”. In: *Transactions of the ASME. Journal of Tribology* 136.1 (2014), pp. 1–7.

[Cur13a] F. Curà and A. Mura. “Experimental procedure for the evaluation of tooth stiffness in spline coupling including angular misalignment”. In: *Mechanical Systems and Signal Processing* 40.2 (2013), pp. 545–555.

[Cur13b] F. Curà, A. Mura, and M. Gravina. “Load distribution in spline coupling teeth with parallel offset misalignment”. In: *Proceedings of the Institution of Mechanical Engineers, Part C: Journal of Mechanical Engineering Science* 227.10 (2013), pp. 2195–2205.

[Cur14a] F. Curà and A. Mura. “Analysis of a load application point in spline coupling teeth”. In: *Journal of Zhejiang University-Science* 15.4 (2014), pp. 302–308.

[Cur14b] F. Curà and A. Mura. “Experimental and theoretical investigation about reaction moments in misaligned splined couplings”. In: *Mechanical Systems and Signal Processing* 45.2 (2014), pp. 504–512.

[Cur17] F. Curà, A. Mura, and F. Adamo. “Fatigue damage in spline couplings: numerical simulations and experimental validation”. In: *Procedia Structural Integrity* 5 (2017), pp. 1326–1333.

[Cur18a] F. Curà and A. Mura. “Theoretical and numerical evaluation of tilting moment in crowned teeth splined couplings”. In: *Meccanica* 53.1-2 (2018), pp. 413–424.

[Cur18b] F. Curà, A. Mura, and F. Adamo. “Experimental investigation about tribological performance of grapheme-nanoplatelets as additive for lubricants”. In: *Procedia Structural Integrity* 12 (2018), pp. 44–51.

[Daf17] M. Daffner, M. Otto, and K. Stahl. “Method of measuring the load distribution of spur gear stages”. In: *Journal of Advanced Mechanical Design, Systems and Manufacturing* 11.6 (2017), pp. 1–10.

[Deb11] S. Debie. “Modellierung und Simulation von Zerspanverfahren mithilfe der Durchdringungsrechnung am Beispiel des Wälzfräsens”. PhD thesis. Universität Bremen, 2011.

[DeC06] B.J. DeCaires. “Variation analysis of involute spline tooth contact”. PhD thesis. Brigham Young University, 2006.

[Deu02] Deutsches Institut für Normung. *DIN 5466: Splined joints, calculation of load capacity.* 2002.

[Dud57a] D.W. Dudley. “How to design involute splines”. In: *Product Engineering* 27 (1957), pp. 196–231.

[Dud57b] D.W. Dudley. “When splines need stress control”. In: *Product Engineering* 28 (1957), pp. 56–59.

[Dup20] C. Dupertuis and J.L. Ligier. “Contact pressure in misaligned spline couplings”. In: *Mechanics and Industry* 21.5 (2020), pp. 1–12.

[Elk02] A.H. Elkholy and M.A. Alfares. “Misalignment loads in splined gear couplings”. In: *International Journal of Computer Applications in Technology* 15.1-3 (2002), pp. 128–137.

[Err12] R. Errichello and J. Muller. *Gearbox reliability collaborative gearbox 1 failure analysis report.* Tech. rep. NREL-National Renewable Energy Laboratory, 2012.

[Fav57] J. Favard. *Cours de Géométrie Différentielle Locale.* Gauthier-Villars, 1957.

[Gim94] D. Gimpert. “The gear hobbing process”. In: *Gear Technology* (1994), pp. 38–44.

[Glo10] H. Globig. “Analyse der Rückstellwirkungen von Zahnkupplungen”. PhD thesis. Technischen Universität Dresden, 2010.

[Gon17] I. Gonzalez-Perez and A. Fuentes. “Implementation of a finite element model for gear stress analysis based on tie-surface constraints and its validation through the Hertz’s theory”. In: *Transactions of the ASME. Journal of Mechanical Design* 140.2 (2017), pp. 1–13.

[Gua18] Y. Guan et al. “Tooth contact analysis of crown gear coupling with misalignment”. In: *Mechanism and Machine Theory* 126 (2018), pp. 295–311.

[Gua19a] Y. Guan, X. Yang, and Z. Fang. “Computerized generation and simulation of meshing of a novel crown gear coupling avoiding edge contact”. In: *Journal of Advanced Mechanical Design, Systems, and Manufacturing* 13.3 (2019), pp. 1–13.

[Gua19b] Y. Guan et al. “Comparative analysis of three geometric models for crown gear coupling”. In: *Mechanism and Machine Theory* 136 (2019), pp. 269–283.

[Gua19c] Y. Guan et al. “Effects of misalignment and crowning on contact characteristics of crown gear coupling”. In: *Proceedings of the Institution of Mechanical Engineers, Part C: Journal of Mechanical Engineering Science* 233.12 (2019), pp. 4397–4417.

[Gua21] Y. Guan et al. “An experimental investigation of contact characteristics of crown gear coupling with angular misalignment”. In: *Journal of Advanced Mechanical Design* 15.5 (2021), pp. 1–14.

[Gua22] Y. Guan et al. “A quick multi-step discretization and parallelization wear simulation model for crown gear coupling with misalignment angle”. In: *Mechanism and Machine Theory* 168 (2022), pp. 1–18.

[Gui05] M. Guingand, J.P. de Vaujany, and C.Y. Jacquin. “Quasi-static analysis of a face gear under torque”. In: *Computer Methods in Applied Mechanics and Engineering* 194.39-41 (2005), pp. 4301–4318.

[Guo13] Y. Guo et al. *Gearbox reliability collaborative analytic formulation for the evaluation of spline couplings*. Tech. rep. NREL-National Renewable Energy Laboratory, 2013.

[Guo16] Y. Guo et al. “Theoretical and experimental study on gear-coupling contact and loads considering misalignment, torque and friction influences”. In: *Mechanism and Machine Theory* 98 (2016), pp. 242–262.

[Gup17a] K. Gupta, N.K. Jain, and R. Laubscher. “Chapter 4: Advances in gear manufacturing”. In: *Advanced Gear Manufacturing and Finishing*. Academic Press, 2017, pp. 67–125.

[Gup17b] K. Gupta, N.K. Jain, and R. Laubscher. “Chapter 7: Measurement of gear accuracy”. In: *Advanced Gear Manufacturing and Finishing*. Academic Press, 2017, pp. 197–218.

[Hah14] S. Hahn. “Coupling connections and splines”. In: *Encyclopedia of Automotive Engineering*. John Wiley & Sons, 2014, pp. 1–14.

[Hak11] Y. Hakozaki and S. Shimachi. “Equalization about the tooth bearing area for the shaft angle of gear coupling”. In: *Transactions of the Japan Society of Mechanical Engineers Series C* 73.726 (2011), pp. 594–601.

[Hen83] G. Henriot and J. Boisset. “Accouplements, alignement des axes”. In: *Engrenages: conception, fabrication, mise en oeuvre*. 5th. Dunod, 1983, pp. 796–818.

[Her99] W.R. Herbstritt and J.H. Paluh. “Mill spindle advanced gear design”. In: *Iron and Steel Engineers* 76.7 (1999), pp. 44–48.

[Hon14a] J. Hong, D. Talbot, and A. Kahraman. “A semi-analytical load distribution model for side-fit involute splines”. In: *Mechanism and Machine Theory* 76 (2014), pp. 39–55.

[Hon14b] J. Hong, D. Talbot, and A. Kahraman. “Load distribution analysis of clearance-fit spline joints using finite elements”. In: *Mechanism and Machine Theory* 74 (2014), pp. 42–57.

[Hon15a] J. Hong, D. Talbot, and A. Kahraman. “A stiffness formulation for spline joints”. In: *Proceedings of the ASME 2015 International Design Engineering Technical Conferences & Computers and Information in Engineering Conference* (2015).

[Hon15b] J. Hong, D. Talbot, and A. Kahraman. “Effects of tooth indexing errors on load distribution and tooth load sharing of splines under combined loading conditions”. In: *Transactions of the ASME. Journal of Mechanical Design* 137.3 (2015), pp. 1–10.

[Hot08] M. Hotait and A. Kahraman. “Experiments on root stresses of helical gears with lead crown and misalignments”. In: *Transactions of the ASME. Journal of Mechanical Design* 130.7 (2008), pp. 1–5.

[Hot11] M. Hotait, A. Kahraman, and T. Nishino. “An investigation of root stresses of hypoid gears with misalignments”. In: *Transactions of the ASME. Journal of Mechanical Design* 133.7 (2011), pp. 1–9.

[Int05] International Organization for Standardization. *ISO 4156: Straight cylindrical involute splines*. 2005.

[Int06] International Organization for Standardization: *ISO 6336-3: Calculation of load capacity of spur and helical gears. Part 3: calculation of tooth bending strengh*. 2006.

[Int07] International Organization for Standardization. *ISO 21771: Gears-Cylindrical involute gears and gear pairs-Concepts and geometry*. 2007.

[Iñu18] A. Iñurritegui et al. “Modelizado bidimensional de engranajes cilindricos por elementos finitos”. In: *Congreso Nacional de Ingeniería Mecánica* (2018), pp. 1–14.

[Iñu20] A. Iñurritegui et al. “Generación virtual de la geometría 3D de acoplamientos dentados abombados”. In: *Congreso Nacional de Ingeniería Mecánica* (2020), pp. 1–10.

[Iñu21] A. Iñurritegui et al. “Computerized generation and tooth contact analysis of spherical gear couplings for high misalignment applications”. In: *Mechanism and Machine Theory* 164 (2021), pp. 1–22.

[Iñu22] A. Iñurritegui et al. “Spherical gear coupling design space analysis for high misalignment applications”. In: *Mechanism and Machine Theory* 173 (2022), pp. 1–21.

[Iñu23] A. Iñurritegui et al. “Load distribution and tooth root stress of highly crowned spherical gear couplings working at high misalignment angles”. In: *Mechanism and Machine Theory* 179 (2023), pp. 1–21.

[Jia19] K. Jia et al. “A general mathematical model for two-parameter generating machining of involute cylindrical gears”. In: *Applied Mathematical Modelling* 75 (2019), pp. 37–51.

[Jin10] X. Jin and J. Han. “K-Means clustering”. In: *Encyclopedia of Machine Learning*. Ed. by C. Sammut and G.I. Webb. Boston, MA: Springer US, 2010, pp. 563–564.

[Kel12] L. Kelemen and J. Szente. “Analysis of cutting process for internal gears”. In: *13th International Conference on Tools* (2012), pp. 351–356.

[Kel14] L. Kelemen and J. Szente. “Two mathematical models for generation of crowned tooth surface”. In: *The Scientific World Journal* 2014 (2014), pp. 1–6.

[Kel16] L. Kelemen. “Fogasgyürüs tengelykapcsoló kapcsoódási viszonyainak elemzése”. PhD thesis. University of Miskolc, 2016.

[Klo14] F. Klocke. “Gear Cutting”. In: *CIRP Encyclopedia of Production Engineering*. 2014.

[Klo16] F. Klocke et al. “Calculating the workpiece quality using a hobbing simulation”. In: *48th CIRP Conference on Manufacturing Systems* (2016), pp. 687–691.

[Kro09] P.V. Krot. “Transient torsional vibrations control in the geared drive trains of the hot rolling mills”. In: *IEEE Control Applications (CCA) & Intelligent Control (ISIC)* (2009), pp. 1368–1373.

[Kro11] J. Kroczak and M. Dudziak. “Tolerance analysis of involute splines”. In: *World Congress on Engineering* 3 (2011), pp. 1–3.

[Kro13] J. Kroczak and M. Dudziak. “Analysis of the pitch deviation in involute splined connections”. In: *Machine Dynamics Research* 37.1 (2013), pp. 65–71.

[Ku75] P.M. Ku and M.L. Valtierra. “Spline wear-effects of design and lubrication”. In: *Journal of Engineering for Industry* 97.4 (1975), pp. 1–7.

[Kum] Kumera. *Cumex gear couplings*.

[Lag12] S. Lagutin, B. Utkin, and A. Klochkov. “Upgrading of the geometry of gear couplings”. In: *7th International KOD Symposium* (2012), pp. 27–30.

[Lar16] J. Larrañaga et al. “Misalignment effect on contact pressure and tooth root strength of spline couplings”. In: *5th International Conference on Power Transmission-BAPT* (2016), pp. 1–6.

[Lee03] S.B. Leen et al. “Fatigue life prediction for a barrelled spline coupling under torque overload”. In: *Proceedings of the Institution of Mechanical Engineers, Part G: Journal of Aerospace Engineering* 217.3 (2003), pp. 123–142.

[Lee22] S.B. Leen. “Chapter 1: Fretting fatigue and wear of spline couplings. From laboratory testing to industrial application through computational modelling”. In: *Wear in advanced engineering applications and materials*. World Scientific, 2022, pp. 1–44.

[Li15] X. Li et al. “The generation principle and mathematical models of double-enveloping internal gear pairs”. In: *Proceedings of the ASME 2015 International Design Engineering Technical Conferences & Computers and Information in Engineering Conference* (2015), pp. 1–8.

[Lig08] H. Ligata, A. Kahraman, and A. Singh. “An experimental study of the influence of manufacturing errors on the planetary gear stresses and planet load sharing”. In: *Transactions of the ASME. Journal of Mechanical Design.* 130.4 (2008).

[Lis17] T.J. Lisle, B.A. Shaw, and R.C. Frazer. “External spur gear root bending stress: A comparison of ISO 6336:2006, AGMA 2101-D04, ANSYS finite element analysis and strain gauge techniques”. In: *Mechanism and Machine Theory* 111 (2017), pp. 1–9.

[Lit02] F.L. Litvin et al. “Design, generation, and stress analysis of two versions of geometry of face-gear drives”. In: *Mechanism and Machine Theory* 37.10 (2002), pp. 1179–1211.

[Lit04] F.L. Litvin and A. Fuentes. *Gear geometry and applied theory.* 2nd. Cambridge University Press, 2004, pp. 1–818.

[Lit05] F.L. Litvin et al. “Computerized developments in design, generation, simulation of meshing, and stress analysis of gear drives”. In: *Meccanica* 40 (2005), pp. 291–324.

[Lit07] F.L. Litvin et al. “Generation of planar and helical elliptical gears by application of rack-cutter, hob, and shaper”. In: *Computer Methods in Applied Mechanics and Engineering* 196.41-44 (2007), pp. 4321–4336.

[Lit09] F.L. Litvin et al. *Noncircular gears: design and generation.* Cambridge University Press, 2009.

[Lit75] F.L. Litvin, N.N. Krylov, and M.L. Erikhov. “Generation of tooth surfaces by two-parameter enveloping”. In: *Mechanism and Machine Theory* 10.5 (1975), pp. 365–373.

[Lit89] F.L. Litvin. *Theory of gearing.* Tech. rep. University of Illinois at Chicago, 1989.

[Lit96] F.L. Litvin and I. Seol. “Computerized determination of gear tooth surface as envelope to two parameter family of surfaces”. In: *Computer methods in applied mechanics and engineering* 138 (1996), pp. 213–225.

[Loc13] S.R. Locke et al. “Coupling credible failure modes and owner options to intervene”. In: *42th Turbomachinery Symposium.* Texas, 2013, pp. 1–30.

[Lov] Lovejoy. *High performance gear couplings.*

[Luo19] Y. Luo, N. Baddour, and M. Liang. “A shape-independent approach to modelling gear tooth spalls for time varying mesh stiffness evaluation of a spur gear pair”. In: *Mechanical Systems and Signal Processing* 120 (2019), pp. 836–852.

[Mai11] Maina. *Gear couplings*. 2011.

[Man86] J.R. Mancuso. *Couplings and joints: design, selection and application*. 2nd ed. CRC Press, 1986.

[Mao07] K. Mao. "Gear tooth contact analysis and its application in the reduction of fatigue wear". In: *Wear* 262.11-12 (2007), pp. 1281–1288.

[Mar12] D. Margineanu et al. "Analytic and experimental study of the load distribution on spline joints length considering the contact rigidity of the bearing surfaces". In: *Applied Mechanics and Materials* 162.March (2012), pp. 74–83.

[Mar19] D. Marano et al. "Misalignment compensation spline design". In: *American Gear Manufacturers Association Fall Technical Meeting* (2019), pp. 1–17.

[Med02a] S. Medina and A.V. Olver. "An analysis of misaligned spline couplings". In: *Proceedings of the Institution of Mechanical Engineers, Part J: Journal of Engineering Tribology* 216.5 (2002), pp. 269–279.

[Med02b] S. Medina and A.V. Olver. "Regimes of contact in spline couplings". In: *Journal of Tribology* 124.2 (2002), pp. 351–357.

[Mil17] R. Miller. "A brief overview of splines". In: *Gear solutions* (2017), p. 1.

[Mit00] K. Mitome et al. "Development of a new hobbing of spherical gear". In: *Transactions of the Japan society of mechanical engineers. Series C* 66.646 (2000), pp. 1975–1980.

[Mur18] A. Mura, F. Curà, and F. Adamo. "Evaluation of graphene grease compound as lubricant for spline couplings". In: *Tribology International* 117 (2018), pp. 162–167.

[Nak88] K. Nakashima. "Teeth contact behaviour and load distribution of gear couplings". In: *Transactions of the Japan Society of Mechanical Engineers Part C* 502.54 (1988), pp. 1302–1307.

[Nea80] Engineering Neale. *Introduction to gear couplings*. Tech. rep. Neale consulting engineers, 1980.

[Oct14] M. Octrue, F. Blanc, and D. Ghribi. *Guide de demensionnement des accouplements à dentures bombées*. Tech. rep. CETIM, 2014.

[Ohs12] F. Ohshima, S. Hirata, and H. Yoshino. "Study on tooth contact of gear couplings". In: *Transactions of the Japan society of mechanical engineers. Series C* 78.786 (2012), pp. 639–649.

[Pad60] F.H. Paddon. “Application and selection of gear type spindles”. In: *Iron and Steel Engineer* (1960), pp. 91–100.

[Par14] D.G. Pardhi and S.D. Khamankar. “Stress analysis of spline shaft using finite element method and its experimental verification by photo elasticity”. In: *International Journal of Mechanical Engineering and Robotics Research* 3.4 (2014), pp. 1–8.

[Ped10] J. Pedrero et al. “Load distribution model along the line of contact for involute external gears”. In: *Mechanism and Machine Theory* 45.5 (2010), pp. 780–794.

[Pun] Punk. *Punk couplings.*

[Rega] Regal. *Jaure crowned tooth gear couplings.*

[Regb] Regal. *Jaure gear spindles.*

[Regc] Regal. *Kop-Flex couplings catalog.*

[Ren] Renk. *Curved tooth couplings.*

[Ren68] P.C. Renzo, S. Kaufman, and D.E. de Rocker. “Gear couplings”. In: *Transactions of the ASME. Journal of Engineering for Industry* 90.3 (1968), pp. 467–474.

[Rob08] Robert R Robins. “Tooth engagement evaluation of involute spline couplings”. PhD thesis. Brigham Young University, 2008, pp. 1–96.

[Rod21] V. Roda-Casanova and I. Gonzalez-Perez. “Investigation of the effect of contact pattern design on the mechanical and thermal behaviors of plastic-steel helical gear drives”. In: *Mechanism and Machine Theory* 164 (2021), pp. 1–20.

[San11] A. Sanders et al. “An experimental investigation of the effect of tooth asymmetry and tooth root shape on root stresses and single tooth bending fatigue life of gear teeth”. In: *Proceedings of the ASME International Design Engineering Technical Conferences & Computers and Information in Engineering Conference* (2011), pp. 1–9.

[Sil10] J. Silvers, C.D. Sorensen, and K.W. Chase. “A new statistical model for predicting tooth engagement and load sharing in involute splines”. In: *American Gear Manufacturers Association Fall Technical Meeting* (2010), pp. 1–15.

[Sur] Sure-Flex. *Flexible gear couplings.*

[Tje01a] A. Tjernberg. “Load distribution and pitch errors in a spline coupling”. In: *Materials & Design* 22.4 (2001), pp. 259–266.

[Tje01b] A. Tjernberg. “Load distribution in the axial direction in a spline coupling”. In: *Engineering Failure Analysis* 8.6 (2001), pp. 557–570.

[Ula18] I. Ulacia et al. “Fatigue life prediction of spherical gear couplings”. In: *American Gear Manufacturers Association Fall Technical Meeting* (2018), pp. 202–207.

[Vau17] J.P. Vaujany, M. Guingand, and B. Schmitt. “Numerical model and parametrical study of spline coupling”. In: *JSME International Conference on Motion and Power Transmissions* (2017), pp. 1–6.

[Ved10] L. Vedmar. “A parametric analysis of the gear surface roughness after hobbing”. In: *Journal of Mechanical Design* 132.11 (2010), pp. 1–8.

[Vol82] B.P. Volfson. “Stress sources and critical stress combinations for splined shaft”. In: *Transactions of the ASME. Journal of Mechanical Design* 104.1 (1982), pp. 551–556.

[Von20] R. Vondra, K. Rehak, and A. Prokop. “Strain-stress analysis of gear coupling”. In: *26th International Conference in Engineering Mechanics* 26 (2020), pp. 520–523.

[Wu14] Y.R. Wu and W.H. Hsu. “A general mathematical model for continuous generating machining of screw rotors with worm-shaped tools”. In: *Applied Mathematical Modelling* 38.1 (2014), pp. 28–37.

[Xia22] L. Xiao et al. “Experimental investigation on the effect of misalignment on the wear failure for spline couplings”. In: *Engineering Failure Analysis* 131 (2022), pp. 1–13.

[Xu21] X. Xu et al. “A novel tooth tip relief method for reducing micro-pitting of spur gears”. In: *Advances in Mechanical Engineering* 13.9 (2021), pp. 1–14.

[Xue19] X. Xue, Q. Huo, and L. Hong. “Fretting wear-fatigue life prediction for aero-engine’s involute spline couplings based on Abaqus”. In: *Journal of Aerospace Engineering* 32.6 (2019), pp. 1–9.

[Yan07] S.C. Yang. “Study on an internal gear with asymmetric involute teeth”. In: *Mechanism and Machine Theory* 42.8 (2007), pp. 977–994.

[Ye21] Z. Ye et al. “Analysis of parallel misalignment of gear coupling in rotor system using EEMD-median filter method”. In: *IEEE Advanced Information Technology, Electronic and Automation Control Conference* 2021.1 (2021), pp. 1113–1118.

[Yos76] H. Yoshitake. “Fatigue strength of parallel spline shaft”. In: *Journal of the Society of Materials Science* 25.271 (1976), pp. 356–362.

[Zan04] C. Zanzi. “Modelo avanzado para la generación de dientes de engranaje con abombamiento longitudinal. Aplicación a transmisiones de engranajes rectos y frontales”. PhD thesis. Universidad Nacional de Educacion a Distancia, 2004.

[Zim16] M. Zimmer. “Berechung und Optimierung von Geometrie und Eingriffsverhalten von Verzahnungen beliebiger Achslage”. PhD thesis. Technische Universität München, 2016.

Believe you can and you're halfway there.

—Theodore Roosevelt

A | Publication I

Computerized generation and tooth contact analysis of spherical gear couplings for high misalignment applications

A. Iñurritegui[a], I. Gonzalez-Perez[b], A. Arana[a], J. Larrañaga[a], I. Ulacia[a]

[a] *Mondragon Unibertsitatea, Department of Mechanical and Industrial Production, Arrasate-Mondragon, Pais Vasco, Spain.*

[b] *Universidad Politécnica de Cartagena, Department of Mechanical Engineering, Materials and Manufacturing, Cartagena, Murcia, Spain.*

Received 24 March 2021; Revised 18 May 2021; Accepted 21 May 2021. Available online 10 June 2021; Version of Record 10 June 2021.

Mechanism and Machine Theory 164 (2021) 104408

Mechanism and Machine Theory 164 (2021) 104408

Contents lists available at ScienceDirect

Mechanism and Machine Theory

journal homepage: www.elsevier.com/locate/mechmachtheory

Research paper

Computerized generation and tooth contact analysis of spherical gear couplings for high misalignment applications

Aurea Iñurritegui[a], Ignacio Gonzalez-Perez[b,*], Aitor Arana[a], Jon Larrañaga[a], Ibai Ulacia[a]

[a] Mondragon Unibertsitatea, Department of Mechanical and Industrial Production, Arrasate-Mondragon, Pais Vasco, SPAIN
[b] Universidad Politécnica de Cartagena, Department of Mechanical Engineering, Materials and Manufacturing, Cartagena, Murcia, SPAIN

ARTICLE INFO

Article history:
Received 24 March 2021
Revised 18 May 2021
Accepted 21 May 2021

Keywords:
Spherical gear coupling
Gear geometry
Undercutting
Tooth contact analysis
High misalignment

ABSTRACT

Spherical gear couplings are a type of toothed coupling where the external spline usually requires highly crowned tooth surfaces to absorb high misalignments. The teeth of the external spline (or hub) may present cross sections with undercutting, particularly when the tooth number is small and the hub teeth are manufactured directly on a shaft. These peculiarities make it difficult to generate accurate hub geometries with the existing models in the literature. This paper proposes a method of generation of the hub tooth surfaces by a hob thread surface, simulating the hobbing process of the external spline and generating undercut profiles. The proposed hub model is compared with existing models where a cutting edge is considered as a generating tool of the hub. The comparison shows that the normal deviations between the hub tooth surfaces of the considered models are significant, especially when high misalignments (typically above 3°) are present and highly crowned tooth surfaces are required. Differences in the location where undercut profiles appear are also observed between the proposed model and those of the literature. Moreover, from the application of unloaded tooth contact analysis and clearance determination, disparities are observed when a misalignment angle is present.

1. Introduction

Gear couplings are widely used to transmit power between shafts due to their high power density compared to other non-splined connections [1]. Spherical gear couplings are specifically designed to work with high misalignments. Thus, they require tooth surfaces with considerable longitudinal crowning to obtain a favorable contact pattern when severe conditions of misalignment are present, typically above 3° and up to 10°. In addition, longitudinal crowning is needed to avoid interference and balance the clearance between the hub and the sleeve teeth, while increasing the contact ratio [2]. Indeed, misalignment failures account for approximately 20% of common crowned gear coupling failures [3]. Fig. 1 shows a typical spherical gear coupling featuring a hub with highly crowned tooth surfaces.

Most of the studies related to gear couplings in the scientific literature are limited to working conditions with misalignments below 3°. Among others, Alfares et al. [2] concluded that coupling misalignment due to manufacture and assembly errors is the main factor to determine tooth clearance distribution. Baker [4] experimentally analyzed the durability of cou-

* Corresponding author.
E-mail address: ignacio.gonzalez@upct.es (I. Gonzalez-Perez).

https://doi.org/10.1016/j.mechmachtheory.2021.104408
0094-114X/

Nomenclature

a_p	parabola coefficient
F_w	hob face width
h_a	rack addendum
h_f	rack dedendum
h_{ha}	hub addendum
h_{hf}	hub dedendum
h_t	hub tip height
h_{wa}	hob addendum
m	module
N_h	hub/sleeve tooth number
N_s	shaper tooth number
N_w	hob thread number
p	screw parameter
p_{ax}	hob axial pitch
r_g	sleeve pitch radius
r_h	hub pitch radius
r_s	shaper pitch radius
r_w	hob pitch radius
r_α	hub tip radius
r_β	tool path radius
s_w	hob displacement during hub generation
u	profile surface parameter
v	lead surface parameter
α	pressure angle
γ	misalignment angle
Δ_{hw}	Vertical displacement of the hob duringgeneration
δ	hob lead parameter
η	hob tip parameter
λ_w	hob lead angle
μ	angle along hob tool path
ρ	hub profile radius
ρ_{edge}	hob tip radius
ϕ_s	shaper rotation during sleeve generation
ϕ_w	hob rotation during hub generation
χ_g	sleeve generating shift coefficient
χ_h	hub generating shift coefficient
ψ_g	generation parameter of the sleeve
ψ_h	generation parameter of the hub
ψ_s	generation parameter of the shaper
ψ_w	generation parameter of the hob

plings with different lubricants and coatings up to a 0.5° misalignment angle, showing a variation of wear mechanism leading to fatigue cracks when misalignment increases. Later, Cuffaro et al. [5] designed a test rig to analyze fretting wear phenomena in aerospace applications up to a 0.2° misalignment angle. Hong et al. [6] developed a finite element model to quantify load distribution variation caused by misalignments until 0.12°, and observed a load concentration at the end of the coupling due to the effect of the tilting moment. They also demonstrated that this effect could be reduced with a proper lead crown modification value. Guo et al. [7] proposed an analytical model to determine the local contact characteristics, which proved that misalignment causes a decrease in the number of teeth in contact, leading to load increase in those in contact. All of these works are focused on the influence of several parameters in contact conditions and load distribution for small misalignments. However, uncertainty still exists in gear coupling behavior for high misalignment applications.

It is true that high misalignments, above 3°, may limit power capacity, but some machinery requires spherical gear couplings to work with high misalignments. Mancuso [8] described the use of gear spindles in heavy duty, high torque applications for a maximum misalignment angle of 6°, while Herbstritt et al. [9] discussed the design optimization of mill spindles up to 3° misalignment. In fact, the metal rolling mills industry is the main sector of application of spherical gear couplings [10], where the small size of the rolls involves working conditions up to 7°, as investigated by Larrañaga et al. [11].

Spherical gear couplings require accurate geometry generation methods to ensure a solid foundation for further investigations, such as tooth contact and clearance, or stress analyses. Employed methods of manufacturing the hub include either

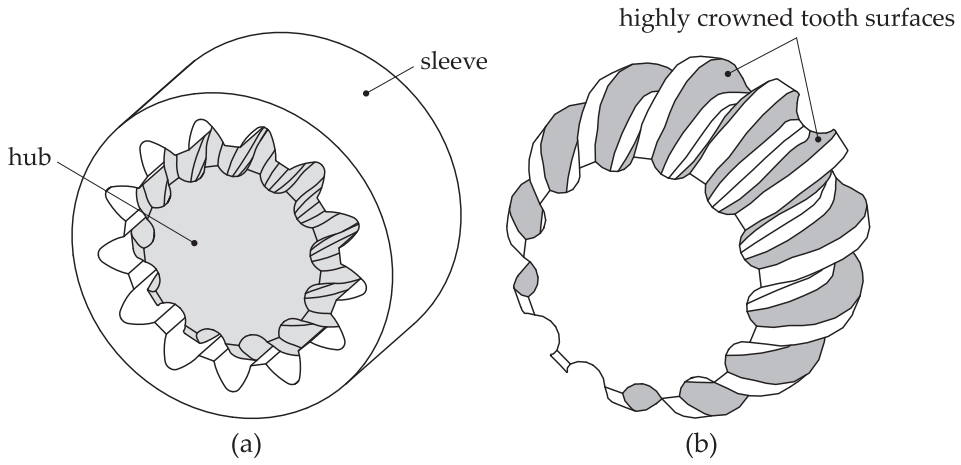

Fig. 1. Spherical gear coupling: (a) assembly of hub and sleeve, and (b) hub with highly crowned tooth surfaces.

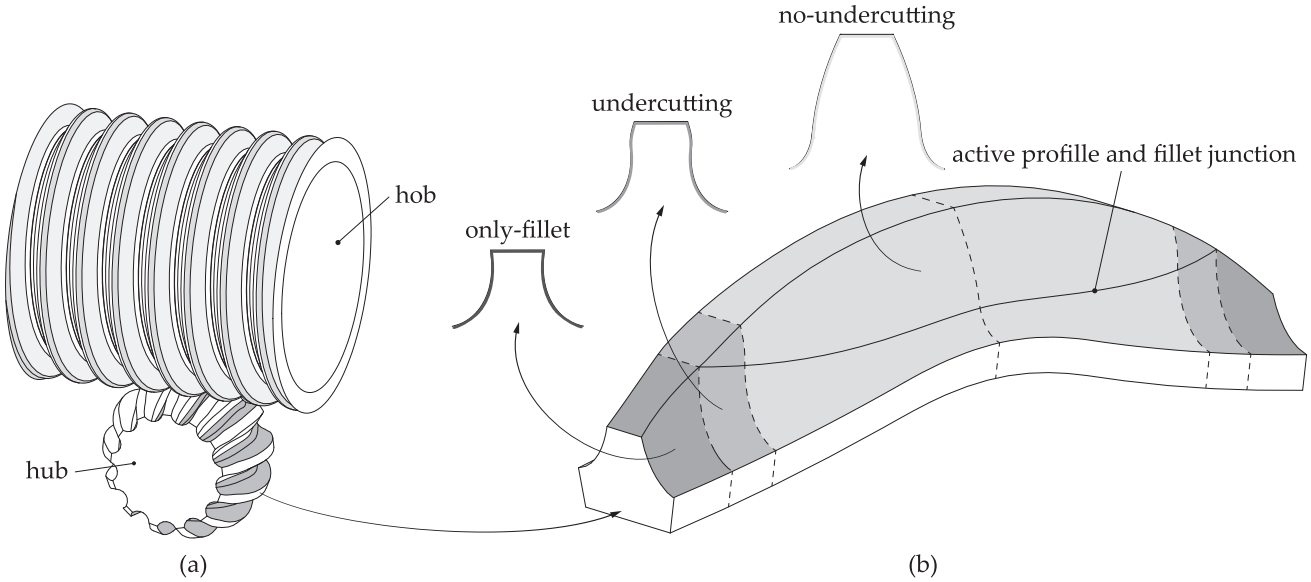

Fig. 2. Generation by a hob: (a) manufacturing of the hub by means of the hob, and (b) types of cross sections in a highly crowned hub tooth.

generation by a disk or by a hob [3,12]. Although generation by a hob (Fig. 2(a)) represents the main procedure of hub cutting, most of the generation methods presented in the literature for gear couplings simplify the hobbing process using a cutting edge. Mitome et al. [13] and Guan et al. [3] simplified the hobbing process by the rotation of the hob middle cross section. However, this method does not allow the existence of undercut profiles when reduced tool path radii are used. On the other hand, Chao et al. [14] and Kelemen et al. [15] considered the path of the cutting edge of the hob middle cross section to obtain the generating tooth surface. None of these methods has a straightforward methodology to be easily adapted to different tool paths of the hob.

Although the methods mentioned above can be accurate for small amounts of crowning, higher crowning values demand exact generation methods, and therefore the geometry of the generating tool surface must be assessed. A hob may be regarded as a set of cutting edges distributed along its thread, and as a result the thread surface has to be considered in the model of the cutting tool to achieve an accurate generation method.

Generation of a gear tooth surface by a hob (or a worm) thread surface was introduced by Litvin et al. [16,17] and employed in some works, such as, generation of face-gear drives [18,19], noncircular gears [20,21] or screw rotors [22]. Later, Jia et al. [23] applied a discrete enveloping method considering a hob among different gear tools. Furthermore, Vedmar [24] investigated the roughness of hobbed gear tooth surfaces and Klocke et al. [25] introduced gear tooth surface deviations caused by a non-ideal hobbing simulation.

However, the amount of crowning that may be required in gear drives is much lower than in spherical gear couplings (see Fig. 1(b)). Thus, their generation introduces new problems including the appearance of singularities. As stated in [17], the appearance of singular points on the generated surface is the warning that the surface may be undercut during the

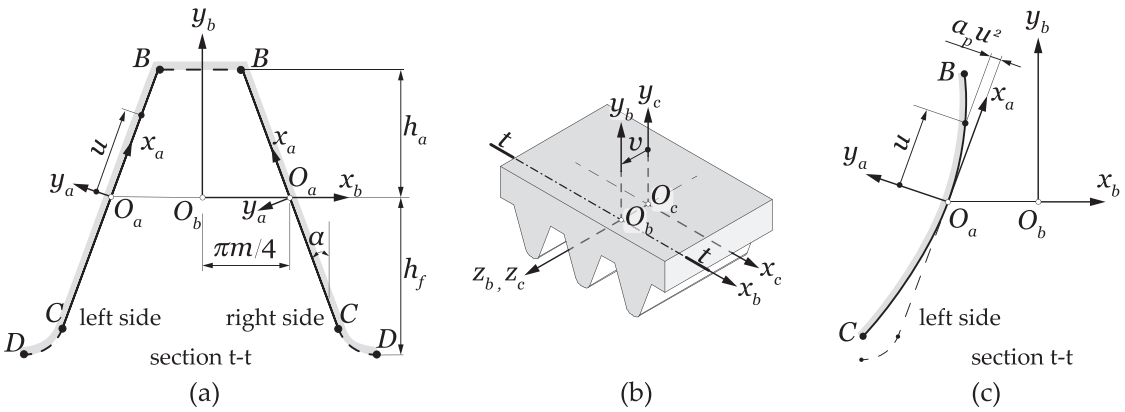

Fig. 3. Rack-cutter tooth surface Σ_c definition: (a) surface parameter u, (b) surface parameter v, and (c) definition of profile crowning.

generation process. Indeed, the existence of undercutting is unavoidable, especially in small parts where the hub teeth are manufactured directly on a shaft [26]. As a consequence, different regions along the length of the tooth can be observed in Fig. 2(b).

Therefore, the main goals of the present research are:

(1) To numerically generate spherical hub tooth surfaces by a hob thread surface, and implement an algorithm for the detection of singularities during the generation process. The proposed generation method identifies three types of cross sections in the generated teeth of the hub (Fig. 2(b)): (i) cross sections where no undercutting exists, (ii) cross sections where the active profile is undercut and coexists with the fillet, and (iii) cross sections where only the fillet exists. Detection of undercutting is important for a better estimation of the bending strength of the hub in further stress analyses.

(2) To compare the hub generation model with two simplified models where the hob thread surface is substituted by a set of cutting edges. These two simplified methods of hub generation by a hob are described in detail in [3,15] and are implemented in this work for the purpose of comparison. The developed algorithm for the detection of singularities is also implemented in these simplified methods. The comparison is based on the determination of normal deviations between the hub tooth surface of the proposed model and the hub tooth surface of the simplified ones. In addition, differences in the location of undercut profiles are investigated.

(3) To analyze unloaded tooth contact when a misalignment angle is present and to determine the clearance between the pairs of teeth of the spherical gear coupling. To this end, a sleeve model is obtained through the computational generation of the sleeve tooth surfaces by a shaper tooth surface.

2. Generation of the hub model

Generation of the hub tooth surface Σ_h by a hob requires prior determination of the hob (or worm) thread surface Σ_w (Secs. 2.2, 2.3). For that purpose, a standard rack-cutter tooth surface Σ_c is defined (Section 2.1) as the generating surface of Σ_w. Once the process to determine the surface Σ_h is described (Section 2.4), an algorithm for the determination of singularities and the location of different types of cross sections in the hub teeth is presented (Section 2.5). Finally, two existing procedures to determine the surface Σ_h are provided (Section 2.6) for the purpose of comparison.

2.1. Definition of the rack-cutter tooth surface Σ_c

Three coordinate systems are considered for the definition of the surface Σ_c as is illustrated in Fig. 3: (i) the system S_a is attached to the rack-cutter profile and allows the surface parameter u to be defined, (ii) the system S_b is located with its origin O_b at a distance $\pi m/4$ from the origin O_a, where m is the module of the gear coupling, and (iii) the system S_c allows the other surface parameter, v, to be defined by locating the origin O_b and coordinate axes x_b and y_b at section $t-t$ (Fig. 3(b)).

The rack-cutter tooth surface Σ_c is obtained in the system S_c as

$$\mathbf{r}_c(u,v) = \mathbf{M}_{cb}(v)\mathbf{M}_{ba}\mathbf{r}_a(u) \tag{1}$$

$$\mathbf{r}_c(u,v) = \begin{bmatrix} 1 & 0 & 0 & 0 \\ 0 & 1 & 0 & 0 \\ 0 & 0 & 1 & v \\ 0 & 0 & 0 & 1 \end{bmatrix} \cdot \begin{bmatrix} \mp\sin\alpha & \mp\cos\alpha & 0 & \pm\dfrac{\pi m}{4} \\ \cos\alpha & \mp\sin\alpha & 0 & 0 \\ 0 & 0 & 1 & 0 \\ 0 & 0 & 0 & 1 \end{bmatrix} \cdot \begin{bmatrix} u \\ 0 \\ 0 \\ 1 \end{bmatrix} \tag{2}$$

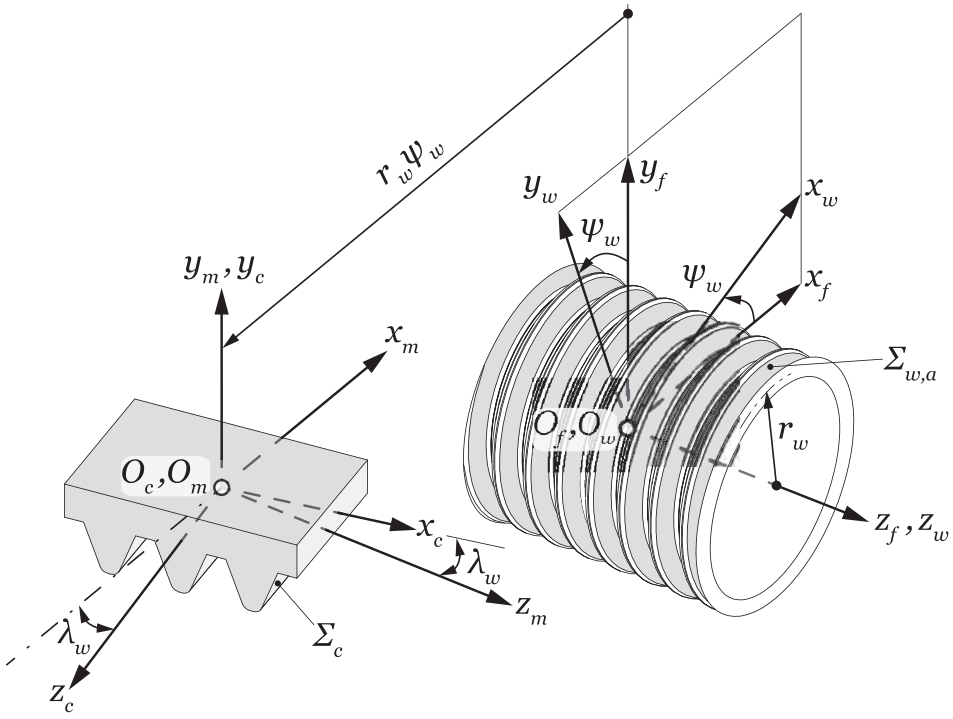

Fig. 4. Determination of the active hob thread surface $\Sigma_{w,a}$.

where α is the pressure angle of the coupling. The upper sign is applied to the right side whereas the lower sign is applied to the left side of the rack-cutter tooth.

When profile crowning is required to avoid edge contact at the tips of the hub and sleeve teeth (Fig. 3(c)), the vector $\mathbf{r}_a(u)$ is obtained as

$$\mathbf{r}_a(u) = [u \quad a_p u^2 \quad 0 \quad 1]^T \tag{3}$$

where a_p is a parabola coefficient.

2.2. Generation of the active hob thread surface $\Sigma_{w,a}$

Fig. 4 shows the coordinate systems that are considered to determine the active hob thread surface $\Sigma_{w,a}$. The coordinate systems S_w and S_c are rigidly connected to the hob and the rack-cutter, respectively. The system S_f is a fixed coordinate system where the rotation of the hob is taken into consideration through the angle ψ_w. The system S_m is an auxiliary coordinate system attached to the rack-cutter that allows the cutter to be positioned on the hob using the lead angle λ_w. The systems S_m and S_c are displaced the value $\psi_w r_w$ in the direction of the axis x_m, which is parallel to the axis x_f. Here, r_w is the pitch radius of the hob and coincides with the shortest distance between the axis x_m and x_f.

The surface $\Sigma_{w,a}$ can be determined as the envelope to the family of generating tooth surfaces Σ_c in the system S_w by simultaneous consideration of the following equations

$$\mathbf{r}_w(u, v, \psi_w) = \mathbf{M}_{wc}(\psi_w)\mathbf{r}_c(u, v) \tag{4}$$

$$f_1(u, v, \psi_w) = \left(\frac{\partial \mathbf{r}_w}{\partial u} \times \frac{\partial \mathbf{r}_w}{\partial v}\right) \cdot \frac{\partial \mathbf{r}_w}{\partial \psi_w} = 0 \tag{5}$$

where

$$\begin{aligned}\mathbf{M}_{wc} &= \mathbf{M}_{wf}\mathbf{M}_{fm}\mathbf{M}_{mc} \\ &= \begin{bmatrix} \cos\psi_w & \sin\psi_w & 0 & 0 \\ -\sin\psi_w & \cos\psi_w & 0 & 0 \\ 0 & 0 & 1 & 0 \\ 0 & 0 & 0 & 1 \end{bmatrix} \cdot \begin{bmatrix} 1 & 0 & 0 & -r_w\psi_w \\ 0 & 1 & 0 & r_w \\ 0 & 0 & 1 & 0 \\ 0 & 0 & 0 & 1 \end{bmatrix} \cdot \begin{bmatrix} \sin\lambda_w & 0 & -\cos\lambda_w & 0 \\ 0 & 1 & 0 & 0 \\ \cos\lambda_w & 0 & \sin\lambda_w & 0 \\ 0 & 0 & 0 & 1 \end{bmatrix}\end{aligned} \tag{6}$$

and $f_1(u, v, \psi_w) = 0$ is the equation of meshing.

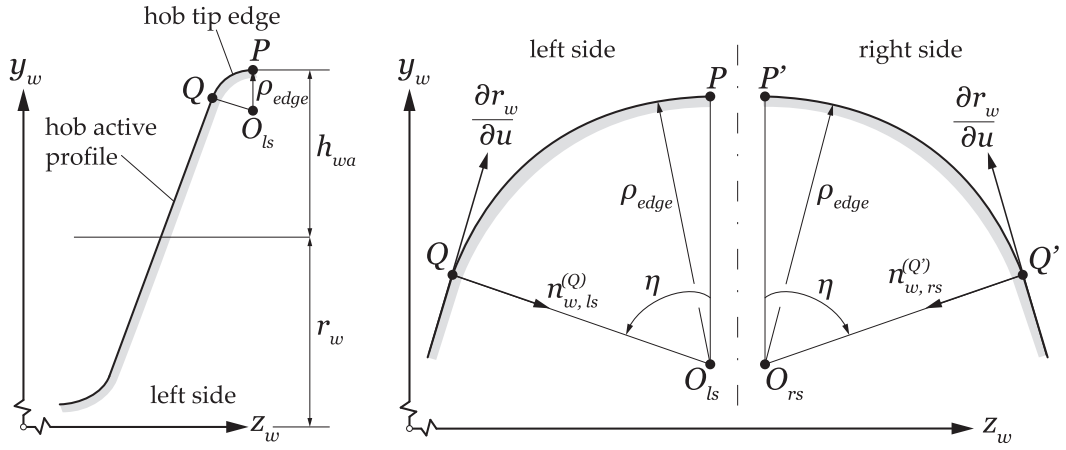

Fig. 5. Definition of the hob tip edge.

2.3. Determination of the tip edge surface $\Sigma_{w,t}$ of the hob thread

The surface $\Sigma_{w,t}$ is built directly on the system S_w as a helicoid with surface parameters η and δ. The tip edge is first defined on the plane $x_w = 0$ (Fig. 5). Points Q and Q' are the left and right joint points between the active profile and the tip edge of the hob thread at each side. The unit normals $\mathbf{n}^{(Q)}_{w,ls}$ and $\mathbf{n}^{(Q')}_{w,rs}$ can be obtained on the plane (y_w, z_w) as

$$\mathbf{n}^{(Q)}_{w,ls} = \mathbf{i}_w \times \frac{\frac{\partial \mathbf{r}_w}{\partial u}|_{u=u_Q}}{\left|\frac{\partial \mathbf{r}_w}{\partial u}|_{u=u_Q}\right|} \tag{7}$$

$$\mathbf{n}^{(Q')}_{w,rs} = -\mathbf{i}_w \times \frac{\frac{\partial \mathbf{r}_w}{\partial u}|_{u=u_{Q'}}}{\left|\frac{\partial \mathbf{r}_w}{\partial u}|_{u=u_{Q'}}\right|} \tag{8}$$

The following condition determines the parameter u_Q (and $u_{Q'}$) of the point Q (and Q')

$$y_w + n_{w,y}\rho_{edge} = r_w + h_{wa} - \rho_{edge} \tag{9}$$

where h_{wa} is the addendum and ρ_{edge} is the tip edge radius of the hob.

The center points O_{ls} and O_{rs} are then computed as

$$\mathbf{r}^{(O_{ls})}_w = \mathbf{r}^{(Q)}_w + \rho_{edge}\mathbf{n}^{(Q)}_{w,ls} \tag{10}$$

$$\mathbf{r}^{(O_{rs})}_w = \mathbf{r}^{(Q')}_w + \rho_{edge}\mathbf{n}^{(Q')}_{w,rs} \tag{11}$$

Next, the tip edges are defined as

$$\mathbf{r}^{(ls)}_w = \mathbf{r}^{(O_{ls})}_w + \rho_{edge}[0 \quad \cos\eta \quad -\sin\eta \quad 1]^T \tag{12}$$

$$\mathbf{r}^{(rs)}_w = \mathbf{r}^{(O_{rs})}_w + \rho_{edge}[0 \quad \cos\eta \quad +\sin\eta \quad 1]^T \tag{13}$$

where

$$\eta_{min} \le \eta \le \eta_{max} \quad \eta_{min} = 0 \quad \eta_{max} = \arccos(-\mathbf{n}^{(Q)}_{w,ls} \cdot \mathbf{j}_w) \tag{14}$$

To define the tip edge surface of the hob thread as a helicoid, a screw motion is applied to the previously determined tip edge considering the screw parameter p,

$$p = \frac{p_{ax}N_w}{2\pi} \tag{15}$$

where p_{ax} is the axial pitch of the hob and N_w the number of threads of the hob.

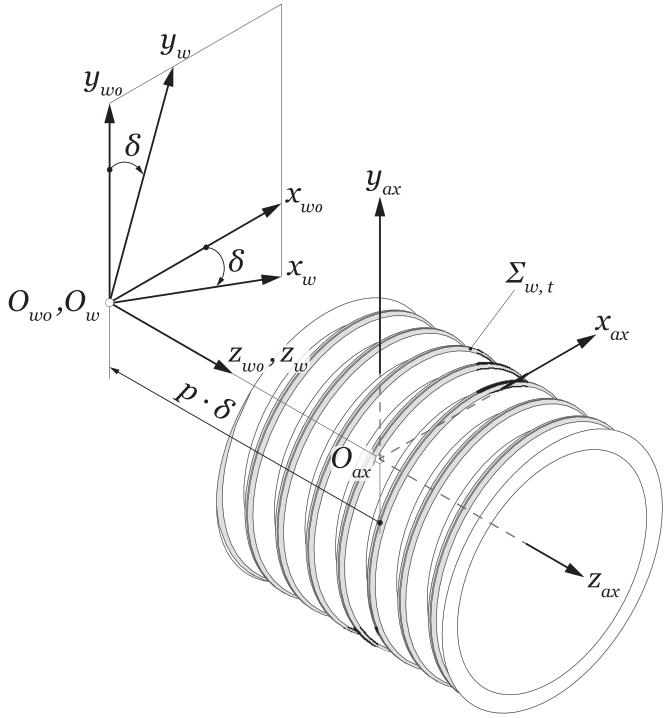

Fig. 6. Derivation of the tip edge surface $\Sigma_{w,t}$ of the hob thread.

Fig. 6 shows an auxiliary fixed coordinate system S_{ax} that coincides with the system S_w when $\delta = 0$. Prior to the screw motion, the tip edges derived in Eqs. (12), (13) are computed in the system S_{ax} as

$$\mathbf{r}_{\mathrm{ax}}(\eta) = [0 \quad y_w(\eta) \quad z_w(\eta) \quad 1]^T \tag{16}$$

Each thread side is considered independently, but indexes *ls* and *rs* are omitted for the purpose of simplicity.

The screw motion implies a rotation δ and a displacement $p\delta$ of the coordinate system S_w with respect to the coordinate system S_{ax} (Fig. 6). The system S_{wo} is another auxiliary coordinate system that displaces with the system S_w but does not rotate. Finally, the tip edge surface $\Sigma_{w,t}$ of the hub thread is determined as

$$\mathbf{r}_{\mathrm{w}}(\delta, \eta) = \mathbf{M}_{\mathrm{w,ax}}(\delta)\mathbf{r}_{\mathrm{ax}}(\eta) = \begin{bmatrix} \cos\delta & \mp\sin\delta & 0 & 0 \\ \pm\sin\delta & \cos\delta & 0 & 0 \\ 0 & 0 & 1 & p\delta \\ 0 & 0 & 0 & 1 \end{bmatrix} \mathbf{r}_{\mathrm{ax}}(\eta) \tag{17}$$

Here, the upper sign is applied to a hob with a right hand helix whereas the lower sign is for a hob with a left hand helix.

2.4. Generation of the hub tooth surface Σ_h

The hub tooth surface Σ_h is composed of the active tooth surface $\Sigma_{h,a}$, and the fillet tooth surface $\Sigma_{h,f}$. The surface $\Sigma_{h,a}$ is generated by the active hob thread surface $\Sigma_{w,a}$, and the surface $\Sigma_{h,f}$ is generated by the tip edge surface $\Sigma_{w,t}$ of the hob thread. Fig. 7 shows the coordinate systems that are involved in the generation process. The system S_f is a fixed coordinate system where rotation of the hub occurs. The auxiliary coordinate systems S_p and S_n displace with the hob through a curved tool path of radius r_β. The system S_p allows the system S_n to be positioned considering the lead angle of the hob λ_w, which is given as

$$\lambda_w = \arctan \frac{p_{ax} N_w}{2\pi r_w} \tag{18}$$

The system S_w, rigidly connected to the hob, moves with the systems S_p and S_n, and in addition rotates the angle ϕ_w. Similarly, the system S_h is rigidly connected to the hub and rotates the angle ψ_h, which is given as

$$\psi_h = \phi_w \frac{N_w}{N_h} \tag{19}$$

where N_h is the number of teeth of the hub.

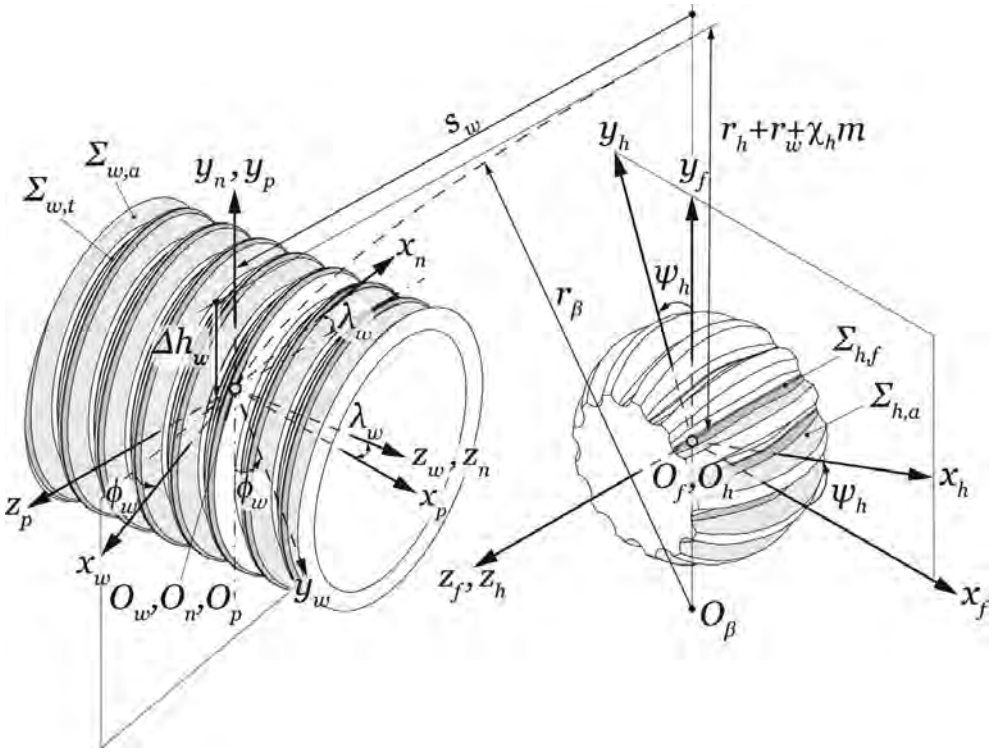

Fig. 7. Derivation of the hub tooth surfaces $\Sigma_{h,a}$ and $\Sigma_{h,f}$.

The generation is considered as a double-enveloping process [17], represented with two independent parameters, ϕ_w and s_w. To determine the active hub tooth surface $\Sigma_{h,a}$, coordinate transformation from system S_w to system S_h

$$\mathbf{r}_{\mathrm{h,a}}(u, v, \psi_w, s_w, \phi_w) = \mathbf{M}_{\mathrm{hw}}(s_w, \phi_w)\mathbf{r}_{\mathrm{w}}(u, v, \psi_w) \tag{20}$$

and corresponding equations of meshing (Eqn 21, 22 and 23–23) are solved.

$$f_1(u, v, \psi_w) = \left(\frac{\partial \mathbf{r}_{\mathrm{w}}}{\partial u} \times \frac{\partial \mathbf{r}_{\mathrm{w}}}{\partial v}\right) \cdot \frac{\partial \mathbf{r}_{\mathrm{w}}}{\partial \psi_w} = 0 \tag{21}$$

$$f_2(u, v, s_w, \phi_w) = \left(\frac{\partial \mathbf{r}_{\mathrm{h,a}}}{\partial u} \times \frac{\partial \mathbf{r}_{\mathrm{h,a}}}{\partial v}\right) \cdot \frac{\partial \mathbf{r}_{\mathrm{h,a}}}{\partial \phi_w} = 0 \tag{22}$$

$$f_3(u, v, s_w, \phi_w) = \left(\frac{\partial \mathbf{r}_{\mathrm{h,a}}}{\partial u} \times \frac{\partial \mathbf{r}_{\mathrm{h,a}}}{\partial v}\right) \cdot \frac{\partial \mathbf{r}_{\mathrm{h,a}}}{\partial s_w} = 0 \tag{23}$$

Likewise, the fillet hub tooth surface $\Sigma_{h,f}$ can be determined with the same coordinate transformation

$$\mathbf{r}_{\mathrm{h,f}}(\eta, \delta, s_w, \phi_w) = \mathbf{M}_{\mathrm{hw}}(s_w, \phi_w)\mathbf{r}_{\mathrm{w}}(\eta, \delta) \tag{24}$$

and corresponding equations of meshing (25,26).

$$f_4(\eta, \delta, s_w, \phi_w) = \left(\frac{\partial \mathbf{r}_{\mathrm{h,f}}}{\partial \eta} \times \frac{\partial \mathbf{r}_{\mathrm{h,f}}}{\partial \delta}\right) \cdot \frac{\partial \mathbf{r}_{\mathrm{h,f}}}{\partial \phi_w} = 0 \tag{25}$$

$$f_5(\eta, \delta, s_w, \phi_w) = \left(\frac{\partial \mathbf{r}_{\mathrm{h,f}}}{\partial \eta} \times \frac{\partial \mathbf{r}_{\mathrm{h,f}}}{\partial \delta}\right) \cdot \frac{\partial \mathbf{r}_{\mathrm{h,f}}}{\partial s_w} = 0 \tag{26}$$

The matrix $\mathbf{M}_{\mathrm{hw}}(s_w, \phi_w)$ is given by $\mathbf{M}_{\mathrm{gw}} = \mathbf{M}_{\mathrm{hf}}\mathbf{M}_{\mathrm{fp}}\mathbf{M}_{\mathrm{pn}}\mathbf{M}_{\mathrm{nw}}$, where

$$\mathbf{M}_{\mathrm{hf}} = \begin{bmatrix} \cos\psi_h & \sin\psi_h & 0 & 0 \\ -\sin\psi_h & \cos\psi_h & 0 & 0 \\ 0 & 0 & 1 & 0 \\ 0 & 0 & 0 & 1 \end{bmatrix} \quad \mathbf{M}_{\mathrm{fp}} = \begin{bmatrix} 1 & 0 & 0 & 0 \\ 0 & 1 & 0 & r_h + r_w + \chi_h m - \Delta h_w \\ 0 & 0 & 1 & s_w \\ 0 & 0 & 0 & 1 \end{bmatrix} \tag{27}$$

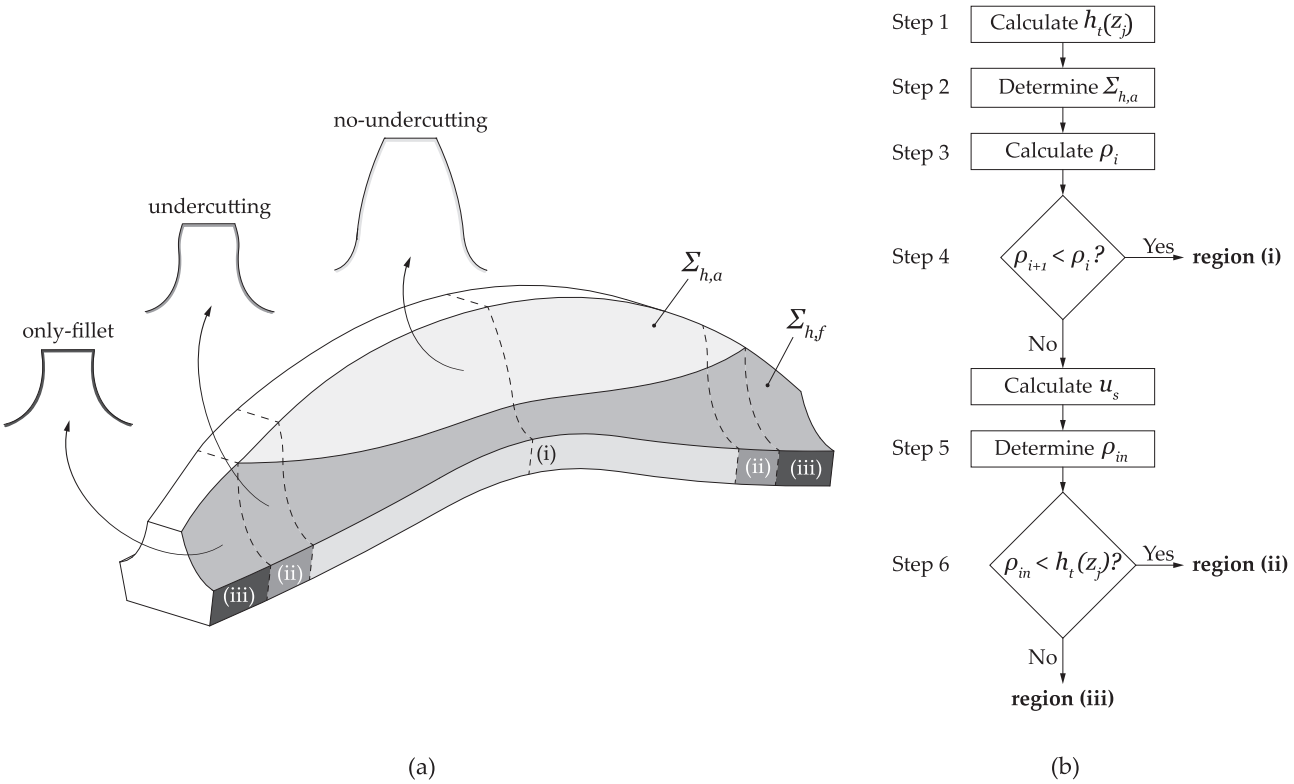

Fig. 8. Hub tooth geometry: (a) different types of cross sections, and (b) algorithm to detect undercutting and identify the region for each cross section.

$$\mathbf{M}_{\text{pn}} = \begin{bmatrix} -\sin\lambda_w & 0 & \cos\lambda_w & 0 \\ 0 & 1 & 0 & 0 \\ -\cos\lambda_w & 0 & -\sin\lambda_w & 0 \\ 0 & 0 & 0 & 1 \end{bmatrix} \quad \mathbf{M}_{\text{nw}} = \begin{bmatrix} -\cos\phi_w & \sin\phi_w & 0 & 0 \\ -\sin\phi_w & -\cos\phi_w & 0 & 0 \\ 0 & 0 & 1 & 0 \\ 0 & 0 & 0 & 1 \end{bmatrix} \tag{28}$$

Here, r_h is the pitch radius of the hub, χ_h is a generating shift coefficient, and $\Delta h_w = r_\beta - \sqrt{r_\beta^2 - s_w^2}$ represents the plunging of the hob when a circular tool path is applied. A negative generating shift coefficient is usually considered when some backlash between the hub and the sleeve teeth is required.

2.5. Singularities in the generation of the hub tooth surface Σ_h

When the hub comprises highly crowned tooth surfaces, an algorithm to detect undercutting is required to generate the hub teeth with different types of cross sections as illustrated in Fig. 8(a). This algorithm allows to detect three different types of cross sections and determine the interval of values for the profile and fillet parameters at each type of cross section. The three different types of cross sections in the hub tooth surface Σ_h are shown in Fig. 8(a): (i) a no-undercutting region where tangency between the surfaces $\Sigma_{h,a}$ and $\Sigma_{h,f}$ is observed, (ii) an undercutting region where the tangency between $\Sigma_{h,a}$ and $\Sigma_{h,f}$ is not observed, and (iii) an only-fillet region where just the surface $\Sigma_{h,f}$ exists. The only-fillet and undercutting regions can be prevented by shortening the face width of the hub or by increasing the tool path radius r_β. Nevertheless, such options are not possible in some hub designs, where space is a constraint and the teeth are manufactured directly on a shaft with highly crowned tooth surfaces to absorb high misalignments [26].

The following algorithm (Fig. 8(b)) was applied to each cross section of the hub tooth to identify its region and determine its geometry:

Step 1 The coordinate z_j, $j = \{1, \ldots, n_j\}$, of the hub tooth is given for each cross section j of a total of n_j sections. The hub tip height $h_t(z_j)$ is determined at each cross section (Fig. 9)

$$h_t(z_j) = r_h + h_{ha} - r_\alpha[1 - \cos\mu(z_j)] \tag{29}$$

where $r_\alpha = r_\beta - r_w - \chi_h m + h_{ha}$ and $\mu(z_j) = \arcsin\left(\frac{z_j}{r_\alpha}\right)$. Here, h_{ha} is the hub addendum.

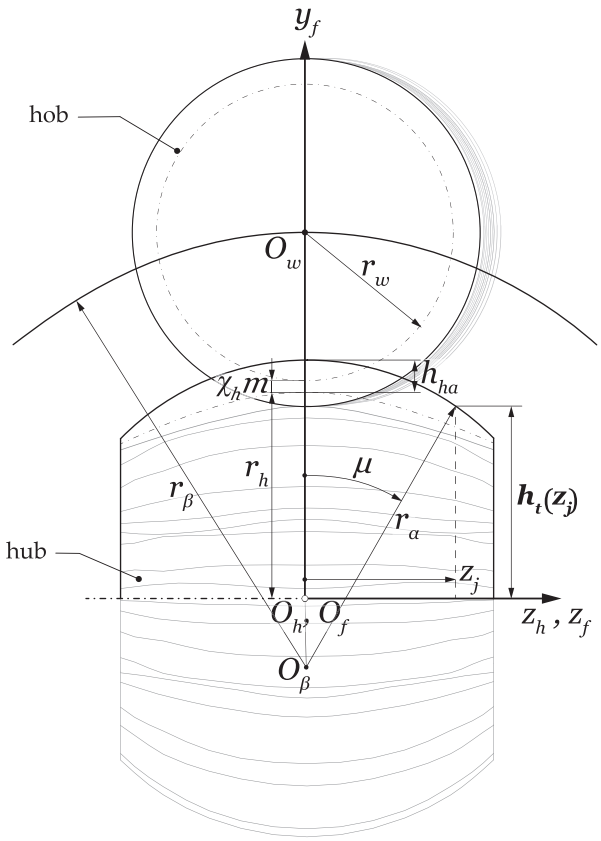

Fig. 9. Derivation of the hub tip height h_t.

Step 2 Variation of the surface parameter u determines the active profile of the cross section considering the following set of equations

$$\begin{aligned} \mathbf{r}_{\mathrm{h,a}}(u, v, \psi_w, s_w, \phi_w) &= \mathbf{M}_{\mathrm{hw}}(s_w, \phi_w)\mathbf{r}_{\mathrm{w}}(u, v, \psi_w) \\ f_1(u, v, \psi_w) &= 0 \\ f_2(u, v, s_w, \phi_w) &= 0 \\ f_3(u, v, s_w, \phi_w) &= 0 \\ f_6(u, v, \psi_w, s_w, \phi_w) &= z_h - z_j = 0 \end{aligned} \tag{30}$$

Equations $f_1 = 0$, $f_2 = 0$ and $f_3 = 0$ correspond to equations (21), (22) and (23), respectively.

Step 3 The tooth profile radii ρ_i, $i = \{1, \ldots, n_i\}$, are computed considering n_i points along the active profile of the cross section. The surface parameter u is varied from $u_{\min}$ (at the tip of the hub tooth) to $u_{\max}$ (at the bottom of the hub profile). Thus, Fig. 10(a) shows how the radii are computed from the tip to the bottom of the active profile as $\rho_i = \sqrt{x_h^2 + y_h^2}$ with $\rho_{i+1} < \rho_i$.

Step 4 When $\rho_{i+1} < \rho_i$, the active profile is free of singularities and the cross section of the tooth is located in the no-undercutting region (i). In the case that $\rho_{i+1} \geq \rho_i$, tangency no longer exists between the active profile and the fillet due to the presence of a second branch (Fig. 10(b)). For the first occurrence i in which $\rho_{i+1} \geq \rho_i$, the parameter u_s of the singular point is obtained.

Step 5 In the case of singularity existence, intersection between the active profile and the fillet (Fig. 10(b)) is determined as follows:

(a) Set of equations (30) represent the active profile of the cross section with surface parameter $u_{\min} \leq u \leq u_s$.

(b) A second set of equations (31) represent the fillet profile of the cross section with surface parameter $\eta_{\min} \leq \eta \leq \eta_{\max}$

$$\begin{aligned} \mathbf{r}_{\mathrm{h,f}}(\eta, \delta, s_w, \phi_w) &= \mathbf{M}_{\mathrm{hw}}(s_w, \phi_w)\mathbf{r}_{\mathrm{w}}(\eta, \delta) \\ f_4(\eta, \delta, s_w, \phi_w) &= 0 \\ f_5(\eta, \delta, s_w, \phi_w) &= 0 \\ f_7(\eta, \delta, s_w, \phi_w) &= z_h - z_j = 0 \end{aligned} \tag{31}$$

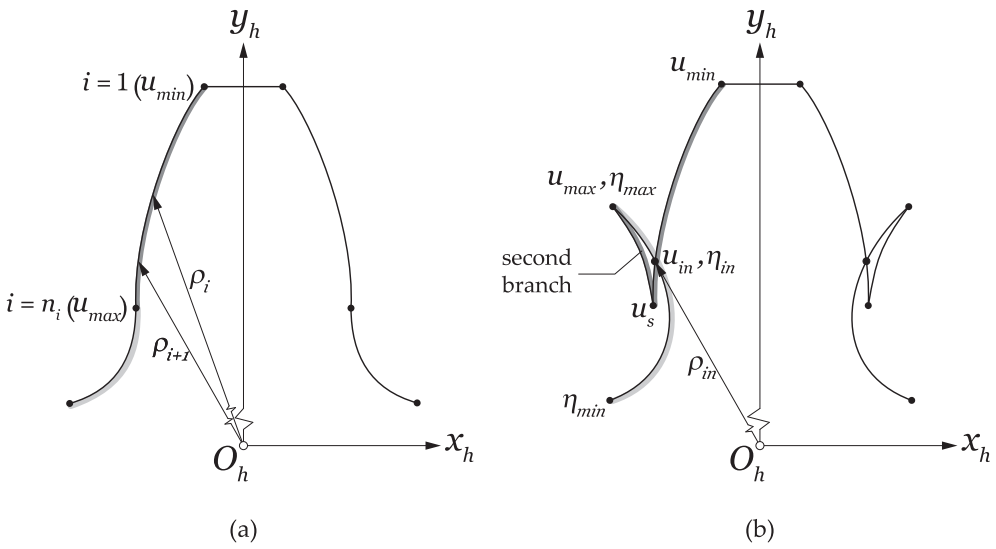

Fig. 10. Hub tooth cross section: (a) without undercutting, and (b) with undercutting.

Equations $f_4 = 0$ and $f_5 = 0$ correspond to equations (25) and (26), respectively.

(c) The intersection of the active and fillet profiles solving both sets of equations, (30) and (31), enables surface parameters u_{in} and η_{in} to be determined.

(d) The corresponding radius of the intersection point between the active profile and the fillet is established as $\rho_{in} = \sqrt{[x_h(u_{in})]^2 + [y_h(u_{in})]^2}$.

Step 6 When $\rho_{in} < h_t(z_j)$, the cross section will be located in the undercutting region (ii), where the active profile is generated with $u_{\min} \le u \le u_{in}$, and the fillet profile with $\eta_{\min} \le \eta \le \eta_{in}$. In contrast, if $\rho_{in} \ge h_t(z_j)$ the cross section will be located in the only-fillet region (iii). In this case, the fillet is generated with $\eta_{\min} \le \eta \le \eta'_{\max}$, where $\eta'_{\max}$ is determined by simultaneous consideration of the set of equations (31) and the following additional equation

$$f_8(\eta, \delta, s_w, \phi_w) = x_h^2 + y_h^2 - h_t^2(z_j) = 0 \tag{32}$$

2.6. Simplified models for generation of the hub

Two simplified models presented in the literature for the generation of a hub by a hob have been implemented for the purpose of comparison with the proposed model.

2.6.1. Model 1

The first model is described in [15] and illustrated in Fig. 11. A cutting edge is defined considering the profile parameter u in the coordinate system S_c. The system S_c is rigidly connected to the auxiliary system S_m, and rotates the angle θ around axis x_m. Parameters u and θ define a generating surface Σ_o in the coordinate system S_o. The displacement $r_h\psi_h$ of the surface Σ_o, rigidly connected to the system S_o, is accompanied by the rotation ψ_h of the hub. This model obtains the hub tooth surface in a single-enveloping process, with ψ_h as the generalized parameter of generation in accordance with the theory of gearing [17].

2.6.2. Model 2

The second model is reported in [3] and [15] and illustrated in Fig. 12. In this case, the hub tooth surface is obtained as a set of independent cross sections, each one generated by a cutting edge defined in the coordinate system S_{ci}. For the positioning of each cutting edge over the hub, a different generating shift coefficient χ_i is used. The displacement $r_h\psi_{hi}$ of the cutting edge is accompanied by the rotation ψ_{hi} of the hub. Each hub tooth profile i is obtained in a single-enveloping process with ψ_{hi} as the generalized parameter of generation. This is also a single enveloping process [17]. In this model, derivation of the normal of the hub tooth surface is not straightforward and requires consideration of u and z_i as surface parameters of the theoretical generating tool surface.

3. Unloaded tooth contact and clearance analyses

Unloaded tooth contact and clearance analyses of the gear coupling are carried out assuming that a misalignment γ is present between the sleeve and the hub. The sleeve model is based on involute tooth surfaces and can be obtained as explained in Appendix A. Fig. 13 shows a fixed coordinate system S_f where the hub and the sleeve models are assembled.

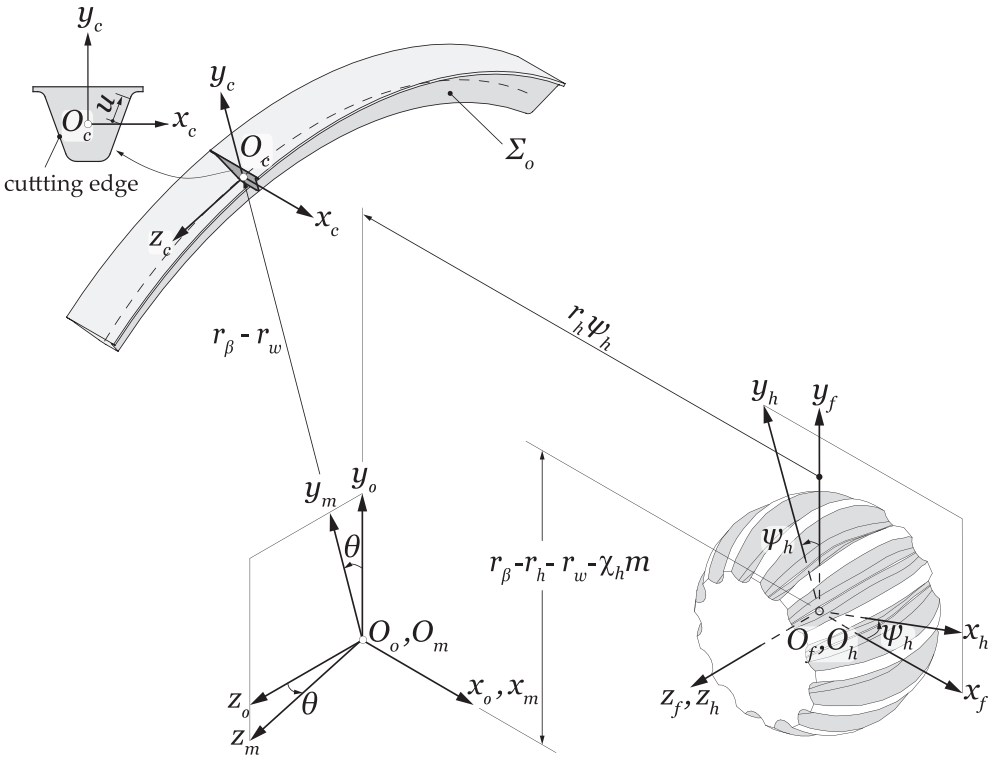

Fig. 11. Derivation of the hub tooth surface in model 1.

The systems S_h and S_g are rigidly connected to the hub and the sleeve models, respectively. The sleeve model is mounted in the system S_f with a misalignment γ around the axis y_f, which coincides with the axis y_g. While the sleeve model is held at rest, the hub model can rotate the angle ϕ_h until one of its teeth makes contact with one sleeve tooth. A counterclockwise rotation of the hub model is supposed.

Point contact is assumed between the surfaces Σ_h and Σ_g due to the double crowned tooth surfaces of the hub model. The following algorithm (divided in 8 steps) was applied to determine the contact point at one pair of teeth, and the clearance for those remaining:

Step 1 The tooth of the hub whose symmetry axis is perpendicular to the misalignment plane for $\phi_h = 0$ is assumed to be the first tooth to make contact with a tooth of the sleeve model [2]. Assuming, for the purpose of simplicity, that (u_h, v_h) are the surface parameters of surface Σ_h (located at the left side of the tooth that comes into contact), the following coordinate transformation represents the surface Σ_h in the system S_f as

$$\mathbf{r}_{\mathrm{f}}^{(\mathrm{hub})}(u_h, v_h, \phi_h) = \mathbf{M}_{\mathrm{fh}}(\phi_h)\mathbf{r}_{\mathrm{h}}(u_h, v_h) \tag{33}$$

Here,

$$\mathbf{M}_{\mathrm{fh}} = \begin{bmatrix} \cos\phi_h & \sin\phi_h & 0 & 0 \\ -\sin\phi_h & \cos\phi_h & 0 & 0 \\ 0 & 0 & 1 & 0 \\ 0 & 0 & 0 & 1 \end{bmatrix} \tag{34}$$

where ϕ_h is the angle of rotation of the hub to make contact with the sleeve. The variables (u_h, v_h, ϕ_h) are the unknowns for the sought-for contact point.

Step 2 The unit normal to surface Σ_h at the sought-for contact point can be obtained in the system S_f as

$$\mathbf{n}_{\mathrm{f}}^{(\mathrm{hub})}(u_h, v_h, \phi_h) = \mathbf{L}_{\mathrm{fh}}(\phi_h)\frac{\dfrac{\partial \mathbf{r}_{\mathrm{h}}}{\partial u_h} \times \dfrac{\partial \mathbf{r}_{\mathrm{h}}}{\partial v_h}}{\left|\dfrac{\partial \mathbf{r}_{\mathrm{h}}}{\partial u_h} \times \dfrac{\partial \mathbf{r}_{\mathrm{h}}}{\partial v_h}\right|} \tag{35}$$

where the matrix $\mathbf{L}_{\mathrm{fh}}$ is of 3×3 order and can be determined from the matrix $\mathbf{M}_{\mathrm{fh}}$ by eliminating the last row and the last column.

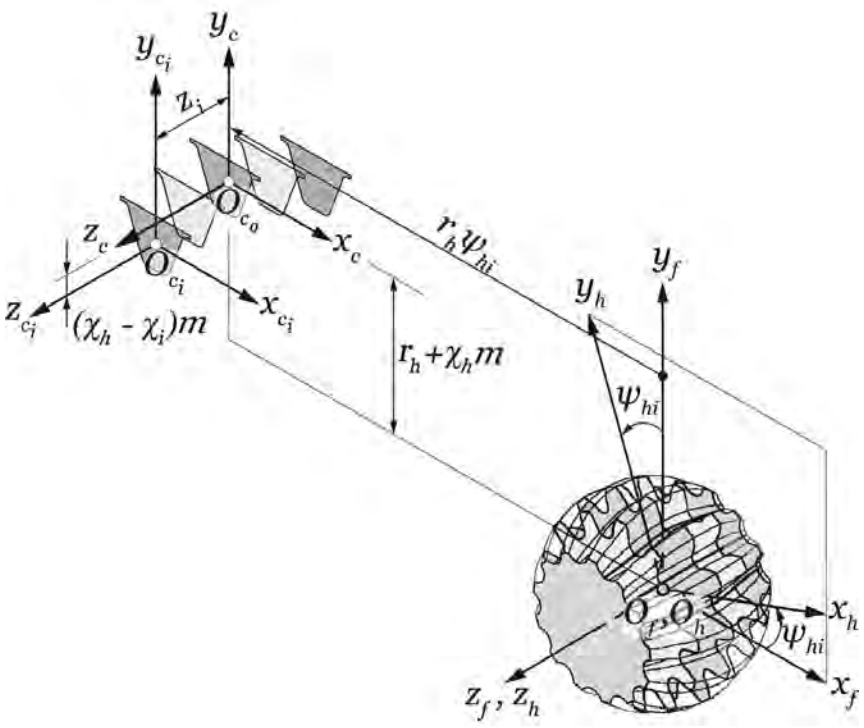

Fig. 12. Derivation of the hub cross sections in model 2.

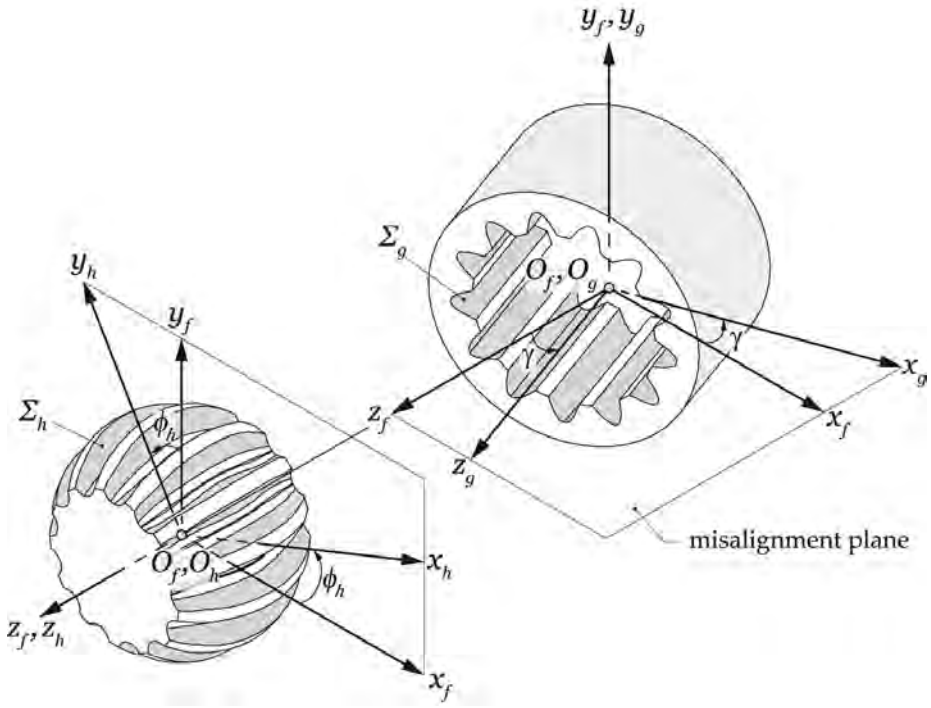

Fig. 13. Coordinate systems applied for the positioning of a gear coupling with shaft misalignment angle γ.

Step 3 The surface Σ_g, located at the left side of the tooth space whose symmetry axis is y_g, is considered to make contact with the surface Σ_h. Assuming, for the purpose of simplicity, that (u_g, v_g) are the surface parameters of the surface Σ_g, the following coordinate transformation allows the surface Σ_g to be represented in the system S_f

$$\mathbf{r}_{\mathrm{f}}^{(\mathrm{sleeve})}(u_g, v_g) = \mathbf{M}_{\mathrm{fg}}\mathbf{r}_{\mathrm{g}}(u_g, v_g) \tag{36}$$

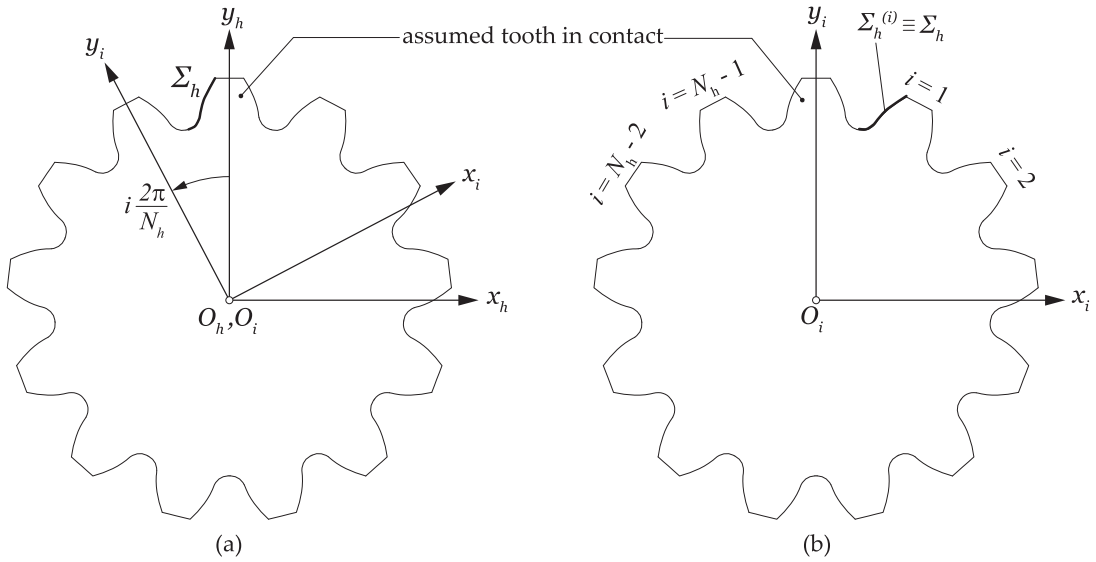

Fig. 14. Derivation of tooth surfaces $\Sigma_h^{(i)}$ at the hub.

Here,

$$\mathbf{M}_{\mathrm{fg}} = \begin{bmatrix} \cos\gamma & 0 & -\sin\gamma & 0 \\ 0 & 1 & 0 & 0 \\ \sin\gamma & 0 & \cos\gamma & 0 \\ 0 & 0 & 0 & 1 \end{bmatrix} \tag{37}$$

where (u_g, v_g) are the unknowns of the sought-for contact point.

Step 4 The unit normal to surface Σ_g at the sought-for contact point can be obtained in the system S_f as

$$\mathbf{n}_{\mathrm{f}}^{(\mathrm{sleeve})}(u_g, v_g) = \mathbf{L}_{\mathrm{fg}} \frac{\frac{\partial \mathbf{r}_{\mathrm{g}}}{\partial u_g} \times \frac{\partial \mathbf{r}_{\mathrm{g}}}{\partial v_g}}{\left| \frac{\partial \mathbf{r}_{\mathrm{g}}}{\partial u_g} \times \frac{\partial \mathbf{r}_{\mathrm{g}}}{\partial v_g} \right|} \tag{38}$$

where the matrix $\mathbf{L}_{\mathrm{fg}}$ is of 3×3 order and can be determined from the matrix $\mathbf{M}_{\mathrm{fg}}$ by eliminating the last row and the last column.

Step 5 A system of five independent scalar equations and unknowns $\{u_h, v_h, \phi_h, u_g\ v_g\}$ is defined as

$$\mathbf{r}_{\mathrm{f}}^{(\mathrm{hub})}(u_h, v_h, \phi_h) = \mathbf{r}_{\mathrm{f}}^{(\mathrm{sleeve})}(u_g, v_g) \tag{39}$$

$$\mathbf{n}_{\mathrm{f}}^{(\mathrm{hub})}(u_h, v_h, \phi_h) = \mathbf{n}_{\mathrm{f}}^{(\mathrm{sleeve})}(u_g, v_g) \tag{40}$$

Equation (40) represents only two independent scalar equations since $|\mathbf{n}_{\mathrm{f}}^{(\mathrm{hub})}| = |\mathbf{n}_{\mathrm{f}}^{(\mathrm{sleeve})}| = 1$.

Step 6 The surfaces $\Sigma_h^{(i)}$ and $\Sigma_g^{(i)}$, $i = \{1, \ldots, N_h - 1\}$, of adjacent teeth are assumed not to be in contact, since contacting tooth surfaces Σ_h and Σ_g are considered to be rigid. Clearance at each adjacent pair of teeth is determined from this step on. The coordinate systems S_i, $i = \{1, \ldots, N_h - 1\}$, are used to define surfaces $\Sigma_h^{(i)}$ and $\Sigma_g^{(i)}$ as illustrated in Fig. 14

$$\mathbf{r}_{\mathrm{i}}(u_h, v_h) = \mathbf{M}_{\mathrm{ih}}\mathbf{r}_{\mathrm{h}}(u_h, v_h) \tag{41}$$

$$\mathbf{r}_{\mathrm{i}}(u_g, v_g) = \mathbf{M}_{\mathrm{ih}}\mathbf{r}_{\mathrm{g}}(u_g, v_g) \tag{42}$$

Here,

$$\mathbf{M}_{\mathrm{ih}} = \begin{bmatrix} \cos\left(i \cdot \frac{2\pi}{N_h}\right) & \sin\left(i \cdot \frac{2\pi}{N_h}\right) & 0 & 0 \\ -\sin\left(i \cdot \frac{2\pi}{N_h}\right) & \cos\left(i \cdot \frac{2\pi}{N_h}\right) & 0 & 0 \\ 0 & 0 & 1 & 0 \\ 0 & 0 & 0 & 1 \end{bmatrix} \tag{43}$$

Table 1
Design data of the spherical gear coupling.

Design parameter	[units]	Hub	Sleeve
Tooth number, N_h		13	
Pressure angle, α	deg	30.0	
Module, m	mm	3.0	
Face width, F	mm	30.0	
Generating shift coefficient, χ		-0.058	-0.035
Addendum, h_{ha}	mm	$0.5m$	
Deddendum, h_{hf}	mm	$0.9m$	

Table 2
Design data of the hob.

Design parameter	[units]	Value
Face width, F_w	mm	80.0
Number of threads, N_w		1
Helix hand		Right
Pitch radius, r_w	mm	30.875
Lead angle, λ_w	deg	2.7847
Addendum, h_{wa}	mm	$0.9m$
Deddendum, h_{wf}	mm	$0.5m$
Tip radius, ρ_{edge}	mm	$0.4m$

Step 7 Steps from 1 to 5 are repeated for each pair of tooth surfaces $\Sigma_h^{(i)}$ and $\Sigma_g^{(i)}$, and the angle $\phi_{h,i}$ of rotation of the hub is calculated to obtain a potential contact point for each pair of teeth where there is some clearance. If the deformation of the tooth is sufficient to allow contact, the potential contact point will become a point of contact between the tooth surfaces $\Sigma_h^{(i)}$ and $\Sigma_g^{(i)}$. Likewise, if the potential contact point is outside the boundaries of the tooth surface, it is disregarded.

Step 8 When a pair of tooth surfaces $\Sigma_h^{(i)}$ and $\Sigma_g^{(i)}$ have a potential contact point, the clearance c_i, $i = \{1, \ldots, N_h - 1\}$, is calculated as

$$c_i = \frac{1}{2}(\phi_{h,i} - \phi_h) m N_h \cos\alpha \tag{44}$$

4. Results

The design data of a spherical gear coupling are shown in Table 1. The generating shift coefficients χ set out in Table 1 are determined with a tolerance class $H7/d7$ in accordance with ISO 4156 [27].

These coefficients allow the hub and the sleeve to be generated with a tooth thickness that guarantees the existence of backlash between both splines in the middle cross section. A tool path radius of $r_\beta = 49.0$ mm is assumed to guarantee existence of backlash between both splines along the face width and for a misalignment angle of $\gamma_{\max} = 6.0°$. The design data of the hob to generate the hub are shown in Table 2.

4.1. Geometry comparison

Fig. 15 shows a comparison between the hub tooth surface Σ_h of the proposed model and the tooth surface Σ_{m1} of the simplified model 1, for both tooth sides. A similar comparison between Σ_h and the surface Σ_{m2} of the simplified model 2 is illustrated in Fig. 16. The normal distances from the surface Σ_h to the surfaces Σ_{m1} and Σ_{m2} are used to compare the geometry. These normal deviations are plotted in the radial projection of the hub tooth with axis z_h and the radial position $\rho_i = (x_h^2 + y_h^2)^{1/2}$. The comparisons are limited to the interval $z_h \in [-9.0, +9.0]$ mm, where the maximum deviations reach about 200 m in model 1 and 600 m in model 2. Furthermore, it is important to point out that the Standard ISO 4156 [27] establishes a maximum deviation allowance of the tooth surfaces as 59 m for a standard coupling of $m = 3$ mm, $z = 13$, and tolerance class 7. This means that the obtained deviations between the three models are significant.

The geometry comparison shows that the differences between the compared models arise further away from the middle plane $z_h = 0$. Here, at $z_h = 0$, the three models provide the same cross section.

On the other hand, Fig. 15 shows that the results obtained for the interval $z_h \in [0.0, +9.0]$ mm in the left tooth side (Fig. 15(a)) are exactly the same as those obtained for the interval $z_h \in [-9.0, 0.0]$ mm in the right tooth side (Fig. 15(b)), and *viceversa*. The same observation can be made comparing Fig. 16(a) and 16(b). Since the simplified models do not cause asymmetry in the tooth profiles, this is evidence that the proposed model of generation by a hob is introducing some asymmetry as a consequence of the twist of the tooth surfaces. This phenomenon has been observed in helical gears generated by a hob [28–30], and also in spur gears generated by a hob, although in the latter case it was said to be negligible [31].

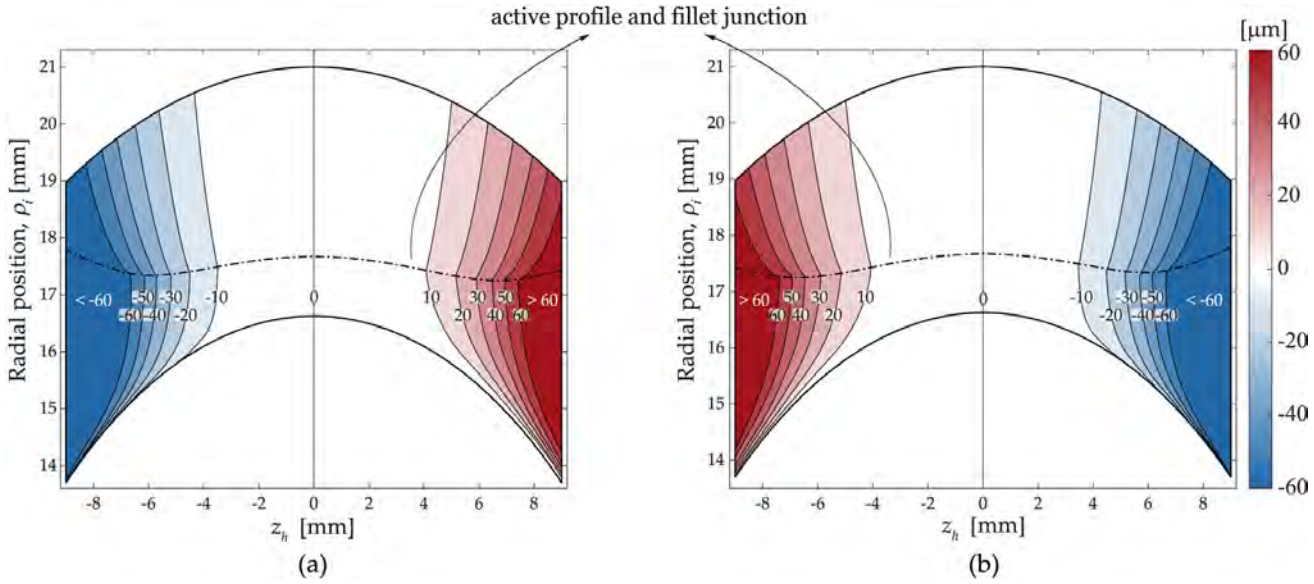

Fig. 15. Normal deviations between Σ_h and Σ_{m1}: (a) left tooth side, and (b) right tooth side.

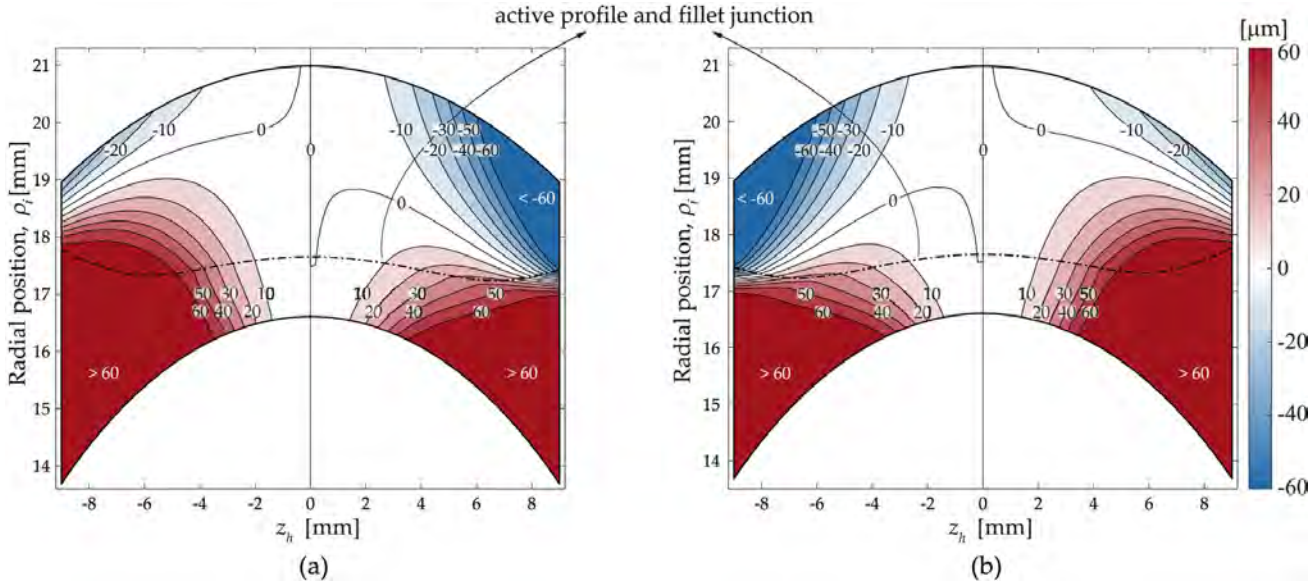

Fig. 16. Normal deviations between Σ_h and Σ_{m2}: (a) left tooth side, and (b) right tooth side.

However, the effect is more notable in spherical gear couplings, as suggested by [12], and may lead to a reduction of the load capacity.

The three models were also compared in terms of the minimum coordinate z_h of the first cross section of the hub tooth where undercutting appears. Fig. 17(a) shows that undercutting emerges at coordinate $z_h = 6.85$ mm in the proposed model, and $z_h = 9.45$ mm in model 2. The location of the cross section where undercutting appears in model 1, $z_h = 7.20$ mm, is very close to that of the proposed model and is not represented in Fig. 17(a) for the purpose of clarity. Fig. 17(b) shows the cross sections of the hub space for the three models at coordinate $z_h = 6.85$ mm, where greater differences can be seen in model 2 than in model 1. It is expected that such differences might have an important effect on the predicted bending strength of the hub, due to the reduction in the tooth thickness. Fig. 17(b) illustrates as well that the tooth profiles of the proposed model are non-symmetric.

In addition, an advantage of the proposed model for hub generation is that it is a procedure focused on the tool path of the hob, in contrast to the other models here compared. Fig. 18(a) shows two possible tool paths: (i) a circular tool path, and (ii) a circular tool path with the influence of the entry and exit of the tool in the hub geometry. Tool entry and exit are relevant to the tooth geometry as stated in AGMA 945-1-B20 [32], especially in those geometries where the teeth are manufactured directly on a shaft and significant reduction of the tooth thickness is undesirable.

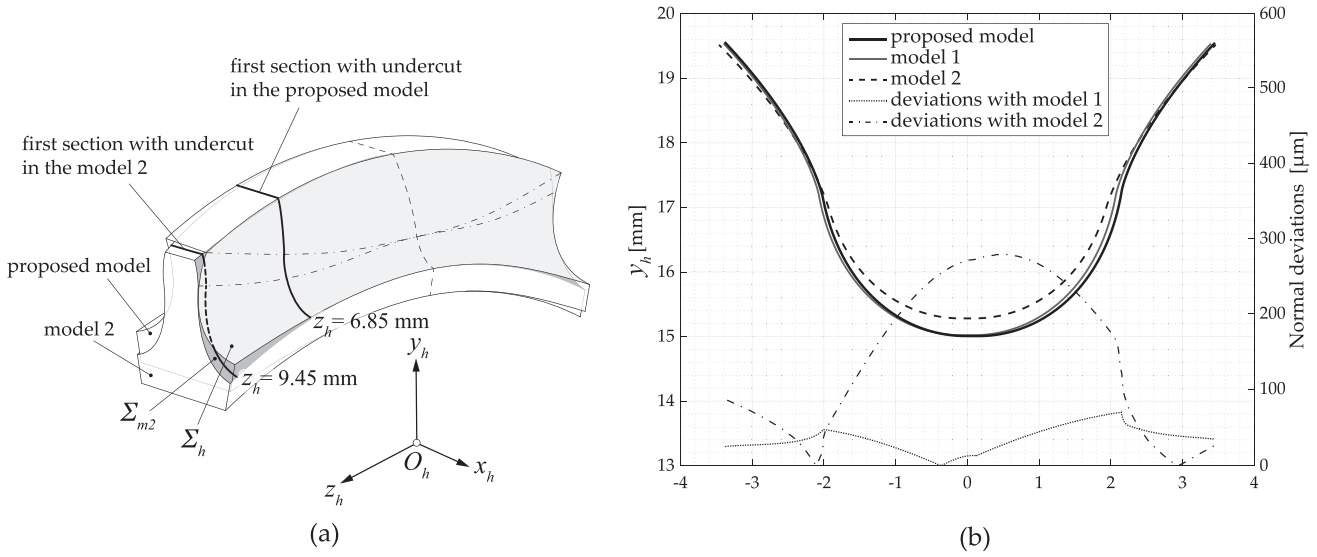

Fig. 17. (a) location of first appearance of undercutting in Σ_h and Σ_{m2}, and (b) hub space cross section comparison at $z_h = 6.85$ mm for Σ_h, Σ_{m1} and Σ_{m2}.

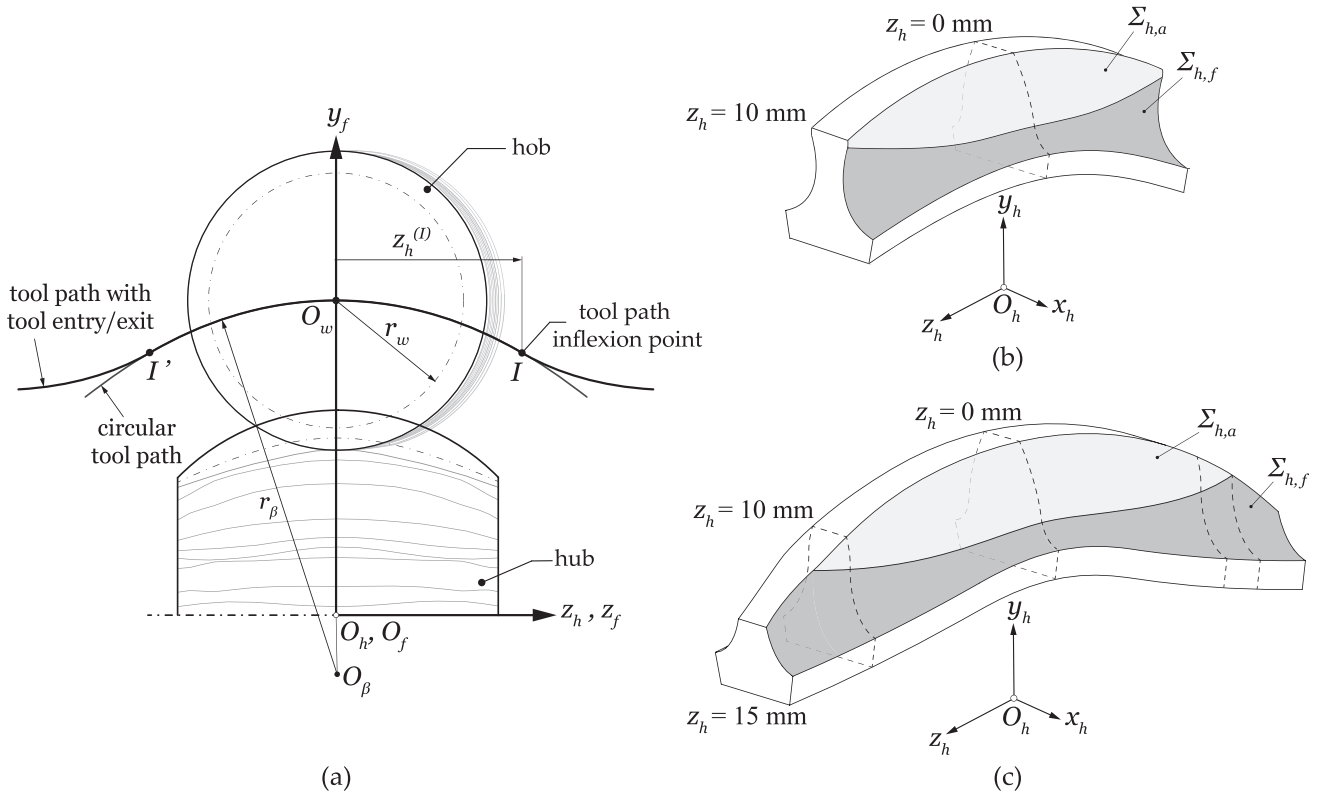

Fig. 18. Tool path entry/exit influence on Σ_h: (a) two types of tool paths, (b) Σ_h using a circular tool path, and (c) Σ_h using a circular tool path with tool entry and exit influence.

Fig. 18 (a) shows that tool entry and exit are controlled through the location of the inflection points I and I', and the curvatures of those tool path sections. Fig. 18(b) illustrates the effect on the hub tooth of a circular path without considering tool entry and exit, and Fig. 18 (c) takes into account its effect. To obtain this geometry with the effect of tool entry and exit, I and I' points are located at $z_h = \pm 15.0$ mm, respectively, and a curvature radii for entry and exit sections equal to the circular tool path radius r_β is used. From both geometries it can be concluded that taking into account the tool entry and exit, a larger face width hub can be generated, preventing the rapid reduction of the tooth thickness, as shown in Fig. 18(b).

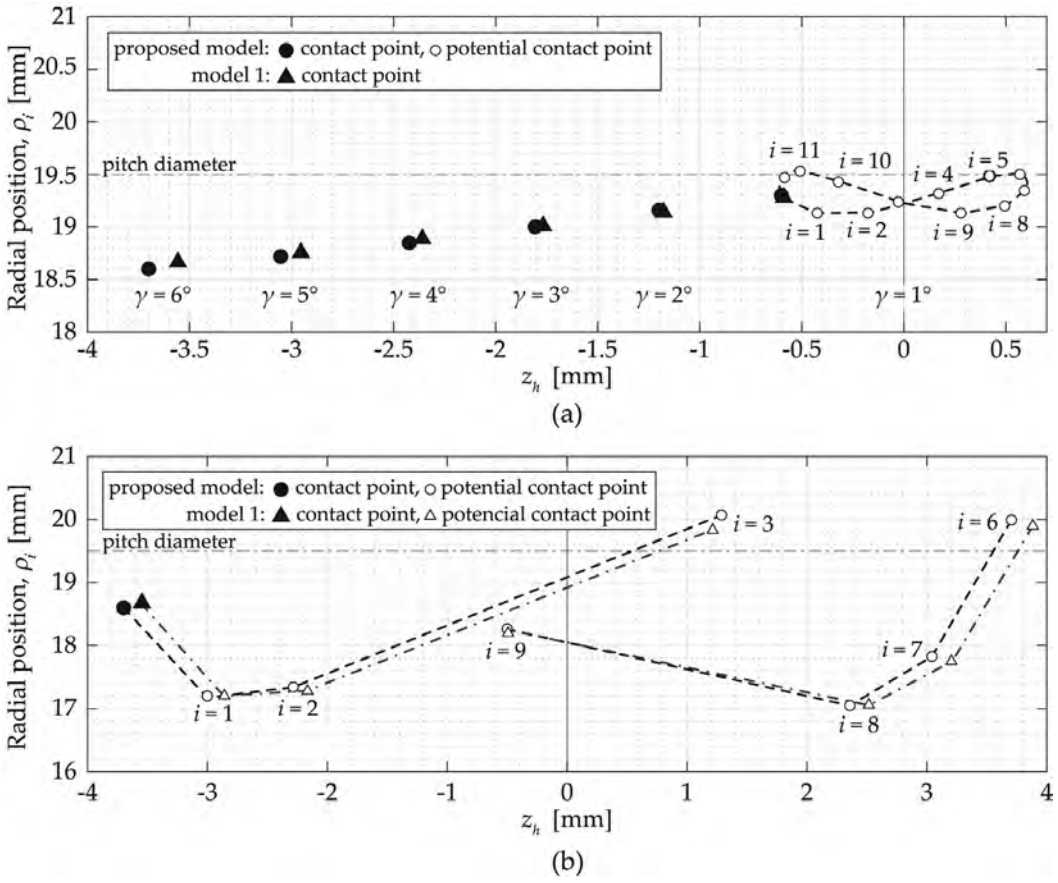

Fig. 19. TCA results: (a) contact points for different values of misalignment angle γ, (b) contact point and potential contact points for $\gamma = 6.0°$.

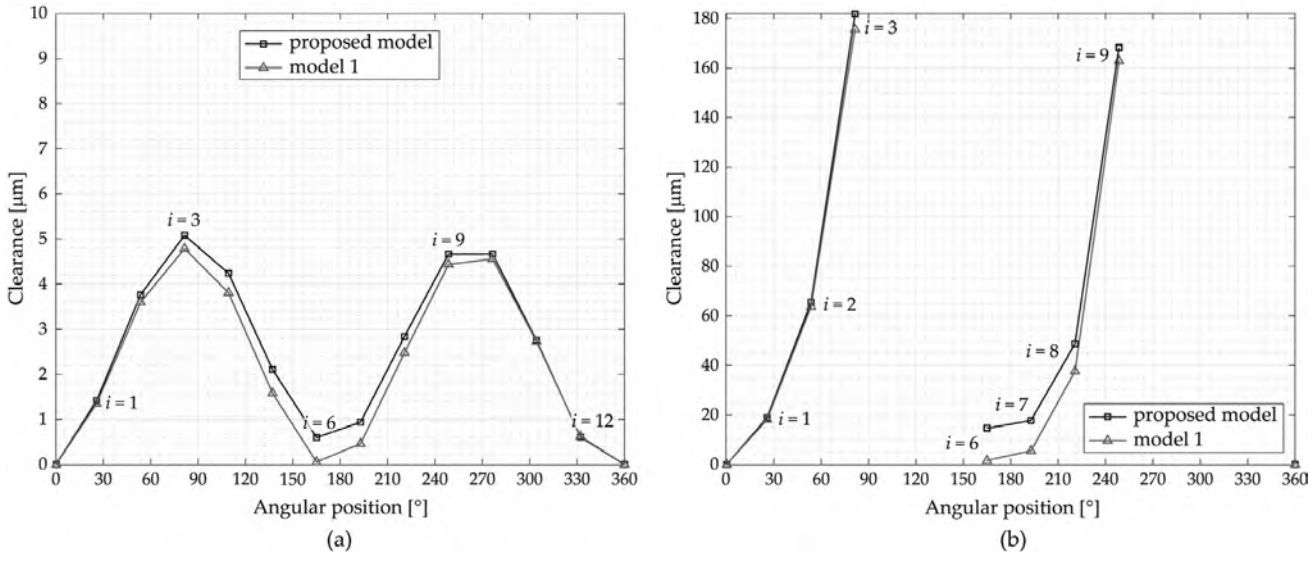

Fig. 20. Clearance values for the potential contact points in case of: (a) $\gamma = 1.0°$, and (b) $\gamma = 6.0°$.

4.2. Unloaded tooth contact and clearance analyses

The results of the tooth contact and clearance analyses of the gear coupling under different values of misalignment γ are illustrated in Figs. 19 and 20. In this section, just the proposed model and model 1 of the hub are being compared, since important geometry differences between the proposed model and model 2 were observed in Section 4.1.

For this analysis, a parabola coefficient $a_p = 0.001$ mm^{-1} (Fig. 3(c)) was used in the generation of the hub to prevent edge contact at the tips of the hub and the sleeve. Fig. 19(a) shows the contact points of the first pair of teeth that comes into contact for misalignment angles $\gamma = \{1^\circ, 2^\circ, 3^\circ, 4^\circ, 5^\circ, 6^\circ\}$. The effect of contact points moving away from the center plane $z_h = 0$ as misalignment increases is in agreement with the literature [12]. The location of the contact points are very similar between the proposed model and model 1 of the hub, although differences increase with the rise of the misalignment angle, up to 144.0 m in coordinate z_h when $\gamma = 6.0^\circ$.

Fig. 19 (a) also depicts the potential contact points for the proposed model of the hub when $\gamma = 1.0^\circ$. Twelve potential contact points are found, numbered from $i = 1$ to $i = 12$ (see also Fig. 14(b)). The locations of the potential contact points for model 1 are very similar to those of the proposed model when $\gamma = 1.0^\circ$, and are not included for clarity. It can also be seen that most of the potential contact points are located below the pitch cylinder of the hub. However, it is expected that the load will cause the contact pattern to be spread over the pitch cylinder [33].

As the misalignment angle increases, not all the tooth pairs have a potential contact point, as those which are out of the hub surface boundaries are disregarded. In case of $\gamma = 6^\circ$, just seven potential contact points are found, in both the proposed model and in model 1 (see Fig. 19(b)).

Clearance distribution is a key parameter to predict load distribution in gear couplings particularly in misaligned conditions, due to its variation along the angular position [2,34,35]. In consequence, Fig. 20 shows clearance distribution at two misalignment angles for those pairs of tooth surfaces $\Sigma_h^{(i)}$ and $\Sigma_g^{(i)}$ that have a potential contact point. It can be observed that clearance is minimum in the pure tilting area (around 0° and 180° of the angular rotation), while it increases in the pure pivoting area (around 90° and 180°), in accordance with the literature. In the case $\gamma = 1.0^\circ$ (Fig. 20(a)), for all the twelve potential contact points found, the clearance distribution and values are very similar for both models of the hub. However, when the misalignment angle is $\gamma = 6.0^\circ$ (Fig. 20(b)), with only seven potential contact points, the differences in the clearance between the proposed model and model 1 are much higher. These deviations may affect load sharing between the teeth of the coupling, as reported in [6,36].

5. Conclusions

This paper presents a procedure to generate an external spherical spline by a hob. This procedure aims to provide a more accurate simulation method for this type of generation process, than methods existing in the scientific literature. To this end, the procedure considers a hob thread surface as a set of cutting edges acting simultaneously during the generation. It makes possible the generation of profiles with undercutting that may appear in the manufacturing of spherical hubs, especially when highly crowned tooth surfaces are required to absorb misalignments above 3°. Moreover, the model presented here can be easily adapted to different tool paths in order to analyze its influence in the generated geometry.

The proposed model for generation of the hub is compared with two existing models in the literature and the following conclusions can be drawn:

(1) The normal deviations between the hub tooth surface of the proposed model and that of the existing models are significant when a high value of crowning is applied to the tooth surface. These differences exceed the maximum deviation allowance established in Standard ISO 4156 [27], especially in the cross sections away from the middle section of the hub.
(2) The prediction of existence of undercutting is closer to the middle cross section according to the proposed model, than that predicted by the existing models. These differences may affect the calculated bending strength of the hub.
(3) The investigation reveals that the proposed model can be easily adapted to follow different tool paths. In this sense, the tool path, which considers the tool entry and exit, is important to obtain larger face widths without thinning the teeth. This will be highly useful in applications where space is limited and the teeth of the hub are directly manufactured on a shaft.
(4) Differences between the proposed model and model 1 of the hub are observed in the location of the contact points and in the clearance values, which may affect contact conditions and thus load distribution. The proposed model predicts slightly larger shifts of the contact points and slightly higher values of clearance than those predicted by the model 1 when misalignment error is present.

The proposed model allows for future work to focus on the optimization of the hub geometry, either through an appropriate tool path of the hob or an appropriate profile crowning of the hub teeth, to balance the clearances, increase the contact ratio and reduce contact and bending stresses of spherical gear couplings.

Declaration of Competing Interest

The authors declare that they have no known competing financial interests or personal relationships that could have appeared to influence the work reported in this paper.

Appendix A. Generation of the sleeve model

Generation of the sleeve tooth surface Σ_g by a shaper requires prior determination of the shaper tooth surface Σ_s. For that purpose, the standard rack-cutter tooth surface Σ_c is defined in Section 2.1 as the generating surface of Σ_s. Finally, the sleeve tooth surface Σ_g is determined.

A1. Generation of the shaper tooth surface Σ_s

Fig. A.21 (a) shows the coordinate systems considered to determine the shaper tooth surface Σ_s. The coordinate systems S_s and S_c are rigidly connected to the shaper and to the rack-cutter, respectively. The system S_n is a fixed coordinate system where the rotation of the shaper is taken into account through the angle ψ_s. The system S_c displaces the value $\psi_s r_s$ in the direction of the axis x_c, which is parallel to the axis x_n. Here, r_s is the pitch radius of the shaper and coincides with the shortest distance between the axes x_c and x_n.

Surface Σ_s can be determined as the envelope to the family of generating tooth surfaces Σ_c in the system S_s by simultaneous consideration of the following equations

$$\mathbf{r}_s(u, v, \psi_s) = \mathbf{M}_{sc}(\psi_s)\mathbf{r}_c(u, v) \tag{A.1}$$

$$f_1(u, v, \psi_s) = \left(\frac{\partial \mathbf{r}_s}{\partial u} \times \frac{\partial \mathbf{r}_s}{\partial v}\right) \cdot \frac{\partial \mathbf{r}_s}{\partial \psi_s} = 0 \tag{A.2}$$

Here,

$$\mathbf{M}_{sc} = \mathbf{M}_{sn}\mathbf{M}_{nc} = \begin{bmatrix} \cos\psi_s & \sin\psi_s & 0 & 0 \\ -\sin\psi_s & \cos\psi_s & 0 & 0 \\ 0 & 0 & 1 & 0 \\ 0 & 0 & 0 & 1 \end{bmatrix} \cdot \begin{bmatrix} 1 & 0 & 0 & -r_s\psi_s \\ 0 & 1 & 0 & r_s \\ 0 & 0 & 1 & 0 \\ 0 & 0 & 0 & 1 \end{bmatrix} \tag{A.3}$$

The shaper teeth are rounded at the tip by considering a tip edge radius. The procedure to define the tip edge of the shaper is similar to the one described for the tip edge of the hob (Section 2.3) and is not described for the purpose of simplicity.

A2. Generation of the sleeve tooth surface Σ_g

Fig. A.21 (b) shows the coordinate systems that are involved in the generation process of the sleeve by a shaper. The system S_f is a fixed coordinate system where rotation of the sleeve is considered. Similarly, system S_n is an auxiliary fixed

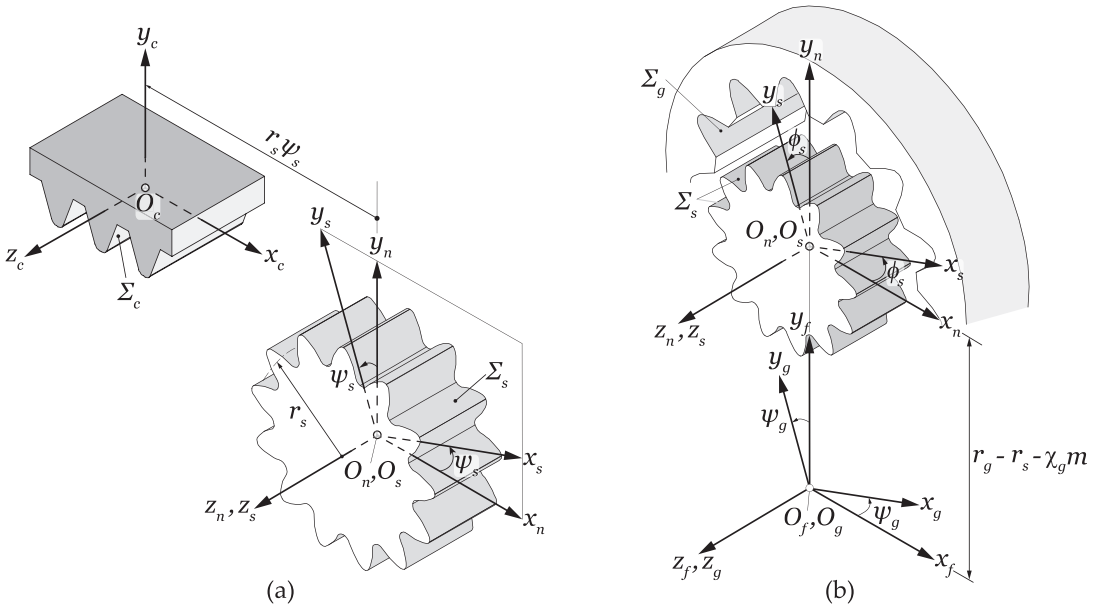

Fig. A.21. Definition of the sleeve model: (a) generation of the shaper tooth surface Σ_s, and (b) generation of the sleeve tooth surface Σ_g.

coordinate system where rotation of the shaper occurs. The system S_s, rigidly connected to the shaper, rotates the angle ϕ_s while the system S_g, rigidly connected to the sleeve, rotates the angle ψ_g, which is given as

$$\psi_g = \phi_s \frac{N_s}{N_h} \tag{A.4}$$

where N_h is the number of teeth of the hub (which is equal to that of the sleeve in a gear coupling) and N_s is the number of teeth in the shaper.

The surface Σ_g is determined as the envelope to the family of surfaces Σ_s in coordinate system S_g by simultaneous consideration of the following equations

$$\mathbf{r}_g(u, v, \psi_s, \phi_s) = \mathbf{M}_{gs}(\phi_s)\mathbf{r}_s(u, v, \psi_s) \tag{A.5}$$

$$f_1(u, v, \psi_s) = \left(\frac{\partial \mathbf{r}_s}{\partial u} \times \frac{\partial \mathbf{r}_s}{\partial v}\right) \cdot \frac{\partial \mathbf{r}_s}{\partial \psi_s} = 0 \tag{A.6}$$

$$f_2(u, v, \psi_s, \phi_s) = \left(\frac{\partial \mathbf{r}_g}{\partial u} \times \frac{\partial \mathbf{r}_g}{\partial v}\right) \cdot \frac{\partial \mathbf{r}_g}{\partial \phi_s} = 0 \tag{A.7}$$

Here, $\mathbf{M}_{gs}$ is the matrix for coordinate transformation from the system S_s to the system S_g

$$\mathbf{M}_{gs} = \mathbf{M}_{gf}\mathbf{M}_{fn}\mathbf{M}_{ns} \tag{A.8}$$

$$\mathbf{M}_{gs} = \begin{bmatrix} \cos\psi_g & \sin\psi_g & 0 & 0 \\ -\sin\psi_g & \cos\psi_g & 0 & 0 \\ 0 & 0 & 1 & 0 \\ 0 & 0 & 0 & 1 \end{bmatrix} \cdot \begin{bmatrix} 1 & 0 & 0 & 0 \\ 0 & 1 & 0 & r_g - r_s - \chi_g m \\ 0 & 0 & 1 & 0 \\ 0 & 0 & 0 & 1 \end{bmatrix} \cdot \begin{bmatrix} \cos\phi_s & -\sin\phi_s & 0 & 0 \\ \sin\phi_s & \cos\phi_s & 0 & 0 \\ 0 & 0 & 1 & 0 \\ 0 & 0 & 0 & 1 \end{bmatrix} \tag{A.9}$$

where r_g is the pitch radius of the sleeve and χ_g is a generating shift coefficient. A negative value of χ_g may be applied to produce some backlash between the hub and the sleeve teeth.

References

[1] S. Hahn, Coupling Connections and Splines, in: Encyclopedia of Automotive Engineering, American Cancer Society, 2014, pp. 1–14, doi:10.1002/9781118354179.auto094.
[2] M. Alfares, A. Falah, A. Elkholy, Clearance distribution of misaligned gear coupling teeth considering crowning and geometry variations, Mech Mach Theory 41 (10) (2006) 1258–1272, doi:10.1016/j.mechmachtheory.2005.11.004.
[3] Y. Guan, X. Yang, Z. Fang, G. Chen, Comparative analysis of three geometric models for crown gear coupling, Mech Mach Theory 136 (2019) 269–283, doi:10.1016/j.mechmachtheory.2019.02.016.
[4] R. Baker, Durability of Steel Spline Couplings, Ph.D. thesis, University of London, 2005.
[5] V. Cuffaro, F. Curà, A. Mura, Test rig for spline couplings working in misaligned conditions, J Tribol 136 (1) (2014) 011104, doi:10.1115/1.4025656.
[6] J. Hong, D. Talbot, A. Kahraman, Load distribution analysis of clearance-fit spline joints using finite elements, Mech Mach Theory 74 (2014) 42–57, doi:10.1016/j.mechmachtheory.2013.11.007.
[7] Y. Guo, S. Lambert, R. Wallen, R. Errichello, J. Keller, Theoretical and experimental study on gear-coupling contact and loads considering misalignment, torque and friction influences, Mech Mach Theory 98 (2016) 242–262, doi:10.1016/j.mechmachtheory.2015.11.015.
[8] J.R. Mancuso, Couplings and joints: design, selection and application, Technology & Engineering (1986). M. Dekker
[9] W. Herbstritt, J. Paluh, Mill spindle advanced gear design, Iron and Steel Engineers 76 (7) (1999) 44–48.
[10] P. Krot, Transient Torsional Vibrations Control in the Geared Drive Trains of the Hot Rolling Mills, in: IEEE International Conference on Control Applications, St. Petersburg, 2009, pp. 1368–1373, doi:10.1109/CCA.2009.5280933.
[11] J. Larrañaga, A. Arana, I. Ulacia, J. Esnaola, I. Torca, Misalignment Effect on Contact Pressure and Tooth Root Strength of Spline Couplings, in: 5th International Conference on Power Transmission-BAPT, Ohrid, Macedonia, 2016.
[12] F. Ohshima, S. Hirata, H. Yoshino, Study on tooth contact of gear couplings, Transactions of the Japan society of mechanical engineers. Series C 78 (786) (2012) 639–649.
[13] K. Mitome, T. Okuda, T. Ohmachi, T. Yamazaki, Development of a new hobbing of spherical gear, Transactions of the Japan society of mechanical engineers. Series C 66 (646) (2000) 1975–1980.
[14] L. Chao, C. Tsay, Contact characteristics of spherical gears, Mech Mach Theory 43 (10) (2008) 1317–1331, doi:10.1016/j.mechmachtheory.2007.10.008.
[15] L. Kelemen, J. Szente, Two mathematical models for generation of crowned tooth surface, The Scientific World Journal (2014), doi:10.1155/2014/641091.
[16] F. Litvin, Theory of Gearing, Tech. rep., University of Illinois at Chicago, 1989.
[17] F. Litvin, A. Fuentes, Gear Geometry and Applied Theory, 2nd Edition, CAMBRIDGE University Press, 2004.
[18] F. Litvin, A. Fuentes, C. Zanzi, M. Pontiggia, Design, generation, and stress analysis of two versions of geometry of face-gear drives, Mech Mach Theory 37 (10) (2002) 1179–1211, doi:10.1016/S0094-114X(02)00050-2.
[19] F. Litvin, D. Vecchiato, E. Gurovich, A. Fuentes, I. Gonzalez-Perez, K. Hayasaka, K. Yukishima, Computerized developments in design, generation, simulation of meshing, and stress analysis of gear drives, Meccanica 40 (2005) 291–324, doi:10.1007/s11012-005-4020-y.
[20] F. Litvin, I. Gonzalez-Perez, K. Yukishima, A. Fuentes, K. Hayasaka, Generation of planar and helical elliptical gears by application of rack-cutter, hob, and shaper, Comput Methods Appl Mech Eng 196 (41–44) (2007) 4321–4336, doi:10.1016/j.cma.2007.05.003.
[21] F. Litvin, A. Fuentes, I. Gonzalez-Perez, K. Hayasaka, Noncircular gears: Design and generation, CAMBRIDGE University Press, 2009.
[22] Y. Wu, W. Hsu, A general mathematical model for continuous generating machining of screw rotors with worm-shaped tools, Appl Math Model 38 (1) (2014) 28–37, doi:10.1016/j.apm.2013.05.056.
[23] K. Jia, J. Guo, S. Zheng, J. Hong, A general mathematical model for two-parameter generating machining of involute cylindrical gears, Appl Math Model 75 (2019) 37–51, doi:10.1016/j.apm.2019.05.021.
[24] L. Vedmar, A parametric analysis of the gear surface roughness after hobbing, J. Mech. Des. 132 (11) (2010) 111004, doi:10.1115/1.4002655.

[25] F. Klocke, C. Brecher, C. Lopenhaus, M. Kromer, Calculating the workpiece quality using a hobbing simulation, Procedia CIRP 41 (2016) 687–691, doi:10.1016/j.procir.2015.12.045.
[26] I. Ulacia, J. Larrañaga, A. Arana, A. Iñurritegui, J. Elizegi, Fatigue Life Prediction of Spherical Gear Couplings, in: American Gear Manufacturers Association Fall Technical Meeting 2018, Illinois, 2018, pp. 202–207.
[27] I.O.f. Standardization, ISO 4156: Straight cylindrical involute splines, 2005.
[28] J. Lange, How Are You Dealing with the Bias Error in Your Helical Gears? in: American Gear Manufacturers Association Fall Technical Meeting, 2008, pp. 227–240.
[29] O. Winkel, New Developments in Gear Hobbing, in: American Gear Manufacturers Association Fall Technical Meeting, 2009, pp. 43–60.
[30] V. Tran, R. Hsu, C. Tsay, Study on the anti-twist helical gear tooth flank with longitudinal tooth crowning, J. Mech. Des. 136 (6) (2014) 061007, doi:10.1115/1.4027166.
[31] LMT-Fette-Inc., Finish hobbing crowned helical gears without twist, Gear Technology February (2006) 12–13.
[32] American Gear Manufacturers Association, AGMA 945-1-b20: Splines design and application, 2020.
[33] R. Cedoz, M. Chaplin, Design guide for involute splines, Society of Automotive Engineers (1994).
[34] K. Nakashima, Teeth contact behaviour and load distribution of gear couplings, Trans. Jpn. Soc. Mech. Eng. 502 (Part C 54) (1988) 1302–1307, doi:10.1299/kikaic.54.1302.
[35] R. Beckmann, Beitrag Zur Auslegung Und Konstruktion Von Balligzahn-kupplungen, Ph.D. thesis, Chemmitz Technology University, 2005.
[36] F. Curà, A. Mura, Experimental and theoretical investigation about reaction moments in misaligned splined couplings, Mech Syst Signal Process 45 (2) (2014) 504–512, doi:10.1016/j.ymssp.2013.12.005.

Our greatest glory is not in never falling, but in rising every time we fall.
—Confucius

B | Publication II

Spherical gear coupling design space analysis for high misalignment applications

A. Iñurritegui[a], A. Arana[a], J. Larrañaga[a], I. Ulacia[a]

[a] *Mondragon Unibertsitatea, Department of Mechanical and Industrial Production, Arrasate-Mondragon, Pais Vasco, Spain.*

Received 3 January 2022; Revised 22 February 2022; Accepted 14 March 2022; Available online 2 April 2022; Version of Record 2 April 2022.

Mechanism and Machine Theory 173 (2022) 104837

Mechanism and Machine Theory 173 (2022) 104837

Contents lists available at ScienceDirect

Mechanism and Machine Theory

journal homepage: www.elsevier.com/locate/mechmt

Research paper

Spherical gear coupling design space analysis for high misalignment applications

Aurea Iñurritegui *, Aitor Arana, Jon Larrañaga, Ibai Ulacia

Mondragon Unibertsitatea, Department of Mechanical and Industrial Production, Arrasate-Mondragon, Pais Vasco, Spain

ARTICLE INFO

Keywords:
Spherical gear coupling
High misalignment
Main design parameter limits

ABSTRACT

Spherical gear couplings are machine elements that enable power transmission between highly misaligned shafts. The highly crowned tooth surfaces and the presence of undercut sections, have been a matter of disagreement between existing geometry generation methods available in the scientific literature. The main reason for this, are the geometry variations which arise in the generated parts, and consequently, the effect of such variations on the contact point location and clearance distribution. In this paper the influence of the main design parameters of spherical gear couplings (namely, the crowning ratio, the pitch diameter, the pressure angle, etc.), on the geometrical properties of the gear tooth surfaces are investigated. An algorithm to calculate the maximum misalignment angle is proposed, which is one of the most crucial design parameters. It shows that the values obtained with models existing in the literature are not applicable to highly crowned spherical gear couplings. Finally, design criteria are described to help the designer choose proper spherical gear coupling tooth geometry parameters to fit in a certain space and achieve a given maximum misalignment angle without further geometrical issues (undercut or pointed teeth).

1. Introduction

Gear couplings are widely used to transmit power between shafts due to their high power density compared to other non-splined connections and their capacity to accommodate axial, radial or angular misalignments [1]. Usually, they are employed in applications where, due to the working conditions, slight misalignment occurs between the axes [2] or manufacturing uncertainties exist [3]. In contrast, spherical gear couplings are specially designed to transmit power between highly misaligned shafts, $\gamma \in \mathbb{R} : 3° \leq \gamma \leq 10°$. They are composed of a highly crowned toothed hub (external part) and a commonly straight [4,5] sleeve (internal part), both of which have the same number of teeth, as it can be seen in Fig. 1.

Spherical gear couplings are used in heavy duty, high torque applications [6], such as in sheet metal rolling mills [7], where due to the small roller size, working conditions of up to 7° misalignment angle can be found [8]. In these applications, the large longitudinal crowning of spherical gear couplings enables a favorable contact pattern [6]. In addition, it balances the clearance between the tooth surfaces to prevent interference between the teeth [3].

To attain the tooth geometry which enables the described working kinematics, hubs are manufactured by hobbing. Generation by a disc is also mentioned in the literature [4,5], however this process is never used to generate sufficient crowning to withstand such high misalignment angles (above 3°). The tooth geometry of the gear coupling is obtained from the combination of the cutter tooth geometry and the kinematics of the machining process. Most of the mathematical approaches existing in the literature simplify the hobbing process, modeling only its central cutting edge [5,9–11]. However, these methods do not consider the threaded surface

* Corresponding author.
E-mail address: ainurritegui@mondragon.edu (A. Iñurritegui).

https://doi.org/10.1016/j.mechmachtheory.2022.104837
Received 3 January 2022; Received in revised form 22 February 2022; Accepted 14 March 2022
Available online 2 April 2022

Nomenclature

a_p	Parabola coefficient for profile crowning
b	Hub face width
$C_{h\beta}$	Amount of longitudinal crowning in the hub
$D_{\text{ext, h}}$	External diameter of the hob
h_{ha}	Hub addendum coefficient
h_{hf}	Hub dedendum coefficient
j	Clearance
k	Clearance factor
m_n	Normal module
N_w	Number of threads of the hob
r_c	Hub crowning radius
r_p	Hub pitch radius
$r_{p,w}$	Hob pitch radius
r_t	Hub tooth transverse crowning radius
r_β	Tool path radius
s_c	Sleeve space width
s_w	Hob displacement during hub generation
t_c	Hub tooth width
u	Profile surface parameter
v	Lead surface parameter
x_{sleeve}	Profile shift coefficient of the sleeve
z	Number of teeth of the hub
α	Pressure angle
γ	Misalignment angle
Δ_{hw}	Vertical displacement of the hob during generation
$\Delta\gamma$	Misalignment angle variation
ε	Crowning ratio
λ_{w}	Hob lead angle
μ	Angle along hob tool path
ρ_{hf}	Hub root radius coefficient
Σ_c	Rack-cutter tooth surface
Σ_h	Generated hub tooth surface
Σ_w	Generating hob-thread tooth surface
ϕ_w	Hob rotation during hub generation
ψ_h	Generation parameter of the hub
ψ_w	Generation parameter of the hob

of the hob (a set of cutting edges distributed along its thread) during the generation. Thus, even if they may be accurate enough for tooth geometries with small amounts of crowning, they present strong deviations when generating highly crowned spherical hub tooth surfaces, as shown by the authors in [12].

In accordance with design criteria and assuming that misalignment is an unavoidable condition, many studies have focused on different aspects of the operating conditions of gear couplings. Alfares et al. [3] showed that the main factors influencing the clearance distribution were the misalignment angle, the tooth surface longitudinal crowning, and the tooth angular position. Hong et al. [13] analyzed the effect of variable clearance distribution due to indexing errors, revealing that tighter manufacturing tolerances exhibit more favorable load sharing characteristics. From this and other similar studies, it has been shown that the contact position moves farther away from the middle section to the edge as misalignment increases, generating undesired load concentrations. For this reason, the main objective of the crowned surface is to prevent edge contact and to center the contact between the hub and the sleeve [3,14,15]. This is achieved by tooth surface geometry upgrades. For instance, early studies [14], propose the Vari-Crown geometry, which increases the contact area significantly, by means of a variable crowning radius along the face width, with the maximum radii being at the load angle. More recently, Guan et al. [15] introduced a novel crown gear coupling, which contains profile crowning in the teeth, together with longitudinal crowning, to center the point of contact. In fact, due to the issues caused by load concentrations in gear couplings, design standards, such as AGMA 945-1-B20 [16,17], limit the tooth surface geometry up to the point where undercutting sections exist [18]. Therefore, geometries with undercutting singularities are discarded in the design phase of spherical gear couplings.

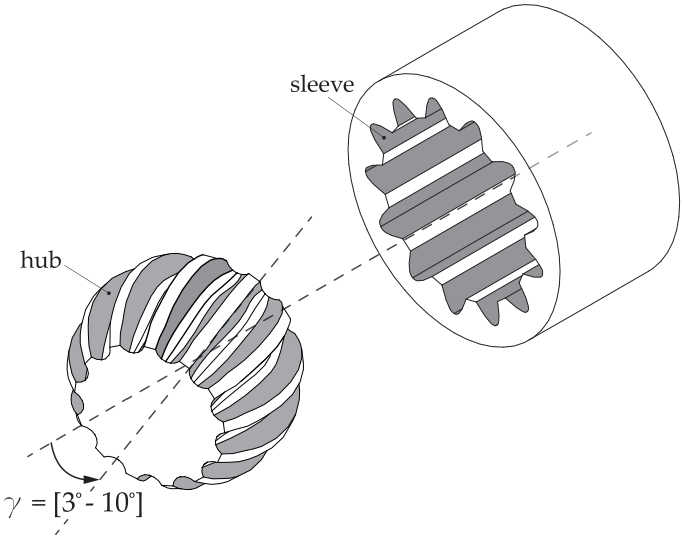

Fig. 1. Spherical gear coupling: highly crowned hub and straight sleeve.

Previous works have provided a great insight into the performance of gear couplings, however they have been mainly focused on small misalignment angles ($\gamma \ll 3°$). Very few papers can be found concerning high misalignment angle applications. Herbstritt and Paluh [19] correlated numerical models with experimental tests showing a considerable effect of the misalignment angle (3°) on tooth bending stresses. Moreover, Ulacia et al. [8] compared tooth root bending fatigue life of spherical couplings at 7° with the stress value obtained with a measured tooth geometry finite element model. All these works have shown the impact of the tooth geometry on tooth stresses and the life of gear couplings, however to the best of the authors knowledge, no design guidelines exist for high misalignment applications. Moreover, the existing standards, DIN 5466 [20], ISO 4156 [17], AGMA 6123-B06 [21] and AGMA 945-1-B20 [16] are mainly focused on small misalignments, and spherical gear couplings for high misalignment applications are referred to as special cases.

Therefore, this paper presents a comprehensive approach to determine the influence of the main design parameters of spherical gear couplings on the achievable misalignment angle, to help manufacturers and designers in a first approach of the design phase. To this end, the main goals of this research are:

(1) Propose an algorithm to determine the maximum misalignment angle in spherical gear couplings based on the generated geometry, and compare them with the results obtained with existing analytical methods from the literature.
(2) Apply the mathematical generation model of spherical gear couplings proposed in [12] to investigate the influence of the main design parameters on the hub tooth surface geometry and achievable maximum misalignment angle.
(3) Determine the preliminary design space which fulfills the required maximum misalignment angle and available space of the application. This will provide the designer with spherical gear coupling geometries, preventing as much as possible tooth surface geometry issues, such as undercutting or tip pointing.

2. Mathematical model to generate spherical hub tooth surfaces

The mathematical hobbing of spherical gear couplings manufacturing process is considered here. Throughout this process, the hob follows a circular feeding motion, where the center distance between the gear and the hob varies continuously. The maximum value of the center distance is equal to the sum of the gear couplings r_p and hobs r_h pitch radii (Fig. 2). The spherical hub tooth surfaces are generated considering the hob thread surface as a set of cutting edges acting at the same time during the generation process, as explained in [12]. Fig. 2 shows a schematic representation of the complete generation process, where the hob thread surface is determined prior to the generation of the hub with the hob.

The generating rack cutter profile is defined in coordinate system S_a as:

$$\mathbf{r}_a(u) = [u \quad 0 \quad 0 \quad 1]^T \tag{1}$$

where u is the surface parameter in the profile direction.

To prevent edge contact at the tips of the hub and sleeve teeth in presence of a high misalignment angle, profile crowning is required and $\mathbf{r}_a(u)$ vector is obtained as:

$$\mathbf{r}_a(u) = [u \quad a_p u^2 \quad 0 \quad 1]^T \tag{2}$$

where a_p is a parabola coefficient, and in this work takes a value of $a_p = 0.001$ mm^{-1}.

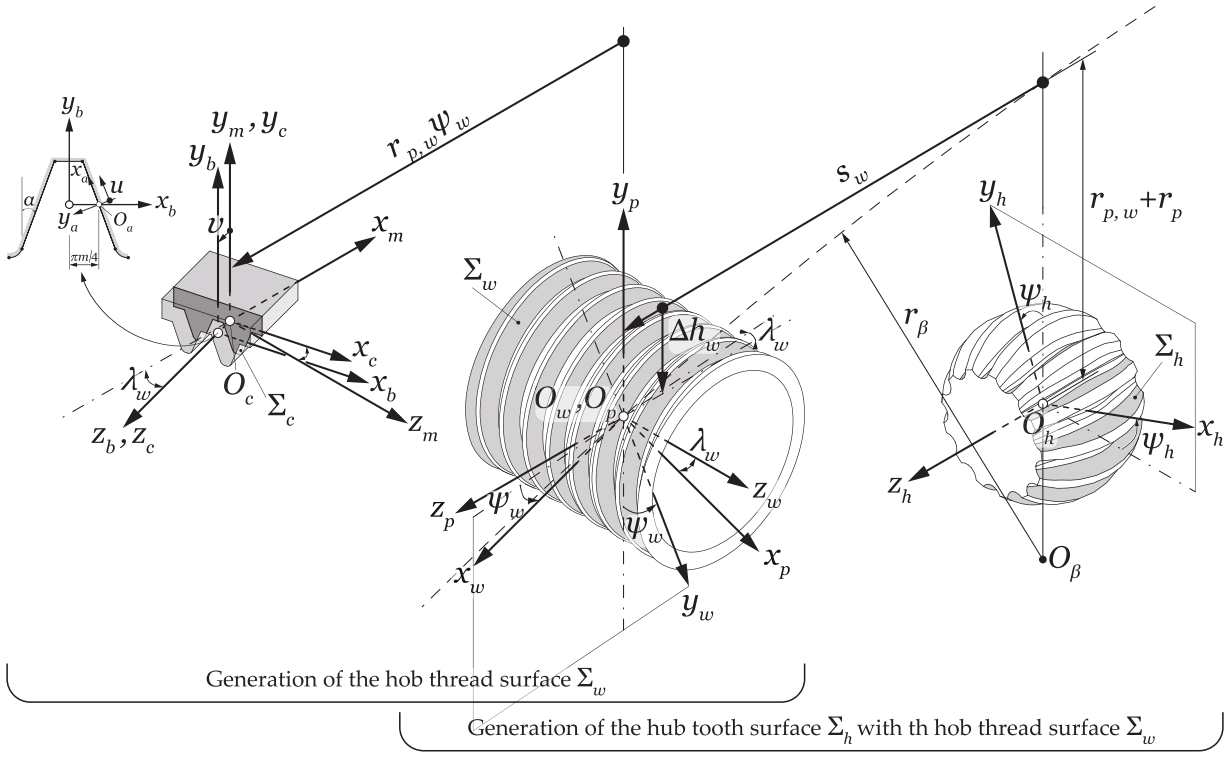

Fig. 2. Derivation of the hub tooth surface Σ_h, with the prior determination of the hob thread surface Σ_w.

Table 1
Hub tooth proportion coefficients in accordance with ISO 4156 [17] and Beckmann [22].

Parameter	Values			
Pressure angle, α	20°	30°	37.5°	45°
Addendum coeff., h_{ha}	0.50	0.50	0.45	0.40
Deddendum coeff., h_{hf}	0.90	0.90	0.70	0.60
Root radius coeff., ρ_{hf}	0.40	0.40	0.30	0.25

Table 2
Hob external diameter $D_{\text{ext,h}}$ definition in terms of the module in accordance with AGMA 1102-A03 [23].

m_n	0.5	1.0	1.5	2.0	3.0	4.0	5.0	6.0	8.0	10.0
$D_{\text{ext,h}}$	32	50	55	65	75	85	95	105	120	130

The rack cutter generating tooth surface Σ_c is represented in coordinate system S_c as:

$$\mathbf{r}_{\text{c}}(u,v) = \mathbf{M}_{\text{cb}}(v)\,\mathbf{M}_{\text{ba}}\,\mathbf{r}_{\text{a}}(u) \tag{3}$$

where matrix $\mathbf{M}_{\text{cb}}$ and $\mathbf{M}_{\text{ba}}$ are coordinate transformation matrix and v is the other surface parameter in the feed direction.

The rack cutter tooth proportions for gear couplings in this research are defined in accordance to the pressure angle value as shown in Table 1.

Coordinate transformation (4) from system S_c to system S_w and consideration of the meshing equation (5) allows the determination of the hob thread surface Σ_w from the rack-cutter tooth surface Σ_c:

$$\mathbf{r}_{\text{w}}(u,v,\psi_w) = \mathbf{M}_{\text{wm}}(\psi_w)\,\mathbf{M}_{\text{mc}}\,\mathbf{r}_{\text{c}}(u,v) \tag{4}$$

$$f_1(u,v,\psi_w) = \left(\frac{\partial \mathbf{r}_{\text{w}}}{\partial u} \times \frac{\partial \mathbf{r}_{\text{w}}}{\partial v}\right) \cdot \frac{\partial \mathbf{r}_{\text{w}}}{\partial \psi_w} = 0 \tag{5}$$

Here, ψ_w is the generation parameter for the hob thread surface and matrices $\mathbf{M}_{\text{wm}}$ and $\mathbf{M}_{\text{mc}}$ are the coordinate transformation matrix.

The external diameter $D_{\text{ext,h}}$ of the hob thread Σ_w is based on the geometry of the hub that will be generated. Standard AGMA 1102-A03 [23] defines the external diameter in terms of the generated hub geometry modulus as shown in Table 2. The rest of the tool parameters, such as, the lead angle are defined depending on it.

Coordinate transformation (6) from system S_w to system S_h and consideration of a double-enveloping process [24] with two independent parameters of generation ϕ_w and s_w (7), (8) enables to determine the hub tooth surface Σ_h by the rotation of the hob thread surface along a curved tool path:

$$\mathbf{r}_{\mathrm{h,a}}(u,v,\psi_w,s_w,\phi_w) = \mathbf{M}_{\mathrm{hp}}(s_w,\phi_w)\,\mathbf{M}_{\mathrm{pw}}\,\mathbf{r}_{\mathrm{w}}(u,v,\psi_w) \tag{6}$$

$$f_2(u,v,s_w,\phi_w) = \left(\frac{\partial \mathbf{r}_{\mathrm{h,a}}}{\partial u}\times\frac{\partial \mathbf{r}_{\mathrm{h,a}}}{\partial v}\right)\cdot\frac{\partial \mathbf{r}_{\mathrm{h,a}}}{\partial \phi_w} = 0 \tag{7}$$

$$f_3(u,v,s_w,\phi_w) = \left(\frac{\partial \mathbf{r}_{\mathrm{h,a}}}{\partial u}\times\frac{\partial \mathbf{r}_{\mathrm{h,a}}}{\partial v}\right)\cdot\frac{\partial \mathbf{r}_{\mathrm{h,a}}}{\partial s_w} = 0 \tag{8}$$

Here, $\mathbf{M}_{\mathrm{hp}}$ and $\mathbf{M}_{\mathrm{pw}}$ are given by:

$$\mathbf{M}_{\mathrm{hp}}\cdot\mathbf{M}_{\mathrm{pw}} = \begin{bmatrix} \cos\psi_h & \sin\psi_h & 0 & 0 \\ -\sin\psi_h & \cos\psi_h & 0 & r_{\mathrm{p,h}}+r_{\mathrm{p,w}}-\Delta h_w \\ 0 & 0 & 1 & s_w \\ 0 & 0 & 0 & 1 \end{bmatrix}\cdot\begin{bmatrix} \cos\psi_w\,\sin\lambda_w & -\sin\lambda_w\,\sin\psi_w & \cos\lambda_w & 0 \\ -\sin\psi_w & -\cos\psi_w & 0 & 0 \\ \cos\lambda_w\,\cos\psi_w & -\cos\lambda_w\,\sin\psi_w & -\sin\lambda_w & 0 \\ 0 & 0 & 0 & 1 \end{bmatrix} \tag{9}$$

where $r_{\mathrm{p,h}}$ is the hub pitch radius, $\psi_h = \phi_w\cdot\left(N_w/z\right)$ is the rotation of the hub during generation, and N_w and z represent the number of threads in the hob and the number of teeth in the hub respectively. $\Delta h_w = r_\beta - \sqrt{r_\beta^2 - s_w^2}$ determines the plunging of the hob when a circular tool path of radius r_β is applied. Indeed, Δh_w will vary depending on the tool path function used.

The simultaneous consideration of Eq. (6) and equations of meshing (5), (7), (8) enables the hub tooth surface to be generated from the rack cutter surface and hob tooth surface definition.

The generation of the fillet hub tooth surface $\Sigma_{\mathrm{h,f}}$ can be obtained following a similar approach to the one described along this section, but it is omitted here for the purpose of simplicity. Moreover, the sleeve generation model is based on involute tooth surfaces and point contact is assumed between hub and sleeve tooth surfaces, due to the double crowned tooth surfaces of the hub. The detailed information of the computerized generation of highly crowned spherical gear couplings and all the coordinate transformation matrix can be found in [12].

3. Determination of the maximum misalignment angle

3.1. Crowning radius r_c and misalignment angle γ relationship

It has been shown that most of the research in the literature is focused on small misalignment angles and that works referring to misalignment angles above 3° are rare. Moreover, Refs. [22,25,26] do mention the existence of gear couplings for larger misalignment angles, but recommend design guidelines only for $\gamma \leq 1.5°$. At the same time, they note that designs for misalignment angles above 1.5° are special cases, and deviate from the generalities discussed for small misalignment designs.

The amount of longitudinal crowning ($C_{h\beta}$) (Fig. 3(b)) is a key parameter to determine the maximum misalignment angle in several works [2,3,27]. However, it is not straightforward to obtain in highly crowned spherical hubs, due to the small tool path radius used in their manufacturing [12]. For this reason, a more suitable parameter related to the manufacturing process should be used to determine the maximum misalignment angle. A more appropriate parameter for this purpose is the crowning radius r_c. This is related to the generated hub geometry and the manufacturing tool path radius, as can be observed in Fig. 3(a). This figure also illustrates the relationship between the pitch radius r_p, the hob pitch radius $r_{p,w}$, crowning radius r_c, and tool path radius r_β, all defined in the pitch-plane of the hub. For a given hub and hob pitch radius, the tool path variation will require a direct change of the crowning radius r_c, and in consequence, in the amount of longitudinal crowning $C_{h\beta}$ generated. At the same time, $C_{h\beta}$ will involve a modification of the maximum attainable misalignment angle $\gamma_{\max}$.

Nevertheless, there are few references that analytically calculate the maximum misalignment angle of spherical gear couplings. This may be due to the predominant use of gear couplings in applications working at small misalignment angles, where the major objective of the crowned surface is the prevention of edge contact and the centering of the contact between the hub and the sleeve.

Among the equations found to define the maximum misalignment angle, those including mathematical simplifications related to small misalignment angles were disregarded [27]. Relevant equations for this analysis include equations that consider tooth design parameters, such as the crowning radius and the module and the clearance value, among others. Thus, the most relevant references that could be applied to high misalignment cases are Eqs. (10), (11) from Beckmann [22] and Guo et al. [2], respectively. It should also be noted that these equations were only used in small misalignments, below 1.5°. All in all, it can be observed that Eq. (10) is in terms of the clearance value between the hub and sleeve, while Eq. (11) does not consider it, and in contrast, includes among its variables the gear coupling face width b.

$$\gamma = \arccos\left(1 - \frac{2km_n\tan(\alpha)}{4r_c - \pi m_n tan(\alpha)}\right) \tag{10}$$

$$\gamma = \arcsin\left(b\frac{\tan(\alpha)}{2r_c}\right) \tag{11}$$

Moreover, a dimensionless parameter relating the generated geometry (r_p) with the hobbing process (r_c) (see Eq. (12)) is proposed in the literature [22,26]. This coefficient, named the crowning ratio ε, relates the gear coupling size (the pitch radius r_p) and the

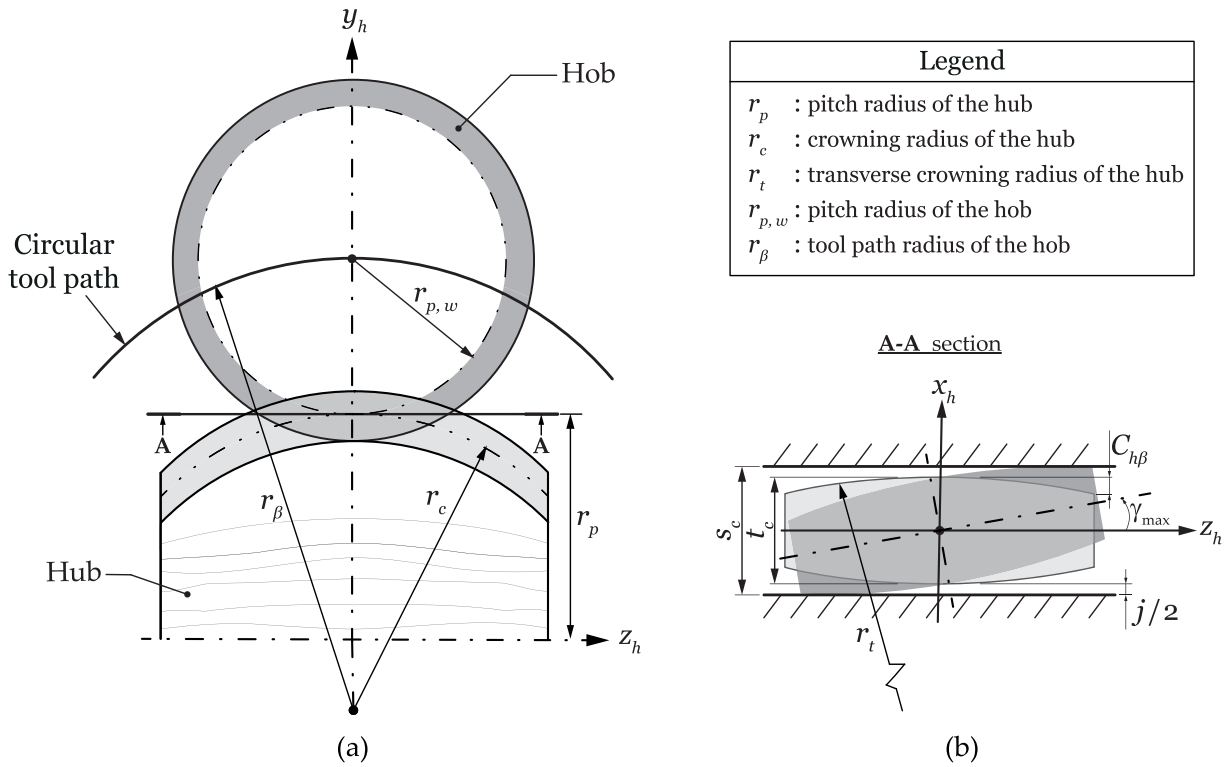

Fig. 3. (a) Definition of characteristic radii in highly crowned hub generation, and (b) pitch-plane of the hub teeth with relevant parameters for the definition of the maximum misalignment angle.

crowning radius r_c, and thus is employed in this work to generate equivalent/comparable geometries in terms of the size and amount of crowning.

$$\varepsilon = r_c / r_p \tag{12}$$

To calculate the maximum misalignment angle, a clearance value between the hub and sleeve has to be defined. This is defined following [22], and is proportional to the module as shown in Eq. (13).

$$j = k \cdot m_n \tag{13}$$

In this research, no profile shift coefficient is employed in the hub, to ensure that this parameter has no influence on the results. In contrast, to ensure the clearance value between the hub and the sleeve, the profile shift coefficient calculated with Eq. (14) is entirety applied to the sleeve.

$$x_{\text{sleeve}} = \frac{j/2}{m_n \sin(\alpha)} = \frac{k}{2\sin(\alpha)} \tag{14}$$

3.2. Algorithm to determine the maximum misalignment angle $\gamma_{\max}$

To define the maximum applicable misalignment angle of the generated hub, Fig. 4(a) depicts a fixed coordinate system S_f where the hub and sleeve tooth surface models are assembled. The system S_h is rigidly connected to the hub and mounted in the system S_f, enabling a misalignment angle around the axis y_f, which coincides with the axis y_h. Both models are held at rest without load and no rotation is imposed on either of them. The standard AGMA 6123-B06 [21] and Guo et al. [2] use the jam angle to determine the geometrical maximum misalignment angle. This is defined as, the angle at which both sides of the hub tooth surfaces contact the sleeve and, therefore, the component becomes blocked. This can be observed in Fig. 3(b), where the maximum misalignment angle is defined in such an angle where contact exists in both sides of the hub tooth surfaces. Thus, a designer must ensure that the jam angle is greater or equal to the misalignment expected during operation. To determine the maximum misalignment angle, a clockwise and counterclockwise angle is applied to consider tooth geometry variations [12] which can occur due to the lead angle (twist effect) [28].

The following algorithm, divided into 5 steps, is applied to determine the contact point between the pair of teeth located in the tilting position (Fig. 4(b)) and deduce the maximum misalignment angle of the spherical gear coupling. The tooth in the tilting position is considered to be critical, as it is the first which comes into contact [3,12,22].

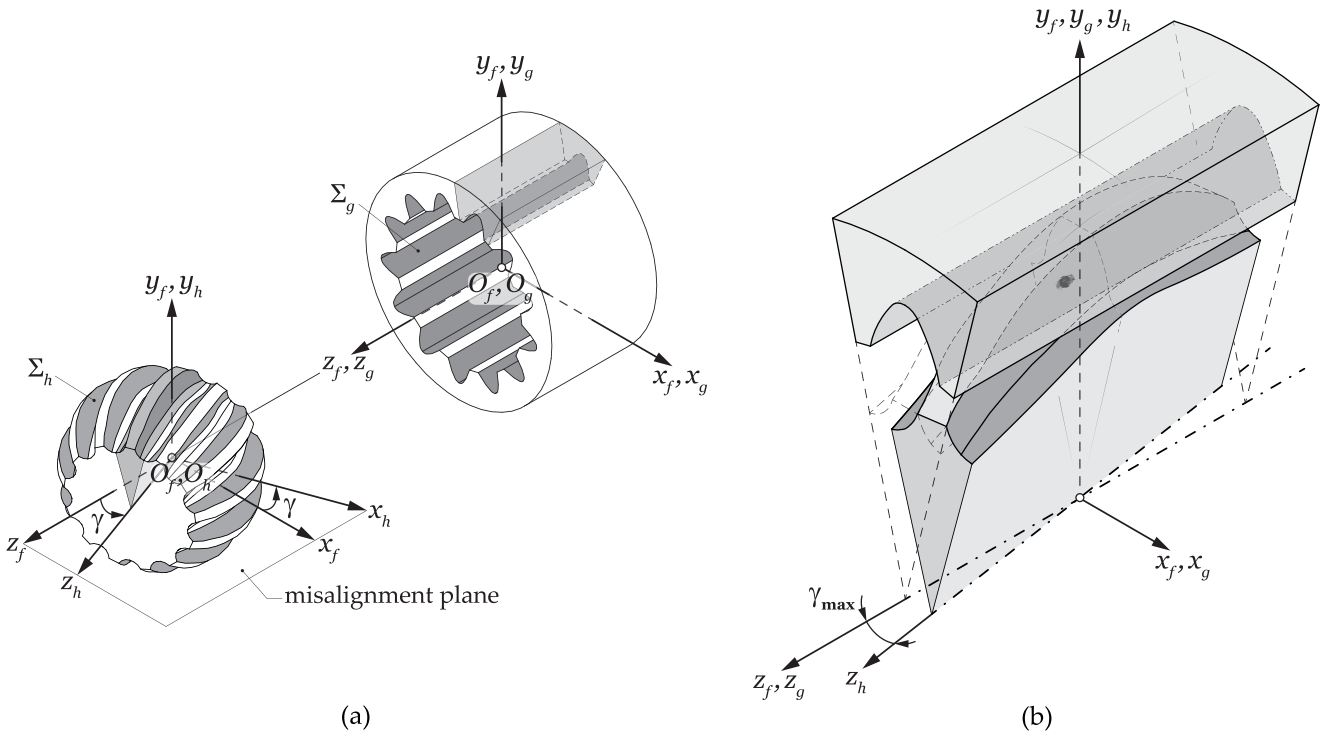

Fig. 4. Maximum misalignment angle determination: (a) Coordinate systems for the positioning of the gear coupling with shaft misalignment γ, and (b) simplification of the teeth and contact in pure tilting position at 0°.

Step 1 The tooth of the hub whose symmetry axis is perpendicular to the misalignment plane, in the tilting position, is selected. A counter-clockwise rotation of the hub is considered to find the misalignment angle γ. Assuming, for the purpose of simplicity, that (u_h, v_h) are the surface parameters of surface Σ_h, the following coordinate transformation (15) allows the surface Σ_h to be represented in the system S_f:

$$\mathbf{r}_f^{(hub)}(u_h, v_h, \gamma) = \mathbf{M}_{fh}\mathbf{r}_h(u_h, v_h) \tag{15}$$

Here, $\mathbf{M}_{fh}$ is given by:

$$\mathbf{M}_{fh} = \begin{bmatrix} \cos\gamma & 0 & \pm\sin\gamma & 0 \\ 0 & 1 & 0 & 0 \\ \mp\sin\gamma & 0 & \cos\gamma & 0 \\ 0 & 0 & 0 & 1 \end{bmatrix} \tag{16}$$

where γ is the angle of misalignment and the upper and lower signs are applied to a clockwise and a counterclockwise rotation, respectively. The variables (u_h, v_h, γ) are the unknowns for the sought-for contact point.

Step 2 The unit normal to surface Σ_h at the sought-for contact point can be obtained in the system S_f as:

$$\mathbf{n}_f^{(hub)}(u_h, v_h, \gamma) = \mathbf{L}_{fh}\frac{\dfrac{\partial \mathbf{r}_h}{\partial u_h} \times \dfrac{\partial \mathbf{r}_h}{\partial v_h}}{\left|\dfrac{\partial \mathbf{r}_h}{\partial u_h} \times \dfrac{\partial \mathbf{r}_h}{\partial v_h}\right|} \tag{17}$$

where the matrix $\mathbf{L}_{fh}$ is of 3×3 order and can be determined from the matrix $\mathbf{M}_{fh}$ by removing the last row and the last column.

Step 3 The tooth surface of the sleeve Σ_g comes into contact with the surface Σ_h, defined by surface parameters (u_g, v_g), for the purpose of simplicity. As the sleeve is held at rest, surface Σ_g is represented in the system S_f as:

$$\mathbf{r}_f^{(sleeve)}(u_g, v_g) = \mathbf{r}_g(u_g, v_g) \tag{18}$$

where (u_g, v_g) are the unknowns of the sought-for contact point.

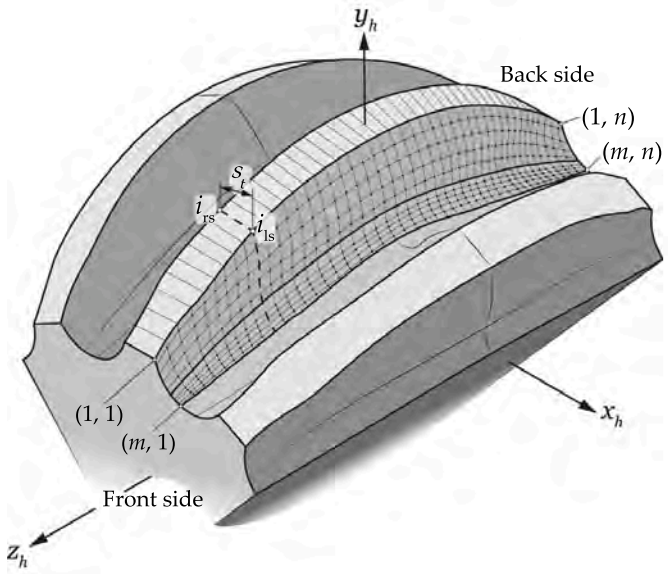

Fig. 5. Determination of the tip width s_t.

In the same way, the unit normal to surface Σ_g at the sought-for contact point is obtained in the system S_f as:

$$\mathbf{n}_f^{(sleeve)}(u_g, v_g) = \frac{\dfrac{\partial \mathbf{r}_g}{\partial u_g} \times \dfrac{\partial \mathbf{r}_g}{\partial v_g}}{\left| \dfrac{\partial \mathbf{r}_g}{\partial u_g} \times \dfrac{\partial \mathbf{r}_g}{\partial v_g} \right|} \tag{19}$$

Step 4 A system of five independent scalar equations with the unknowns $\{u_h, v_h, \gamma, u_g, v_g\}$ is defined as:

$$\mathbf{r}_f^{(hub)}(u_h, v_h, \gamma) = \mathbf{r}_f^{(sleeve)}(u_g, v_g) \tag{20}$$

$$\mathbf{n}_f^{(hub)}(u_h, v_h, \gamma) = \mathbf{n}_f^{(sleeve)}(u_g, v_g) \tag{21}$$

In fact, Eq. (21) represents only two independent scalar equations since $|\mathbf{n}_f^{(hub)}| = |\mathbf{n}_f^{(sleeve)}| = 1$.

Step 5 Steps 1 to 4 are repeated for a clockwise rotation. That way, the geometry deviations related to the twist-effect are also considered [12,28]. The smallest value of both is established to be the maximum misalignment angle of the gear coupling.

4. Conditions of existence for spherical gear couplings working in high misalignment applications

In the following subsections, three tooth surface geometry existence conditions are presented to evaluate the quality of the generated hub tooth surfaces. The first two, pointed teeth and undercut, are commonly used for gears and are taken into account in gear coupling standards [16,17] while the third, is a new parameter proposed for highly crowned spherical gear couplings.

4.1. Pointed teeth

Fig. 5 shows the definition of the tip width (s_t) of the spherical hub tooth surfaces, where the tooth flanks are discretized into $m \times n$ points. m represents the number of points across the tooth profile direction and n the number of points along the face width direction of the hub flank. As shown in Fig. 5, a point in the addendum edge and the front side of the tooth is defined as $(1, 1)$ and a point at the root and back side is defined as (m, n).

For spherical crowned hubs, apart from the geometry parameters (d_p, α, etc.) of the generated hub, the crowning radius plays a significant role in the tip width (Fig. 6(a)). Similar to the general rule specified for cylindrical gears, ISO 4156 [17] states the following Eq. (22) for the tip thickness limit.

$$s_{t,n} \geq 0.25 \cdot m_n \tag{22}$$

Tip width $s_{t,n}$ refers to the distance between right side i_{rs} and left side i_{ls} top points of each n section, which can be represented as:

$$s_{t,n} = \sqrt{(x_{i,rs} - x_{i,ls})^2 + (y_{i,rs} - y_{i,ls})^2 + (z_{i,rs} - z_{i,ls})^2} \tag{23}$$

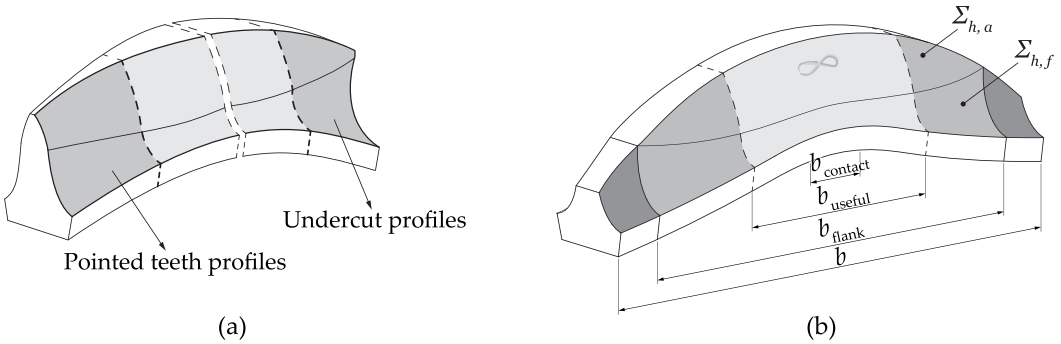

Fig. 6. Hub geometry characteristics: (a) undercut and pointed teeth profiles, and (b) gear coupling face width b, active profile length b_{flank}, length of no undercutting or pointed teeth flank b_{useful}, and contact length b_{contact} definitions.

where $(x_{i,\text{rs}}, y_{i,\text{rs}}, z_{i,\text{rs}})$ and $(x_{i,\text{ls}}, y_{i,\text{ls}}, z_{i,\text{ls}})$ denote the coordinates of points i_{rs} and i_{ls} in the fixed coordinate system S_f. The range for index i goes from 1 to n. The right and left side profiles are limited to the positive and negative side of the S_h coordinate system, respectively, to prevent crossover.

4.2. Undercut profiles

Using the algorithm described in [12] the undercutting and only-fillet regions can be detected and the length of the face width at which they appear can be determined. Indeed, when tangency no longer exists between the active profile $\Sigma_{h,a}$ and the fillet $\Sigma_{h,f}$, a singularity occurs and the profiles are undercut (Fig. 6(a)).

4.3. Useful flank

The relative slenderness of the gear coupling is called the aspect ratio. It is a dimensionless coefficient which relates the face width b and the pitch diameter d_p of the gear coupling; that is to say, the stiffness of the teeth of the hub. For this reason, in the gear coupling standard DIN 5466 [20] it is used for the calculation of the bending moment, torsional moment, and surface maximum pressure, among other strength parameters.

However, for highly crowned spherical hubs, the length of the hub b is not equivalent to the length of the active profile b_{flank} as shown in Fig. 6(b). Indeed, sections with only-fillet profiles might occur as was presented in [12]. Moreover, AGMA 945-1-B20 [16] defines the concept of the axial engagement length, referring to the b_{contact} in Fig. 6(b), and recommends this distance to be as great as possible to reduce contact, shear and bending stresses. Thus, in this study, with the purpose of comparing different geometries and determining whether they are geometrically more appropriate to withstand a given misalignment, two dimensionless parameters are defined:

- The flank ratio: b_{flank}/d_p
- The useful flank ratio: b_{useful}/d_p

The lengths are indicated in Fig. 6(b), where b_{flank} corresponds to the length of the face width containing an active profile, and b_{useful} to the length of the active profile without undercut or pointed teeth.

Between two equivalent geometries, that with the largest value of useful flank ratio should be chosen, as it will provide better contact surface and stiffness to the gear coupling. In the same way, a hub with the same aspect ratio, flank ratio and useful flank ratio that fulfills the design criteria will be the ideal geometry for the target application.

5. Definition of the cases of study

In this study two types of analysis were done: (a) a comparison of the method to calculate the misalignment angle with scientific literature models, and (b) influence of geometry variables.

5.1. Comparison with the scientific literature models

To analyze how maximum misalignment angle is determined in the scientific literature and compare it with the model proposed here, four gear coupling geometries from the literature (**L**) and four representative case studies (**CS**) were defined as shown in Table 3. This table contains all the design characteristics, along with the maximum misalignment angle for which the different literature models (**L**) were analyzed in the literature, and the maximum misalignment angle of the proposed case studies (**CS**), calculated with the model in Section 2.

Table 3
Gear coupling geometry parameters for misalignment angle comparison.

Parameter	L1	L2	L3	L4	CS1	CS2	CS3	CS4
d_p [mm]	75	79	1016	120	99	51	99	51
m_n [mm]	2.50	3.175	10.16	3	3	3	3	3
z [–]	30	25	100	40	33	17	33	17
α [°]	20	30	20	20	30	30	30	30
b/d_p	0.367	0.625	0.125	0.150	0.30	0.30	0.30	0.30
j [mm]	0.50	0.62	0.64	0.71	0.71	0.71	0.71	0.71
ϵ [–]	∞	62.99	3.94	1.67	1.00	1.00	0.40	0.40
γ_{max} [°]	0.20	0.06	0.80	0.80	4.50	4.75	2.94	7.90
Tool path shape	Circular							
$D_{ext,h}$ [mm]	$f(m_n)$ acc. to AGMA 1102-A03 [23] (Table 2)							

On the one hand, the literature models (**L**) chosen are considered as references that have recently worked in misaligned crowned gear couplings. The first is a straight gear hub **L1** defined by Xiao et al. 2022 [29], while the rest are geometries with larger crowning ratios: **L2** by Hong et al. 2015 [30], **L3** by Guo et al. 2016 [2] and **L4** from Guan et al. 2021 [31]. It should be pointed out that **L1** is a straight gear coupling which consequently will exhibit edge contact when misalignment is present, unlike the rest of the cases analyzed here.

On the other hand, the case studies (**CS**) were chosen to clearly show the differences between Eqs. (10), (11) and the proposed model, considering the influence of the crowning ratio and the size. **CS1** and **CS2** represent relatively high crowning ratio geometries in the context of the present study, but low within the scientific literature. In contrast, **CS3** and **CS4** are highly crowned hubs (small crowning ratio). Moreover, **CS2** and **CS4** refer to small pitch diameter gear couplings, while **CS1** and **CS3** represent big diameters. Thus, these four cases are selected to showcase the influence of the crowning ratio on the calculated misalignment angle.

5.2. Definition of reference geometries and variables considered

The investigation was carried out on the basis of a reference hub geometry, which was chosen as a representative case for the scope of this research: small and highly crowned geometry suitable for a high misalignment angle application. In this study, a total of 11,480 geometries were generated.

The range of values selected together with the reference value for each design variable were determined in regards to the following considerations and are shown in Table 4 (underlined values correspond to the reference values):

- Number of teeth, z or associated module, m_n.
  No reference value was selected.
  Range: 0.5–10, taken from the standard ISO 4156 [17], where a minimum of 6 teeth and a maximum of 100 is recommended.
- Crowning ratio, ϵ.
  No reference value was selected.
  Range: $\epsilon \leq 1.0$, as they are special cases in the existing literature [22,25], and have not been previously studied. In this analysis crowning ratios below this limit were chosen, with the minimum mathematical limit of $\epsilon = 0.4$.
- Pressure angle, α.
  Reference value: 30°, because it is the most used in gear coupling applications [16,20,22].
  Range: defined from the standard ISO 4156 [17], and additionally a 20° pressure angle was considered, as it is a reference in load capacity calculations of gears and is also one of the most used in gear couplings [22].
- Aspect ratio, b/d_p.
  Reference value: 0.30, as it is suggested for gear couplings working in high misalignment angle applications in the specialized literature [22,32,33].
  Range: selected in accordance to literature recommendations: $b/d_p = 0.15$, for the purpose of comparison; $b/d_p = 0.60$, reference value for the standard DIN 5466 [20]; and, $b/d_p = 0.90$, since it is recommended that the length must be less than the gear pitch diameter to prevent torsional twist concentrations in external gears [34].
- Pitch diameter, d_p.
  Reference value: 50 mm, for being an appropriate size for the current analysis.
  Range: 36–400 mm, so that a wide range of sizes is covered, and general conclusions can be drawn.
- Clearance factor, k
  Reference value: 0.07, since it is the highest value from the range recommended [22], and a bigger clearance will enable a higher misalignment angle.
  Range: 0.04–0.08, to analyze a wider range than the one recommended in literature [22], which at the same time, gives no guidelines to choose an appropriate value.

Table 4
Definition of the design variables for the research case studies.

Parameter	Values considered
m_n [mm]	0.5, 1.0, 1.5, 2.0, 3.0, 4.0, 5.0, 6.0, 8.0, 10.0
ε [–]	0.4, 0.5, 0.6, 0.7, 0.8, 0.9, 1.0
α [°]	20, 30, 37.5, 45
b/d_p [–]	0.15, 0.30, 0.60, 0.90
d_p [mm]	36, 50, 100, 200, 400
k [–]	0.04, 0.05, 0.06, 0.07, 0.08

Additionally, to generate these geometries a circular tool path was used, as it is the most commonly used in gear couplings [5, 11,27]. Here, the tool path radius r_β was defined based on the crowning ratio ε, the pitch radius r_p and the hob pitch radius r_{pw} (see Fig. 3(a)), as:

$$r_\beta = \varepsilon \cdot r_p + r_{pw} \tag{24}$$

In all the cases, a spherical gear blank was employed to generate the different geometries, with an external radius equivalent to the tip radius of the hub. This geometry was selected to prevent interference in misaligned applications when rotating relative to the pivoting position of the gear coupling [35].

6. Results

The geometries were generated following the model described in Section 2. The geometrical properties were verified according to the conditions of existence in Section 4, and the achievable maximum misalignment was calculated with the proposed algorithm in Section 3.2.

In the following sections the effect of the design parameters on the maximum misalignment angle and geometry characteristics is analyzed.

6.1. Maximum misalignment angle: literature comparison

First, the misalignment value obtained with Eqs. (10), (11) from the literature was compared with the model proposed in Section 3.2. To this end, the equations were applied to gear coupling geometries from the literature (**L**) and some representative case studies (**CS**) to determine the maximum misalignment angle. All the geometry properties are summarized in Table 3.

Fig. 7 shows the results of the models ordered from the highest to the lowest crowning ratio value ε, together with the geometry generated by the model summarized in Section 2.

The straight gear coupling **L1** has the highest ε value, with an infinite crowning radius. It can be seen that there is disparity between the results obtained with the different equations. Indeed, due to the infinite value of the crowning radius r_c, the equations give a null misalignment angle. By contrast, the proposed model gives a $\gamma \approx 0.2°$ due to the consideration of the tooth geometry and the existing clearance in the gear coupling. Even though, this would not be an appropriate working angle due to the stress concentration resulting from edge contact [29]. Thus, it can be said that the equations are not suitable to analyze straight gear couplings with an infinite crowning radius r_c.

In the case of **L2**, **L3** and **L4** geometries, all equations present similar results. These geometries have a high value crowning radius r_c, and thus a small amount of longitudinal crowning $C_{h\beta}$. Moreover, it can be seen that the pitch diameter does not have a significant effect on the results for cases **L2** and **L3**. However, differences can be perceived with Eq. (11) in **L4**, which is a relatively small gear coupling with a low crowning ratio.

This observation is reinforced by the results obtained with **CS1** and **CS2**, where it can be seen that for relatively small pitch diameters and $\varepsilon = 1.0$ the values obtained with Eq. (11) differ to a greater extent.

The lowest ε value in this analysis corresponds to the case studies **CS3** and **CS4**, where deviations are more noticeable. Differences with Eq. (11) are even greater than for the previous cases, due to the lower crowning ratios. Indeed, a lower crowning ratio ε means a smaller crowning radius r_c and thus, a higher amount of crowning $C_{h\beta}$.

The figure clearly shows that Eq. (10), gives similar results to the proposed model for the literature cases (**L1**, **L2**, **L3**, **L4**) and the case studies with a high crowning ratio (**CS1**, **CS2**). However, for the case studies with a smaller crowning ratio (**CS3**, **CS4**) differences increase. The deviations are particularly visible in **CS3**, where due to the bigger pitch diameter, the face width of the hub is increased to keep a constant aspect ratio. This feature causes the maximum misalignment angle to decrease, which is not considered in Eq. (10).

Hence, it is shown that either the crowning ratio or the pitch diameter have an impact on the calculated misalignment angle value. This demonstrates the need for a more in-depth analysis to determine the influence of gear coupling design variables, which is developed in the subsequent sections.

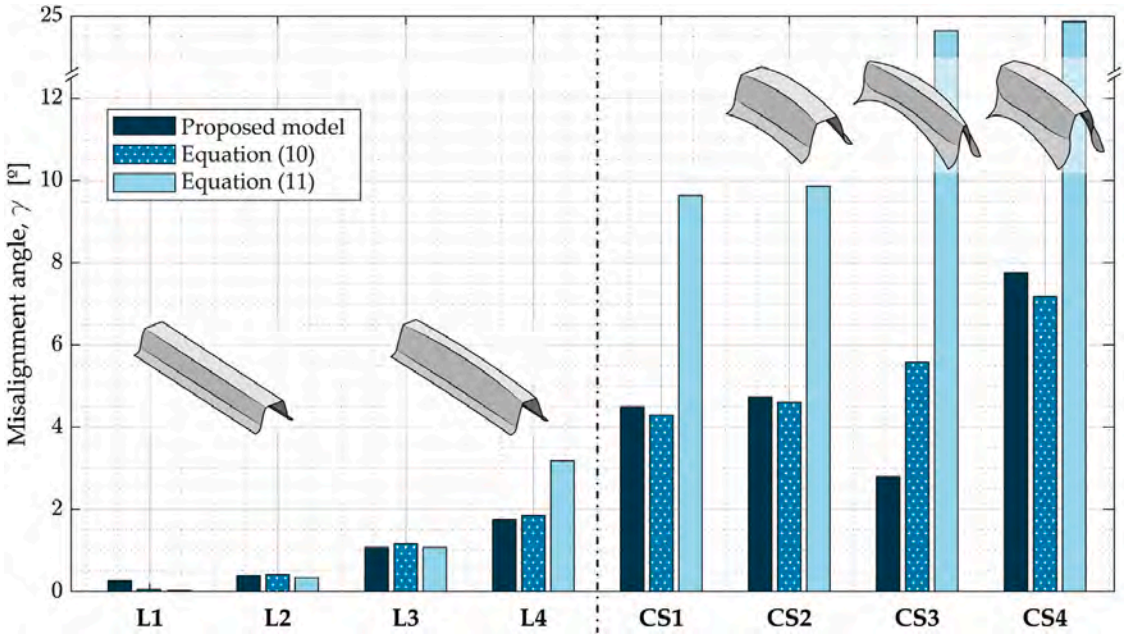

Fig. 7. Maximum misalignment angle calculated according to the literature and the proposed model applied to the geometries defined in Table 3.

6.2. *Influence of the module and the number of teeth*

To analyze the influence of the design variables in terms of the number of teeth z and the crowning ratio ε, every geometry for each number of teeth and crowning ratio was generated for the corresponding pitch diameter.

In this case the analyzed geometries were generated with the following parameters:

- Constant parameters: $d_p = 50$ mm, $\alpha = 30°$, $b/d_p = 0.3$, and $k = 0.07$.
- Variable parameters: m_n and ε.

Fig. 8 shows the maximum misalignment angle achieved with each of the hub geometries generated according to Table 4. Black markers in Fig. 8, illustrate the geometries obtained with the reference value of $\varepsilon = 0.4$, while the rest of the points with a constant number of teeth represent the geometries generated with the same parameters, but a different crowning ratio value.

It can be seen that the maximum misalignment angle decreases for a constant pitch diameter as the number of teeth increases (or module decreases), regardless of the crowning ratio. However, the crowning ratio has a higher influence on geometries with low numbers of teeth. The maximum misalignment angle ($\gamma_{max} = 11.5°$) may be reached with a $z = 6$ and $\varepsilon = 0.4$ hub geometry. Moreover, the maximum variation observed due to the change in the number of teeth is of $\Delta\gamma = 9.19°$, which corresponds to an effect of 79.91%.

Moreover, the figure shows two areas, corresponding to the geometries that do and do not verify the conditions of existence, proposed in Section 4. Each region is delimited by a convex hull, which refers to the smallest convex polygon that includes all the points in a 2D space. Here, this is determined by Andrew's monotone chain convex hull algorithm [36].

A representative hub tooth geometry corresponding to each of the zones can be seen on the right side of Fig. 8. The zone that fulfills the conditions of existence (so-called *Verified*) covers the lower part of the graph (striped zone), where the smallest misalignment angles are achieved. The hub geometries in this zone do not have any undercut sections nor pointed teeth issues. It should also be noted that this area can be further extended to lower misalignment values with higher crowning ratios ($\varepsilon > 1.0$), however these common geometries are out of the scope of this research.

On the left of the figure, where the highest misalignment angles are achieved, undercut sections (▲) prevail. Moreover, if a misalignment angle above 6° is required, undercut sections will be unavoidable, and thus it is necessary to generate and control the geometry of the undercut sections properly by using the tooth generation procedure described in [12].

Concerning the pointed teeth zone (■), the figure shows that it appears in geometries with higher numbers of teeth. It can also be found, in small numbers of teeth for very high misalignment angles, which require large longitudinal crowning.

Finally, with regard to the useful flank, Fig. 8 depicts the limit (straight and thick line) at which the useful flank length is smaller than the flank length (which is equal to the face width of the hub). This limit coincides with the lower limit at which undercut and pointed teeth start, confirming that the geometries inside the *Verified* region are the most appropriate from the point of view of stiffness or larger contact surface (the aspect ratio is equivalent to the useful flank ratio). Indeed, once the hub geometry presents singularities, the length of the useful profile b_{useful} starts to decrease. In cases with a large number of teeth, the limiting line that defines the misalignment angle from which the flank length is smaller than the face width hub ($b_{flank} < b$) is denoted with a dashed and dotted line. The geometries above this boundary are the ones with the smallest useful flank ratios.

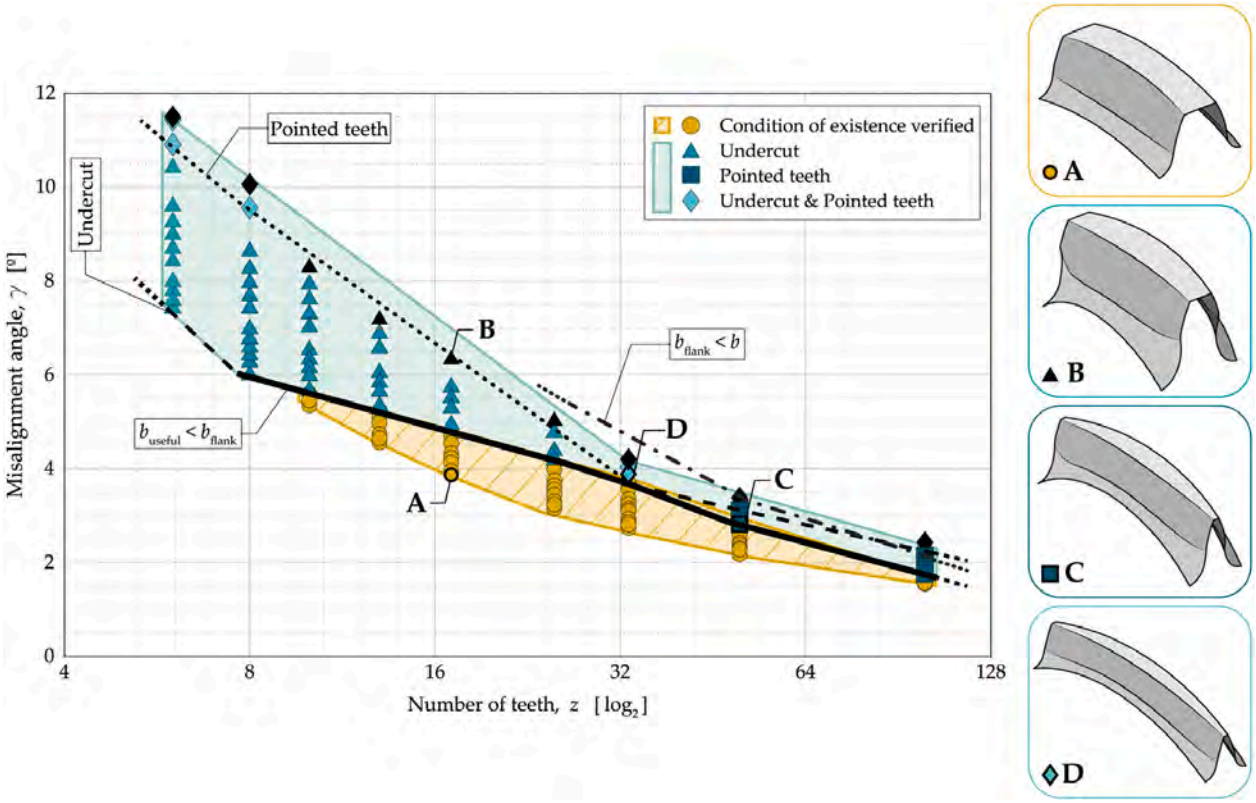

Fig. 8. Maximum misalignment angle for $d_p = 50$ mm, $\alpha = 30°$, and $b/d_p = 0.3$ geometries (black symbols for $\varepsilon = 0.4$) and geometrical boundaries in terms of the number of teeth z: Dashed line (– –) for undercut, dotted line (· ·) for pointed teeth, and dashed and dotted line (– ·) for flank length shorter than the face width.

6.3. *Influence of the crowning ratio* ε

The geometries analyzed herein were generated with the same parameters from the precedent section:

- Constant parameters: $d_p = 50$ mm, $\alpha = 30°$, $b/d_p = 0.3$, and $k = 0.07$.
- Variable parameters: m_n and ε.

Related to the results presented above, Fig. 9 shows the influence of the crowning ratio on the maximum misalignment angle. In addition to the maximum misalignment angle represented with the contour plot, the hub geometries in each zone of the figure are also displayed to graphically illustrate the influence of the design variables on the generated tooth geometry.

It can be seen that as the number of teeth and the crowning ratio increases, the maximum misalignment angle decreases. Even if a decrease of the crowning ratio presents a direct increase of the misalignment angle, it will not increase with the same amount for all geometries. Moreover, the misalignment angle evolution decreases as the number of teeth increases, for the same crowning ratio variation. For instance, a decrease from $\varepsilon = 1.0$ (geometry **E**) to $\varepsilon = 0.4$ (geometry **F**) of two geometries with $z = 6$, results in an increase of the maximum misalignment angle of $\Delta\gamma = 4.03°$. However, for the same pitch diameter in two geometries with $z = 100$ (**G** and **H**), the same crowning ratio variation ($\Delta\varepsilon = 0.6$) only produces an increase of the misalignment angle of $\Delta\gamma = 0.86°$. The maximum variation observed due to the change in the crowning ratio is of $\Delta\gamma = 4.03°$, which corresponds to an effect of 35.04%.

The conditions of existence are represented in Fig. 9 with the undercut boundary as a dashed line, and the pointed teeth boundary as a dotted line. The small number of teeth (high module) geometries are more likely to have undercutting sections, while geometries with a higher number of teeth (small module) present pointed teeth. This result is consistent with the gear literature [37]. Furthermore, these results clearly show that to achieve a high misalignment angle the presence of undercut is mandatory.

Concerning the flank length, the geometries inside the non-shaded region (e.g. geometries **A** and **G**) contain hubs with a useful flank b_{useful} equivalent to the flank length b_{flank} and face width b of the hub. Below this boundary, the useful flank is shorter than the flank length. For smaller crowning ratios and at high numbers of teeth, with a dashed and dotted line, the flank length is shorter than the face width (e.g. geometry **H**), thus more flexible geometries are obtained.

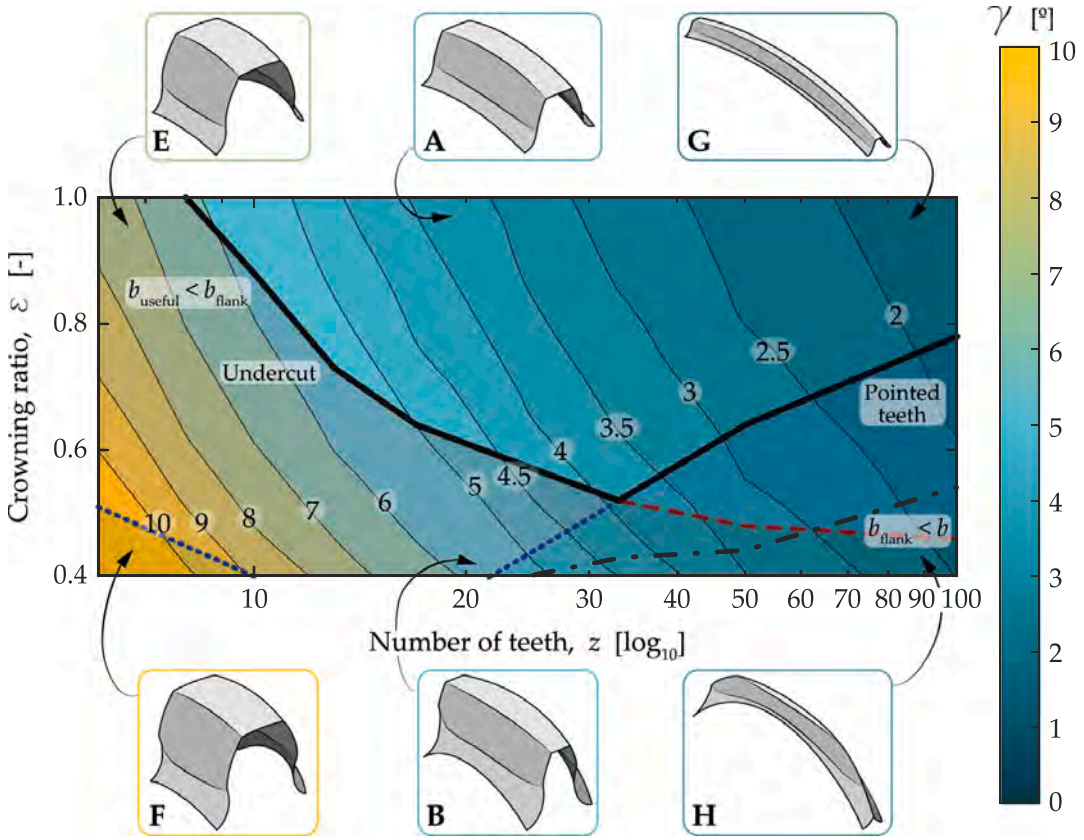

Fig. 9. Maximum misalignment angle in terms of the crowning ratio and the number of teeth for $d_p = 50$ mm, $\alpha = 30°$, and $b/d_p = 0.3$ geometries. Dashed line (– –) represent the undercut condition, while the dotted line (· ·) the pointed teeth, and the dashed and dotted line (– ·) the limit where the flank length is shorter than the face width.

6.4. *Influence of the pressure angle α*

Here, geometries were generated with the corresponding parameters:

- Constant parameters: $d_p = 50$ mm, $b/d_p = 0.3$, and $k = 0.07$.
- Variable parameters: α, m_n and ε.

Fig. 10 depicts the influence of the pressure angle on the maximum misalignment angle. The four graphs in the figure represent the maximum misalignment angle for each pressure angle in terms of the number of teeth, and a representation of $\mathbf{B}_x$ geometry is also depicted.

Fig. 10 shows a decrease of the maximum misalignment angle as the number of teeth increases, regardless of the pressure angle. Moreover, it can be observed that for the same geometry with the same parameters, the achievable maximum misalignment angle increases as the pressure angle increases. For instance, geometry $\mathbf{B_{20}}$ attains a maximum misalignment of $\gamma = 4.95°$ for $\alpha = 20°$, while it increases up to $\gamma = 8.78°$ in geometry $\mathbf{B_{45}}$ for $\alpha = 45°$. Furthermore, the influence of the number of teeth increases as the pressure angle increases; i.e. for a geometry of $\alpha = 20°$ and $\varepsilon = 0.4$, a change of the number of teeth can vary the maximum misalignment angle as much as $\Delta\gamma = 5.84°$, whereas for a $\alpha = 45°$ and $\varepsilon = 0.4$, it may vary up to $\Delta\gamma = 15.53°$. The maximum misalignment angle ($\gamma_{\max} = 20.36°$) may be reached with a $z = 6$ and $\alpha = 45°$ hub geometry. Moreover, the maximum variation observed due to the change in the pressure angle is of $\Delta\gamma = 12.56°$, which corresponds to an effect of 61.69%.

Concerning the conditions of existence, the results show that as the pressure angle increases the pointed teeth region increases, while the undercutting region is reduced to small number of teeth geometries.

It should also be noted, that if very high misalignment angles need to be achieved undercutting is necessary, for all pressure angles. Nevertheless, for high misalignment angles between 3–10° it can be seen that geometries with low numbers of teeth and a large pressure angle (37.5° or 45°) can prevent undercut sections.

Fig. 11 illustrates the useful flank, undercut and pointed teeth limits in terms of the crowning ratio and number of teeth. Fig. 11(a) shows how the useful flank region increases towards the bottom left corner, as the pressure angle increases, making it clear that a higher pressure angle with low number of teeth provide a more suitable gear hub from the geometrical point of view. Fig. 11(b) and (c) present similar trends: the undercut region is reduced when the pressure angle increases, and at the same time, the pointed teeth area is enlarged when the pressure angle increases.

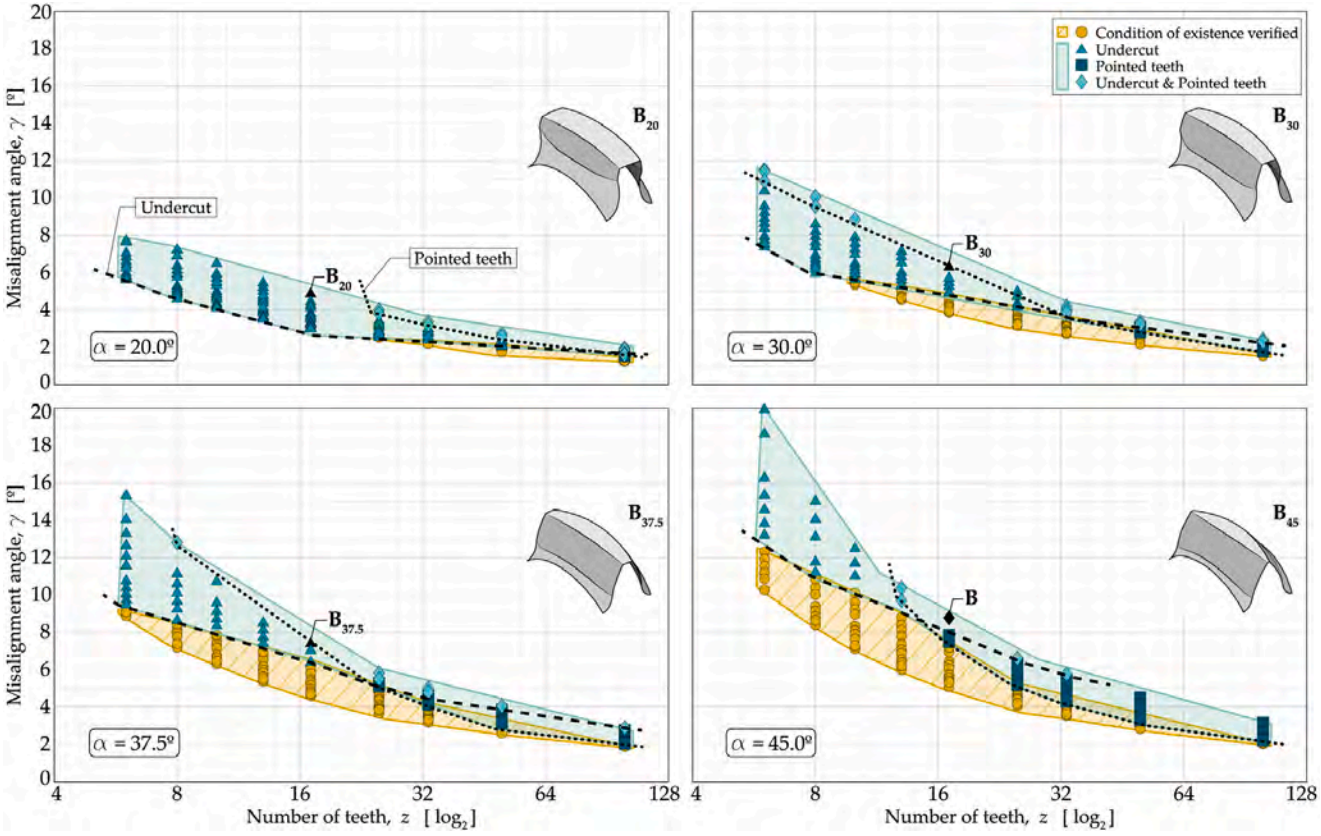

Fig. 10. Maximum misalignment angle for different pressure angles for $d_p = 50$ mm and $b/d_p = 0.3$ geometries. Dashed line (– –) represent the undercut condition, while the dotted line (··) the pointed teeth limit.

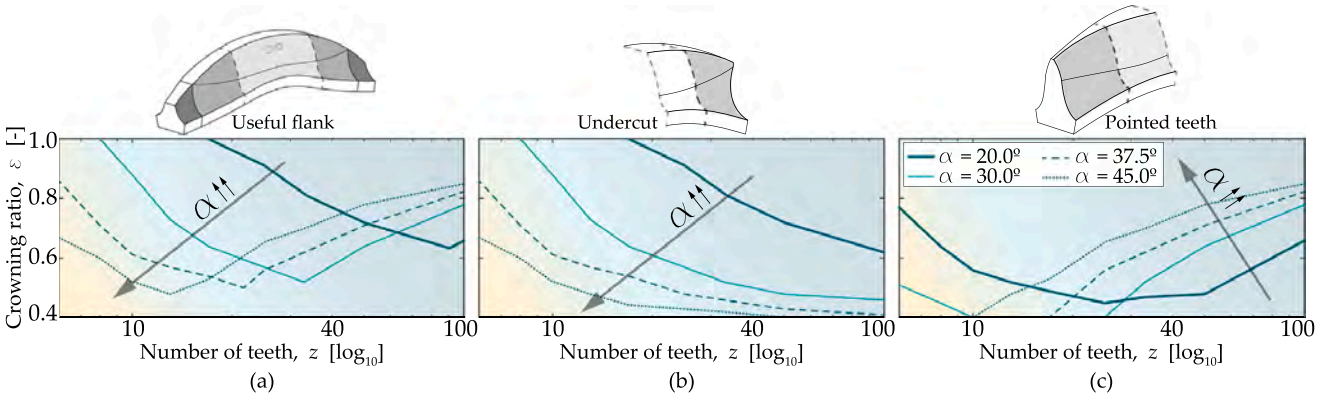

Fig. 11. Conditions of existence for $d_p = 50$ mm and $b/d_p = 0.3$ geometries in terms of the pressure angle: (a) useful flank, (b) undercut, and (c) pointed teeth.

6.5. *Influence of the aspect ratio* b/d_p

To analyze the influence of the varying face width, these geometry parameters were used:

- Constant parameters: $d_p = 50$ mm, $\alpha = 30°$, and $k = 0.07$.
- Variable parameters: b/d_p, m_n and ϵ.

Fig. 12 shows the maximum misalignment in terms of the number of teeth, together with the representation of the geometry $\mathbf{B}_x$ according to the aspect ratio. It can be seen, that an enlargement of the face width does not affect the achievable misalignment angle, except for small numerical deviations, even though there is a severe increase of the pointed teeth region. The maximum variation observed due to the change in the aspect ratio is of $\Delta\gamma = 0.05°$, which corresponds to an effect of only 0.56%.

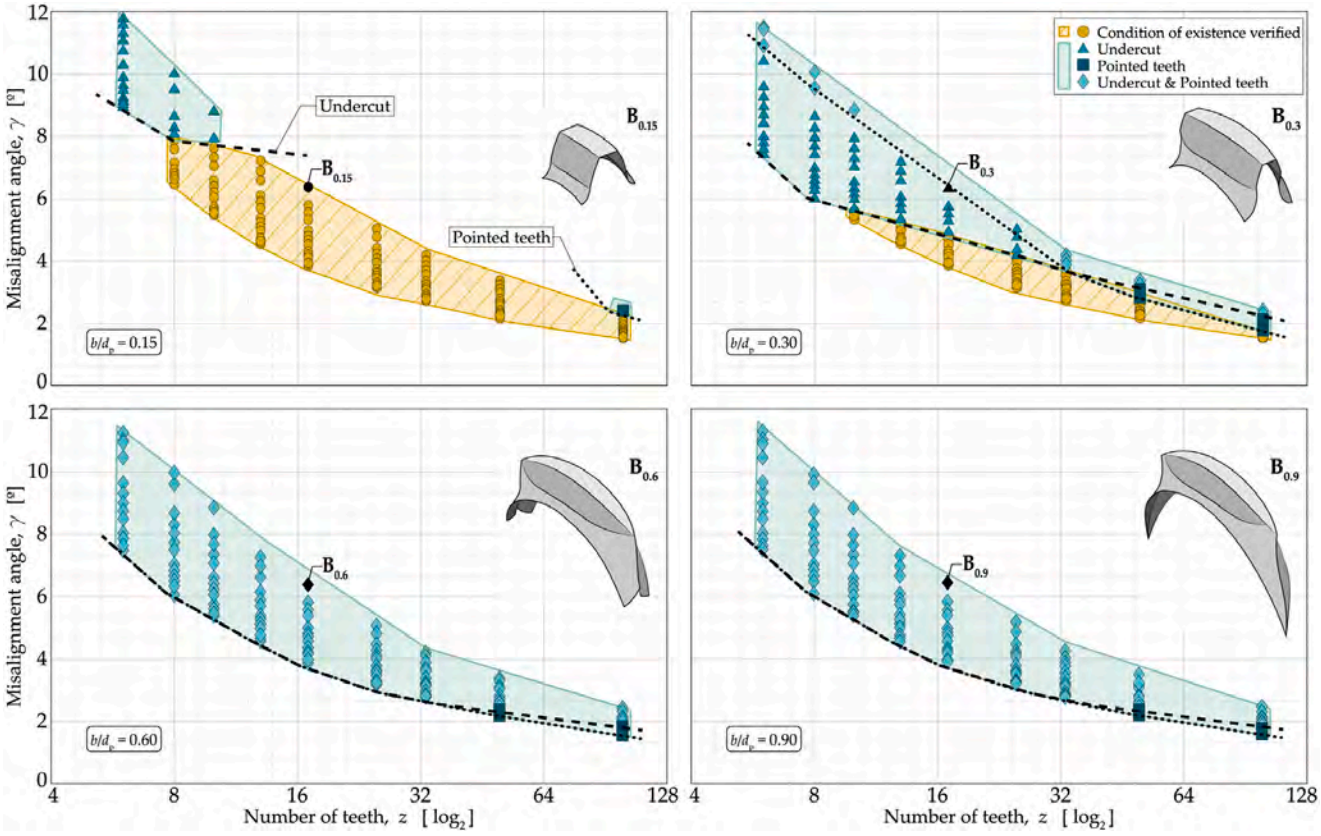

Fig. 12. Maximum misalignment angle for different aspect ratios in $d_p = 50$ mm and $\alpha = 30°$ geometries. Dashed line (– –) represent the undercut condition, while the dotted line (· ·) the pointed teeth limit.

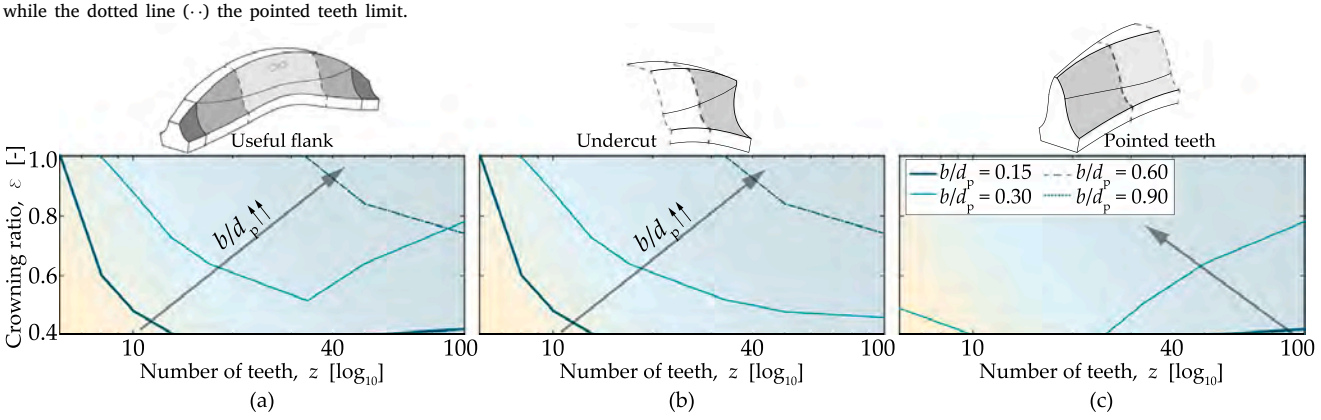

Fig. 13. Conditions of existence for $d_p = 50$ mm and $\alpha = 30°$ in terms of the aspect ratio: (a) useful flank, (b) undercut, and (c) pointed teeth.

Fig. 13 depicts that a value of the aspect ratio $b/d_p > 0.6$ adversely affects the geometrical properties in small pitch diameters, due to the excessive pointed teeth. Moreover, no apparent increase in the misalignment angle is observed.

Concerning lower aspect ratio values ($b/d_p = 0.15$–0.3), a stress analysis is required, as the achievable misalignment angle will remain constant for small pitch diameter geometries.

6.6. *Influence of the pitch diameter d_p*

To this point, the influence of the design variables has been analyzed considering a constant space constraint, that is, a constant pitch diameter of $d_p = 50$ mm. In this section the impact of the pitch diameter is described and geometry parameters were set as follows:

- Constant parameters: $\alpha = 30°$, $b/d_p = 0.3$, and $k = 0.07$.
- Variable parameters: d_p, m_n and ε.

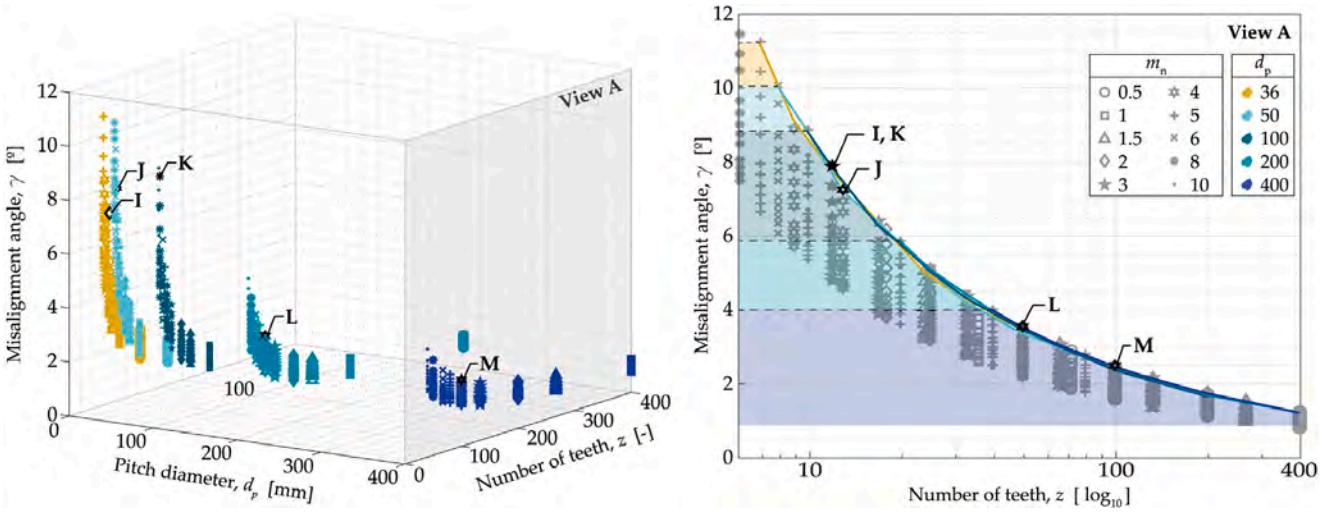

Fig. 14. (a) Maximum misalignment angle under different pitch diameter and numbers of teeth for $\alpha = 30°$ and $b/d_p = 0.3$ geometries. (b) Maximum misalignment angle achieved in terms of the number of teeth for each pitch diameter. (For interpretation of the references to color in this figure legend, the reader is referred to the web version of this article.)

Fig. 14(a) shows a general overview of the maximum misalignment angle achieved with all the generated geometries, in terms of the pitch diameter and the number of teeth.

It can be observed that the highest misalignment angles are achieved with small pitch diameters ($d_p < 100$ mm), regardless of the crowning ratio used. In other words, as the pitch diameter increases the maximum misalignment angle decreases (Fig. 14(b)). In addition, the variation of the obtained maximum misalignment angle is smaller as the pitch diameter increases. The figure also illustrates the decrease of the achievable maximum misalignment angle while the number of teeth increases, with a common limiting surface, regardless of the pitch diameter.

For a constant number of teeth and crowning ratio, the maximum misalignment angle achieved is very similar, regardless of the pitch diameter. For instance, for geometries **I** ($z = 12$), **J** ($z = 13$) and **K** ($z = 12$), and $\varepsilon = 0.4$, and the maximum misalignment angle is 7.87°, 7.23° and 7.91°, respectively (see Fig. 15). These slight differences are associated with the different number of teeth, due to the predefined module values in the ISO 4156 standard [17]. The maximum variation observed due to the change in the pitch diameter by the module is of $\Delta\gamma = 0.98°$, which corresponds to an effect of 7.80%.

Similarly, if the same module and crowning ratio geometries are compared for different pitch diameter values, a significant decrease of the maximum misalignment angle is observed; e.g. for geometries **J**, **L** and **M** with $m_n = 4$ mm and $\varepsilon = 0.4$, a maximum misalignment angle of 7.23°, 3.53° and 2.47° is achieved, respectively. The maximum variation observed due to the change in the pitch diameter by the number of teeth is of $\Delta\gamma = 6.57°$, which corresponds to an effect of 73.99%. It can therefore be concluded, that although the module and the number of teeth are variables dependent on each other ($d_p = m_n z$), the number of teeth z has a greater impact on the achievable maximum misalignment angle.

Indeed, within the recommended module and number of teeth values from ISO 4156 [17], it can be observed that as the pitch diameter increases, the available area is reduced (geometries outside the boundaries are shaded: $z < 6$ and $z > 100$). The misalignment angle differences within this area are thus reduced, and a geometry that verifies the conditions of existence is easier to obtain. Nevertheless, if the design demands a high misalignment angle, from Fig. 15 it can be deduced that geometries with a small pitch diameter and low number of teeth are the most suitable, even if undercut singularities exist.

To clearly state the limiting values of the crowning ratio at which conditions of existence are fulfilled, Fig. 16 shows the similarity of the boundaries for the useful flank (a), undercut (b) and pointed teeth (c) for all the pitch diameters. The slight differences are related to the numerical deviations. In fact, it is evidenced that the crowning ratio has no influence on the pitch diameter.

6.7. Influence of the clearance factor k

Finally, the influence of the clearance between the hub and the sleeve tooth surfaces was analyzed, using the clearance factor k, and with the subsequent parameters:

- Constant parameters: $d_p = 50$ mm, $\varepsilon = 0.4$, $\alpha = 30°$, and $b/d_p = 0.3$.
- Variable parameters: k and m_n.

Even if clearance distribution changes as a function of the teeth angular position or due to manufacturing errors [16,38], attention was paid to the minimum clearance value in the tilting position (see Fig. 17), to analyze its effect on the misalignment angle.

Fig. 17 shows the increase of the misalignment angle as the clearance factor k increases, in terms of the number of teeth.

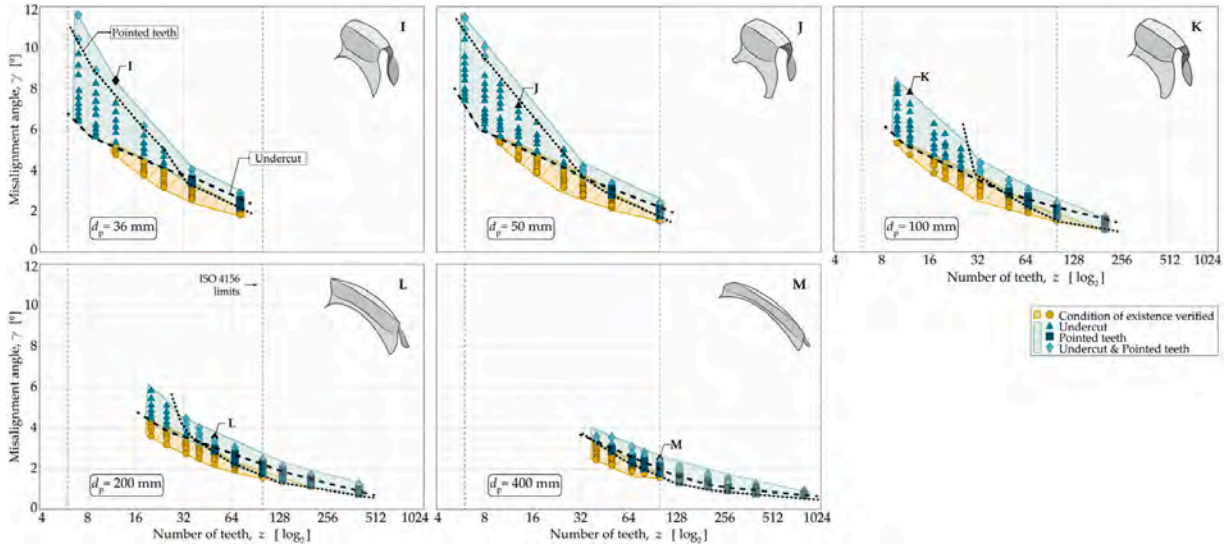

Fig. 15. Maximum misalignment angle for $\alpha = 30°$ and $b/d_p = 0.3$ geometries for each pitch diameter. Dashed line (– –) represent the undercut condition, while the dotted line (· ·) the pointed teeth limit.

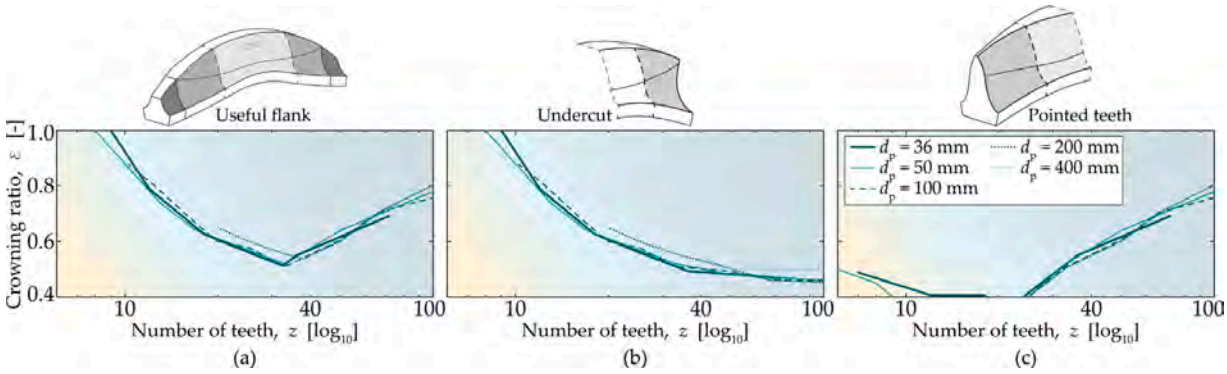

Fig. 16. Conditions of existence for $\alpha = 30°$ and $b/d_p = 0.3$ geometries in terms of the pitch diameter. (a) useful flank, (b) undercut, and (c) pointed teeth.

The clearance value ($j = k \cdot m_n$) is in terms of the module, and thus for a constant pitch diameter, a smaller number of teeth will have a greater clearance value. This is also consistent with the observation that the influence of the clearance factor is more marked in geometries with a small number of teeth. Hence, if a $z = 6$ and $z = 100$ are compared, the misalignment variation reduces from $\Delta\gamma = 2.30°$ to $\Delta\gamma = 0.83°$ in terms of the clearance factor k. The maximum variation observed due to the change in the clearance factor is of $\Delta\gamma = 2.30°$, which corresponds to an effect of 18.70%.

7. Discussion

In accordance with the analytical models in the literature proposed in Eqs. (10), (11) to determine the misalignment angle, it has been shown that deviations arise for small crowning ratios or big face width gear couplings, as these are oriented for small misalignment angles. Indeed, these equations do not consider all the parameters involved or the real geometry of the hub tooth, such as the face width, the module or the clearance. Related to this, in Eq. (11) simplifications associated with the transverse crowning radius r_t calculation are made. Indeed, in Eq. (11) the transverse crowning radius is approximated as: $r_t = r_c \cdot \tan(\alpha)^{-1}$, but this equivalence is only satisfied when the transverse crowning radius r_t is large enough (big crowning ratios), and the contact point is in the pitch diameter.

From the parameters analyzed in this paper it can be concluded that geometries with low numbers of teeth are the most suitable to attain higher misalignment angles, even if they are susceptible to undercut singularities. This is in agreement with the design criteria proposed by Herbstritt and Paluh [19]. They found that larger and fewer teeth with a small curvature (r_c) result in significant stress reduction and increased life of the component, which makes them more suitable for high misalignment applications [38]. In the same vein, Section 6.6 shows that small pitch diameters provide the largest design space for high misalignment angles.

Concerning the design variables, the present paper has shown that crowning radius is a key parameter in the design of highly misaligned hubs. Similarly, some works have noted that longitudinal crowning is necessary to compensate for misalignment [3,16].

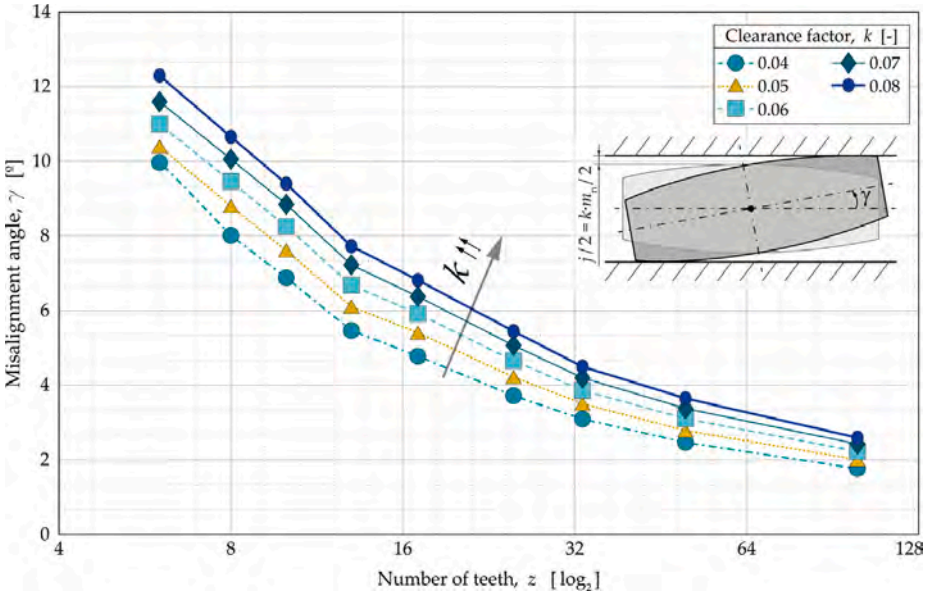

Fig. 17. Misalignment angle in terms of the clearance factor k for $d_p = 50$ mm, $\alpha = 30°$ and $b/d_p = 0.3$, and representation of misalignment angle variation.

Moreover, it is said that an excessive longitudinal crowning (reduced crowning radius) leads to uneven clearance distribution [3]. This can also be observed in Figs. 8 and 9, by the fact that a geometry optimized for a higher misalignment angle than the angle it is working at, will have bigger undercut singularities, and thus a lower stiffness. The aforementioned issue is dependent on the useful flank, as crowning ratio is reduced, the useful flank is also reduced. However, if crowning ratio is kept constant and the face width of the gear coupling varies, neither the misalignment angle nor the useful flank values change significantly, due to the small value crowning radius r_c existing in these geometries. This appears to be in agreement with Dudley [39], who stated that in flexible gear couplings the face width does not necessarily contribute to load-carrying capacity, and concluded that increasing the face width will not increase the load capacity. In fact, in Fig. 12 it is observed that there is a limit b/d_p ratio above which the maximum misalignment angle does not vary. AGMA 945-1-B20 [16] also stated that a face width limit exists, above which root stresses are not reduced. Hence, it can be concluded that the most suitable aspect ratio values are $0.15 < b/d_p < 0.3$, which is in agreement with recommended values from the literature [22,32,33], even if these latter were never verified for such big misalignment angles.

On the other hand, the standard pressure angles commonly applied in the literature are 20° [3,22] or 30° [17,20]. Nevertheless, the present work demonstrates that large pressure angles (45°) offer the best geometry adapted to high misalignment applications. Indeed, a higher pressure angle will generate a wider tooth root and ultimately a stiffer tooth. Alfares et al. [3] sets a minimum pressure angle of 25° for high misalignment applications, even if wear problems arise with values higher than 40°. The discrepancy with the proposed suitable pressure angle of 45° in the present paper, might be due to the non extended use of gear couplings in high misalignment applications. Moreover, wear failures are common in slight misalignment applications [40], and there are no evidence of wear failures in high misalignment applications.

Finally, concerning the clearance, standards [17,20] recommend increasing the clearance values when misalignment occurs, but no guide values are provided. This work has shown that an increase of the clearance value does in fact increase the maximum misalignment angle. However, it is known that smaller clearance values lead to increased uniformity of tooth loading [3,38], while higher values generate less uniform load distributions [41]. There are some works that propose clearance values depending on the pitch diameter [39] or module [22], but they are not adapted to working operations at high misalignment angles.

8. Conclusions

In this work, an algorithm to calculate the maximum misalignment angle is proposed, which considers real gear coupling teeth geometries and all the design parameters involved in the misalignment angle calculation. After comparing the results with other models in the literature, it is concluded that:

(1) The proposed model, can be applied for all type of gear coupling geometries, and it is not limited to gear couplings with small amounts of crowning ($\ll 100 \cdot 10^{-3}$ mm), as is the case with existing methods.
(2) The transverse crowning radius cannot be approximated to the crowning radius by $r_t = r_c / \tan(\alpha)$, in highly crowned spherical gear couplings.
(3) The face width and the module must be considered when calculating the maximum misalignment angle, together with the crowning radius, the pressure angle, and the clearance.

Secondly, the influence of the main design parameters of spherical gear couplings on the geometrical properties of gear tooth surfaces that work in high misalignment applications was investigated. These analyses allow the following conclusions to be drawn:

(4) The proposed procedure to define the limits of the main design parameter for spherical gear couplings is effective to prevent tip pointing and undercutting profiles in highly crowned spherical gear couplings.
(5) Gear couplings adapted to high misalignment angles ($\gamma > 5°$) must have undercutting profiles, which in consequence need to be accurately generated with an appropriate model.
(6) The maximum effect of each design parameter on the maximum misalignment angle individually are, from highest to lowest: the number of teeth (79.91%), the pressure angle (61.69%), the crowning ratio (35.04%), the clearance factor (18.70%), and the pitch diameter (7.80%). The aspect ratio, has no significant influence on small geometries (0.55%), with the most appropriate value being $0.15 < b/d_p < 0.3$.
(7) High pressure angle geometries give rise to hub tooth surfaces with verified geometric tooth surfaces at high misalignment angles.

This work serves as a tool for designers and manufacturers to choose the most appropriate highly crowned spherical gear coupling geometry adapted to a required maximum misalignment angle.

This design space will require future validation with a stress analysis. Indeed, in load conditions, the number of teeth in contact will vary in the presence of high misalignment and thus, flexibility of the gear coupling will be modified giving as a result slightly larger misalignment angles.

Declaration of competing interest

The authors declare that they have no known competing financial interests or personal relationships that could have appeared to influence the work reported in this paper.

References

[1] S. Hahn, Coupling connections and splines, in: Encyclopedia of Automotive Engineering, John Wiley & Sons, 2014, pp. 1–14, http://dx.doi.org/10.1002/9781118354179.auto094.
[2] Y. Guo, S. Lambert, R. Wallen, R. Errichello, J. Keller, Theoretical and experimental study on gear-coupling contact and loads considering misalignment, torque and friction influences, Mech. Mach. Theory 98 (2016) 242–262, http://dx.doi.org/10.1016/j.mechmachtheory.2015.11.015.
[3] M. Alfares, A. Falah, A. Elkholy, Clearance distribution of misaligned gear coupling teeth considering crowning and geometry variations, Mech. Mach. Theory 41 (10) (2006) 1258–1272, http://dx.doi.org/10.1016/j.mechmachtheory.2005.11.004.
[4] F. Ohshima, S. Hirata, H. Yoshino, Study on tooth contact of gear couplings, Trans. Japan Soc. Mech. Eng. C 78 (786) (2012) 639–649, http://dx.doi.org/10.1299/kikaic.78.639.
[5] Y. Guan, X. Yang, Z. Fang, G. Chen, Comparative analysis of three geometric models for crown gear coupling, Mech. Mach. Theory 136 (2019) 269–283, http://dx.doi.org/10.1016/j.mechmachtheory.2019.02.016.
[6] J.R. Mancuso, Couplings and Joints: Design, Selection and Application, Technology & Engineering. M. Dekker, 1986.
[7] P. Krot, Transient torsional vibrations control in the geared drive trains of the hot rolling mills, in: IEEE International Conference on Control Applications, St. Petersburg, 2009, pp. 1368–1373, http://dx.doi.org/10.1109/CCA.2009.5280933.
[8] I. Ulacia, J. Larrañaga, A. Arana, A. Iñurritegui, J. Elizegi, Fatigue life prediction of spherical gear couplings, in: American Gear Manufacturers Association Fall Technical Meeting 2018, Illinois, 2018, pp. 202–207.
[9] K. Mitome, T. Okuda, T. Ohmachi, T. Yamazaki, Development of a new hobbing of spherical gear, Trans. Japan Soc. Mech. Eng. C 66 (646) (2000) 1975–1980, http://dx.doi.org/10.1299/kikaic.66.1975.
[10] L. Chao, C. Tsay, Contact characteristics of spherical gears, Mech. Mach. Theory 43 (10) (2008) 1317–1331, http://dx.doi.org/10.1016/j.mechmachtheory.2007.10.008.
[11] L. Kelemen, J. Szente, Two mathematical models for generation of crowned tooth surface, Sci. World J. 2014 (2014) http://dx.doi.org/10.1155/2014/641091.
[12] A. Iñurritegui, I. Gonzalez-Perez, A. Arana, J. Larrañaga, I. Ulacia, Computerized generation and tooth contact analysis of spherical gear couplings for high misalignment applications, Mech. Mach. Theory 164 (2021) http://dx.doi.org/10.1016/j.mechmachtheory.2021.104408.
[13] J. Hong, D. Talbot, A. Kahraman, Effects of tooth indexing errors on load distribution and tooth load sharing of splines under combined loading conditions, J. Mech. Des. (2015) http://dx.doi.org/10.1115/1.4029282.
[14] P. Renzo, S. Kaufman, D. de Rocker, Gear couplings, J. Eng. Ind. (1968) 467–474.
[15] Y. Guan, X. Yang, Z. Fang, Computerized generation and simulation of meshing of a novel crown gear coupling avoiding edge contact, J. Adv. Mech. Des. Syst. Manuf. 13 (3) (2019) http://dx.doi.org/10.1299/jamdsm.2019jamdsm0055.
[16] American Gear Manufacturers Association, AGMA 945-1-B20: Splines – Design and Application, American Gear Manufacturers Association, Virginia, 2020.
[17] International Organization for Standardization, ISO 4156: Straight Cylindrical Involute Splines, International Organization for Standardization, Geneve, 2005.
[18] J. Hong, D. Talbot, A. Kahraman, Load distribution analysis of clearance-fit spline joints using finite elements, Mech. Mach. Theory 74 (2014) 42–57, http://dx.doi.org/10.1016/j.mechmachtheory.2013.11.007.
[19] W. Herbstritt, J. Paluh, Mill spindle advanced gear design, Iron Steel Eng. 76 (7) (1999) 44–48.
[20] Deutsches Institut für Normung, DIN 5466: Splined Joints, Calculation of Load Capacity, 2002.
[21] American Gear Manufacturers Association, AGMA 6123-B06: Design Manual for Enclosed Epicyclic Gear Drives, 2006.
[22] R. Beckmann, Beitrag zur Auslegung und Konstruktion von Balligzahn-Kupplungen (Ph.D. thesis), Chemmitz Technology University, 2005.
[23] American Gear Manufacturers Association, AGMA 1102-A03: Tolerance Specification for Shaper Cutters, 2010.
[24] F. Litvin, A. Fuentes, Gear Geometry and Applied Theory, second ed., Cambridge University Press, 2004, p. 818.
[25] G. Henriot, J. Boisset, Accouplements, alignement des axes, in: Engrenages: Conception, Fabrication, Mise en Oeuvre, fifth ed., Dunod, 1983, pp. 796–818.
[26] M. Octrue, F. Blanc, D. Ghribi, Guide de Demensionnement des Accouplements à Dentures Bombées, CETIM, 2014.
[27] D. Marano, M. Lorenzini, L. Mastrandrea, F. Pulvirenti, M. Turci, N. Fillault, Misalignment compensation spline design, in: American Gear Manufacturers Association Fall Technical Meeting 2019, Dallas, 2019.

[28] V. Tran, R. Hsu, C. Tsay, Study on the anti-twist helical gear tooth flank with longitudinal tooth crowning, J. Mech. Des. 136 (6) (2014) 061007, http://dx.doi.org/10.1115/1.4027166.
[29] L. Xiao, Y. Xu, X. Sun, H. Xu, L. Zhang, Experimental investigation on the effect of misalignment on the wear failure for spline couplings, Eng. Fail. Anal. 131 (2022) http://dx.doi.org/10.1016/j.engfailanal.2021.105755.
[30] J. Hong, A Semi-Analytical Load Distribution Model of Spline Joints (Ph.D. thesis), The Ohio State University, 2015, p. 245.
[31] Y. Guan, J. Chen, H. Chen, S. Hu, X. Liu, An experimental investigation of contact characteristics of crown gear coupling with angular misalignment, J. Adv. Mech. Des. 5 (5) (2021) http://dx.doi.org/10.1299/jamdsm.2021jamdsm0062.
[32] R. Cedoz, M. Chaplin, Design Guide for Involute Splines, Society of Automotive Engineers, 1994.
[33] E. Neale, Introduction to Gear Couplings, Tech. rep., Neale consulting engineers, 1980.
[34] S. Radzevich, Dudley's Handbook of Practical Gear Design and Manufacture, third ed., CRC Press, Taylor & Francis group, 2016.
[35] R. Heinz, Untersuchung der zahnkraft- und reibungsverhältnisse in zahnkupplungen, Konstruktion 12 (1978) 483–492.
[36] A. Andrew, Another efficient algorithm for convex hulls in two dimensions, Inform. Process. Lett. 9 (5) (1979) 216–219, http://dx.doi.org/10.1016/0020-0190(79)90072-3.
[37] International Organization for Standardization, ISO 21771: Gears-Cylindrical Involute Gears and Gear Pairs-Concepts and Geometry, 2007.
[38] B. De Caires, Variation Analysis of Involute Spline Tooth Contact (Ph.D. thesis), Brigham Young University, 2006.
[39] D. Dudley, How to design involute splines, Prod. Eng. (1957) 196–231.
[40] S. Medina, A.V. Olver, Regimes of contact in spline couplings, J. Tribol. 124 (2) (2002) 351–357, http://dx.doi.org/10.1115/1.1403456.
[41] N. Zafirah, A. Bakar, L. Ghee, H. Hussain, Reasarch on load distribution of different involute spline clearance, TEST Eng. Manage. 82 (2020) 3058–3068.

If you tell the truth you don't have to remember anything.
—Mark Twain

C | Publication III

Load distribution and tooth root stress of highly crowned spherical gear couplings working at high misalignment angles

A. Iñurritegui[a], J. Larrañaga[a], A. Arana[a], I. Ulacia[a]

[a] *Mondragon Unibertsitatea, Department of Mechanical and Industrial Production, Arrasate-Mondragon, Pais Vasco, Spain.*

Received 09 September 2022; Accepted 24 September 2022. Available online 11 October 2022; Version of Record 11 October 2022.

Mechanism and Machine Theory 179 (2023) 105104

Mechanism and Machine Theory 179 (2023) 105104

Contents lists available at ScienceDirect

Mechanism and Machine Theory

journal homepage: www.elsevier.com/locate/mechmt

Research paper

Load distribution and tooth root stress of highly crowned spherical gear couplings working at high misalignment angles

Aurea Iñurritegui *, Jon Larrañaga, Aitor Arana, Ibai Ulacia

Mondragon Unibertsitatea, Department of Mechanical and Industrial Production, Arrasate-Mondragon, Pais Vasco, Spain

ARTICLE INFO

Keywords:
Spherical gear coupling
High misalignment
Load distribution
Tooth root bending stress
Finite element method

ABSTRACT

Spherical gear couplings are commonly used mechanical components to transmit power between highly misaligned rotating shafts. For that, gear couplings are manufactured with high longitudinal crowning and are usually small due to space restrictions, with the probability to contain undercutting sections. High misalignment angles cause the number of teeth in contact to decrease drastically, resulting in the failure of the component by tooth root fatigue breakage.

This paper investigates the load distribution and the tooth root stress of highly crowned spherical gear couplings working at high misalignment angles using a finite element model. Moreover, a deep understanding of the bending tooth root stresses in terms of the operating conditions is presented, which is novel for such high misalignment angles ($\gamma \geq 3°$). Results show that different mechanical behaviors are observed at low or high misalignment angles since teeth in the pivoting position lose contact. This results in a tooth root stress history change from a sinusoidal cycle to a pulsating cycle. Finally, this study shows evidence that current sizing methods are not suitable, and underlines the need for further research to determine the spherical gear coupling life to tooth root bending fatigue.

1. Introduction

Spherical gear couplings are mechanical components used to transmit power between misaligned shafts. They are preferred over other non-splined connections, due to their high power density and capacity to accommodate angular misalignments [1,2]. For example, they are used in sheet metal rolling mills [3–5], where high misalignment angles ($\gg 3°$) are required due to the reduced space between rollers.

They are composed of a highly crowned toothed hub (external part) and a commonly straight sleeve (internal part) [6,7], both of which have the same number of teeth. For the generation of highly crowned surfaces of the hub, it is necessary to consider the threaded surface of the generating hob and the kinematics of the hobbing process. Indeed, it is likely that undercutting sections appear, as previously shown by the authors in [8].

The most common use of gear couplings is in applications where slight misalignment occurs. Damage occurring as a result of surface wear [9–12] caused by improper lubrication represents 75% of all gear coupling failures [13,14]. Low misalignment angles decrease the longitudinal sliding between the hub and the sleeve, which leads to fretting damage on the surface [15–17]. The next most common failure stems from misalignment (20%), which leads to tooth root breakage failure [18]. Moreover, this latter is significantly increased in highly crowned spherical gear couplings, as undercutting sections are more frequent [5,8].

Works in the literature have shown the relationship between the design parameters and the misalignment angle [19]. Indeed, they have shown that an adequate selection of the number of teeth, the pressure angle, and the crowning ratio, among others, can

* Corresponding author.
E-mail address: ainurritegui@mondragon.edu (A. Iñurritegui).

https://doi.org/10.1016/j.mechmachtheory.2022.105104
Received 9 September 2022; Accepted 24 September 2022

Nomenclature

A	Coefficient to comprise the variables related to the geometry in tooth root stress
b	Face width of the gear coupling
b_{eff}	Effective face width of the gear coupling
C	Number of teeth in contact
C_{eff}	Number of effective teeth in contact
d_p	Pitch diameter of the gear coupling
e	Thickness of the tooth surface with smaller mesh elements
F_{CN}	Total contact normal force
j_n	Normal clearance
K	Coefficient to comprise the rest of the coefficients affecting tooth root stress
k_F	Overload coefficient
k_{ls}	Load sharing factor
k_m	Load distribution factor
LD_{z_i}	Load distribution in each tooth z_i
m_n	Normal module
n_{z_i}	Total contact nodes in each tooth z_i
r_c	Crowning radius of the hub
Y	Lewis factor
z	Total number of teeth in the gear coupling
α	Pressure angle
Γ	Applied torque
γ	Misalignment angle
$\delta_{\max}$	Maximum displacement of the contact point from the reference section along the face width
θ_i	Angular position of the hub
σ	Tooth root bending stress

produce a spherical gear coupling design that can achieve misalignment angles greater than 15°. Nevertheless, existing works for sizing and designing gear couplings [14,20–25] are mainly focused on low misalignment angles, and spherical gear couplings for high misalignment applications are referred to as special cases. The equations from the cited works are derived from gear tooth root bending calculations and all have the same structure represented in Eq. (1).

$$\sigma = \frac{\Gamma \cdot K}{A} k_m \cdot k_{ls} \tag{1}$$

where, Γ is the applied torque, A is a coefficient to include the geometrical variables to represent the moment of inertia and resistant section of the tooth (e.g., the module m_n, the pitch diameter d_p, the face width b...). Likewise, K is a factor to include all the coefficients which influence tooth root stresses (e.g., the application factor k_a, the quality coefficient Z_Q...). Two relevant coefficients for spherical gear coupling are remarked to account for the number of teeth in contact (k_{ls}) and the effective face width (k_m) supporting the load.

On the one hand, the load distribution factor (k_m) considers the length of the face width actually carrying the load. In ideal aligned conditions, all the teeth are engaged and contact is centered on the face width [26]. When slight misalignment occurs, however, the spatial motion becomes complex and the relative position between both hub and sleeve differs depending on the meshing position [25,27,28]. The relative motion between hub and sleeve is made up of pivoting (swinging) and tilting movements, and the contact pattern and position changes accordingly, presenting a lemniscata shape [8,29–31]. The evolution of the contact point caused by the misalignment angle results in a variation of the effective face width supporting the load [27]. Some works in the literature [11,32] propose an Eq. (2) to determine the maximum contact point displacement ($\delta_{\max}$), and then define the portion of the tooth supporting the load. However, very little data exists related to the effective face width, and how to consider it in high misalignment applications [20,22,33].

$$\delta_{\max} = r_c \sin(\gamma) \cos\left(2\pi \frac{z_i}{z}\right) \tag{2}$$

where, r_c is the crowning radius, γ is the misalignment angle, z is the total number of teeth, and z_i is the position of each tooth.

On the other hand, the load sharing factor (k_{ls}) is used to account for the number of teeth actually carrying the load. Indeed, the tilting position (in the perpendicular plane to the misalignment angle) is the most critical one, because teeth in this angular position are the first to come into contact. As they have the smallest clearance value [8,29], they suffer the highest stresses [34]. Torque value, associated with the available clearance, makes the gear coupling stiffness vary [35], and increase as the number of teeth in contact rises. However, if manufacturing errors occur, clearance will no longer be constant. For this reason, Beckmann [23] also

includes a coefficient to account for the manufacturing quality and its effect on the number of teeth in contact. Indeed, indexing errors can imply an increase of 22% in the stress values supported by the gear coupling [23]. On top of that, the non-uniformity of load distribution will be increased [36–38].

In the presence of low misalignment angles, gear couplings have already shown a non-uniform load distribution [11,26,30,39]. That is why, efforts have been focused on the increase of the contact surface to reduce stresses and obtain more uniform load distribution by modifying the longitudinal amount of crowning [28,40,41].

The majority of works published in the literature only focus on the effect of the misalignment angle ($\gamma \leq 1.5°$) on the number of teeth in contact [1,14,24,28,36,42]. However, these values were not experimentally validated and loading conditions were not considered. As a consequence, commonly used conservative criteria in gear coupling sizing is to assume that half of the teeth are carrying the load [14,22,24]. Nevertheless, it has been shown that tooth stiffness and torque have a significant impact [5,39], thus, it is expected that this criterion will oversize the part to a great extent depending on the geometry of the gear coupling or the working conditions.

Due to the complex kinematics of misaligned gear couplings, and the effect of multiple variables, analytical models exist to analyze the influence of each of the variables individually; e.g., clearance distribution [29,31,43] or load distribution [11,44], among others. However, it is known that parameters are interrelated and that they cannot be independently analyzed, especially when high misalignment angles are present. That is why, recently, the use of finite element models has grown. 2D models have been used to determine load distribution and the number of teeth in contact under different loading conditions [45] or under the effect of pitch errors [46]. However, to analyze the effect of the misalignment angle 3D models are required [47–49]. Moreover, the accuracy of the geometry has shown to have a great influence on the non-loaded tooth contact analysis (NLTCA) resulting from the small crowning radius and the appearance of undercutting sections [8]. That is why it is expected to be of relevance in the loaded tooth contact analysis (LTCA) due to the possible stress concentrations. For instance, Guan et al. [30] presented the evolution of the load distribution with misalignment angles up to $\gamma = 0.2°$ while showing high risk of tip edge contact due to the misalignment angle.

From the literature review, it can be confirmed that the number of teeth in contact and the contact position significantly vary in terms of low misalignment angles. This variation affects the load distribution, and consequently the tooth root stress distribution. The complex mechanical behavior and the complexity of the geometry itself (presence of undercutting sections) make FE models a very suitable tool for the analysis. However, the works cited earlier are principally focused on misalignment angles below one degree. Thus, the behavior at higher misalignment angles is uncertain, and the application of current sizing criteria to determine load distribution and maximum tooth root stresses can result in over sizing, or even what may be more critical, under sizing of the component.

Therefore, this paper numerically determines the load distribution and the tooth root stress behavior of a highly crowned spherical gear coupling working at high misalignment angle applications, considering the variation of the contact position and the number of teeth in contact. To this end, the main goals of this research are:

(1) To develop a finite element model, based on the mathematical geometry generation model (already presented in [8]) for spherical gear couplings working in high misalignment applications. This model will be capable of accurately representing all the geometry features of spherical gear couplings, such as undercutting sections.
(2) To analyze the influence of the misalignment angle, specially $\gamma \gg 1.5°$, and the applied torque on the number of teeth in contact, the load distribution, and the tooth root stress.

2. Geometry of the spherical gear coupling tooth surfaces

The main tooth modification employed in spherical gear couplings is longitudinal crowning or barreling [5,19,29,50,51] to achieve a more uniform contact pressure distribution and to prevent the undesired edge contacts caused by slight misalignments during operation or assembly.

Barreling involves a tooth thickness variation in the hub tooth surfaces and a tooth clearance change along the face width [29,51]. In the reference section, the tooth thickness is the greatest, and a constant clearance between the hub and the sleeve tooth active profiles can be observed in aligned conditions (Fig. 1(a)). From the literature [8,52], it is known that contact moves further away from the central section when misalignment is present, thus, longitudinal crowning and clearance distribution will lead to different contact conditions. Indeed, as the section moves further away, the hub tooth surfaces will no longer conform nominally to the tooth surface of the sleeve [16,36] (Fig. 1(a)).

As shown in Fig. 1(b.1), the whole active involute tooth surfaces are in contact in aligned (A) and loaded conditions without tip relief, because of the constant clearance between the hub and the sleeve tooth surfaces. However, in tooth sections further away from the central section (misaligned conditions, M), the non-constant variation of the clearance value will cause tip edge contact between the fillet tooth surface of the sleeve and the tip edge tooth surface of the hub, resulting in high contact pressure values. To avoid it, in this research, the hub and sleeve tooth surfaces are generated with a chamfer tip relief to center the contact on the active tooth profile, as shown in Fig. 1(b.2). It is already known that tip relief modification has an effect on load distribution of spur gears [53,54], that is why for this research the lowest possible tip chamfer was considered to avoid edge contact in the analyzed working conditions.

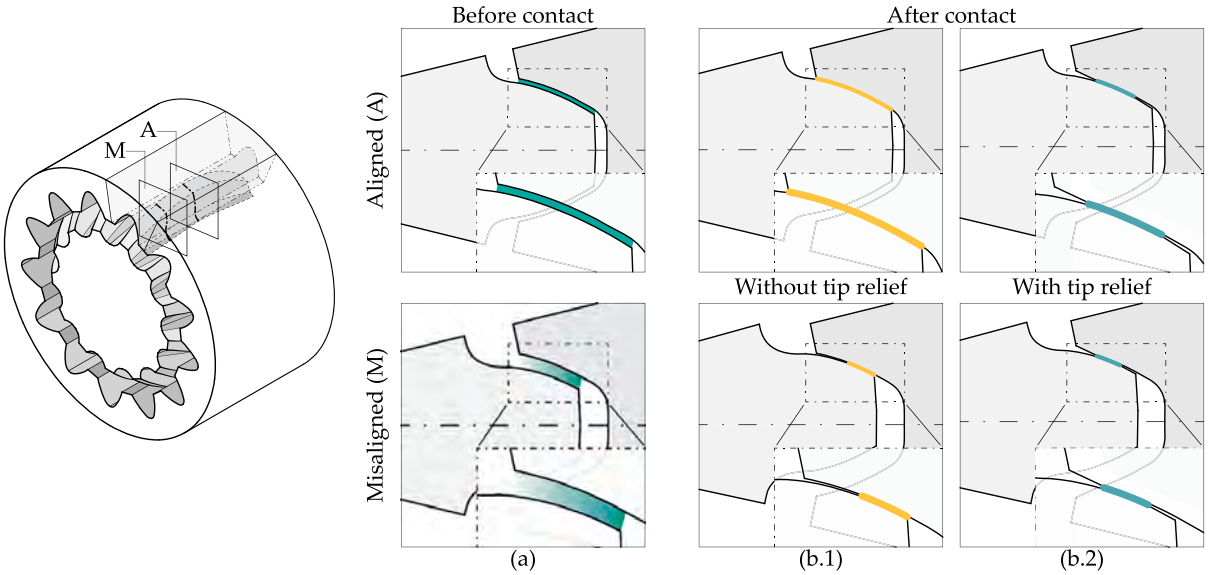

Fig. 1. (a) clearance and (b) contact conditions of spherical gear couplings in aligned (b.1) and misaligned (b.2) working conditions, showing the benefit of applying the tip relief.

For this purpose, the generating rack cutter tooth surface is modified by a linear tip-relief (enlarged for clarity in Fig. 2) which is defined in coordinate system S_a as follows:

$$\mathbf{r}_{\mathrm{a}}(u) = \begin{cases} \text{if } u_{\mathrm{lim}} < u \le u_{\mathrm{max}} & [u \quad 0 \quad 0 \quad 1]^{\mathrm{T}} \\ \text{if } u_{\mathrm{min}} \le u \le u_{\mathrm{lim}} & [u \quad -(u+u_{\mathrm{lim}})\sin(\alpha_{\mathrm{ch}}) \quad 0 \quad 1]^{\mathrm{T}} \end{cases} \tag{3}$$

where u_{lim} is the active profile limit from which the chamfer is defined and α_{ch} is the chamfer angle. In this research, $u_{\mathrm{lim}} = 0.3$ and $\alpha_{\mathrm{ch}} = 3.5°$ are considered. Further research would be required to optimize the value or analyze the influence of different types of tip reliefs, but it is out of the scope of this paper.

The hub and sleeve tooth surfaces are generated considering the manufacturing method, the meshing theory, and the double-enveloping process [55] defined in-depth by the authors in [8]. Fig. 2 provides an overview of the generation of the hub (lower part) and the sleeve (upper part), starting from the rack-cutter tooth surface with tip relief.

In the case of the hub, a hob thread surface Σ_{w} is generated as the cutting tool from the generating rack-cutter tooth surface Σ_{c}. This follows a circular feeding motion which determines the hub tooth surface Σ_{h} as the envelope to the family of surfaces of the hob. The hob thread surface is determined from the rack-cutter tooth surface Σ_{c} considering the meshing equation (5). The hub tooth surface is then generated by coordinate transformation (4) from system S_{c} to system S_{h}, taking into consideration the double-enveloping process [55] with two independent parameters of generation ϕ_w and s_w ((6), (7)).

$$\mathbf{r}_{\mathrm{h}}(u, v, \psi_w, s_w, \phi_w) = \mathbf{M}_{\mathrm{hw}}(s_w, \phi_w)\,\mathbf{M}_{\mathrm{wc}}(\psi_w)\,\mathbf{r}_{\mathrm{c}}(u, v) \tag{4}$$

$$f_1(u, v, \psi_w) = \left(\frac{\partial \mathbf{r}_{\mathrm{w}}}{\partial u} \times \frac{\partial \mathbf{r}_{\mathrm{w}}}{\partial v}\right) \cdot \frac{\partial \mathbf{r}_{\mathrm{w}}}{\partial \psi_w} = 0 \tag{5}$$

$$f_2(u, v, s_w, \phi_w) = \left(\frac{\partial \mathbf{r}_{\mathrm{h}}}{\partial u} \times \frac{\partial \mathbf{r}_{\mathrm{h}}}{\partial v}\right) \cdot \frac{\partial \mathbf{r}_{\mathrm{h}}}{\partial \phi_w} = 0 \tag{6}$$

$$f_3(u, v, s_w, \phi_w) = \left(\frac{\partial \mathbf{r}_{\mathrm{h,a}}}{\partial u} \times \frac{\partial \mathbf{r}_{\mathrm{h}}}{\partial v}\right) \cdot \frac{\partial \mathbf{r}_{\mathrm{h}}}{\partial s_w} = 0 \tag{7}$$

Here, ψ_w is the generation parameter for the hob thread surface, and matrices $\mathbf{M}_{\mathrm{hw}}$ and $\mathbf{M}_{\mathrm{wc}}$ are the coordinate transformation matrix [8].

As regards the sleeve, a shaper Σ_{s} is generated as the cutting tool from the generating rack-cutter tooth surface, with the meshing equation (9). This follows a straight tool path to determine the tooth surfaces of the sleeve Σ_{g}, as the envelope to the family of surfaces of the shaper. Coordinate transformation (8) from system S_{c} to system S_{g} and consideration of the meshing Eqs. (10) by parameter ψ_s enables to determine the sleeve tooth surface.

$$\mathbf{r}_{\mathrm{g}}(u, v, \psi_s, \phi_s) = \mathbf{M}_{\mathrm{gs}}(\phi_s)\,\mathbf{M}_{\mathrm{sc}}(\psi_s)\,\mathbf{r}_{\mathrm{c}}(u, v) \tag{8}$$

$$f_4(u, v, \psi_s) = \left(\frac{\partial \mathbf{r}_{\mathrm{s}}}{\partial u} \times \frac{\partial \mathbf{r}_{\mathrm{s}}}{\partial v}\right) \cdot \frac{\partial \mathbf{r}_{\mathrm{s}}}{\partial \psi_{\mathrm{s}}} = 0 \tag{9}$$

$$f_5(u, v, \psi_s, \phi_s) = \left(\frac{\partial \mathbf{r}_{\mathrm{g}}}{\partial u} \times \frac{\partial \mathbf{r}_{\mathrm{g}}}{\partial v}\right) \cdot \frac{\partial \mathbf{r}_{\mathrm{g}}}{\partial \phi_s} = 0 \tag{10}$$

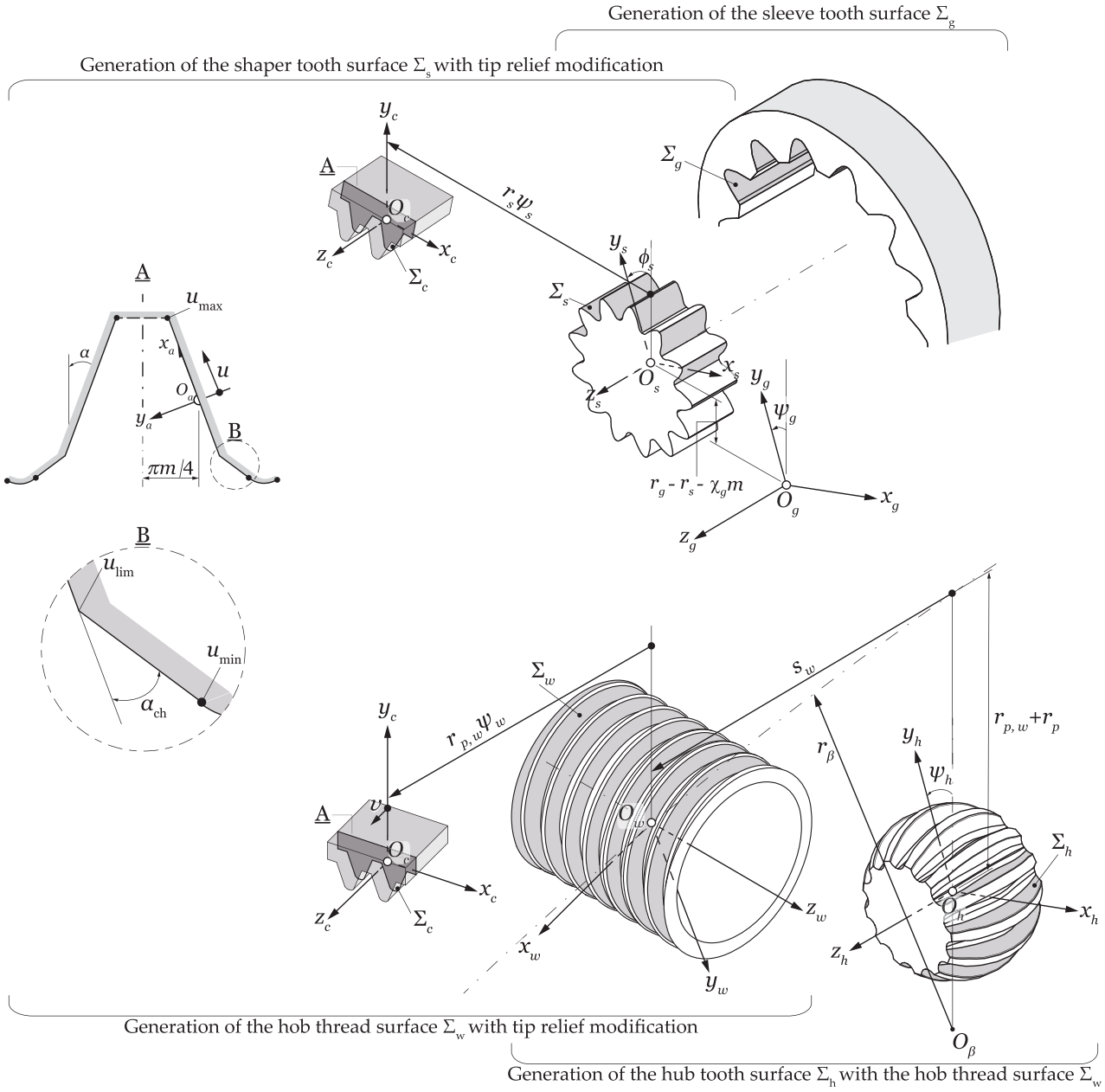

Fig. 2. Derivation of the hub tooth surface Σ_h and sleeve tooth surface Σ_g with linear tip relief, with the prior determination of the hob thread surface Σ_w and shaper tooth surface Σ_s.

3. Definition of spherical gear couplings finite element model

The FE method is employed to simulate the contact path and mechanical behavior of spherical gear couplings. Compared to other analytical methods, this approach has the advantage of taking into account the effects derived from the elastic deformations of all the teeth in the gear coupling and body, including tooth stiffness, tilting-moment effect generated by misalignment, and modifications of the load-sharing between the teeth.

3.1. Mesh

The meshing of the hub and sleeve is based on the method proposed in [56], which is commonly employed for gear analysis. This well-known meshing procedure produces a uniform structured mesh over the gear geometries, dividing the teeth into five sections: right and left active and fillet profiles of the gear tooth, and the gear body.

The mesh is produced automatically from the generated geometry using the generation model described in Section 2. Fig. 3(a) shows a detailed view of the hexahedral element mesh in the hub. The same meshing technique is employed in the sleeve. The

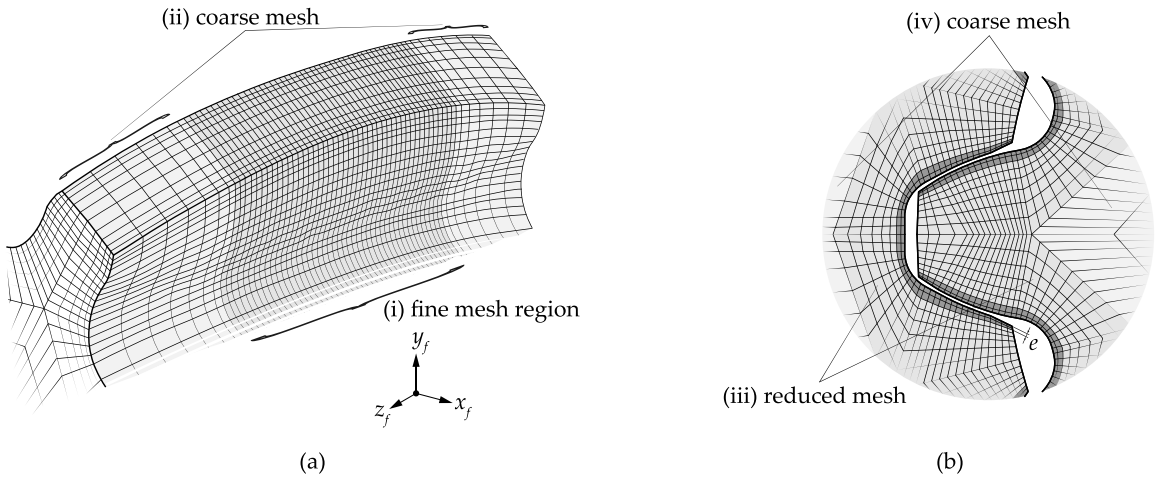

Fig. 3. Finite element mesh: (a) hub longitudinal mesh discretization with a (i) fine mesh in the potential contact zone and tooth root, and (ii) a coarser mesh up to the edges; and (b) detail of the hub and sleeve teeth transversal mesh with a (iii) reduced mesh in the tooth comprising a non-biased contact layer, and a (iv) coarse mesh in the body part.

mesh is developed with the aim of capturing tooth root stresses, and with a non refined mesh in the contact zone of the teeth. This stems from the main objective of this study, which is the analysis of tooth root stress distribution. The novelty of the meshing employed for spherical gear couplings in this paper compared to the methodologies commonly used [47–49], lies in a finer mesh in the tooth root region below the potential contact zone region. This provides smaller elements in those zones with higher stress gradients without increasing the number of elements, and thus the computational cost. Fig. 3(a) depicts: (i) a fine mesh across the contact area of the gear coupling, and (ii) a coarser mesh that transitions from the fine mesh up to the hub (or sleeve) edges with a bias factor. The finer mesh region is delimited for each misalignment angle by a NLTCA [8], plus an additional 25% as commonly done for spur gears.

Additionally, Fig. 3(b) illustrates the transverse meshing employed for the hub and sleeve teeth composed of: (iii) a reduced mesh in the root and flank and a coarser mesh in the body of the teeth, where stress gradients are smaller. Moreover, this mesh comprises several layers of smaller elements near the surface of the flank and fillet regions, characterized by thickness $e = 0.15m_n$ [57]. The refined mesh between the surface layer and the body is generated with a bias factor for a smoother transition.

The element size in the contact zone and the fillet of the hub is of 0.08 mm.

3.2. Model assembly

Fig. 4(a) shows a fixed coordinate system S_f where the hub and sleeve geometries are assembled. An auxiliary system S_m is defined parallel to S_f and enables the misalignment of the sleeve around axis x_m, while it remains fixed during the analysis. The origin (O_f, O_m) of coordinate systems S_f and S_m is located in the central section of the gear coupling (0,0,0).

The hub and sleeve models are defined in coordinate systems S_1 and S_2, respectively. The nodes located on the inner hub radius and the external rim of the sleeve form rigid surfaces. These surfaces are represented in yellow and green, in Fig. 4(b). A hub reference node O_1 is defined at the origin of system S_1 and is rigidly connected to its corresponding rigid surface while allowing rigid body motion between the reference node and the rigid surface. The same procedure is followed for the sleeve reference node O_2 and the external rim rigid surface in the coordinate system S_2. The assembly of system S_2 in the auxiliary coordinate system S_m is made with the misalignment angle around axis x_m. In consequence, the characteristic positions of the gear coupling will be defined as follows: (i) pivoting position, $\pi/2$ rad and $3\pi/2$ rad, parallel to the misalignment axis and, (ii) tilting position, 0 rad and π rad, perpendicular to the misalignment axis.

To carry out the FE analysis and ensure suitability for post-processing, a cylindrical coordinate system (r, θ, z_f) is defined, as shown in Fig. 4(b).

In real working conditions, the spherical gear coupling is connected to a shaft at its ends. This generates the load distribution to be delocalized along the face width. Moreover, maximum tooth root stresses will also increase due to the bending moments generated by the shaft [32]. As the main objective of this research is to explain the mechanical behavior of highly crowned spherical gear couplings, the shaft to which the hub or sleeve is connected is not considered. This also suppresses the effect of the shaft on the load distribution. Hence, any non-symmetry of the load distribution will be related to the contact position and the effect of the working conditions (torque and/or misalignment).

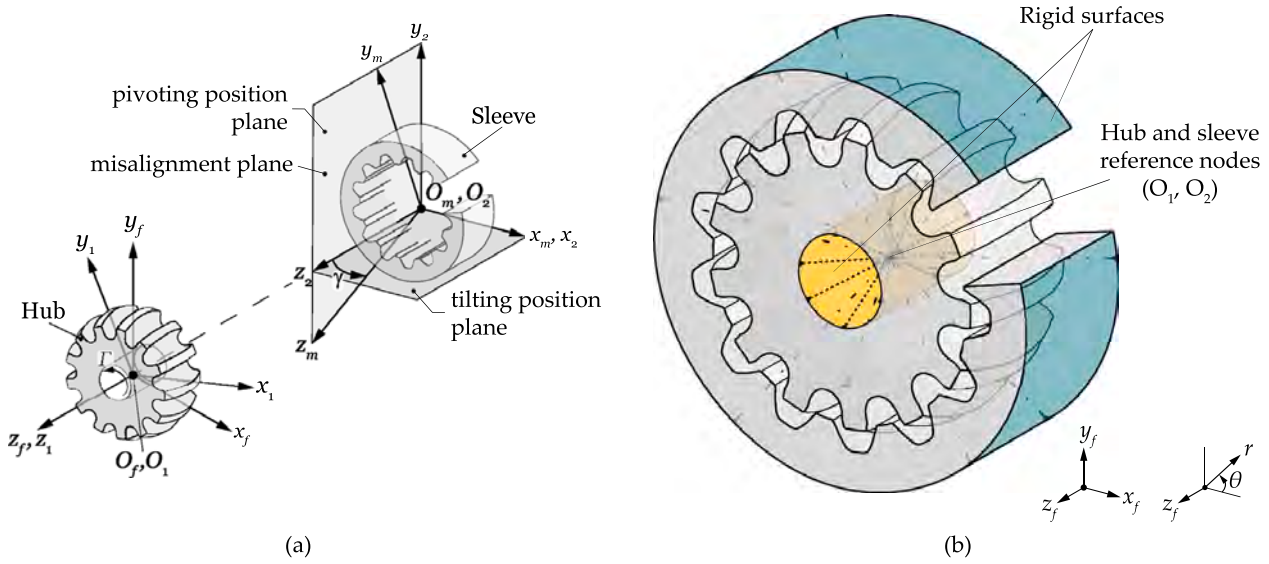

Fig. 4. Description of the spherical gear coupling finite element model for the loaded tooth contact analysis: (a) coordinate system for the model assembly, and (b) definition of rigid surfaces and reference nodes. (For interpretation of the references to color in this figure legend, the reader is referred to the web version of this article.)

3.3. Load cases and boundary conditions

Each simulation is carried out at a certain angular position along the meshing line (Fig. 4). The degrees of freedom of the sleeve reference node are blocked. Torque Γ is applied through the released degree of freedom of the hub reference node around axis z_1 (Fig. 4(a)). The rest of the degrees of freedom of the hub reference node are also blocked.

Node-to-segment contact pairs are specified between the teeth of the hub and the sleeve. Friction can be considered in the tangential behavior of the contact, however, it is out of the scope of this research and has not been included. During the contact process, it is unlikely that a node makes exact contact with the surface, and for that reason, a contact tolerance is associated with each surface. If a node is within the contact tolerance, it is considered to be in contact with the segment. In this analysis, a tolerance value of 1/20 of the smaller element size was selected, centered on both sides of the segment (Fig. 5(b)).

A linear elastic material is defined for the model, under the assumption that the deformations are so small that they may be studied under the small strains theory. The element type considered for the analysis is a first-order isoparametric hexahedral element (type 7 [58]).

3.4. Post-processing of the results

3.4.1. Contact pattern and number of teeth in contact

To determine the contacting teeth, the contact status output [58] is extracted from the traction active profile nodes of the hub. An indicator for contact is recognized by a congruent representation of the contact status output in the master and slave contact bodies, as depicted in Fig. 5(a). These positions are then replaced by the centroid of all the nodes in contact in each tooth, for comparison in the contact pattern graphs. Throughout the simulation and the iterative process, the motion of the nodes is checked to verify whether the nodes are near a segment or not, considering the contact tolerance as defined in Fig. 5(b).

It is important to note at this point, that the values of the centroid and contact position are dependent on the mesh size and the contact tolerance employed in the simulation, as the information is extracted from the position of the nodes. Nevertheless, the mesh used in this research is sufficient to analyze the evolution of the contact pattern and the influence of the operating conditions.

3.4.2. Load distribution

The load distribution for each tooth is obtained by the summation of the contact normal force (F_{CN}) of the nodes in contact (Eq. (11)). Once calculated, the contact normal force is divided by the total normal force applied to the whole gear coupling to obtain the load distribution, as shown in Eq. (12).

$$F_{CN,z_i}(\xi) = \sum_{n=1}^{n_{z_i}} F_{CN}(n) \tag{11}$$

$$LD_{z_i}(\xi) = \frac{F_{CN,z_i}(\xi)}{\sum_{z_i=1}^{z} F_{CN,z_i}(\xi)} \tag{12}$$

where, F_{CN,z_i} corresponds to the total contact normal force for tooth z_i at increment ξ, n_{z_i} refers to the total contact nodes in each tooth z_i, and LD_{z_i} is the load distribution of each tooth.

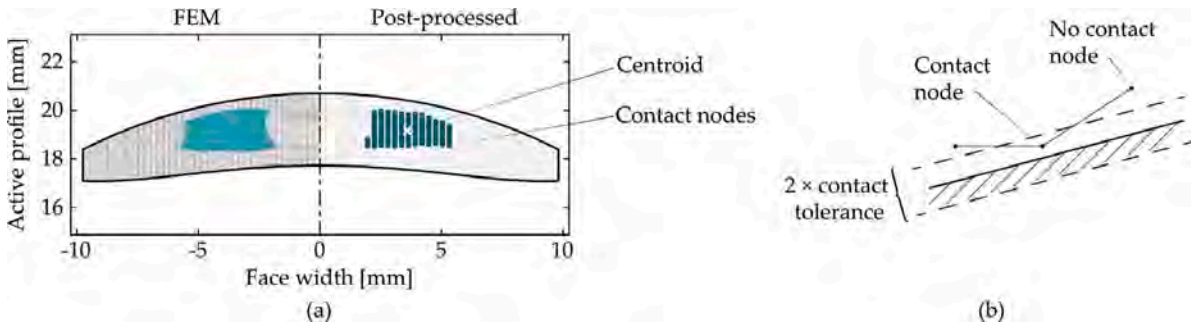

Fig. 5. Contact nodes definition: (a) contact status output from FE solver and post-processed contact nodes and centroid, and (b) check of node contact with the contact tolerance definition (adapted from [58]).

3.4.3. Tooth root stresses

Tooth root stresses are obtained in every element of the fillet region of the traction part of each tooth (Fig. 6(a)). Although compression side root stresses are higher than those from the traction side [20,59,60], only the traction side stresses were analyzed as these are critical for tooth root fatigue life.

The component of the stress tensor reflecting the bending stress of the gear hub is the stress value analyzed in this work, i.e. the component in the transverse direction to the tooth. For this reason, the bending direction corresponds to $\sigma_{22} = \sigma_{\theta\theta}$, taking into account the cylindrical coordinate system in which the model is built (Fig. 4(b)).

The stiffness of the hexahedron element type employed in the model is formed using eight Gaussian integration points (type 7 in Marc solver [58]). To this end, as depicted in Fig. 6(a), stress values in each element are calculated at every integration point of the hexahedral element. Nodal values are then obtained by interpolating those values linearly from the element surface integration points to the nodes of the element [58] (Fig. 6(b)).

Tooth root stresses are calculated in all the teeth (Fig. 7(a)), however, due to the high mesh density and complex geometry, values are still difficult to see without the mesh (Fig. 7(b)). That is why traction side teeth projections are illustrated in this research as shown in Fig. 7(c). Here, the tilting position tooth root stress distribution is shown in the whole teeth (active profile and root). Moreover, to compare different working conditions the tooth root stress distribution along the face width is represented (the maximum tooth root stress radius), as shown in Fig. 7(d).

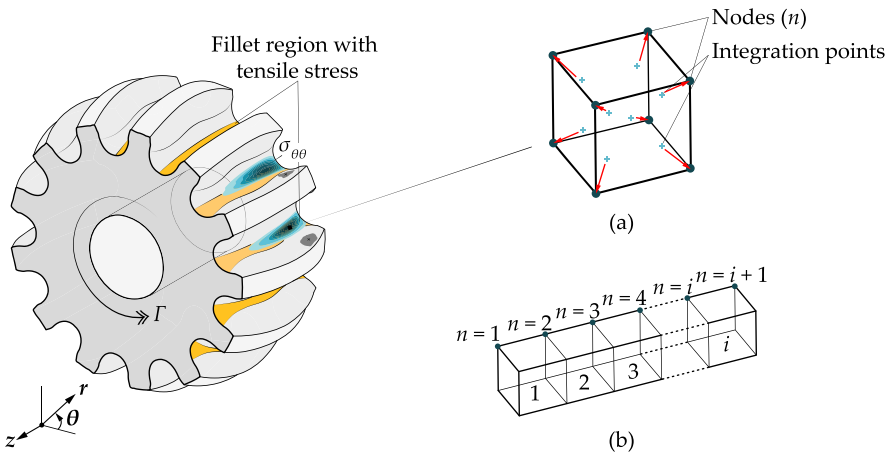

Fig. 6. Tooth root stress determination region: (a) nodal stress calculation from FE solver, and (b) representative stress nodal value for each element.

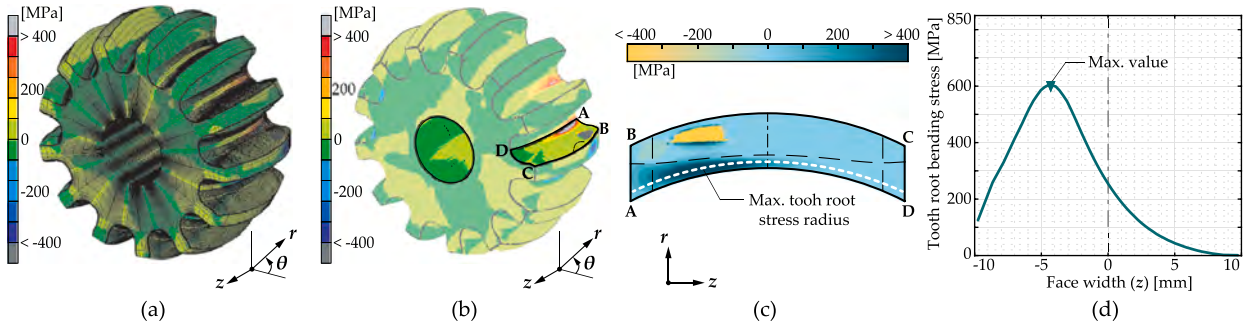

Fig. 7. Tooth root stress representation along the research: (a) tooth root bending stress in the whole gear coupling with the FE mesh, and (b) without the mesh, (c) tilting position traction side tooth root stress projection, and (d) maximum tooth root stress radius along the face width.

4. Definition of the case of study and types of analysis

In this research, the behavior of highly crowned spherical gear couplings is analyzed using a geometry with the following distinguishing features, and based on an industrial application of a roll-leveling machine [5,33]:

- Small pitch diameter.
- Small number of teeth.
- Small crowning radius, which involves a large amount of longitudinal crowning.
- Hub tooth surface with undercut sections due to the small crowning radius.
- High maximum working misalignment angle ($\gamma_{max} = 7.5°$).

The parameters of the case study are described in Table 1. A common carburized and quenched 15NiCr11 steel is used in the spherical gear coupling model defined by its linear elastic properties (Table 1).

Loaded tooth contact analysis was conducted following the indications of Section 3 in Marc solver [61], a general-purpose FE analysis computer program.

Two types of static simulations were performed, with two different objectives:

- Single toothed gear coupling model
  The aim is to understand the evolution of the contact pattern in terms of the angular position when working at high misalignment angles, and its impact on tooth root stresses.
  Without the convective effects of the adjacent teeth, it is analyzed as a function of the applied torque and misalignment angle. The model is composed of a single hub and sleeve tooth at a certain angular position θ_i, as shown in Fig. 8(a). The static analysis is repeated for several angular positions distributed in the cycle of meshing, under the same working conditions. The angular position θ_i of each analysis varies between 0 and $(2\pi - 2\pi/z)$, i.e., $\Delta\theta_i = \pi/9$ rad, with a total of 20 angular positions simulated for each working condition. In each simulation, the contact pattern, and the tooth root stress distribution are obtained directly from the FE solver, with the procedure described in Sections 3.4.1 and 3.4.3.

Table 1
Design parameters, operating conditions, and material properties for the highly crowned spherical gear coupling case study.

Parameter	Case study
Pitch diameter, d_p [mm]	39
Normal module, m_n [mm]	3
Number of teeth, z [–]	13
Normal pressure angle, α [°]	30
Aspect ratio, b/d_p [–]	0.5
Backlash, j_n [mm]	0.285
Crowning radius, r_c [mm]	24
Misalignment angle, γ [°]	0–7.5
Applied torque, Γ [Nm]	0–1500
Young's modulus, E [GPa]	210
Poisson coefficient, υ [–]	0.33
Density, ρ [kg/m^3]	7850
Yield stress, σ_y [MPa]	850
Ultimate stress, σ_u [MPa]	1010
Fatigue stress limit, σ_e [MPa]	520

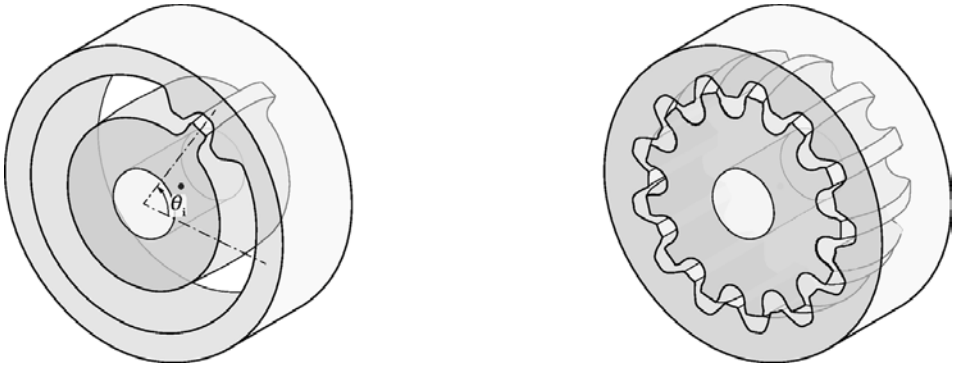

Fig. 8. Types of FE model analysis: (a) single toothed gear coupling, and (b) complete gear coupling.

- Complete gear coupling model
  The goal is to understand the load distribution based on the number of teeth in contact, and its effect on the tooth root stress history.
  This is also examined as a function of the applied torque and misalignment angle. The model is composed of all the teeth in the hub and sleeve as depicted in Fig. 8(b). The contact position, the number of teeth in contact, the load distribution, and the tooth root stress distribution are obtained from the FE solver, following the procedures in Sections 3.4.1–3.4.3.

5. Results

5.1. Mechanical behavior of single toothed gear coupling as a function of the angular position

5.1.1. Contact pattern evolution

Fig. 9 shows the active profile of the hub with the contact pattern in terms of the working conditions (Γ and γ). As it can be observed in Fig. 9(a), the contact pattern evolves from a centered and stable position in aligned conditions (point contact), to a wider and longer contact pattern as the misalignment angle increases (lemniscata shape). Indeed, it is observed that the contact amplitude ($\delta_{\max}$) increases, while it remains centered around the reference section of the hub.

In the case of a constant misalignment angle in Fig. 9(b), it can be seen that as torque increases the contact pattern is flattened. However, this has a negligible effect on the amplitude. Moreover, contact is spread over the pitch diameter as load increases, which is consistent with the literature [8,24]. This confirms that the behavior of highly crowned spherical gear couplings is consistent with them at this point.

The maximum contact displacement from the reference section ($\delta_{\max}$) can be seen in Fig. 9(c) and (d) as a function of the misalignment angle and the applied torque, respectively. These values correspond to the teeth in the tilting angular position, as being the ones with the maximum displacement. It can be seen that the misalignment angle is the main contributor to the variation of the contact position along the face width. The influence of torque arises from the stiffness of the component and is nearly negligible.

5.1.2. Tooth root stress evolution

Fig. 10 shows the maximum tooth root stress distribution along the contact path of the hub at a constant misalignment angle of 6° (Fig. 10(a)). Tooth root stresses in Fig. 10(b) are normalized relative to the maximum tooth root stress value in the pivoting position (Eq. (13)) to depict their variation depending on the contact position along the face width, i.e., angular position.

$$\sigma_{\text{normalized}} = \frac{\sigma}{\sigma_{\text{pivoting}}} \tag{13}$$

It is observed that the maximum value of the tooth root stress along the face width is positioned right at the contact section. Moreover, this position evolves together with the contact pattern, that is, it is shifted from the reference section as the contact displaces. It can also be seen that tooth root stresses increase up to 10% from the pivoting position (contact in the reference section) to the tilting position (most displaced contact point). This demonstrates that tooth geometry and stiffness affect tooth root stresses in misaligned conditions, regardless of the load distribution. The slight non-symmetry of tooth root stress in symmetrical angular positions is linked to the twist-effect phenomena present in highly crowned hub tooth surfaces [8].

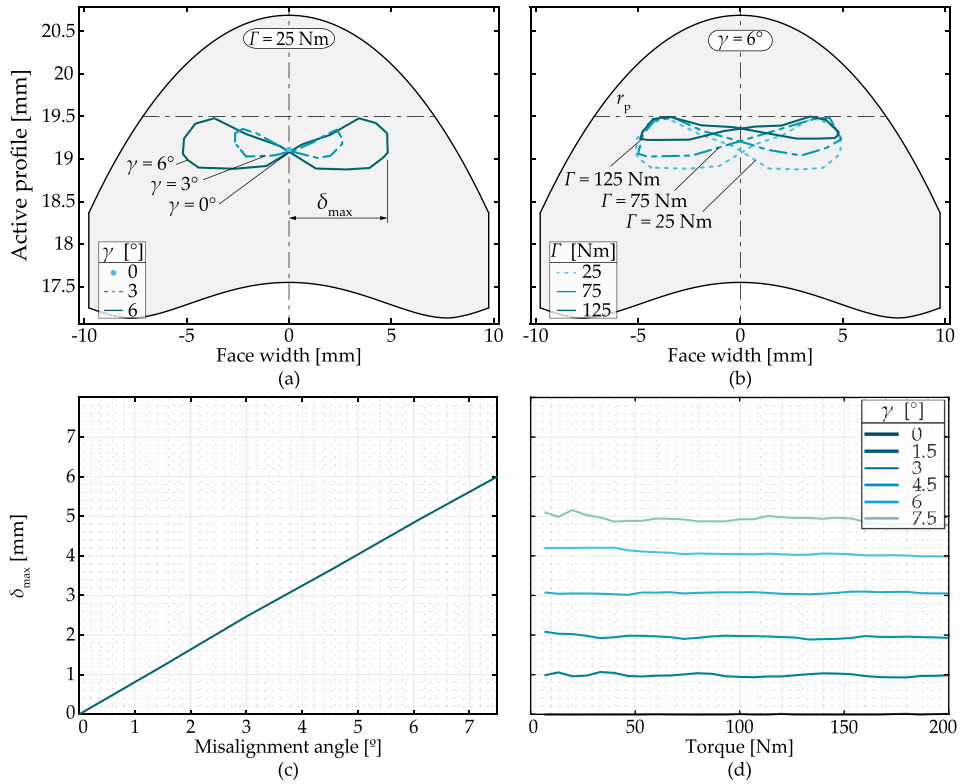

Fig. 9. Contact pattern centroid evolution for every angular position and the variation of the maximum displacement of the contact point (δ_{max}): (a) contact pattern centroid evolution as a function of the misalignment angle for a constant torque applied $\Gamma = 25$ Nm, and (b) as a function of the applied torque for a constant misalignment angle $\gamma = 6°$, (c) δ_{max} as a function of the misalignment angle, and (d) δ_{max} as a function of the applied torque.

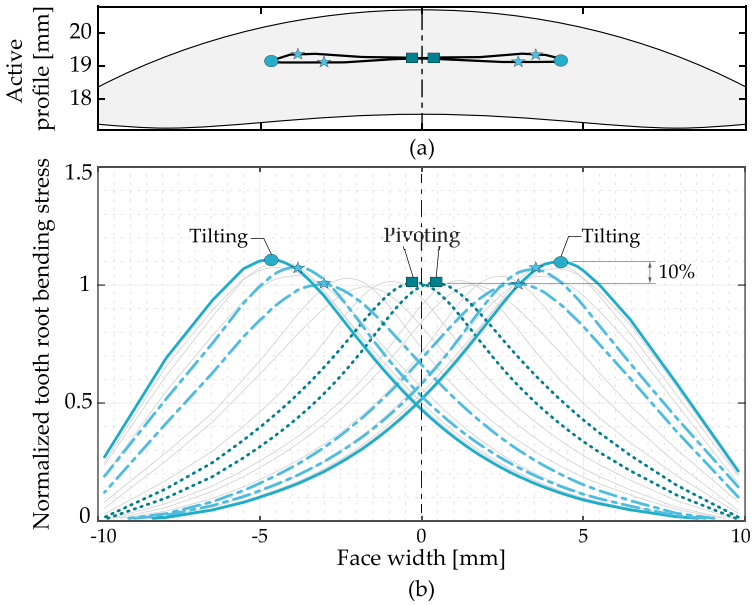

Fig. 10. (a) contact pattern centroids, and (b) maximum tooth root stress distribution along the face width according to the angular position for $\Gamma = 100$ Nm and $\gamma = 6°$.

5.2. Mechanical behavior of complete gear coupling as a function of the misalignment angle and torque

5.2.1. Stiffness

Fig. 11(a) shows the relationship between the applied torque and the angular deflection of the gear coupling, i.e., it reflects the stiffness of the component. It can be observed that the angular deflection increases as the misalignment angle increases. This is fundamentally based on the lower number of teeth which are transferring the applied torque.

At low misalignment angles ($\gamma < 1.5°$), the slope (Fig. 11(b)) of this trend remains quasi constant as a function of torque. Indeed, with all the teeth making contact the increase of stiffness mainly resides in the existence of a bigger contact area due to the tooth surface deformations.

As the misalignment angle increases, stiffness values are reduced. Moreover, the increase of the slope in Fig. 11(b) is observed as more teeth make contact as torque increases. For higher misalignment angles ($\gamma = 6°$ or $\gamma = 7.5°$), a quasi constant slope is not observed as torque values are not big enough so that all the teeth make contact.

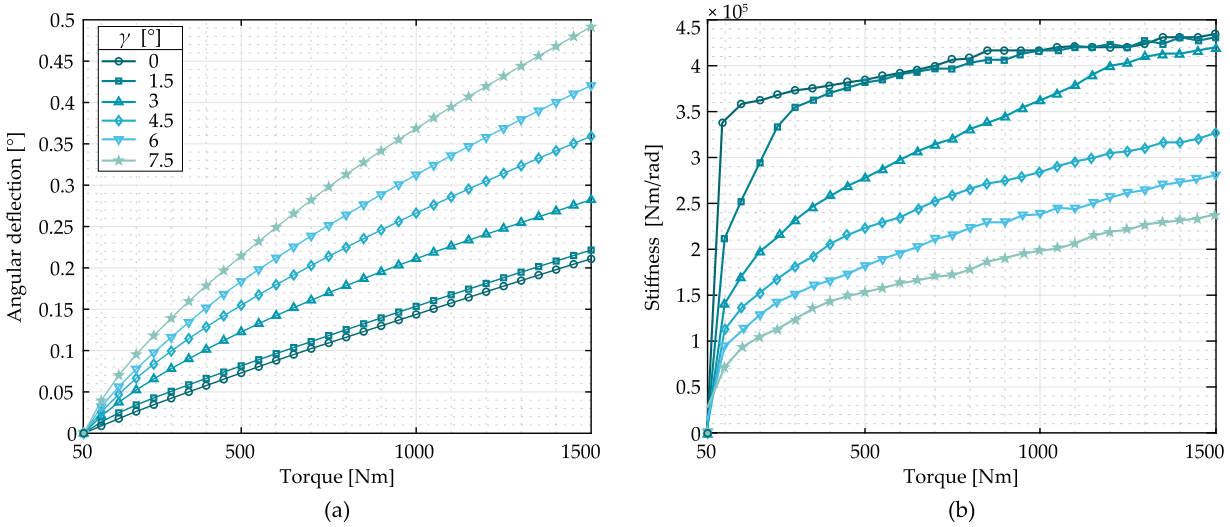

Fig. 11. (a) angular deflection, and (b) stiffness of a highly crowned spherical gear coupling as a function of the applied torque.

5.2.2. Contact pattern evolution

Compared to Section 5.1.1 (where all tooth positions are considered without the convective effects of adjacent teeth), the contact pattern no longer shows the lemniscata shape at high misalignment angles. What is more, the number of teeth in contact is reduced and principally located in the tilting position (most displaced positions from the reference section), as can be seen in Fig. 12. The contacting teeth centroid is represented together with the arrows showing that contact passes from one half of the active profile to the other.

The evolution of the contact pattern as a function of the applied torque or the misalignment angle is not represented for the purpose of simplicity, as it presents the same behavior as the one shown in Fig. 9 for the single teethed gear coupling.

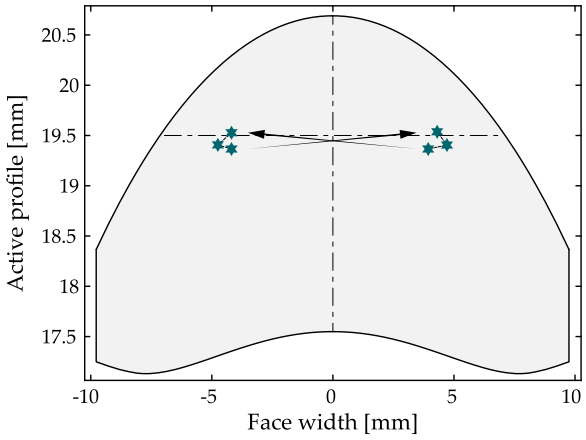

Fig. 12. Contact pattern centroids for $\Gamma = 1000$ Nm and $\gamma = 6°$.

5.2.3. Load distribution

Fig. 13 describes the load distribution in terms of the misalignment angle and the applied torque (bar colors). Each set of bars refers to one of the teeth of the gear coupling. The abscissa axis shows the angular position of the tooth, while the ordinate axis represents the percentage of the total load carried by each tooth in that angular position. Pivoting and tilting positions are also marked for ease of understanding. The last set of bars is the same as the first, to represent the whole circular load distribution.

It is observed that at low misalignment (γ = 1.5°) load is more evenly distributed than at higher misalignment angles, as the number of teeth in contact is higher. Moreover, it can be seen that the teeth which support the highest loads are those in the tilting positions, as they are the first entering into contact, even at low misalignment.

Furthermore, lower torques are the most critical ones in terms of load distribution, since very few teeth come into contact, i.e., the deformation caused by the torque is smaller than the angular backlash. Indeed, the load is mainly shared among three to four teeth when the misalignment angle increases. It can also be seen that the load in the tilting angular position is increased as the misalignment angle increases. At the same time, the load supported by those teeth in the pivoting angular position decreases or even loses contact as the misalignment angle increases. In addition, regardless of the misalignment angle, when torque is increased, as tooth deflections are greater than the clearance, more teeth come into contact and load distribution is more evenly shared. In this manner, the load supported by all the teeth gets closer to the aligned case: for the tilting position the supported load decreases, while for the pivoting position it increases.

To better understand the sequence in which load is distributed, Fig. 14 shows the cumulative percentage of load carried by the teeth engaged in the spherical gear coupling at different misalignment angles. The slashed line shows the case of the aligned conditions where a constant slope increase can be seen, meaning an equal load distribution among all the teeth. However, in misaligned conditions, the curves no longer present a constant slope and shift away from the aligned curve as torque decreases.

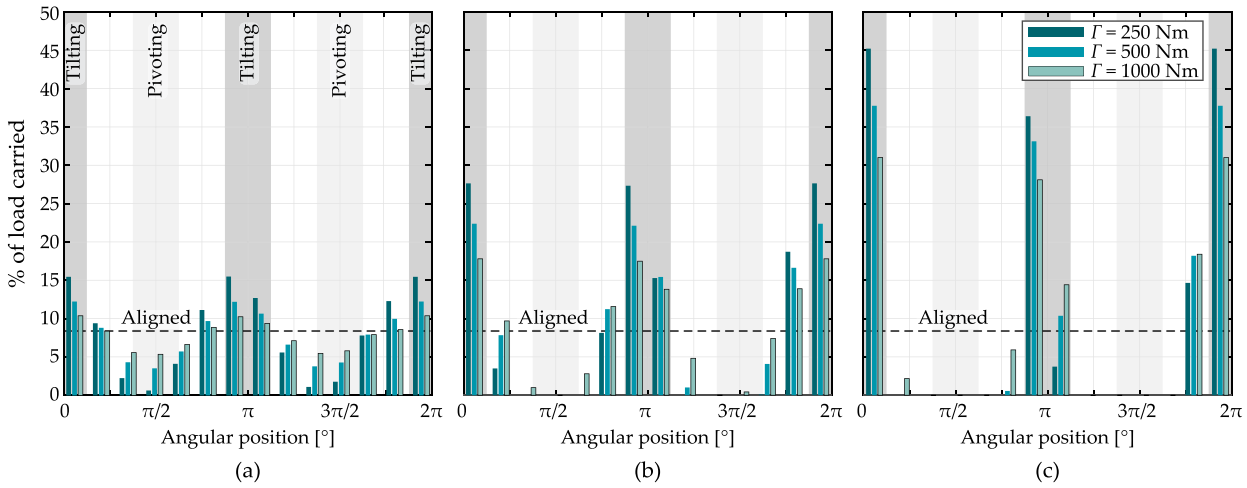

Fig. 13. Effect of the applied torque and the misalignment angle (a) γ = 1.5°, (b) γ = 3°, and (c) γ = 6° in the load distribution of a highly crowned spherical gear coupling. (For interpretation of the references to color in this figure legend, the reader is referred to the web version of this article.)

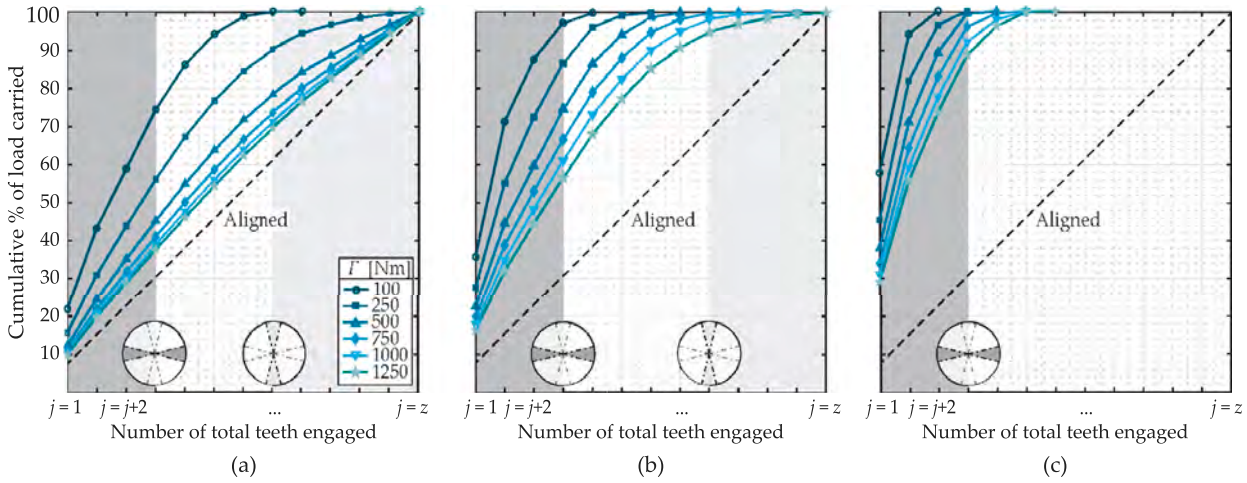

Fig. 14. (a) cumulative percentage of load carried by the teeth engaged at (a) γ = 1.5°, (b) γ = 3°, and (c) γ = 6° as a function of the applied torque.

Moreover, as the misalignment angle increases the curves are more shifted away from the aligned case, which means fewer teeth in contact with less homogeneous load distribution.

The curves present a steep slope among the first teeth engaged (those in the tilting angular position), while as the load is spread over more teeth, the slope decreases. Indeed, this demonstrates that the last teeth engaging (those in the pivoting angular position) contribute nearly nothing to the total load transferred by the gear coupling.

5.2.4. *Tooth root stresses*

Maximum tooth root stress

In Section 5.1.2 it is shown that the maximum tooth root stress position displaces considerably from the reference section in the presence of a misalignment angle, moving together with the contact point. In this section, the modification of the tooth root stress value due to the non-uniform load distribution among the teeth in presence of the misalignment angle is discussed.

From the load distribution analysis, it is concluded that teeth in the tilting angular position are the ones that support the highest loads, thus they are the ones suffering the highest tooth root stresses. Fig. 15(b) shows the tooth root stress distribution of the tilting angular position along the face width as a function of the misalignment angle. It depicts how as the contact centroid displaces from the reference section (Fig. 15(a)), tooth root stress distribution is no longer symmetric. It is also shown how the maximum value increases with the misalignment angle, and shifts together with the contact centroid along the face width direction.

Fig. 15(c) shows the stress distribution on the traction side of the tooth of the hub. Contact stresses are not displayed since it is not the objective of this research. It can be seen that stresses decrease drastically after the contact, which may lead to think that not all the face width of the gear coupling is supporting the load as already described in [20,22]. Moreover, it is observed that there is no stress concentration or discontinuity when undercutting sections start, even if higher values are observed when the contact point is close to them ($\gamma = 6°$).

Even if the maximum tooth root stress occurs at the tilting angular position, for the aim of comparing, Fig. 16 shows the maximum stress values of (a) tilting and (b) pivoting angular positions as a function of the applied torque and the misalignment angle.

It can be seen that stress values in pivoting angular positions are very low and do not follow the same trend as those in the tilting position. This is because, as shown in the previous section, only at low misalignment angles ($\gamma \leq 1.5°$) all the teeth in the gear coupling are in contact, and thus, as torque increases the stresses increase in either of the positions.

However, when the misalignment angle increases the number of teeth in contact decreases, especially those in the pivoting position. In consequence, the stress values in the pivoting position decrease, as teeth in the tilting position support the highest stresses. Moreover, it can be observed that for the pivoting position (Fig. 16(b)) at lower torques no stresses (due to the loss of contact) are supported by the teeth.

These results clearly remark that stress values vary significantly according to the angular position of the gear coupling and, thus, when sizing according to tooth-root fatigue it becomes very important to analyze the tooth root stress cycle.

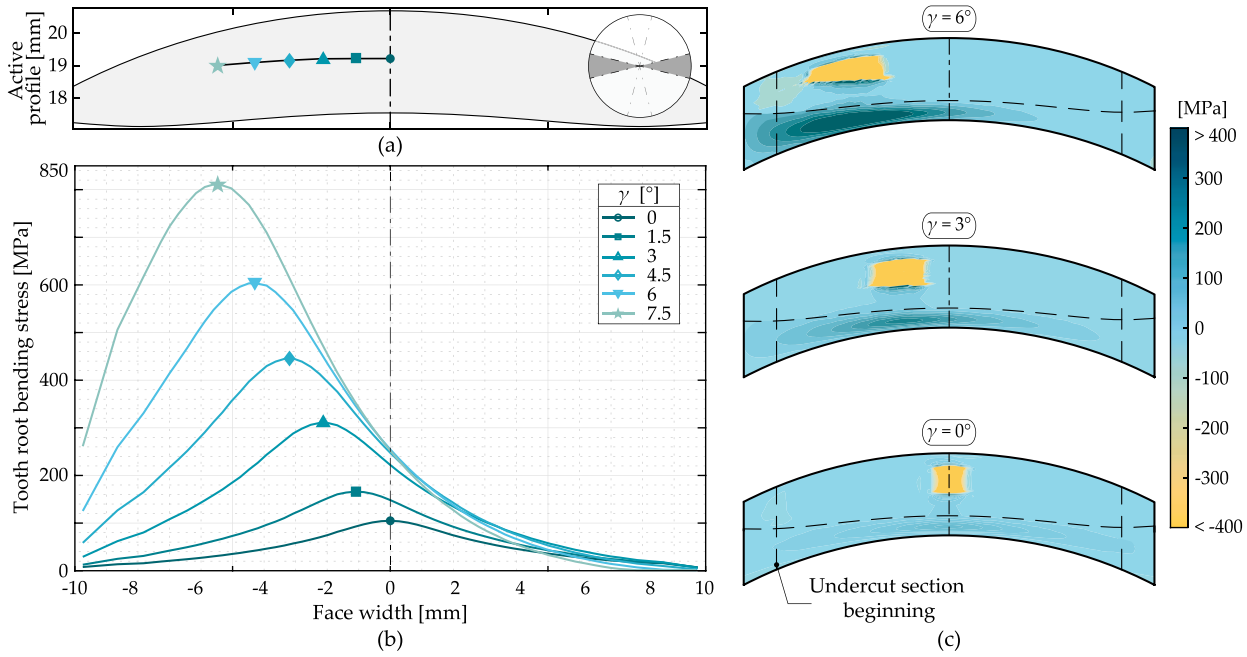

Fig. 15. (a) the centroid evolution, and (b) the tooth root bending stress along the hub face width of the tilting angular position at $\Gamma = 500$ Nm in terms of the misalignment angle, together with (c) the stress distribution in the traction side of the tooth surface.

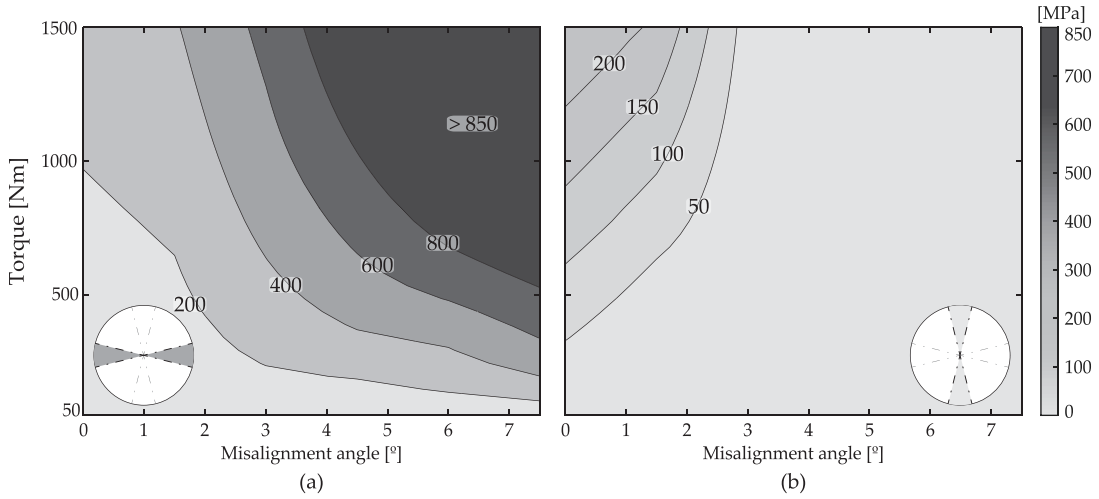

Fig. 16. Maximum tooth root bending stress in terms of the applied torque and misalignment angle (a) in the tilting position, and (b) in the pivoting position.

Tooth root stress cycle

It has already been seen that the stress state at different angular positions is different. That is why, with the aim of better understanding the behavior towards fatigue tooth root breakage, Fig. 17 shows the tooth root stress evolution at various sections along the face width to analyze if the maximum stresses are always located at the same section. The different positions shown in Fig. 17 at a constant torque of 500 Nm are: (a) the reference section, (b) the contact section in the tilting position which varies together with the misalignment angle, and (c) the undercut beginning section.

It is observed that the highest bending stresses occur in the contact (Fig. 17(b)) and in the undercutting (Fig. 17(c)) sections at the tilting position. For the case of the undercutting section, it is seen that stresses along the cycle are very low and close to the value of the aligned case. Indeed, it is shown that tilting positions are a stress concentration location along the cycle, which will need to be considered especially when the contact point displaces due to the misalignment angle nearby the undercutting section (e.g., see stress value increase between the contact section and the undercutting section at 0 rad for $\gamma = 7.5°$).

With regard to the contact section (Fig. 17(b)), the stress cycle is also characterized by the peak values in the tilting position, while it is more homogeneous along the rest of the cycle at low misalignment angles. At high misalignment angles, stress values in parts of the cycle (i.e., pivoting positions) are null since the teeth lose contact.

Concerning the reference section (Fig. 17(a)) of the gear hub, the stress cycle is close to that of the contact section, while it does not present so high values in the tilting position. Moreover, it can also be seen that in each revolution, a tooth will pass twice through each stress state. However, when getting closer to the edges of the gear coupling (e.g., the undercutting section) it can be observed that in each revolution there is just one stress cycle. In consequence, this is another reason why the spherical gear coupling bending fatigue differs from what has been previously described in the literature.

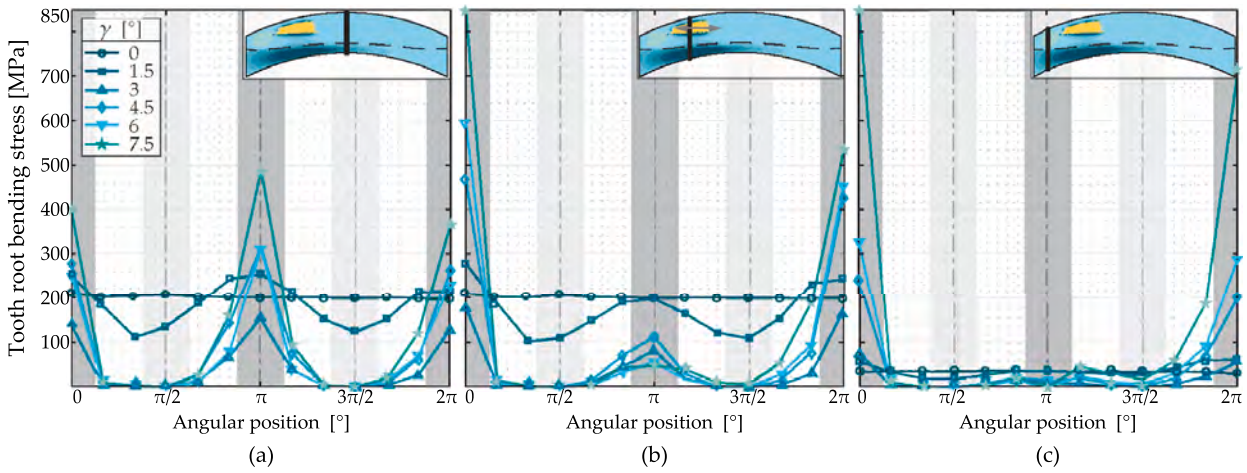

Fig. 17. Maximum tooth root bending stress cycle at $\Gamma = 500$ Nm at: (a) the reference section, (b) the contact section in tilting position, and (c) the undercut beginning section.

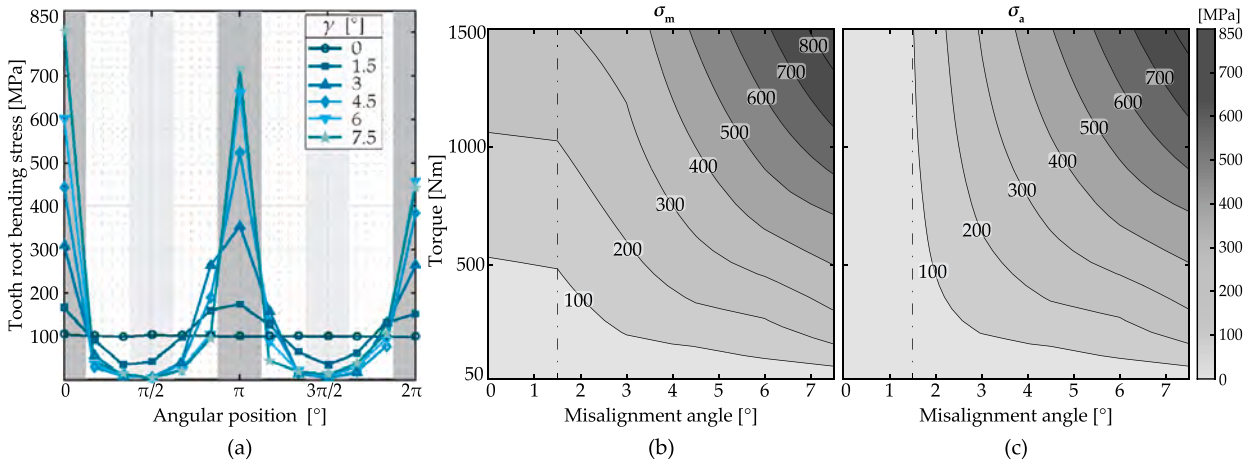

Fig. 18. (a) maximum tooth root bending stress cycle of a gear coupling at $\Gamma = 500$ Nm in terms of the misalignment angle, (b) the mean, and (c) the alternating stress level in terms of the applied torque and the misalignment angle.

Since the mechanical behavior varies considerably from section to section, Fig. 18(a) presents the general case of maximum tooth root bending stresses to examine the fatigue cycle endured by the gear coupling hub. The maximum stress values are in the tilting position and the lower (or even null) in the pivoting positions. Moreover, the double cycle supported by the gear coupling in each revolution is observed. Indeed, each tooth will pass twice through each position in each revolution.

According to this cycle, Fig. 18(b) and (c) represent the mean and alternating stress level of the cycle in terms of the applied torque and misalignment angle. In these graphs, two different trends can be observed (divided with a slash and dotted line). The first behavior is up to $\gamma \leq 1.5°$, where a sinusoidal fluctuating stress cycle is observed (positive fatigue stress ratio, $R > 0$). Here, teeth do not completely lose contact in any angular position, and stress values oscillate around the stress value of the aligned case.

The second behavior arises from $\gamma > 1.5°$, where teeth lose contact in the pivoting position, thus stresses descend to zero in those angular positions. This produces a repeated tensile (or pulsating tension) stress cycle ($R = 0$). This pulsating stress cycle has not been previously discussed in the literature related to gear coupling tooth root fatigue analysis, and hence, this work highlights that the behavior is more complex and that it needs a deeper understanding.

6. Discussion

Spherical gear couplings working at high misalignment angles have shown to have a very complex and different mechanical behavior from what has been previously analyzed in the specialized literature. From the tooth root sizing equations described in the introduction, the importance of two coefficients to account for the influence of the misalignment angle was shown: the load sharing factor (k_{ls}), and the load distribution factor (k_m). In the following paragraphs, the influence of both coefficients will be discussed based on the results obtained from the loaded tooth contact analysis.

Concerning the load sharing factor, one of the most remarkable aspects of highly crowned spherical gear couplings working at high misalignment angles is the reduction of the number of teeth in contact depending on the working conditions (Γ and γ). Furthermore, it has also been seen that not all the teeth support the load equally, which is in agreement with some works of the literature [22,34,62]. Indeed, due to the non-uniformity of the load distribution, knowing the number of teeth in contact is sometimes not sufficient to determine the maximum tooth root stresses. That is why some authors [34,62,63] propose determining the effective number of teeth in contact (C_{eff}), or which is equivalent the overload coefficient (k_F). This is defined following Eq. (14), and is a more representative value than the number of teeth in contact since it considers the number of teeth which are really transferring the load. This value is obtained by dividing the average load supported by each tooth (Γ_{avg_j}), and the load carried by the most charged one (Γ_{max_j}). For instance, in aligned conditions $C = C_{\text{eff}}$, that is $k_F = 1$, meaning all the teeth are equally loaded.

$$C_{\text{eff}} = \frac{\Gamma_j}{\Gamma_{\text{max}_j}} = \frac{\Gamma/z}{\Gamma_{\text{max}_j}} = \frac{1}{k_F} = \frac{1}{k_{ls}^*} \tag{14}$$

In Fig. 19, both, the number of teeth (a) and the effective number of teeth (b) are shown. It can be seen that as the applied torque decreases and the misalignment angle increases, the number of teeth in contact decreases drastically. Moreover, it is observed that even if in applications with $\gamma \leq 2°$ and $\Gamma \geq 800$ Nm all the teeth are in contact (Fig. 19(a)), only the 80% of them are transferring the charge (Fig. 19(b)). Furthermore, working conditions with less than 20% of their teeth carrying the load is wide. This will imply tooth root stresses which can be more than five times higher than those supported under aligned conditions.

The commonly used criteria in the literature for sizing is considering that half of the teeth are in contact, regardless of the geometry or working conditions [14,22,42]. In Fig. 19 this value is highlighted, and it is clearly depicted that this criterion is very conservative when applied to low misalignment angles. However, for higher misalignment angles (especially in lower torques), this

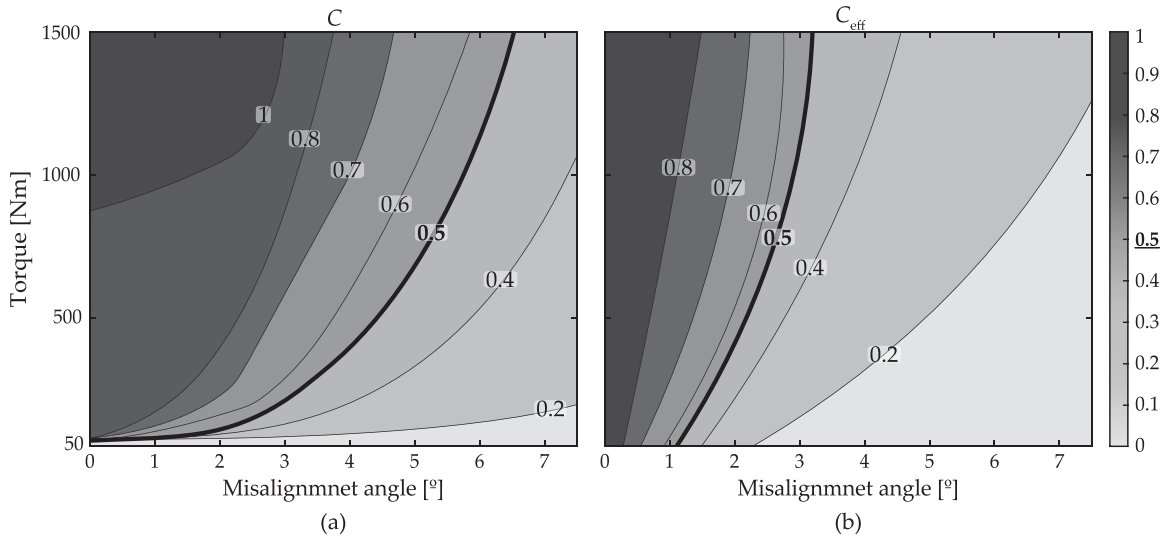

Fig. 19. (a) number of teeth in contact C, and (b) effective number of teeth in contact C_{eff} as a function of the applied torque and the misalignment angle compared to the criterion of half of the teeth in contact [14].

criterion undersize the component, which may lead to non-compliance with the technical requirements or premature failure. It can be observed that the undersized area is greater if the effective number of teeth is considered, concluding that C_{eff} is a parameter that must be taken into account during sizing.

AGMA 945 B20 [22] hard codes a value of 2 or 3 for the load sharing coefficient giving as a reference the criteria of half of the teeth carrying the load, thus in this work the overload coefficient k_F is defined to substitute it in the sizing equation by the k^*_{ls} coefficient.

On the other hand, concerning the load distribution factor, another remarkable behavior of highly crowned gear couplings working at high misalignment angles is the displacement of the contact point along the face width of the active profile. The contact point and the contact pattern are in agreement with the literature [29–31]. Nevertheless, these works were oriented to low misalignment angles $\gamma \ll 1°$ and geometries with high crowning radius (i.e., low longitudinal crowning), thus they had a high risk of edge or tip contact. To avoid this problem, the use of a tip relief has yielded satisfactory results in this research, even if further research is required to obtain the most optimized value.

Referring to the maximum displacement along the face width, Fig. 20 compares the values obtained in this research with those calculated with the equation from the literature (Eq. (2)) [11,32]. It is observed that the maximum displacement of the contact point (δ_{max}) is largely increased with the misalignment angle (torque has a negligible effect). Fig. 20 shows that differences between the LTCA and the literature are very relevant and that the literature values remain way lower. Indeed, these equations make simplifications in the geometrical parameters, as they are developed for geometries with low values of longitudinal crowning.

Thereby, there is a major displacement of the contact during the operation of a highly crowned spherical gear coupling compared to those commonly used in quasi-aligned conditions. Indeed, there will be an increase in the entrainment velocity thanks to which lubricant will properly flow across the tooth surfaces. In short, fretting wear will no longer be the main failure mechanism, and thus, tooth root fatigue failure should be analyzed to avoid component breakage.

In AGMA 945 B20 [22] the load distribution factor is obtained dividing the face width by the amplitude of the contact pattern. However, this might not be an appropriate definition for highly crowned hubs, as they give higher coefficients at aligned than at misaligned conditions. Indeed, as shown in Fig. 20 the contact pattern amplitude ($2\delta_{\text{max}}$) increases with the misalignment angle. For that reason, in this work, it is suggested to define the effective face width b_{eff} by calculating the length of the face width that is bearing stresses above the 70% of the maximum tooth root bending stress ($0.3\,\sigma_{\text{max}}$), as shown in Fig. 21(a). According to the figure, it can be observed that as the misalignment angle increases the effective face width does not significantly vary for a constant torque (e.g., $b_{\text{eff}} = 10.4$ mm for $\gamma = 6°$, while $b_{\text{eff}} = 11$ mm for $\gamma = 1.5°$). In Fig. 21(b) it is indeed observed that the normalized effective face width trends are close to the same values at high torque values. Different behavior for the case of $\gamma = 7.5°$ is observed, which may be linked to the excessive displacement of the contact point compared to the face width of the case study. These results suggest that the effective face width is a parameter linked principally to the gear hub geometry, and not highly dependent on the misalignment angle.

In consequence, a modified load distribution coefficient (k^*_m) is defined to use it in the tooth root stress equation, considering the effective face width results (Eq. (15)). As depicted in Fig. 21(b), values for all the misalignment angles but that from 7.5° gather around $b_{\text{eff}} \approx 10$ mm, which corresponds to a load distribution coefficient of $k^*_m \approx 2$.

$$k^*_m = \frac{b}{b_{\text{eff}}} \tag{15}$$

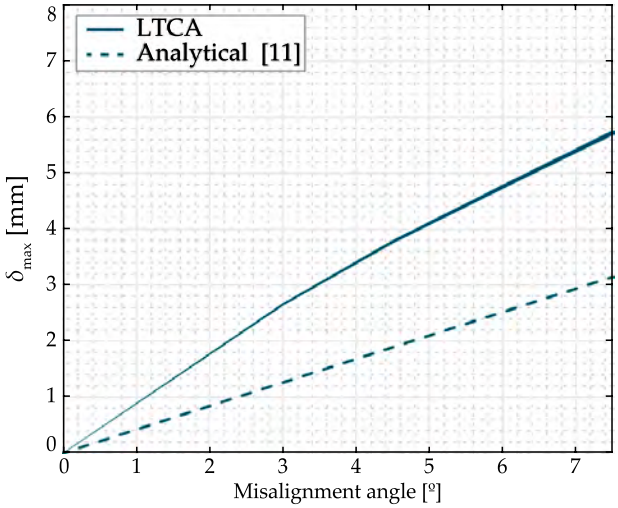

Fig. 20. Maximum contact position displacement amplitude for highly crowned spherical gear couplings compared with [11] Eq. (2).

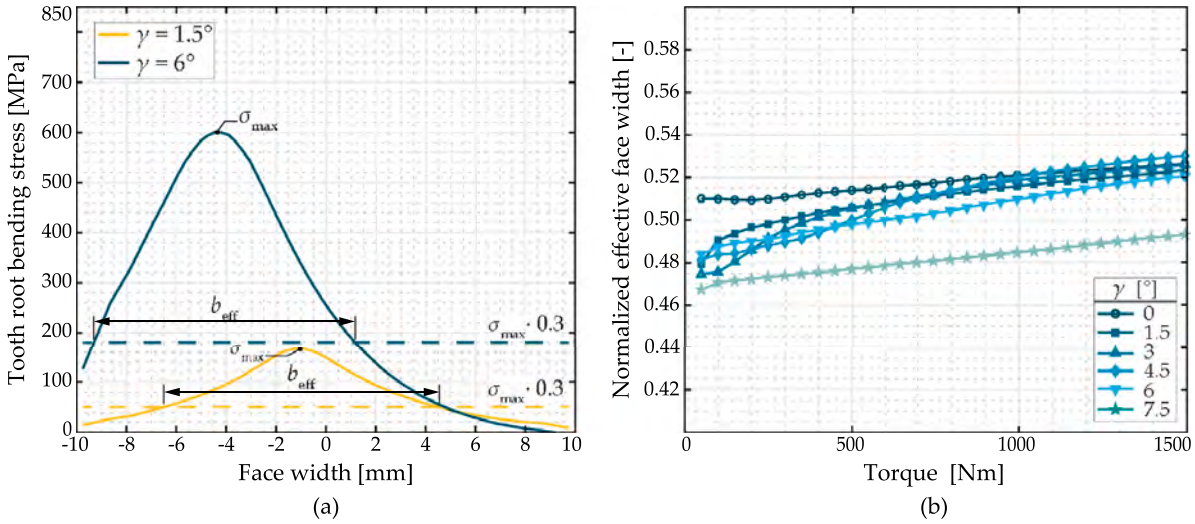

Fig. 21. (a) suggested definition of the effective face width (b_{eff}) for highly crowned gear couplings, and (b) normalized b_{eff} evolution as a function of the applied torque and the misalignment angle.

With k_m^* and k_{ls}^* coefficients already re-defined by the authors, bending tooth root stress is calculated based on [22] with Eq. (16).

$$\sigma = k_a\, k_m^*\, k_{ls}^*\, \frac{2000\, \Gamma}{d_p^2\, b\, Y} \tag{16}$$

Fig. 22(a) shows LTCA results at low and high misalignment angles against those obtained with [22] and its coefficients. Leaving aside the application factor ($k_a = 1$), the load sharing (k_{ls}) and load distribution (k_m) coefficients were defined following the recommendations of the standard. Even if the standard does not give coefficient values for such high misalignment angles, the most critical from those proposed were chosen.

From these results, it can be seen that even at low misalignment angles significant differences emerge, and undersize the stresses suffered by the component. This indicates one more time that the definition of the coefficients in the standard is not accurate enough to represent the mechanical behavior of highly crowned spherical gear couplings. It is indeed concluded that sizing spherical gear couplings working in high misalignment angles can result in a premature breakage of the component, due to the undersized results obtained with the current standard.

By contrast, Fig. 22(b) shows the results obtained with Eq. (16), where, k_m^* and k_{ls}^* factors are changed according to the results obtained with the LTCA. k_m^* is adjusted with the effective face width, and k_{ls}^* factor is based on the overload coefficient k_F, i.e., the effective number of teeth in contact ($k_{ls}^* = k_F = 1/C_{\text{eff}}$). It is observed, that calculated values are very close to those from the LTCA at low or high misalignment angles. The difference is below the 10% at $\gamma = 6°$ from $\Gamma = 200$ Nm onward; e.g., at 250 Nm LTCA gives 442.5 MPa, while those obtained with the modified coefficients in the standard gives 403.7 MPa.

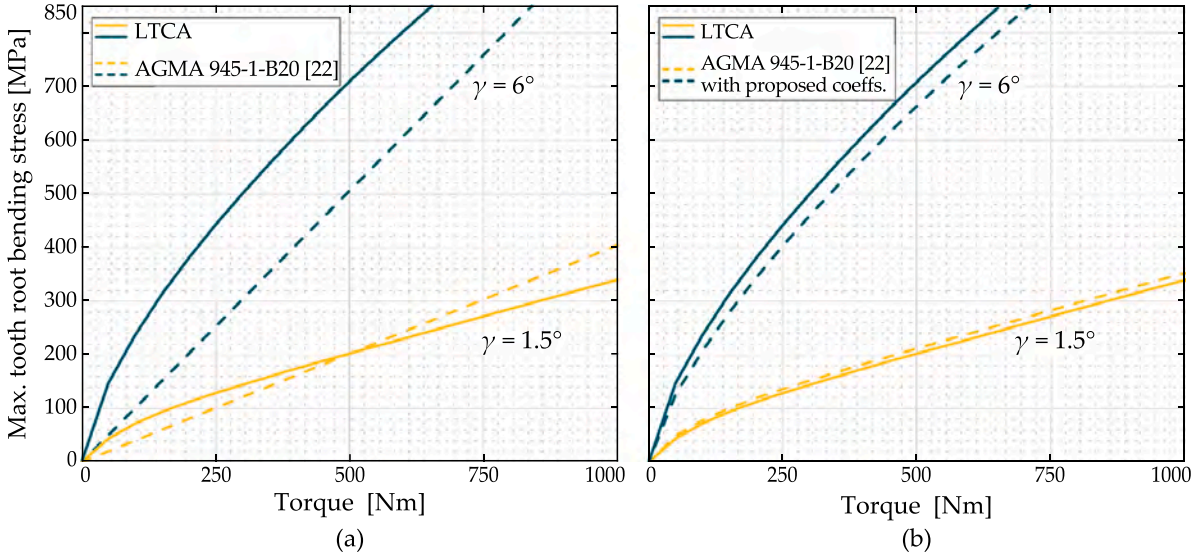

Fig. 22. Comparison of the maximum tooth root bending stress at $\gamma = 1.5°$ and $\gamma = 6°$: (a) between LTCA and [22], and (b) between LTCA and [22] with the proposed coefficients k_m^* and k_{ls}^* deduced from LTCA results.

That is why it is concluded that tooth root bending stress of highly crowned spherical gear couplings working at high misalignment angles can be accurately represented with a deeper analysis in the determination of the load sharing and load distribution factors. This analysis, among others, will enable ensuring a common and accurate procedure to determine tooth root stress of spherical gear couplings working at low or high misalignment angles.

7. Conclusions

This paper describes the mechanical behavior of highly crowned spherical gear couplings and the influence of the operating conditions by means of a FE model developed for this purpose. The research aims to provide a more accurate definition of the influencing variables when working at high misalignment angles, to enable non-oversized and competitive designs of spherical gear couplings. Moreover, the model presented here can be easily adapted to different geometries or working conditions.

From the LTCA and the comparison with the literature the following conclusions can be drawn:

(1) The number of teeth in contact decreases drastically to less than 40% of the total number of teeth of the gear coupling at low torque values and high misalignment angles $\gamma > 3°$. As a result, the stiffness of the component is reduced and tooth root stresses are increased considerably.
(2) In addition to the decrease in the number of teeth in contact, the misalignment angle induces a non homogeneous load distribution among those in contact.
(3) Tooth root bending stresses are influenced by the contact position variation in as much as 10% of the load supported.
(4) The stress state between tilting and pivoting angular positions changes considerably at high misalignment angles, which leads to a complex tooth root fatigue life. Due to the loss of contact of some of the teeth at high misalignment angles, the fatigue cycle changes from a sinusoidal fluctuating stress cycle ($\gamma \leq 1.5°$) to a pulsating tension stress cycle ($\gamma > 1.5°$). Consequently, the fatigue life of the component might be reduced.
(5) Sizing highly crowned spherical gear couplings to tooth root breakage with actual standards may lead to under sizing in some working conditions. As a consequence, an early breakage of the component and an increase in maintenance costs are expected.
(6) The bending tooth root stresses may be accurately predicted with a proper definition of the load distribution and the load sharing coefficients. To this end, it is essential to correctly define the effective face width and the overload coefficient.
(7) The contact pattern of highly crowned spherical gear couplings working at high misalignment angles spreads over more than 50% of the face with. This leads to adequate lubrication of the component, and thus decreases wear and fretting fatigue fracture risk of this type of component.

The proposed model allows for future work to focus on the influence of different design parameters, such as the pitch diameter, the number of teeth, the pressure angle or the aspect ratio in the load distribution, and the tooth root stress of highly crowned spherical gear couplings. Moreover, this will enable further understanding of the tooth root fatigue cycle. Finally, this analysis will enable a more accurate definition of the load distribution and the load sharing coefficients, taking into account the effect of the design parameters, and making it possible to obtain the proper value for sizing coefficients.

Declaration of competing interest

The authors declare that they have no known competing financial interests or personal relationships that could have appeared to influence the work reported in this paper.

Data availability

Data will be made available on request.

Acknowledgment

This research did not receive any specific grant from funding agencies in the public, commercial, or not-for-profit sectors.

References

[1] J.R. Mancuso, Couplings and Joints: Design, Selection and Application, Technology & Engineering. M. Dekker, 1986.
[2] S. Hahn, Coupling connections and splines, in: Encyclopedia of Automotive Engineering, John Wiley & Sons, 2014, pp. 1–14, http://dx.doi.org/10.1002/9781118354179.auto094.
[3] W. Herbstritt, J. Paluh, Mill spindle advanced gear design, Iron Steel Eng. 76 (7) (1999) 44–48.
[4] P. Krot, Transient torsional vibrations control in the geared drive trains of the hot rolling mills, in: IEEE International Conference on Control Applications, St. Petersburg, 2009, pp. 1368–1373, http://dx.doi.org/10.1109/CCA.2009.5280933.
[5] I. Ulacia, J. Larrañaga, A. Arana, A. Iñurritegui, J. Elizegi, Fatigue life prediction of spherical gear couplings, in: American Gear Manufacturers Association Fall Technical Meeting 2018, Illinois, 2018, pp. 202–207.
[6] F. Ohshima, S. Hirata, H. Yoshino, Study on tooth contact of gear couplings, Trans. Jpn. Soc. Mech. Eng. C 78 (786) (2012) 639–649, http://dx.doi.org/10.1299/kikaic.78.639.
[7] Y. Guan, X. Yang, Z. Fang, G. Chen, Comparative analysis of three geometric models for crown gear coupling, Mech. Mach. Theory 136 (2019) 269–283, http://dx.doi.org/10.1016/j.mechmachtheory.2019.02.016.
[8] A. Iñurritegui, I. Gonzalez-Perez, A. Arana, J. Larrañaga, I. Ulacia, Computerized generation and tooth contact analysis of spherical gear couplings for high misalignment applications, Mech. Mach. Theory 164 (2021) http://dx.doi.org/10.1016/j.mechmachtheory.2021.104408.
[9] P. Ku, M. Valtierra, Spline wear-effects of design and lubrication, J. Eng. Ind. 97 (4) (1975) 7, http://dx.doi.org/10.1115/1.3438738.
[10] S. Medina, A.V. Olver, Regimes of contact in spline couplings, J. Tribol. 124 (2) (2002) 351–357, http://dx.doi.org/10.1115/1.1403456.
[11] Y. Guo, S. Lambert, R. Wallen, R. Errichello, J. Keller, Theoretical and experimental study on gear-coupling contact and loads considering misalignment, torque and friction influences, Mech. Mach. Theory 98 (2016) 242–262, http://dx.doi.org/10.1016/j.mechmachtheory.2015.11.015.
[12] L. Xiao, Y. Xu, X. Sun, H. Xu, L. Zhang, Experimental investigation on the effect of misalignment on the wear failure for spline couplings, Eng. Fail. Anal. 131 (2022) http://dx.doi.org/10.1016/j.engfailanal.2021.105755.
[13] S. Locke, M. Burgess, S. Steve, W. Virginia, J. Corcoran, T. Hess, J. Joe, T. Hess, Coupling credible failure modes and owner options to intervene, in: 42th Turbomachinery Symposium, Texas, 2013, pp. 1–30.
[14] D. Dudley, When splines need stress control, Prod. Eng. 28 (1957) 56–59.
[15] X. Xue, Q. Huo, L. Hong, Fretting wear-fatigue life prediction for aero-engine's involute spline couplings based on Abaqus, J. Aerosp. Eng. 32 (6) (2019) http://dx.doi.org/10.1061/(asce)as.1943-5525.0001058.
[16] S. Leen, Fretting fatigue and wear of spline couplings: from laboratory testing to industrial application through computational modelling, in: Wear in Advanced Engineering Applications and Materials, World Scientific, 2022, pp. 1–44, http://dx.doi.org/10.1142/9781800610699.
[17] Y. Guan, J. Chen, Z. Fang, S. Hu, A quick multi-step discretization and parallelization wear simulation model for crown gear coupling with misalignment angle, Mech. Mach. Theory 168 (2022) http://dx.doi.org/10.1016/j.mechmachtheory.2021.104576.
[18] Z. Ye, Z. Chen, H. Lu, S. Wang, Z. Li, M. Yang, W. Wu, Analysis of parallel misalignment of gear coupling in rotor system using EEMD-median filter method, in: IEEE Advanced Information Technology, Electronic and Automation Control Conference (IAEAC), 2021, pp. 1113–1118, http://dx.doi.org/10.1109/IAEAC50856.2021.9390976.
[19] A. Iñurritegui, A. Arana, J. Larrañaga, I. Ulacia, Spherical gear coupling design space analysis for high misalignment applications, Mech. Mach. Theory 173 (2022) 104837, http://dx.doi.org/10.1016/j.mechmachtheory.2022.104837.
[20] Deutsches Institut für Normung, DIN 5466: Splined joints, calculation of load capacity, 2002.
[21] International Organization for Standardization, ISO 4156: Straight cylindrical involute splines, Geneve, 2005.
[22] American Gear Manufacturers Association, AGMA 945-1-B20: Splines – Design and application, Virginia, 2020.
[23] R. Beckmann, Beitrag zur Auslegung und Konstruktion von Balligzahn-Kupplungen (Ph.D. thesis), Chemmitz Technology University, 2005.
[24] R. Cedoz, M. Chaplin, Design guide for involute splines, Society of Automotive Engineers, 1994.
[25] M. Octrue, F. Blanc, D. Ghribi, Guide de demensionnement des accouplements à dentures bombées, CETIM, 2014.
[26] J. Hong, D. Talbot, A. Kahraman, Load distribution analysis of clearance-fit spline joints using finite elements, Mech. Mach. Theory 74 (2014) 42–57, http://dx.doi.org/10.1016/j.mechmachtheory.2013.11.007.
[27] E. Neale, Introduction to gear couplings, Tech. rep., Neale consulting engineers, 1980.
[28] F. Paddon, Application and selection of gear type spindles, Iron Steel Eng. (1960) 91–100.
[29] M. Alfares, A. Falah, A. Elkholy, Clearance distribution of misaligned gear coupling teeth considering crowning and geometry variations, Mech. Mach. Theory 41 (2006) 1258–1272, http://dx.doi.org/10.1016/j.mechmachtheory.2005.11.004.
[30] Y. Guan, Z. Fang, X. Yang, G. Chen, Tooth contact analysis of crown gear coupling with misalignment, Mech. Mach. Theory 126 (2018) 295–311, http://dx.doi.org/10.1016/j.mechmachtheory.2018.04.019.
[31] K. Nakashima, Teeth contact behaviour and load distribution of gear couplings, Trans. Jpn. Soc. Mech. Eng. 502 (Part C 54) (1988) 1302–1307, http://dx.doi.org/10.1299/kikaic.54.1302.
[32] F. Curà, A. Mura, Theoretical and numerical evaluation of tilting moment in crowned teeth splined couplings, Meccanica 53 (1–2) (2018) 413–424, http://dx.doi.org/10.1007/s11012-017-0730-1.
[33] J. Larrañaga, A. Arana, I. Ulacia, J. Esnaola, I. Torca, Misalignment effect on contact pressure and tooth root strength of spline couplings, in: 5th International Conference on Power Transmission-BAPT, Ohrid, Macedonia, 2016, pp. 1–6.
[34] J. Silvers, C. Sorensen, K. Chase, A new statistical model for predicting tooth engagement and load sharing in involute splines, in: AGMA - 10FTM07, 2010.

[35] K. Chase, C.D. Sorensen, B.J. DeCaires, Variation analysis of tooth engagement and loads in involute splines, IEEE Trans. Autom. Sci. Eng. 7 (4) (2010) 746–754, http://dx.doi.org/10.1109/TASE.2009.2033033.
[36] C. Bünder, Analyse der Beanspruchungen der Verzahnung von Zahnkupplungen (Ph.D. thesis), Technische Universität Dresden, 2000.
[37] J. Hong, D. Talbot, A. Kahraman, Effects of tooth indexing errors on load distribution and tooth load sharing of splines under combined loading conditions, J. Mech. Des. (2015) http://dx.doi.org/10.1115/1.4029282.
[38] M. Benatar, D. Talbot, A. Kahraman, An experimental investigation of the load distribution of spline joints under gear loading conditions, J. Adv. Mech. Des. 11 (6) (2017) 1–12, http://dx.doi.org/10.1299/jamdsm.2017jamdsm0084.
[39] F. Curà, A. Mura, M. Gravina, Load distribution in spline coupling teeth with parallel offset misalignment, Proc. Inst. Mech. Eng. C 227 (10) (2013) 2195–2205, http://dx.doi.org/10.1177/0954406212471916.
[40] P. Renzo, S. Kaufman, D. de Rocker, Gear couplings, J. Eng. Ind. (1968) 467–474.
[41] S. Lagutin, B. Utkin, A. Klochkov, Upgrading of the geometry of gear couplings, in: 7th International KOD Symposium, Hungary, 2012, pp. 27–30.
[42] G. Henriot, J. Boisset, Accouplements, alignement des axes, in: Engrenages: conception, fabrication, mise en oeuvre, fifth ed., Dunod, 1983, pp. 796–818.
[43] B. Volfson, Stress sources and critical stress combinations for splined shaft, J. Mech. Des. 104 (1) (1982) 551–556, http://dx.doi.org/10.1115/1.3256385.
[44] A. Elkholy, M. Alfares, Misalignment loads in splined gear couplings, Int. J. Comput. Appl. Technol. 15 (1–3) (2002) 128–137, http://dx.doi.org/10.1504/IJCAT.2002.000288.
[45] Z. Kahn, S. Wright, Finite element analysis of an involute spline, J. Mech. Des. 122 (2) (2000) 239, http://dx.doi.org/10.1115/1.533573.
[46] J. Kroczak, M. Dudziak, Analysis of the pitch deviation in involute splined connections, Mach. Dyn. Res. 37 (1) (2013) 65–71.
[47] D. Marano, M. Lorenzini, L. Mastrandrea, F. Pulvirenti, M. Turci, N. Fillault, Misalignment compensation spline design, in: American Gear Manufacturers Association Fall Technical Meeting 2019, Dallas, 2019, pp. 1–17.
[48] R. Vondra, K. Rehak, A. Prokop, Strain-stress analysis of gear coupling, Eng. Mech. 26 (2020) 520–523, http://dx.doi.org/10.21495/5896-3-520.
[49] C. Dupertuis, J. Ligier, Contact pressure in misaligned spline couplings, Mech. Ind. 21 (5) (2020) http://dx.doi.org/10.1051/meca/2020049.
[50] Y. Guan, Z. Fang, X. Yang, G. Chen, Effects of misalignment and crowning on contact characteristics of crown gear coupling, J. Mech. Eng. Sci. (2018).
[51] J. Wei, Y. Yao, K. Zhang, Contact analysis and surface optimization of crowning gear coupling, in: Proc. of the 2nd International Conference on High Performance and Optimum Design of Structures and Materials, Vol. 166, 2016, pp. 455–465, http://dx.doi.org/10.2495/HPSM160421.
[52] R. Heinz, Untersuchung der Kraft- und Reibungsverhältnisse in Zahnkupplungen für grobe Leistungen (Ph.D. thesis), TU Darmstadt, 1977.
[53] J. Pedrero, M. Pleguezuelos, M. Sánchez, Load sharing model for high contact ratio spur gears with long profile modifications, Forsch. Ing. 83 (3) (2019) 401–408, http://dx.doi.org/10.1007/s10010-019-00379-w.
[54] X. Xu, Y. Liang, S. Zuo, P. Tenberge, P. Dong, Y. Liu, S. Wang, Z. Wang, A novel tooth tip relief method for reducing micro-pitting of spur gears, Adv. Mech. Eng. 13 (9) (2021) 1–14, http://dx.doi.org/10.1177/16878140211044641.
[55] F. Litvin, A. Fuentes, Gear geometry and applied theory, second ed., Cambridge University Press, 2004, p. 818.
[56] J. Argyris, A. Fuentes, F. Litvin, Computerized integrated approach for design and stress analysis of spiral bevel gears, Comput. Methods Appl. Mech. Engrg. 191 (11–12) (2002) 1057–1095.
[57] I. Gonzalez-Perez, A. Fuentes, Implementation of a finite element model for gear stress analysis based on tie-surface constraints and its validation through the hertz's theory, Trans. ASME, J. Mech. Des. (ISSN: 10500472) 140 (2) (2017) 1–13, http://dx.doi.org/10.1115/1.4038301.
[58] MSC.Software, Marc 2019 - Volume B: Element Library, 2019.
[59] K. Fujita, F. Obata, K. Miyanishi, Gear tooth stress calculation method for heavily crowned gear, Bull. JSME 17 (104) (1974).
[60] K. Wesolowski, Dreidimensionale Beanspruchungszustaande und Festigkeitsnachweis Drehmomentbelasteter Zahnwellen-Verbindungen unter Elastischer und Teilplastischer Verformung (Ph.D. thesis), TIB Hannover, Düsseldorf, 1997, pp. 1–206.
[61] MSC.Software, Marc 2019 - User's Guide, 2019.
[62] B. De Caires, Variation analysis of involute spline tooth contact (Ph.D. thesis), Brigham Young University, 2006.
[63] J. Cavaillès, F. Groix, Etude de la répartition de la charge appliquée sur un accouplement délignable à petites dents fonctionnant en position délignée, Bull. Assoc. Tech. Marit. Aéronaut. (1971).

We live in a Newtonian world of Einsteinian physics ruled by Frankenstein logic.
—David Russell

D | Publication IV

Numerical-experimental analysis of highly crowned spherical gear couplings working in high misalignment applications

A. Iñurritegui[a], J. Larrañaga[a], A. Arana[a], I. Ulacia[a]

[a] *Mondragon Unibertsitatea, Department of Mechanical and Industrial Production, Arrasate-Mondragon, Pais Vasco, Spain.*

Received 08 December 2022; Revised 18 January 2023; Accepted 19 January 2023. Available online 14 February 2023; Version of Record 14 February 2023.

Mechanism and Machine Theory 183 (2023) 105260

Mechanism and Machine Theory 183 (2023) 105260

Contents lists available at ScienceDirect

Mechanism and Machine Theory

journal homepage: www.elsevier.com/locate/mechmt

Research paper

Numerical-experimental analysis of highly crowned spherical gear couplings working at high misalignment angles

Aurea Iñurritegui *, Jon Larrañaga, Aitor Arana, Ibai Ulacia

Mondragon Unibertsitatea, Department of Mechanical and Industrial Production, Arrasate-Mondragon, Pais Vasco, Spain

ARTICLE INFO

Keywords:
Spherical gear coupling
High misalignment
Meshing test
Contact pattern detection

ABSTRACT

Spherical gear couplings are characterized by their high capacity to transfer power between rotating shafts in highly misaligned conditions. They are usually small because of space restrictions and require a high amount of longitudinal crowning, which sometimes leads to undercutting profiles. These issues have been solved recently with analytical models for the generation of tooth surfaces that consider the hob thread surface, however, they are not experimentally validated. Likewise, it has been numerically concluded that the number of teeth in contact in high misalignment conditions decreases, and thus may fail by tooth root breakage. Nevertheless, published experimental tests for such high misalignment angles are scarce. This paper presents test techniques to study highly crowned spherical gear couplings, together with a test rig design adapted to high misalignment angles. The tooth surface geometry, maximum misalignment, stiffness, and contact pattern are compared. The results demonstrate that the analytical and numerical models employed accurately represent the mechanical behavior of spherical gear couplings working at high misalignment applications.

1. Introduction

Gear couplings are widely used to transmit power between shafts due to their high power density compared to other non-splined connections [1]. Spherical gear couplings are specifically designed to work with high misalignment angles (≫1°). Such couplings require tooth surfaces with considerable longitudinal crowning to obtain a favorable contact pattern when severe misalignment conditions ($3° \leq \gamma \leq 10°$) are present. In addition, this longitudinal crowning prevents interference and balances the clearance between the hub and the sleeve teeth, while increasing the contact ratio [2]. A large amount of longitudinal crowning (≫100 μm), together with the small tool path radius used in manufacturing, presents challenges when analytically generating the hub tooth surfaces of highly crowned spherical gear couplings. One of the most significant of these challenges is the appearance of singularities (corresponding to regions where undercut is present). For this reason, an analytical geometry generation model that accounts for the hob-threaded surface during the generation process has been developed by the authors [3]. This model presents advantages over other published models [4–8] for tooth geometries with small amounts of crowning, which do not generate undercutting sections. In addition, none of these models have been previously validated with experimental measurements.

Crowned gear couplings need to have a specific amount of backlash (or clearance) to prevent interference while withstanding a certain misalignment angle [5,9–11]. The angular backlash is the angle of rotation that exists when rotating the hub while keeping the sleeve stationary, i.e., from the point where the left flanks are in contact to the point where the right flanks are in contact [9,12]. As the tooth surface is crowned and misalignment exists, the clearance value will not be constant for all the teeth [2,13]. Indeed,

* Corresponding author.
E-mail address: ainurritegui@mondragon.edu (A. Iñurritegui).

https://doi.org/10.1016/j.mechmachtheory.2023.105260
Received 8 December 2022; Received in revised form 18 January 2023; Accepted 19 January 2023

Nomenclature

d_p	Pitch diameter of the gear coupling [mm]
E	Elastic modulus of the material [GPa]
k	Experimental stiffness value [Nm/rad]
m_n	Normal module [mm]
$m,\ n$	Number of grid points in the abscissa and ordinate direction [–]
pt	Number of points in the measured profile [–]
$\mathbf{r}$	Measured tooth profile vector
r_p	Pitch radius of the hub [mm]
r_β	Tool path radius [mm]
$r,\ \theta,\ z_f$	Cylindrical coordinate system for post-processing of FEM
s_n	arclength of the measured tooth profile [mm]
$x_f,\ y_f,\ z_f$	Cartesian coordinate system of the gear coupling
z	Number of teeth in the gear coupling [–]
α	Pressure angle [rad]
Γ	Applied torque [Nm]
γ	Misalignment angle [°]
$\gamma_{\max}$	Maximum misalignment angle (°)
$\gamma'_{x,z}$	Measured maximum experimental misalignment angle in $y_f\,z_f$ and $y_f\,x_f$ planes [°]
δ	Geometry deviations of the tooth surface in the normal direction [μm]
ϵ	Experimental deviation for the measured maximum misalignment [°]
θ	Angular rotation of the node in the hub [rad]
ν	Poisson coefficient of the material [–]
ρ	Density of the material [kg/m^3]
$\sigma_{y,u,e}$	Yield, ultimate and fatigue stress of the material [MPa]
$\tau_{h,s}$	Angular pitch of the hub, sleeve [rad]
φ_j	Circumferential backlash or clearance [rad]

tilting angular positions will present a smaller clearance than those in the pivoting position, and thus the teeth will make contact in a progressive manner [14].

In this way, teeth in the tilting angular position will be the first to make contact and will suffer the highest tooth root stresses [15–17]. Furthermore, the unequal clearance distribution will make the number of teeth in contact vary according to the applied torque and misalignment angle, causing the gear coupling stiffness to vary [18]. To determine the number of teeth in contact finite element models [16,19–22] and tooth contact analysis algorithms (TCA) [3,23] can be found in the literature. However, the standards [9,11,24–27] do not include the effect of the geometry or the loading conditions in their equations. I.e., they define the percentage of the number of teeth in contact only in terms of the misalignment angle regardless of the stiffness or the working conditions [10,28–30]. For this reason, it is a common criterion to consider that half of the teeth are in contact [9–11,24]. This criterion may be adequate for small misalignment applications ($\gamma \gg 1°$), however numerical works [22,31] have shown that this is not applicable in high misalignment applications. This is because the number of teeth in contact may be even smaller, especially in low torque and high misalignment applications. Furthermore, to the authors' knowledge, no experimental works to verify these results in high misalignment angles exist in the literature.

As gear couplings are frequently employed in applications with small misalignment angles [17,32,33], most experimental works and test rigs are oriented to these working conditions [34–36]. Among others, Cuffaro et al. [34] analyzed the pressure distribution in spline couplings with pressure-sensitive films and analytically and numerically validated the obtained contact pressures. The main aim of these studies was oriented to surface fretting failure [24,37,38]. However, Mancuso [28] showed that the common failures of gear couplings working in heavy-duty high torque applications up to $\gamma = 6°$ were related to tooth root breakage and reinforced that the misalignment angle was the most damaging variable.

Concerning misaligned conditions, and in view of the significance of the misalignment angle analytical works have determined the relationship between the design parameters of the gear coupling and the achievable maximum misalignment angle [39]. Moreover, they have shown that the number of teeth and the pressure angle are the predominant design parameters, followed by the crowning radius to define the maximum misalignment at which a gear coupling can work. However, no experimental analysis has been carried out on the real misalignment angle spherical gear couplings can withstand.

In the scientific literature, various test rigs exist to conduct tests in controlled misaligned angles [33,40–42]. Studies carried out in this type of setup have demonstrated that the contact pattern is not centered and constant in misaligned conditions [5,42], and that wear increases due to the misalignment angle [41]. Nevertheless, these test rigs are limited to a maximum misalignment angle

of $\gamma \ll 1°$. For higher misalignment angles, experimental published data is scarce. For example, Herbstritt et al. [19] measured tooth root bending at a maximum misalignment angle of $\gamma = 3°$, and validated a finite element model with a margin of error of 15%, however limited information was given concerning the experimental setup.

Hence, the literature has shown that highly-crowned spherical gear couplings present a number of challenges in terms of geometry generation and mechanical behavior. Moreover, the standards still consider them exceptional cases and do not provide accurate sizing criteria. Recently, many advances have been made in developing analytical and finite element models to determine the geometry of the tooth surfaces and the mechanical behavior of highly crowned spherical gear couplings. However, there still remains a lack of experimental tests which can validate the observed findings.

Therefore, the main goals of the present research are:

(1) Design a dedicated test rig that withstands high misalignment angles and enables the static analysis of spherical gear couplings.
(2) Experimentally study the mechanical behavior of highly crowned spherical gear couplings working at high misalignment applications: the manufactured geometry, maximum misalignment angle, stiffness, number of teeth in contact, and the contact pattern. These results will be used to validate the analytical geometry generation model [3], and the finite element model [22] previously presented by the authors.

2. Case study

The geometry parameters of the case study in which the research is based are described in Table 1. This type of gear coupling (Fig. 1(b)) is currently employed in the roll-leveling industry for high-strength steels and is depicted in Fig. 1(a). The high number of small rollers, together with the use of large gearboxes to transmit high torque values, causes the misalignment angle between these and the gearbox to increase up to 7.5° [21,31].

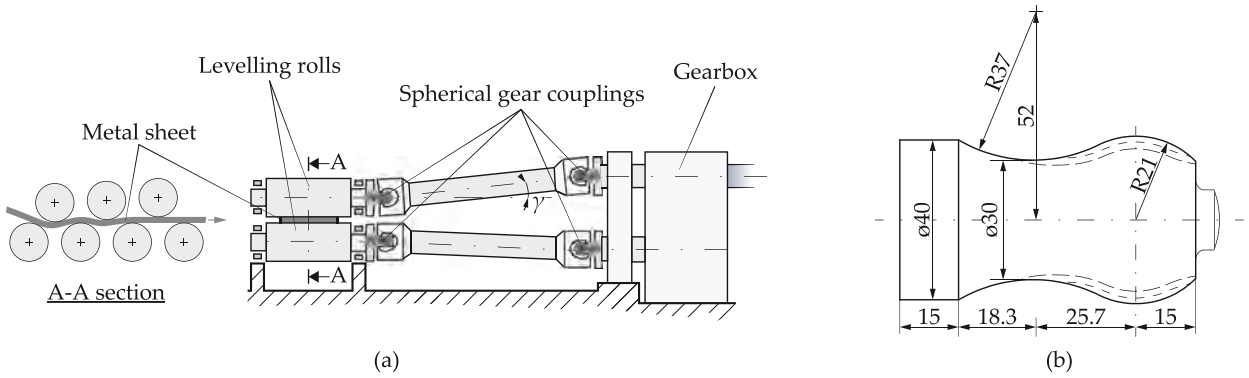

Fig. 1. Case study: (a) the roll-leveling machine where this type of gear coupling is employed, and (b) the geometry of the gear coupling.

The gear coupling has three different positioning key shafts to place it in the test rig so that the influence of different meshing positions can be analyzed. The material employed is a carburized and quenched 15NiCr11 steel with the mechanical properties set out in Table 1. It was manufactured with a hob of $m_n = 3$ AP 30° DIN-3972-II [43] and a circular tool path radius of 49 mm. Based on the pitch deviations measured in the manufactured part, the manufacturing class corresponds to class 6 of standard ISO 4156 [26].

The working conditions analyzed in this work are a minimum torque value of 100 Nm and a maximum of 1000 Nm, in a range from 0° to 7° misalignment angle.

3. Reconstruction of the spherical gear coupling tooth surface from the measured point cloud

The procedure of reconstruction starts with the measurement of the tooth surfaces of the hub and the sleeve which will provide the point cloud. Here, a coordinate measurement machine (CMM) Mitutuyo CRYSTA-Apex S 7106 was used with a 1 mm diameter stylus and an accuracy of ± 0.3 μm. To obtain the point cloud of the tooth surfaces the tooth-space of a single tooth in the hub and in the sleeve was measured. The tooth profiles at intervals of 0.5 mm in the longitudinal direction were measured as illustrated in Fig. 2(a–b).

Moreover, the whole perimeter of the hub and the sleeve were also measured in the reference plane to determine the existing indexing errors in the spline coupling. To this aim, the angular pitch of the hub (τ_h) and sleeve (τ_s) were calculated as shown in Fig. 2(c). The angular pitch (τ) is the angle in the transverse section of the spline that results from dividing the complete perimeter of a circle into z equal parts [12]. When the angular pitch of the hub or sleeve differ from their theoretical value, indexing errors exist [9].

Once the point cloud of the hub tooth space was obtained (Fig. 3(a)), the reconstruction of the tooth surfaces was accomplished through the following steps:

Table 1
Highly crowned spherical gear coupling case study.

Parameter	Case study
Pitch diameter, d_p [mm]	39
Normal module, m_n [mm]	3
Number of teeth, z [–]	13
Normal pressure angle, α [°]	30
Circumferential backlash, φ_j [°]	2
Tool path radius, r_β [mm]	49
Young's modulus, E [GPa]	210
Poisson coefficient, υ [–]	0.33
Density, ρ [kg/m^3]	7850
Yield stress, σ_y [MPa]	850
Ultimate stress, σ_u [MPa]	1010
Fatigue stress limit, σ_e [MPa]	520
Misalignment angle, γ [°]	0–3–5–7
Applied torque, Γ [Nm]	100–500–1000
Repetitions per test	3

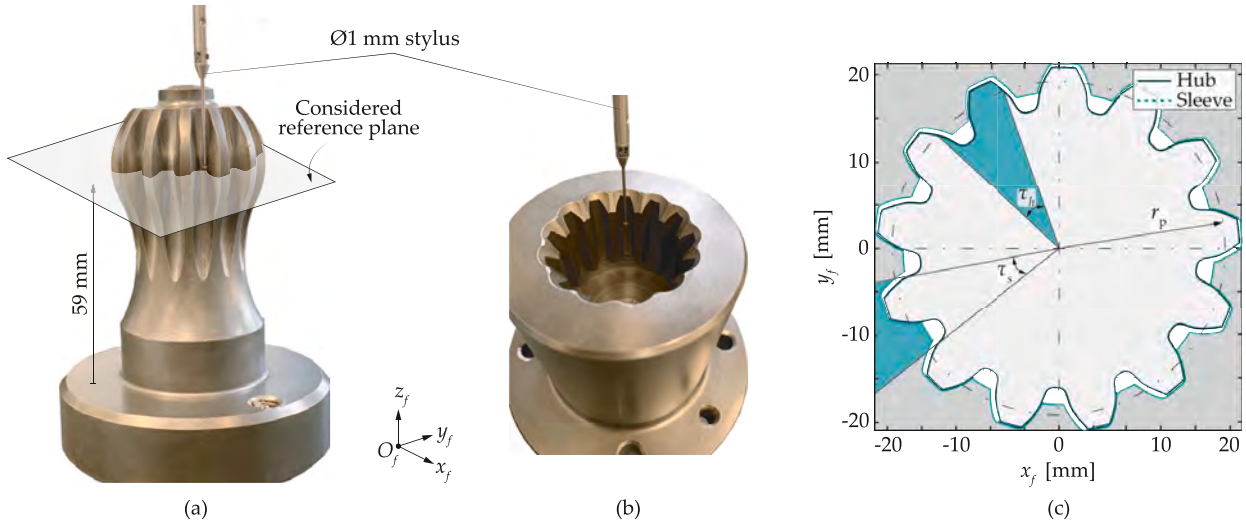

Fig. 2. CMM measurement of the (a) hub and the (b) sleeve, and the (c) definition of the angular pitch (τ_h, τ_s) to determine the indexing errors.

Step 1 Alignment of the point cloud with respect to the reference diameters.
The process starts with the localization of the centering circles that represent the origin of the coordinate system from which the measurements were done. Fig. 3(b) shows the centering circle points (×) which are used to define the center of the coordinate system (O_f). The cylinder made up of the points was used prior to the measurement in the CMM to construct a vertical axis and manually align the measured data. This limits the inaccuracies resulting from the part positioning and clamping in the machine, and thus only those related to the measured part were captured.

Step 2 Deletion of the outliers in the point cloud and determining the boundaries of the active and fillet profiles.
Although contact metrology reduces the amount of non-representative points obtained with non-contact metrology [44], there still remain points which are not necessary for the reconstruction of the tooth surfaces. These points, which include, bottom regions and those points out of the pitch angle, were deleted. Fig. 3(b) shows the raw point cloud and the non-relevant points for the reconstruction. In addition, the limiting bottom and tip edges defined for the reconstruction can be observed.

Step 3 Computation of a regular grid for the active and fillet tooth surfaces from the curves resulting from the point cloud.
An equally spaced grid formed by $m \times n$ points was generated in the active and fillet profiles of the right and left teeth for each section. To this aim, *interparc*, a built-in function in Matlab was used [45], which is based on the following steps:

(a) The cumulative linear arclength (s_n) of the profile ($\mathbf{r}$) is computed using a connect-the-dots function. The normalized arclength ($\Delta s_{n,i}$) between each point of the profile is calculated with Eq. (1). In this way, the cumulative linear arc length values are always between [0 .. 1]. O corresponds to the first measured point of $\mathbf{r}$ and 1 to the last measured point.

$$s_{n,i} = \sqrt{\Delta r_x{}^2 + \Delta r_y{}^2} \qquad \Rightarrow \qquad \Delta s_{n,i} = \frac{s_{n,i}}{\sum_{s=1}^{pt-1} s_{n,i}} \tag{1}$$

where $\mathbf{r}$ corresponds to the measured tooth profile vector and pt to the number of measured points in that profile.

(b) An interpolating spline is fitted to the profile points in each dimension (in this case x_f and y_f), as a function of the cumulative linear arclength. These functions are cubic polynomial segments, and their derivatives are also calculated.
(c) Each of the arclength differential segments is integrated using the ordinary differential equation solver (ODE45 in Matlab), with a relative error tolerance of 10^{-9}, to find the point at which the function crosses the points of the grid. This is the most important characteristic of the interpolation method used in this procedure since it locates the m grid points along the curve at specific equal distances (in arclength) from the starting point.

Step 4 Regeneration of the whole space width for the posterior meshing of the finite element model.
Once the grid was formed for all the measured planes (corresponding to n variable), the whole tooth was reconstructed as shown in Fig. 3(c). The difference between the cleaned point cloud and the reconstructed spline geometry is less than 3 μm. The same procedure was replicated for the sleeve tooth space, but only the geometry of the hub is presented in Fig. 3 as it is the most representative.

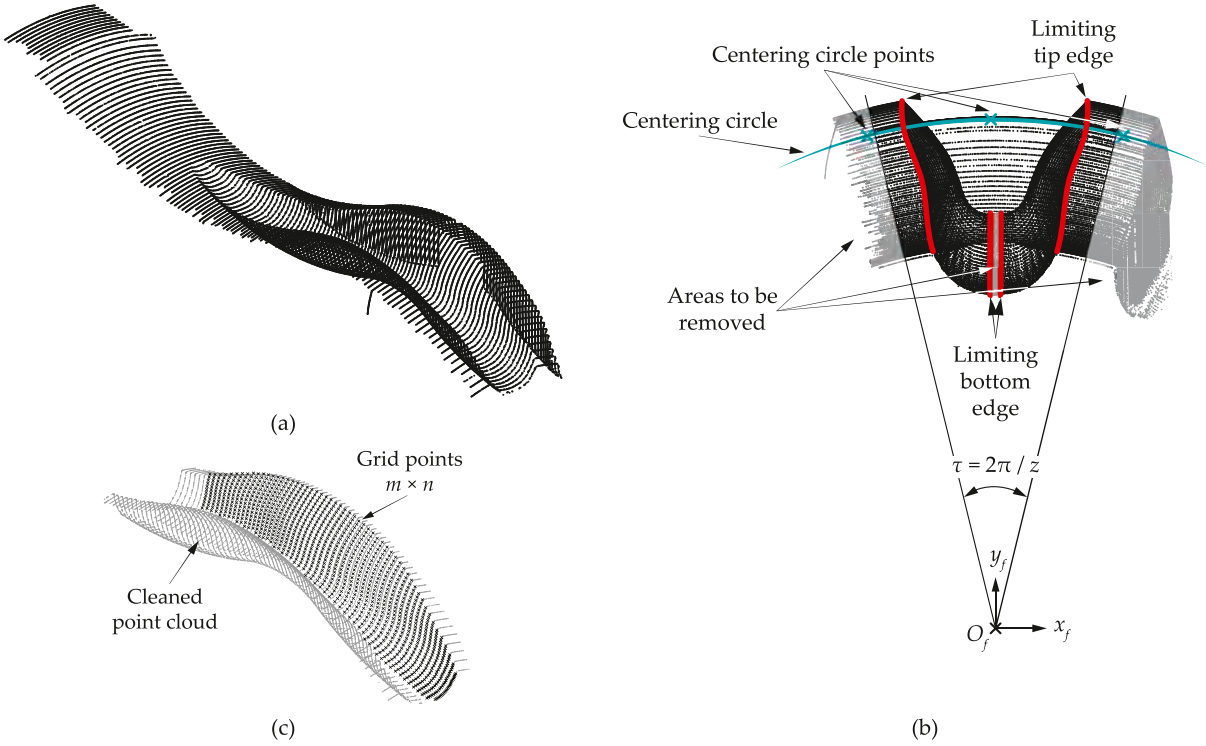

Fig. 3. (a) measured point cloud of the hub, (b) centering points, removed zones, and limiting edges, and (c) reconstructed hub geometry.

4. Generation of the hub and the sleeve tooth surfaces and comparison with the measured data

The hub tooth surface was generated following the two-parameter envelope theorem [46] and the model described in [3]. The distinguishing feature of this model compared with others in the literature (e.g. [8,13]) is that the generated tooth surface (Σ_h) is derived from the geometry and the kinematics of the tooth surface (Σ_w) of the generating tool (hob), which at the same time is derived from the tooth surface of the generating rack-cutter (Σ_c). Indeed, the generating tool is a hob thread surface which is considered as a set of cutting edges and follows the user-defined tool path (commonly circular or parabolic).

The hub tooth surface was generated by coordinate transformation (2) from system S_c to system S_h, taking into consideration the double-enveloping process [46] with two independent parameters of generation ϕ_w and s_w (4), (5). Here ψ_w is the generation parameter for the hob thread surface, and $\mathbf{M}_{hw}$ and $\mathbf{M}_{wc}$ are the coordinate transformation matrices [3].

$$\mathbf{r}_h(u_h, v_h) = \mathbf{M}_{hw}(s_w, \phi_w)\,\mathbf{M}_{wc}(\psi_w)\,\mathbf{r}_c(u_h, v_h) \tag{2}$$

$$f_1(u_h, v_h, \psi_w) = \left(\frac{\partial \mathbf{r}_w}{\partial u_h} \times \frac{\partial \mathbf{r}_w}{\partial v_h}\right) \cdot \frac{\partial \mathbf{r}_w}{\partial \psi_w} = 0 \tag{3}$$

$$f_2(u_h, v_h, s_w, \phi_w) = \left(\frac{\partial \mathbf{r}_h}{\partial u_h} \times \frac{\partial \mathbf{r}_h}{\partial v_h}\right) \cdot \frac{\partial \mathbf{r}_h}{\partial \phi_w} = 0 \tag{4}$$

$$f_3(u_h, v_h, s_w, \phi_w) = \left(\frac{\partial \mathbf{r}_h}{\partial u_h} \times \frac{\partial \mathbf{r}_h}{\partial v_h}\right) \cdot \frac{\partial \mathbf{r}_h}{\partial s_w} = 0 \tag{5}$$

4.1. Geometry comparison

The reconstructed geometry and the generated geometry of the hub tooth space are depicted in Fig. 4(a). The deviations (δ) between both tooth profiles (generated vs. reconstructed) were calculated for each measured cross sections (n section) in the normal direction of the generated tooth profile, which is defined in Eq. (6). The deviations in plane $z = -6$ mm are illustrated in Fig. 4(b), as it is one of the cross-sections with the highest deviations inside the analyzed region.

$$\mathbf{n}_{\mathrm{h}}(u_{\mathrm{h}}, v_{\mathrm{h}}) = \frac{\dfrac{\partial \mathbf{r}_{\mathrm{h}}}{\partial u_{\mathrm{h}}} \times \dfrac{\partial \mathbf{r}_{\mathrm{h}}}{\partial v_{\mathrm{h}}}}{\left| \dfrac{\partial \mathbf{r}_{\mathrm{h}}}{\partial u_{\mathrm{h}}} \times \dfrac{\partial \mathbf{r}_{\mathrm{h}}}{\partial v_{\mathrm{h}}} \right|} \tag{6}$$

As represented in Fig. 4(b), deviations were calculated from the generated tooth surface to the measured tooth surface, along the contact area. For this type of gear coupling and working conditions, the contact path does not exceed ±6 mm width, relative to the reference plane. Fig. 4(c) shows the variations on the whole left side tooth surface of the spherical gear coupling. Deviations are distinguished in accordance with the manufacturing tolerance classes defined in ISO 4156 standard [26]. Deviations below the highest manufacturing class 4 ($\delta = \pm 23$ μm) are considered negligible, while the maximum tolerances are those corresponding to class 7 ($\delta = \pm 92$ μm).

The indexing errors calculated from the measured perimeter in the reference plane of the hub and the sleeve, correspond to the manufacturing class 6 (≈50 μm). As the hub was carburized and quenched, distortions are expected to appear in the part and a one-class accuracy reduction might have occurred [9,11]. In Fig. 4(c) it can be seen that the deviations between the generated and the reconstructed hub tooth surface are below class 6, which demonstrates that the analytically generated geometry [3] has good agreement with the manufactured geometry.

In the case of the sleeve, deviations were below 20 μm in the active and fillet profiles. These deviations may be linked to surface waviness and were considered to be negligible.

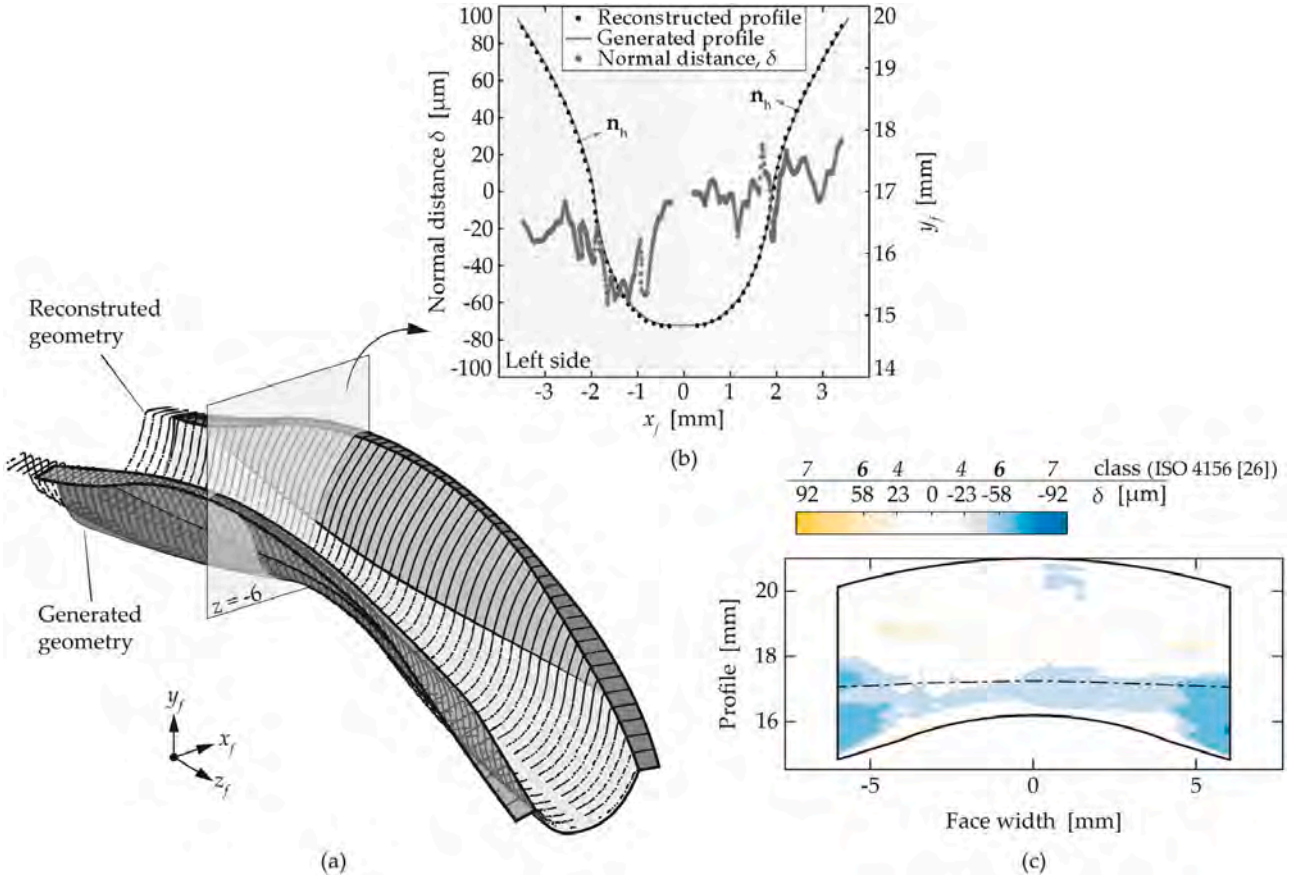

Fig. 4. (a) the reconstructed and the generated hub tooth space, (b) comparison of the tooth profiles and the normal deviations δ of a cross-section ($z = -6$ mm), and (c) the normal deviations δ of the left side hub tooth surface.

5. Tooth contact analysis

5.1. Non-loaded tooth contact analysis (NLTCA)

The unloaded tooth contact analysis is conducted to determine the maximum misalignment at which the gear coupling can operate. The algorithm for its calculation is precisely described in [39]. The sleeve is fixed in S_f coordinate system and the angle (γ) at which the hub makes contact with the sleeve is sought in the tilting angular position. The tooth surface of the hub and the sleeve are represented in the fixed coordinate system S_f as shown in Eqs. (7), (8). Here $\mathbf{M}_{fh}$ is the coordinate transformation matrix and $\mathbf{r}_h$ was previously described in Eq. (2).

$$\mathbf{r}_f^{(hub)}(u_h, v_h, \gamma) = \mathbf{M}_{fh}\mathbf{r}_h(u_h, v_h) \tag{7}$$

$$\mathbf{r}_f^{(sleeve)}(u_g, v_g, \gamma) = \mathbf{r}_g(u_g, v_g) \tag{8}$$

The normal vectors to the tooth surfaces of the hub and the sleeve are also represented in S_f coordinate system as shown by Eqs. (9), (10). Here $\mathbf{L}_{fh}$ is a 3×3 order matrix and can be determined from $\mathbf{M}_{fh}$, and $\mathbf{n}_h$ was previously described in Eq. (6).

$$\mathbf{n}_f^{(hub)}(u_h, v_h, \gamma) = \mathbf{L}_{fh}\mathbf{n}_h(u_h, v_h) \tag{9}$$

$$\mathbf{n}_f^{(sleeve)}(u_g, v_g, \gamma) = \mathbf{n}_g(u_g, v_g) \tag{10}$$

To determine the maximum misalignment angle (γ), the angle at which tooth surfaces are in point contact is sought in the tilting angular position. Indeed, according to literature the maximum misalignment a gear coupling can withstand is established at the tilting angular position since these are the teeth to first make contact in a gear coupling [2,3,27,33]. At this point, tooth surface points and normal vectors are equal, thus a system of five independent scalar equations with five unknowns is constructed. The unknowns are the hub tooth surface parameters $\{u_h, v_h\}$, the sleeve tooth surface parameters $\{u_g, v_g\}$, and the maximum misalignment angle $\{\gamma\}$. The equations are summarized in Eqs. (11), (12), taking into account that Eq. (12) represents only two independent scalar equations since $|\mathbf{n}_f^{(hub)}| = |\mathbf{n}_f^{(sleeve)}| = 1$.

$$\mathbf{r}_f^{(hub)}(u_h, v_h, \gamma) = \mathbf{r}_f^{(sleeve)}(u_g, v_g) \tag{11}$$

$$\mathbf{n}_f^{(hub)}(u_h, v_h, \gamma) = \mathbf{n}_f^{(sleeve)}(u_g, v_g) \tag{12}$$

5.2. Loaded tooth contact analysis (LTCA)

To conduct the loaded tooth contact analysis a finite element model is employed. This is created following the methodology described in [22] on the basis of the spherical gear coupling geometry generated. The same procedure could also have been used to mesh the reconstructed geometry, but the analytically generated geometry was used in this research, to validate the finite element model. The structured mesh is generated automatically with a high density of elements in the hub and the sleeve tooth surfaces [22], and a minimum element size of 0.08 mm. The mesh transition from the fine mesh of the tooth surface until the body is achieved with a bias factor. Even if this methodology can be applied to generate the model in any FE analysis computer program (Ansys, Abaqus, Marc, etc.), in this case, it was created in Marc solver [47].

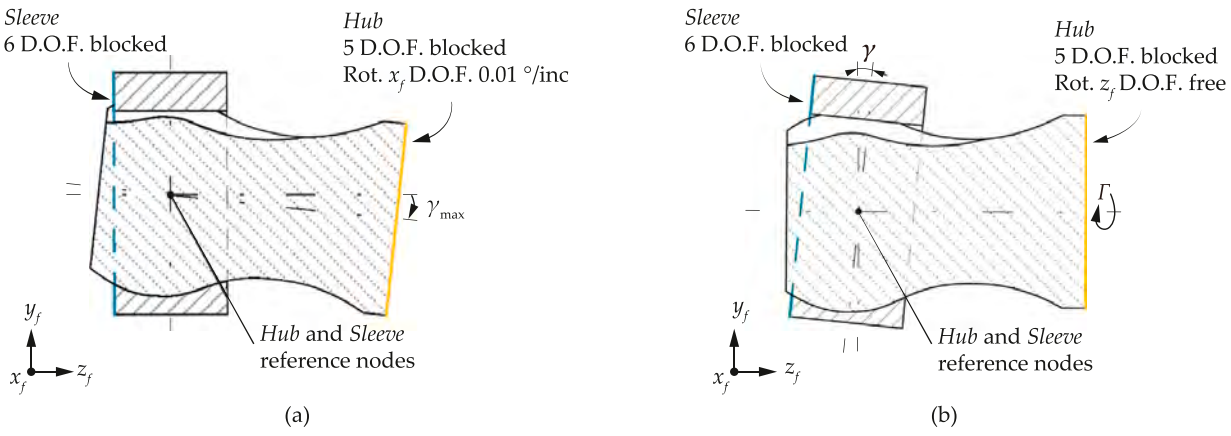

Fig. 5. Boundary condition definition for each analysis: (a) maximum misalignment angle model, and (b) contact pattern and stiffness model.

As one of the main objectives of this research is to validate the numerical results with experimental data, two different FE models were created, depending on the boundary conditions (B.C.) that represent the experimental tests carried out, as shown in Fig. 5. For the maximum misalignment, all the degrees of freedom of the sleeve reference node were blocked, while for the hub the three displacements and two rotations (γ'_z, γ'_y) were blocked. A rotation of 0.01°/inc was imposed through the released degree of freedom of the hub, as seen in Fig. 5(a). On the other hand, in Fig. 5(b) the B.C. to calculate the stiffness and the contact pattern are depicted. Torque was applied in the released degree of freedom of the hub, and the misalignment angle was set in the sleeve. Indeed, the hub was not misaligned since a cylindrical coordinate system (r, θ, z_f) was defined to facilitate the post-processing of the results as explained [22].

Node-to-segment contact pairs were defined between the hub and sleeve tooth surfaces without any friction, and a contact tolerance of 0.004 mm was set. A linear elastic material was defined, whose properties are shown in Table 1, while the element type considered for the analysis was a first-order isoparametric hexahedral element (type 7 [47]).

5.3. Post-processing of the results

The maximum misalignment angle was defined directly from the increment at which the hub tooth made contact at both tooth sides, that is when the jamming angle was reached [33,39].

To determine the stiffness two variables were considered: (i) the applied torque through the released degree of freedom of the hub; and (ii) the angular rotation around z_f axis of a node in the surface of the hub and out of the effects of local deformations. The stiffness was then determined as the derivative of the torque relative to the angular rotation (θ) curve as Eq. (13).

$$k_i = \frac{\Delta\Gamma_i}{\Delta\theta_i} \qquad [\mathrm{Nm/rad}] \tag{13}$$

To determine the number of teeth in contact, the contact status [47] output of the active profile nodes of the hub was observed. The contact status determines if a node is within the contact tolerance. Thus, the contact pattern was recognized by a congruent representation of the contact status output in the master and slave surface in contact, as described in [22]. The contact pattern was defined from the position of the nodes, as a consequence, the contact pattern might be slightly influenced by the mesh size and the contact tolerance employed.

6. Experimental setup

6.1. Test rig

For the experimental tests, a specifically developed test rig was designed and constructed. This test rig is inspired by similar test benches in the scientific literature [34,35], with the feature that it is specially intended to withstand high misalignment angles in a controlled manner.

The test bench can be seen in Fig. 6. It is composed of two principal parts: the static side, where the sleeve is located and the torque is applied, and the moving side, where the hub is placed and the misalignment angle is set. Torque was applied in the sleeve using calibrated weights in the loading mechanism up to 1000 Nm. The applied torque was measured by a full-bridge torsion gage CEA-06-250US-350 from Micromeasurements. The gage was calibrated with a high-precision torque measuring unit KiTorq type 4541AN1, and a precision of ±20 Nm was achieved. Moreover, the angular rotation of this part was measured with a magnetic encoder (stator: PMIS4-50-2048-50KHZ-TTL24V-Z0-2M-S and Rotor: PMIR5-50-96-O-133), positioned around the sleeve.

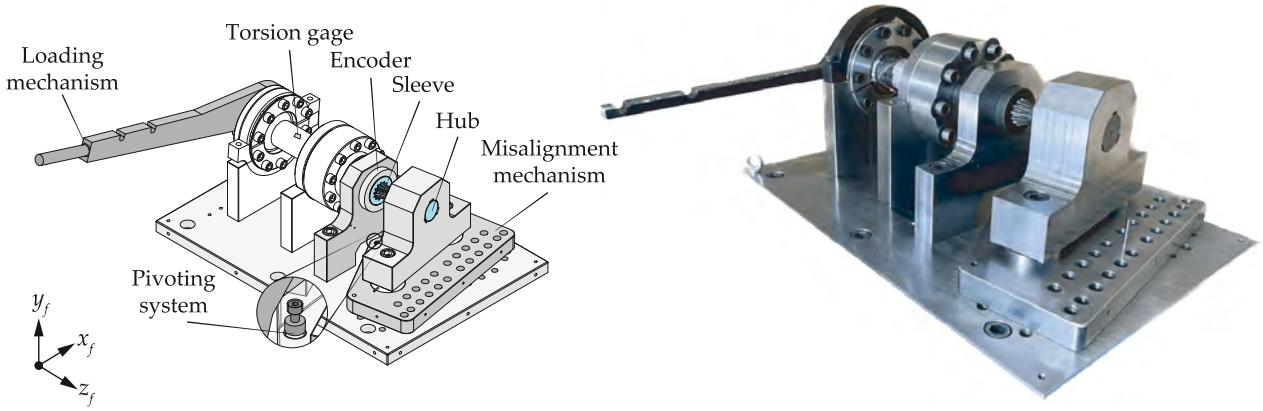

Fig. 6. (a) design of the test rig and the important parts, and the (b) experimental setup.

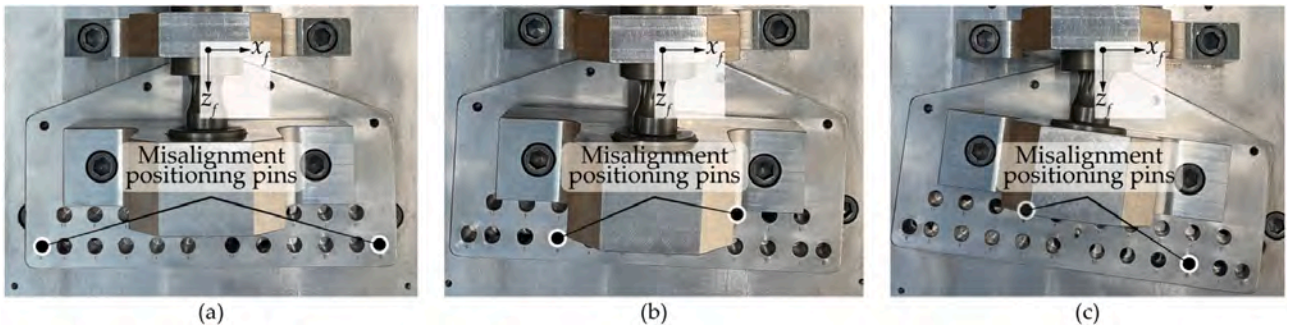

Fig. 7. Misalignment mechanism with the misalignment positioning pins position for: (a) $\gamma = 0°$, (b) $\gamma = 3°$, and (c) $\gamma = 7°$.

The hub is placed in the moving part with three key shafts, which enable the positioning of the hub at different angular positions.

The misalignment is applied by means of the pivoting system shown in Fig. 6(a). Together with the holes in the moving part and the base of the test rig, a misalignment angle up to 10° can be set, with steps of 1°. The misalignment angle is applied in the clockwise direction. To fix the system at the desired misalignment angle, two positioning pins are aligned with the corresponding holes on the base plate on which the moving part slides. In this manner, controlled and repeatable experimental testing with a precision of ±0.2° is achieved. This misalignment angle was also verified by means of an inclinometer. Fig. 7 shows the misalignment positioning pins in their corresponding positions, depending on the misalignment angle desired, 0°, 3° or 7°.

6.2. Maximum misalignment angle test technique

To measure the maximum misalignment angle a special part was designed and 3D printed to hold the inclinometer around the hub as shown in Fig. 8(a). This part enables holding the inclinometer horizontally and capturing the misalignment angle of the hub. During the tests, DAS-30-A inclinometer from Level Developments was used which measures the voltage variations between the initial and final states in both planes ($y_f\, z_f$ and $y_f\, x_f$). Even if the major objective was to measure the maximum misalignment angle only in plane $y_f\, z_f$, slight misalignment in the third axis was unavoidable, since there was not any guiding mechanism. Thus, the resultant misalignment angle was determined by (Eq. (14)).

$$\gamma_{\max} = \sqrt{\Delta\gamma'^{2}_{x} + \Delta\gamma'^{2}_{z}} \tag{14}$$

where $\Delta\gamma'_{x,z}$ is the difference between the initial and final state angle.

The experimental tests were carried out by keeping the sleeve static, meshing each of the hub teeth, and dropping it by the effect of gravity. This was repeated three times for each meshing tooth (13 for this case study) to ensure repeatability. The hub drops up to the point where contact exists on both sides of the tooth (jamming angle [33,39]), more precisely this will occur in those teeth located in the tilting angular position [2,39,48].

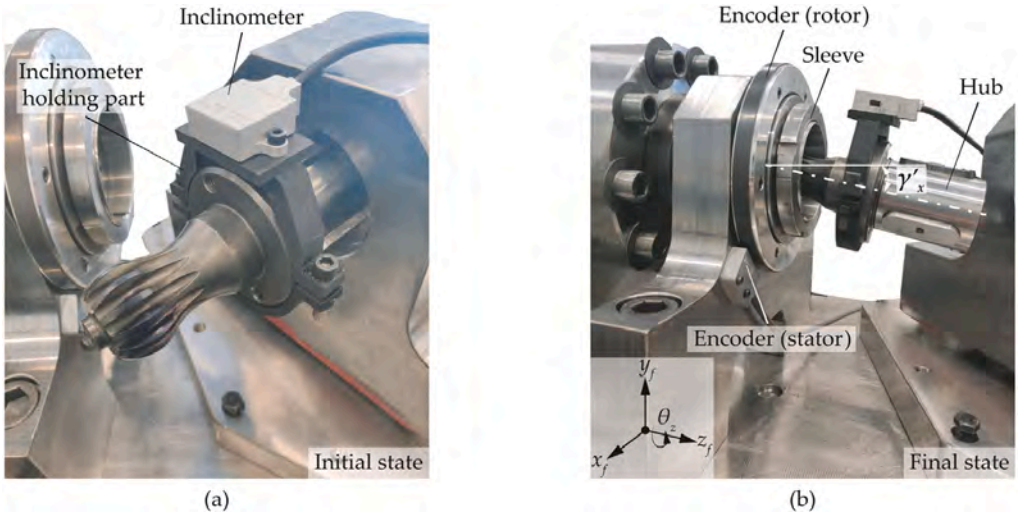

Fig. 8. Experimental setup for the maximum misalignment measurement: (a) designed tooling for the inclinometer in the initial position, and (b) the test final position with the misalignment angle measurement and the encoder.

6.3. Stiffness test protocol

Using the described test rig, with the torsion gage for the applied torque measurement and the encoder for the angular rotation measurement, the stiffness of the spherical gear coupling was computed. The encoder, placed in the sleeve, may be observed in Fig. 8(b).

Torque was applied up to $\Gamma = 1000 \pm 20$ Nm at different misalignment angles (0–7°). These tests were repeated three times to verify test repeatability and remove any looseness that the mechanism may have. Moreover, tests were repeated for different key-shaft positions of the hub to account for the influence of several indexing error combinations, which gives a series of nine repetitions for each misalignment angle tested.

6.4. Contact pattern and number of teeth in contact test technique

For the contact pattern test, a layer of 4.5 μm ±1.5 μm of a blue marking fluid (Dykem) was applied to the hub teeth. This was measured with Positector 6000 Series Coating Thickness Gage (F0S microprobe). Additionally, the reference section and another mark to a measured distance of 10 mm were done with a scribe for the post-processing (see Fig. 9(a)). To carry out each test the hub was positioned in the middle of the backlash, making sure that the tooth surfaces of the hub and the sleeve did not touch each other. Then, the desired torque was applied with the calibrated weights and a small amplitude vibration of 20 Hz was generated in the system to ensure the blue marking fluid was correctly removed from the contact region. The loading was taken off and put back on three times, for this purpose. Finally, the hub was pulled out of the sleeve with care, to avoid creating additional marks, and pictures of the teeth were taken.

Pictures were taken with a Nikon Coolpix P100 camera macro mode, together with a tripod and a turntable so that these were always taken at the same distance and angular position for every tooth. Each tooth picture was taken by turning the turntable by the theoretical angular pitch (i.e., in accordance with the case study, $2\pi/13°$). Black background and white light were used to take pictures and facilitate the post-processing.

The tests were carried out at the operating conditions described in Table 1, for three torque values and four misalignment angles. Each test was repeated three times to reduce possible errors during the tests or the post-processing.

The post-processing of the pictures was done with a dedicated algorithm developed for this purpose, whose aim is to detect the contact pattern automatically and to enable the calculation of the centroid of the contact area of each tooth to compare it with the numerical results. The following algorithm divided into five steps was applied to each of the taken photos:

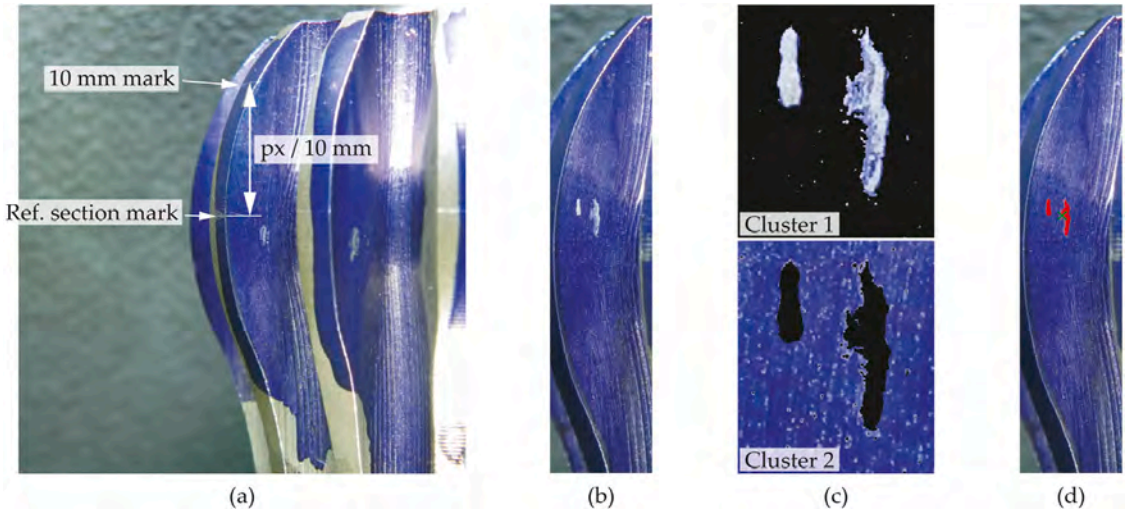

Fig. 9. Post-processing of the photos: (a) marks to define the scale of the taken photo, (b) cropped region of each tooth, (c) clustering of the contact region, and (d) cropped region of each tooth with the contact area and its centroid. (For interpretation of the references to color in this figure legend, the reader is referred to the web version of this article.)

Step 1 Define the scale of the photo, by cropping the length of the figure between the marks previously done in the hub teeth (Fig. 9(a)). This allows calculating the position of the centroid and area of each contact region, by the pixels per millimeters ratio.

Step 2 Define the area of interest and crop and merge all the photos that correspond to the same test.

Step 3 Align all images with the reference plane to decrease possible clamping errors when taking pictures. One of the cropped images can be seen in Fig. 9(b).

Step 4 Detect the contact region in the tooth by the use of color image segmentation K-Means clustering [49]. For this, the color in the image must be first expressed in terms of numbers or objects, that is why colors in the figure are represented in a three-axis color space $L^*a^*b^*$. L^* corresponds to the brightness (0 for black and 100 for white), a^* is the chromatic abscissa coordinate of red (positive values) and green (negative values), and b^* is the chromatic ordinate coordinate of

yellow (positive values) and blue (negative values) [50,51]. In this case, due to the brightness slight modifications and contact pattern different intensities, the detection was best-suited with $L^*a^*b^*$, as it enables easier segmentation of colors independent of lightness (compared to the most commonly used RGB or CYMK color representations). K-means clustering treats each group as having a certain location in the space and finds partitions so that the distance within objects of the same cluster is as close as possible, and as far from objects in other clusters. The distance function used is the euclidean distance. In this case, two clusters (K) were defined, with the purpose of distinguishing the region in contact in each tooth, as shown in Fig. 9(c).

Step 5 The contact region is colored in red and the centroid is calculated, as depicted in Fig. 9(d). When all the photos of the same test are post-processed, the result is ready to be compared with the numerical results.

7. Experimental results of the contact pattern

Fig. 10 shows the contact pattern and the centroid location evolution of the case study in terms of the misalignment angle for an applied constant torque value of $\Gamma = 500$ Nm. Moreover, in line with the axis in which the misalignment angle was applied, teeth in the tilting and the pivoting positions are highlighted. The contact pattern evolves from a constant position along the reference section in aligned conditions to a sinusoidal contact pattern as the misalignment angle increases. The quasi-constant contact in aligned conditions is due to the different contact positions derived from the surface waviness of both the hub and the sleeve.

Moreover, it can be seen that the contact moves farther away from the reference section, reaching close to ±4 mm (symmetrically distributed on both sides) as the misalignment angle increases. I.e., the contact path amplitude increases together with the misalignment angle. For misalignment angles $\gamma > 3°$, the sinusoidal is not complete, i.e., the number of teeth in contact decreases (represented in the figure with dashed lines). The teeth which lose contact faster are those in the pivoting position, which is in agreement with the literature [5,23,27]. Furthermore, the contact region in those teeth making contact at high misalignment angles increases compared to that where all teeth make contact. This behavior shows that teeth in the tilting angular position will support higher stresses as indicated in [14,18,22]. A non-homogeneous contact region may be observed in some teeth, corresponding to the tooth surface waviness and the way in which the blue marking liquid was removed from the tooth surface of the hub.

In Fig. 11 the influence of the applied torque is shown for a constant misalignment angle of $\gamma = 5°$, together with the teeth corresponding to each characteristic angular position (tilting or pivoting). In this case, the contact pattern centroid position does not change in terms of the applied torque. However, the number of teeth in contact and the contact surface do change. As torque increases, the number of teeth in contact increases, meaning the load is supported by more teeth. For this reason, when torque is higher for a constant misalignment angle, the contact region in each of the teeth in contact increases. In every case, the contact regions corresponding to the tilting angular position teeth are greater than those on the pivoting angular position. Moreover, the contact region shifts from the middle (pitch radius) of the tooth towards the tip, especially in those teeth in the tilting angular position. This may be explained by the fact that tooth surfaces were not manufactured with a tip relief, which helps center the contact and prevents interference, as explained in [22,42].

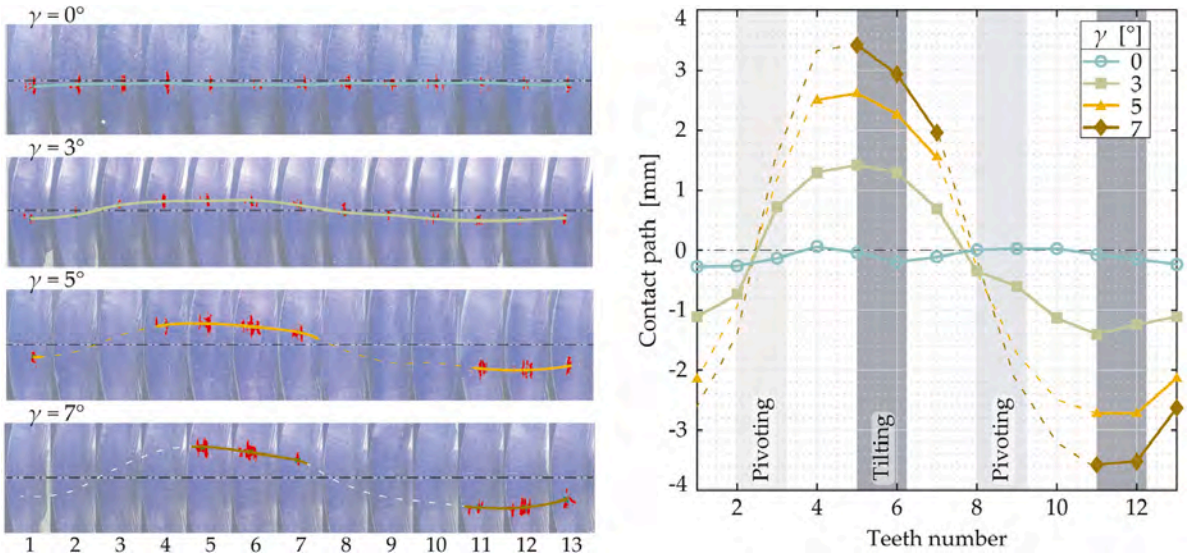

Fig. 10. Contact pattern at $\Gamma = 500$ Nm as a function of the misalignment angle, with the contact centroid positions.

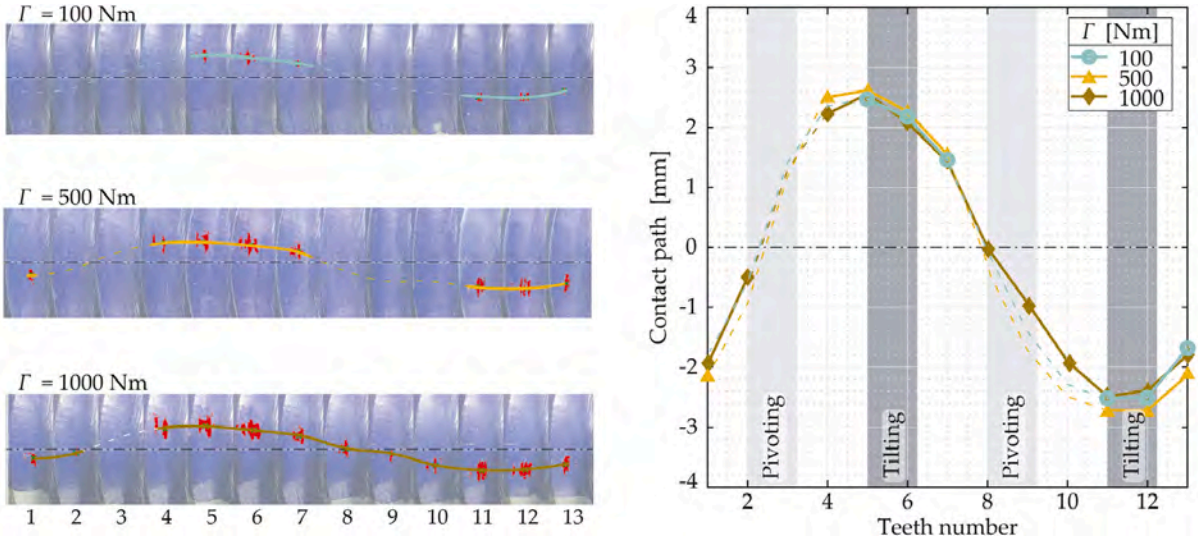

Fig. 11. Contact pattern evolution at $\gamma = 5°$ as a function of the applied torque, with the centroid positions.

8. Validation of the finite element model and discussion

In this section, the experimental results are compared with the numerical results (LTCA) with the aim of validating the finite element model defined in [22]. The maximum misalignment angle, stiffness, number of teeth in contact, and the contact pattern are compared.

8.1. Maximum misalignment angle

Fig. 12(a) shows the average value of the maximum misalignment angle obtained from the experimental tests, together with the maximum and minimum values measured (ϵ). Overall, the mean value of all the meshing positions was 8.9° with a maximum deviation of a ±4% in the third meshing position. Moreover, at different meshing positions, the maximum misalignment angle varied approximately 0.5°, which is linked to the difference in the angular clearance observed in Fig. 12(b).

As reported in [2,3,16,22] those teeth with the minimum clearance are the first to come in contact (corresponding with the tilting angular position), and that is why this value is related to the maximum misalignment angle of the gear coupling. Fig. 12(b) shows the minimum angular clearance (φ_j) for each meshing position. This is larger than the design value in Table 1 and non-constant in every meshing position, caused by manufacturing errors, and in particular indexing errors. In fact, positive indexing errors will increase the existing angular clearance between two adjacent teeth. In this manner, the meshing positions with a smaller clearance will result in a smaller maximum misalignment angle as seen in Fig. 12. Hence, these results demonstrate that the angular clearance variation has a direct impact on the maximum misalignment angle measured.

In addition, Fig. 12(a) shows the maximum misalignment value obtained from the loaded tooth contact analysis (LTCA) plotted together with that of the non-loaded tooth contact analysis (NLTCA). The NLTCA value is the lowest since it does not consider the stiffness of the gear coupling. The LTCA value is very close to the mean experimental value, although it does not take into account indexing errors. Nonetheless, the error between the value obtained with the finite element model and the mean value from the experimental tests is lower than 5%, which is considered acceptable.

8.2. Stiffness

Fig. 13 shows the angular rotation of the hub in terms of the applied torque for the experimental tests (markers) and loaded tooth contact analysis (lines). The differences between both are smaller than 5%, and thus the results are acceptable. In this graph, two zones can be observed. Zone (i): a steady region where torque is applied and free rotation of the hub occurs, due to the presence of the angular backlash. In Fig. 13 the angular backlash of $\gamma = 7°$ is depicted. Zone (ii): contact occurs between the hub and the sleeve teeth and torque increases. During this phase, teeth make contact progressively and the deflection of the teeth becomes greater than the existing backlash.

It is observed that at low torque values ($\Gamma =$ < 100 Nm) angular deflection (understood as the difference of the angular rotation) is larger than at higher torque values, suggesting there are fewer teeth in contact. In the same manner, as the misalignment angle increases the angular deformation increases, meaning that the gear coupling is less rigid (i.e, fewer teeth in contact). Moreover, the available backlash reduction as the misalignment angle increases is clearly shown.

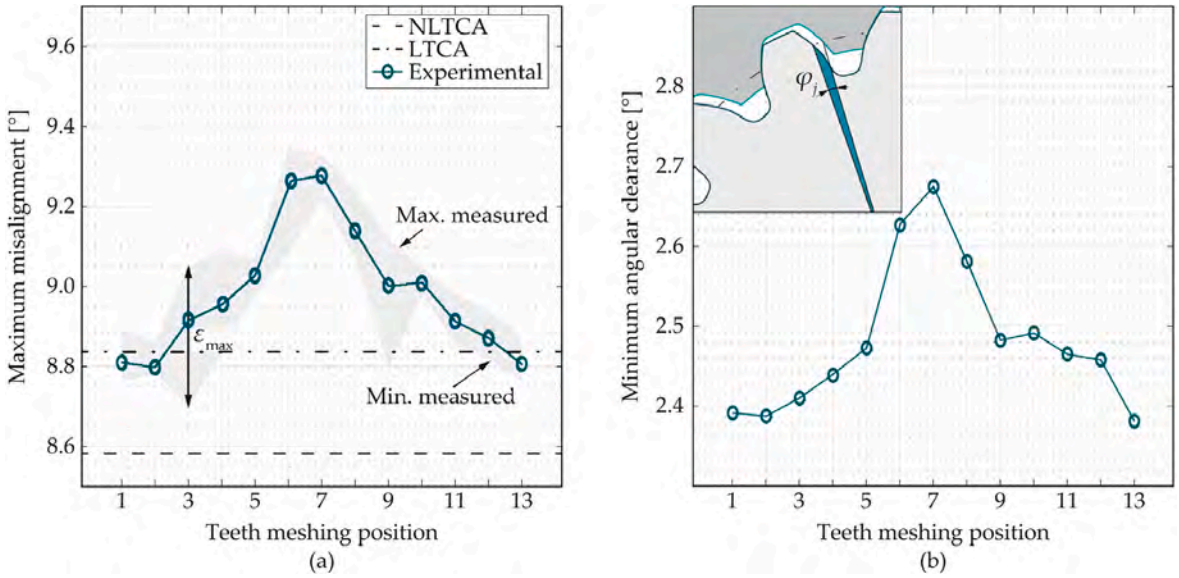

Fig. 12. (a) measured experimental maximum misalignment angle, with data from the NLTCA and LTCA, and (b) angular clearance (or backlash) in each meshing position.

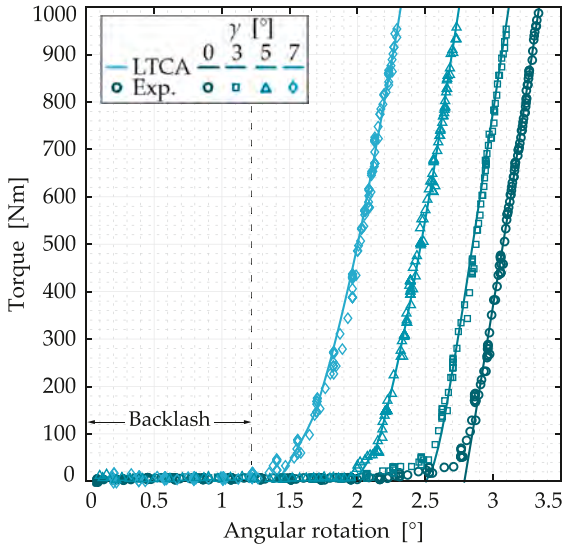

Fig. 13. Stiffness in terms of the torque applied for different misalignment angles: experimental tests vs. loaded tooth contact analysis.

8.3. Number of teeth in contact

Fig. 14 illustrates the results obtained from the experimental tests and those from the loaded tooth contact analysis at 100 Nm, 500 Nm, and 1000 Nm. Moreover, some of the references currently employed to determine the number of teeth in contact in terms of the misalignment angle (up to $\gamma \leq 8°$) [24,28–30] are depicted. Both the experimental (markers) and numerical (lines) values get closer to the values from the literature as torque decreases. Indeed, only the small torque values will follow the literature trend and the rest of the working conditions will be above it.

As regards the experimental results, these correspond to the values obtained with the finite element model. At lower torques (Γ =100–500 Nm) slight differences exist (+1 tooth in the experimental tests). This may be related to the non-consideration of the indexing errors in the finite element model, or the possible errors in the contact detection with the blue marking liquid at low torque levels. However, these slight differences disappear as torque increases, which indicates that the effects of indexing errors are less significant when torque increases. This is in agreement with [52], who showed the load increase factor decreased as the applied torque increased for the same level of manufacturing quality.

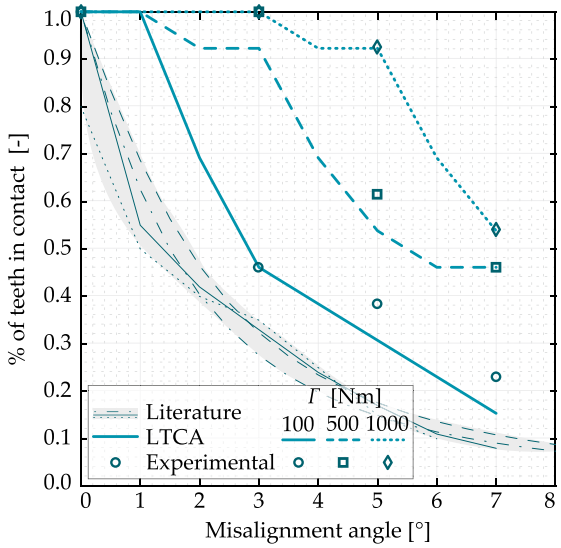

Fig. 14. Normalized number of teeth in contact in the scientific literature [24,28–30], experimental tests, and loaded tooth contact analysis for different torque values.

The commonly used conservative criterion in gear coupling sizing assumes that half of the teeth carry the load [9,11,24]. However, in this research, it is experimentally demonstrated that in certain working conditions (in high misalignment and lower torque values) the number of teeth in contact is below the criterion, and thus will undersize the component design.

8.4. Contact pattern

Fig. 15 shows a comparison of the contact pattern post-processed from the experimental tests and that obtained from the loaded tooth contact analysis at a constant torque $\Gamma = 500$ Nm for different misalignment angles. As explained in Section 7, the contact path moves farther away from the reference section as the misalignment angle increases. The number of teeth in contact also decreases, i.e., teeth that correspond to the pivoting angular position lose contact as the misalignment angle increases (2–3, 8–9).

From the comparison, it can be said that the contact pattern follows the same trend in both the experimental and numerical results. For the cases of $\gamma = 3°$ and $\gamma = 5°$, ± 1 tooth difference can be observed, which is related to the effect of indexing errors or the possible errors in the experimental contact detection. Moreover, in both cases, the contact in the experimental test is small compared to that of the other teeth and thus is concluded to be acceptable.

Slight differences can be seen in the contact pattern and position between the experimental and numerical results. Apart from the manufacturing errors, differences may be also linked to the mesh size and the contact tolerance used in the finite element model. Nonetheless, these are considered to be negligible against manufacturing errors and permit comparing the desired data.

In Fig. 16 the location of the centroid of the contact region is compared for every working condition; the straight line represents the loaded tooth contact analysis results, while the circles represent the experimental data.

In aligned conditions, the finite element model shows a constant contact path in the reference section, however, it is experimentally demonstrated that contact slightly displaces from the reference section (+0.1/−0.3 mm). This is related to the surface waviness and the manufacturing errors. Moreover, as in the case of the indexing errors effect, contact is more constant along the reference section when torque increases.

In low torque values and as the misalignment angle increases, deviations are observed in the number of teeth in contact (cases: $\Gamma = 100$ Nm, $\gamma = 3$–$5°$), and in the position of the tooth in contact (cases: $\Gamma = 100$ Nm, $\gamma = 5$–$7°$). These differences are caused by indexing errors and are almost negligible at higher torque values.

Concerning the centroid position, differences between the numerical and experimental results reach an error of 15% in extreme working conditions (high misalignment angle and low torque). Even so, these results closely represent the reality of highly crowned spherical gear couplings working in high misalignment applications.

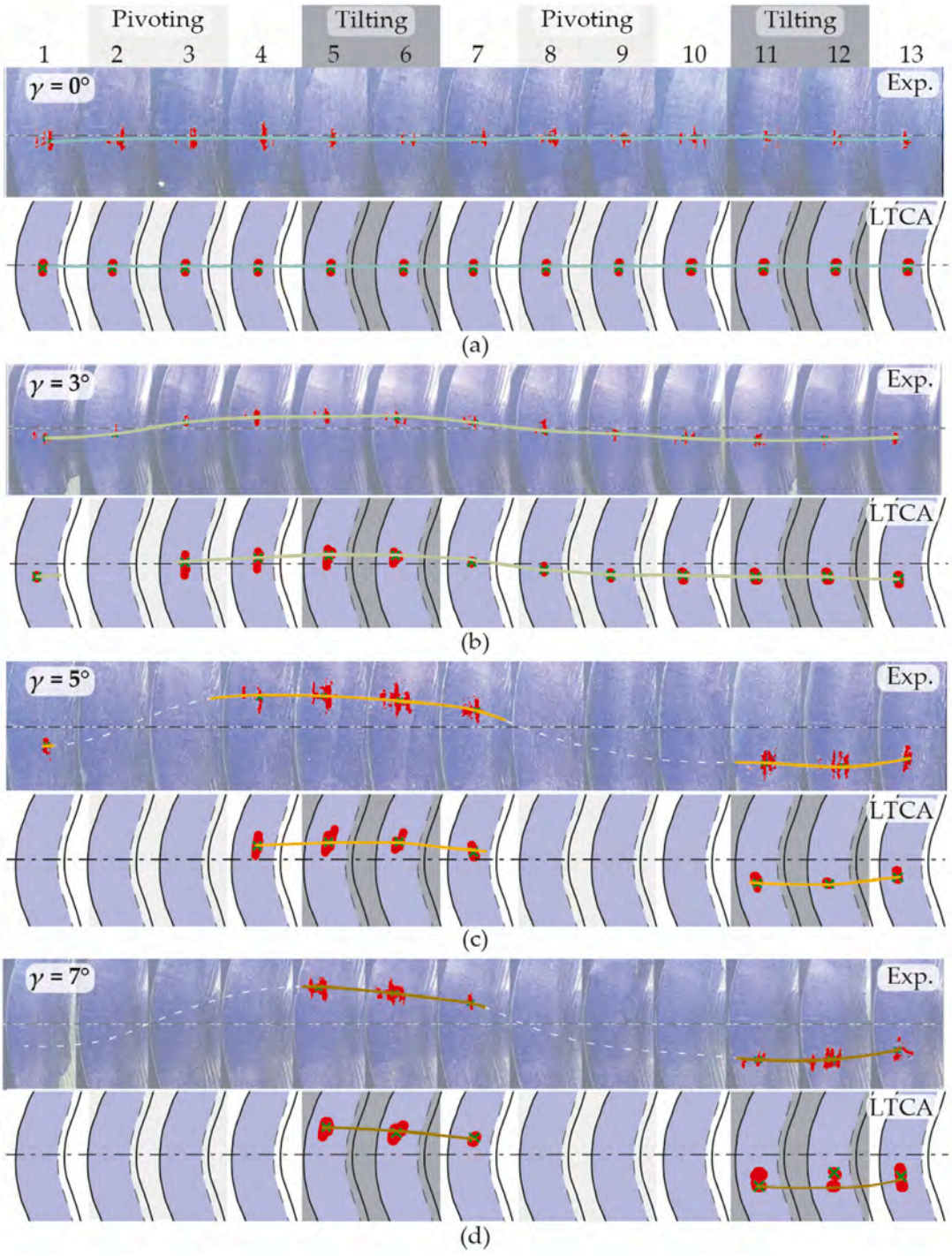

Fig. 15. Contact pattern at $\Gamma = 500$ Nm: experimental tests vs. loaded tooth contact analysis: (a) $\gamma = 0°$, (b) $\gamma = 3°$, (c) $\gamma = 5°$, and (d) $\gamma = 7°$.

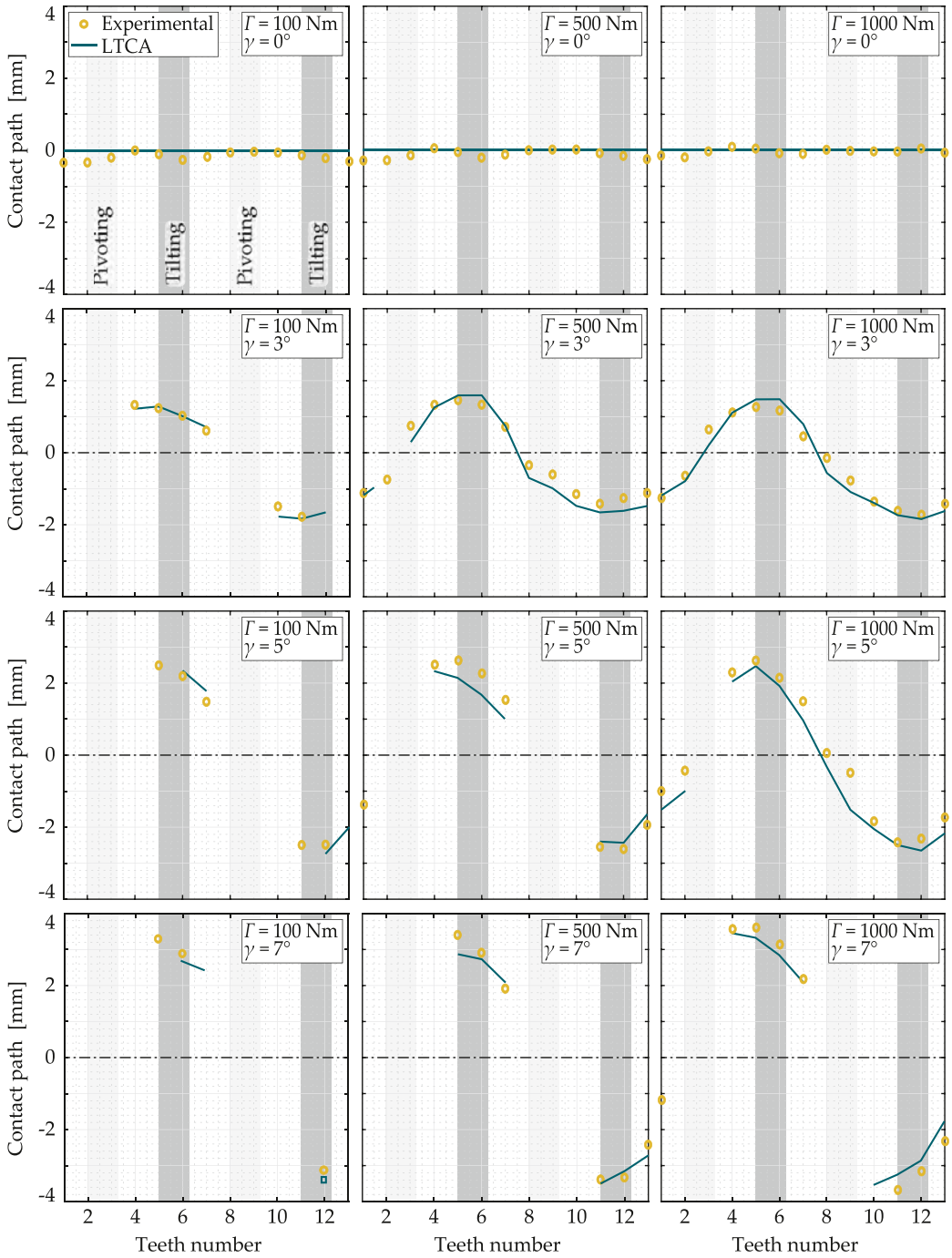

Fig. 16. Contact pattern centroid position evolution in terms of the applied torque and misalignment angle: experimental tests vs. loaded tooth contact analysis.

9. Conclusions

This paper presents a dedicated test rig to statically test in a controlled and repeatable manner spherical gear couplings at high misalignment angles (0°–10°). Moreover, a test technique to measure and study these types of gear couplings is described, from the geometry to the contact pattern. Finally, the obtained experimental results are discussed and compared to previously developed analytical and numerical models. From the results of this study the following conclusions can be drawn:

(1) The analytical geometry generation model presented in [3] is employed to generate the highly crowned spherical hub in agreement with the manufactured part geometry, with an accuracy that meets the manufacturing tolerance class 6 as defined in ISO 4156 [26]. The proposed measurement methodology has not been previously reported in literature related to crowned gear couplings.

(2) A novel experimental technique and post-processing algorithm to detect the contact pattern in spherical gear couplings has been proposed. Results show that such technique is adequate to determine the number of teeth in contact and the contact path of highly crowned spherical gear couplings, particularly when operating under high misalignment conditions.
(3) It is experimentally demonstrated that teeth in the pivoting angular position are the ones which first lose contact when the misalignment angle increases in spite of the indexing errors.
(4) It is experimentally verified that the contact path amplitude increases as the misalignment angle increases, and remains constant with torque variation.
(5) Experimental tests have shown that certain working conditions have considerably fewer teeth in contact than the conservative criterion considered in some standards. This has not been previously shown in the scientific literature.
(6) The loaded tooth contact analysis results obtained with the finite element model proposed in [22] agree well with the experimental results as they accurately capture the mechanical behavior at high misalignment angles, such as the variation of the contact position or the reduction of the number of teeth in contact.

This research has permitted to evaluate the geometry generation model and the loaded tooth contact analysis for highly crowned gear couplings with empirical data. All in all, it is important to remark on the necessity of an appropriate generation model that accurately represents the geometry of highly crowned spherical gear couplings, including its singularities, which could not be assessed with the existing geometry models in the scientific literature. Moreover, it has been shown that in spite of the theoretically accurate geometry representation, there are still manufacturing parameters, such as indexing errors or tooth surface waviness that need to be considered to improve the loaded tooth contact analysis results and reduce the differences with the experimental results.

Declaration of competing interest

The authors declare that they have no known competing interests or personal relationships that could have appeared to influence the work reported in this paper.

Data availability

Data will be made available on request.

Acknowledgments

The authors express their deep gratitude to the Economic Development, Sustainability, and Environment department of the Basque Government for the partial financial support of the research project BISUM of the Elkartek program (KK-2021/00089).

The authors would like to acknowledge the help of an undergraduate student Irene Berganzo, and the laboratory technician, Julen Maskariano for their valuable help during all the experimental testing.

References

[1] S. Hahn, Coupling connections and splines, in: Encyclopedia of Automotive Engineering, John Wiley & Sons, 2014, pp. 1–14, http://dx.doi.org/10.1002/9781118354179.auto094.
[2] M. Alfares, A. Falah, A. Elkholy, Clearance distribution of misaligned gear coupling teeth considering crowning and geometry variations, Mech. Mach. Theory 41 (10) (2006) 1258–1272, http://dx.doi.org/10.1016/j.mechmachtheory.2005.11.004.
[3] A. Iñurritegui, I. Gonzalez-Perez, A. Arana, J. Larrañaga, I. Ulacia, Computerized generation and tooth contact analysis of spherical gear couplings for high misalignment applications, Mech. Mach. Theory 164 (2021) http://dx.doi.org/10.1016/j.mechmachtheory.2021.104408.
[4] Y. Guan, X. Yang, Z. Fang, G. Chen, Comparative analysis of three geometric models for crown gear coupling, Mech. Mach. Theory 136 (2019) 269–283, http://dx.doi.org/10.1016/j.mechmachtheory.2019.02.016.
[5] F. Ohshima, S. Hirata, H. Yoshino, Study on tooth contact of gear couplings, Trans. Japan Soc. Mech. Eng. Ser. C 78 (786) (2012) 639–649, http://dx.doi.org/10.1299/kikaic.78.639.
[6] K. Mitome, T. Okuda, T. Ohmachi, T. Yamazaki, Development of a new hobbing of spherical gear, Trans. Japan Soc. Mech. Eng. Ser. C 66 (646) (2000) 1975–1980, http://dx.doi.org/10.1299/kikaic.66.1975.
[7] L. Chao, C. Tsay, Contact characteristics of spherical gears, Mech. Mach. Theory 43 (10) (2008) 1317–1331, http://dx.doi.org/10.1016/j.mechmachtheory.2007.10.008.
[8] L. Kelemen, J. Szente, Two mathematical models for generation of crowned tooth surface, Sci. World J. 2014 (2014) http://dx.doi.org/10.1155/2014/641091.
[9] American Gear Manufacturers Association, AGMA 945-1-B20: Splines – Design and Application, American Gear Manufacturers Association, Virginia, 2020.
[10] G. Henriot, J. Boisset, Accouplements, alignement des axes, in: Engrenages: Conception, Fabrication, Mise En Oeuvre, fifth ed., Dunod, 1983, pp. 796–818.
[11] R. Cedoz, M. Chaplin, Design Guide for Involute Splines, Society of Automotive Engineers, 1994.
[12] International Organization for Standardization, ISO 21771: Gears-Cylindrical Involute Gears and Gear Pairs-Concepts and Geometry, International Organization for Standardization, 2007.
[13] Y. Guan, Z. Fang, X. Yang, G. Chen, Tooth contact analysis of crown gear coupling with misalignment, Mech. Mach. Theory 126 (2018) 295–311, http://dx.doi.org/10.1016/j.mechmachtheory.2018.04.019.
[14] B. De Caires, Variation Analysis of Involute Spline Tooth Contact (Ph.D. thesis), Brigham Young University, 2006.
[15] Y. Guan, Z. Fang, X. Yang, G. Chen, Effects of misalignment and crowning on contact characteristics of crown gear coupling, J. Mech. Eng. Sci. (2018).
[16] J. Hong, D. Talbot, A. Kahraman, Load distribution analysis of clearance-fit spline joints using finite elements, Mech. Mach. Theory 74 (2014) 42–57, http://dx.doi.org/10.1016/j.mechmachtheory.2013.11.007.
[17] S. Medina, A.V. Olver, Regimes of contact in spline couplings, J. Tribol. 124 (2) (2002) 351–357, http://dx.doi.org/10.1115/1.1403456.
[18] J. Silvers, C. Sorensen, K. Chase, A New Statistical Model for Predicting Tooth Engagement and Load Sharing in Involute Splines, AGMA - 10FTM07, 2010.

[19] W. Herbstritt, J. Paluh, Mill spindle advanced gear design, Iron Steel Eng. 76 (7) (1999) 44–48.
[20] F. Curà, A. Mura, M. Gravina, Load distribution in spline coupling teeth with parallel offset misalignment, Proc. Inst. Mech. Eng. C 227 (10) (2013) 2195–2205, http://dx.doi.org/10.1177/0954406212471916.
[21] I. Ulacia, J. Larrañaga, A. Arana, A. Iñurritegui, J. Elizegi, Fatigue life prediction of spherical gear couplings, in: American Gear Manufacturers Association Fall Technical Meeting 2018, Illinois, 2018, pp. 202–207.
[22] A. Iñurritegui, J. Larrañaga, A. Arana, I. Ulacia, Load distribution and tooth root stress of highly crowned spherical gear couplings working at high misalignment angles, Mech. Mach. Theory 179 (2023) http://dx.doi.org/10.1016/j.mechmachtheory.2022.105104.
[23] K. Nakashima, Teeth contact behaviour and load distribution of gear couplings, Trans. Jpn. Soc. Mech. Eng. 502 (Part C 54) (1988) 1302–1307, http://dx.doi.org/10.1299/kikaic.54.1302.
[24] D. Dudley, When splines need stress control, Prod. Eng. 28 (1957) 56–59.
[25] D.I. für Normung, DIN 5466: Splined Joints, Calculation of Load Capacity, Deutsches Institut für Normung, 2002.
[26] International Organization for Standardization, ISO 4156: Straight Cylindrical Involute Splines, International Organization for Standardization, Geneve, 2005.
[27] R. Beckmann, Beitrag zur Auslegung und Konstruktion von Balligzahn-Kupplungen (Ph.D. thesis), Chemmitz Technology University, 2005.
[28] J.R. Mancuso, Couplings and Joints: Design, Selection and Application, Technology & Engineering. M. Dekker, 1986.
[29] C. Bünder, Analyse der Beanspruchungen der Verzahnung von Zahnkupplungen (Ph.D. thesis), Technische Universität Dresden, 2000.
[30] F. Paddon, Application and selection of gear type spindles, Iron Steel Eng. (1960) 91–100.
[31] J. Larrañaga, A. Arana, I. Ulacia, J. Esnaola, I. Torca, Misalignment effect on contact pressure and tooth root strength of spline couplings, in: 5th International Conference on Power Transmission-BAPT, Ohrid, Macedonia, 2016, pp. 1–6.
[32] P. Ku, M. Valtierra, Spline wear-effects of design and lubrication, J. Eng. Ind. 97 (4) (1975) 7, http://dx.doi.org/10.1115/1.3438738.
[33] Y. Guo, S. Lambert, R. Wallen, R. Errichello, J. Keller, Theoretical and experimental study on gear-coupling contact and loads considering misalignment, torque and friction influences, Mech. Mach. Theory 98 (2016) 242–262, http://dx.doi.org/10.1016/j.mechmachtheory.2015.11.015.
[34] V. Cuffaro, F. Curà, A. Mura, Analysis of the pressure distribution in spline couplings, Proc. Inst. Mech. Eng. C 226 (12) (2012) 2852–2859, http://dx.doi.org/10.1177/0954406212440670.
[35] M. Benatar, D. Talbot, A. Kahraman, An experimental investigation of the load distribution of spline joints under gear loading conditions, J. Adv. Mech. Des. 11 (6) (2017) 1–12, http://dx.doi.org/10.1299/jamdsm.2017jamdsm0084.
[36] D. Margineanu, E. Margineanu, E. Zăbavă, A.M. Fârtă, Analytic and experimental study of the load distribution on spline joints length considering the contact rigidity of the bearing surfaces, Appl. Mech. Mater. 162 (March) (2012) 74–83, http://dx.doi.org/10.4028/www.scientific.net/AMM.162.74.
[37] S. Leen, Fretting fatigue and wear of spline couplings: from laboratory testing to industrial application through computational modelling, in: Wear in Advanced Engineering Applications and Materials, World Scientific, 2022, pp. 1–44, http://dx.doi.org/10.1142/9781800610699.
[38] Y. Guan, J. Chen, Z. Fang, S. Hu, A quick multi-step discretization and parallelization wear simulation model for crown gear coupling with misalignment angle, Mech. Mach. Theory 168 (2022) http://dx.doi.org/10.1016/j.mechmachtheory.2021.104576.
[39] A. Iñurritegui, A. Arana, J. Larrañaga, I. Ulacia, Spherical gear coupling design space analysis for high misalignment applications, Mech. Mach. Theory 173 (2022) 104837, http://dx.doi.org/10.1016/j.mechmachtheory.2022.104837.
[40] R. Baker, Durability of Steel Spline Couplings (Ph.D. thesis), University of London, 2005.
[41] V. Cuffaro, F. Curà, A. Mura, Experimental investigation about surface damage in straight and crowned misaligned splined couplings, Key Eng. Mater. 577–578 (2014) 353–356, http://dx.doi.org/10.4028/www.scientific.net/KEM.577-578.353.
[42] Y. Guan, J. Chen, H. Chen, S. Hu, X. Liu, An experimental investigation of contact characteristics of crown gear coupling with angular misalignment, J. Adv. Mech. Des. 5 (5) (2021) http://dx.doi.org/10.1299/jamdsm.2021jamdsm0062.
[43] Deutsches Institut für Normung, DIN 3972: Reference profiles of gear-cutting tools for involute tooth systems according to DIN 867, 1952, pp. 1–2.
[44] I. Gonzalez-Perez, P. Guirao-Saura, A. Fuentes-Aznar, Application of the bilateral filter for the reconstruction of spiral bevel gear tooth surfaces from point clouds, Trans. ASME, J. Mech. Des. 143 (5) (2021) http://dx.doi.org/10.1115/1.4048219.
[45] J. D'Errico, Interparc, 2011.
[46] F. Litvin, A. Fuentes, Gear Geometry and Applied Theory, second ed., Cambridge University Press, 2004, p. 818.
[47] MSC.Software, Marc 2019 - user's guide, 2019.
[48] M. Octrue, F. Blanc, D. Ghribi, Guide de Demensionnement Des Accouplements à Dentures BombÉEs, CETIM, 2014.
[49] X. Jin, J. Han, K-Means clustering, in: C. Sammut, G. Webb (Eds.), Encyclopedia of Machine Learning, Springer US, Boston, MA, 2010, pp. 563–564, http://dx.doi.org/10.1007/978-0-387-30164-8_425.
[50] International Commission on Illumination, Recommendations on Uniform Color Spaces, Color-Difference Equations, Psychometric Color Terms, Vol. CIE publication, Bureau central de la CIE, 1978.
[51] X. Zhang, B. Wandell, A spatial extension of CIELAB for digital color-image reprodcution, J. Soc. Inf. Disp. 5 (1) (1997) 61–63, http://dx.doi.org/10.1889/1.1985127.
[52] H. Globig, Analyse der Rückstellwirkungen von Zahnkupplungen (Ph.D. thesis), 2010, http://dx.doi.org/10.1056/NEJMcpc1607091.